

Modeling creep and anelasticity in particle strengthened alloys with strain gradient crystal plasticity

Citation for published version (APA):

Ertürk, I. (2012). *Modeling creep and anelasticity in particle strengthened alloys with strain gradient crystal plasticity*. [Phd Thesis 1 (Research TU/e / Graduation TU/e), Mechanical Engineering]. Technische Universiteit Eindhoven. <https://doi.org/10.6100/IR732572>

DOI:

[10.6100/IR732572](https://doi.org/10.6100/IR732572)

Document status and date:

Published: 01/01/2012

Document Version:

Publisher's PDF, also known as Version of Record (includes final page, issue and volume numbers)

Please check the document version of this publication:

- A submitted manuscript is the version of the article upon submission and before peer-review. There can be important differences between the submitted version and the official published version of record. People interested in the research are advised to contact the author for the final version of the publication, or visit the DOI to the publisher's website.
- The final author version and the galley proof are versions of the publication after peer review.
- The final published version features the final layout of the paper including the volume, issue and page numbers.

[Link to publication](#)

General rights

Copyright and moral rights for the publications made accessible in the public portal are retained by the authors and/or other copyright owners and it is a condition of accessing publications that users recognise and abide by the legal requirements associated with these rights.

- Users may download and print one copy of any publication from the public portal for the purpose of private study or research.
- You may not further distribute the material or use it for any profit-making activity or commercial gain
- You may freely distribute the URL identifying the publication in the public portal.

If the publication is distributed under the terms of Article 25fa of the Dutch Copyright Act, indicated by the "Taverne" license above, please follow below link for the End User Agreement:

www.tue.nl/taverne

Take down policy

If you believe that this document breaches copyright please contact us at:

openaccess@tue.nl

providing details and we will investigate your claim.

**Modeling Creep and Anelasticity in Particle Strengthened
Alloys with Strain Gradient Crystal Plasticity**

This research was carried out within the project WP IV-C-I of the MicroNed program

CIP-DATA LIBRARY TECHNISCHE UNIVERSITEIT EINDHOVEN

Ertürk, İsa

Modeling Creep and Anelasticity in Particle Strengthened Alloys with Strain Gradient Crystal Plasticity

Eindhoven University of Technology, 2012.
Proefschrift.

A catalogue record is available from the Eindhoven University of Technology Library:
ISBN: 978-90-386-3145-5

Copyright © 2012 by İsa Ertürk. All rights reserved.

This thesis is prepared with L^AT_EX 2_ε

Cover design: Atike Dicle Pekel (Atike Design)

Printed by the Universiteitsdrukkerij TU Eindhoven, Eindhoven, The Netherlands.

Modeling Creep and Anelasticity in Particle Strengthened Alloys with Strain Gradient Crystal Plasticity

PROEFSCHRIFT

ter verkrijging van de graad van doctor aan de Technische Universiteit Eindhoven, op gezag van de rector magnificus, prof.dr.ir. C.J. van Duijn, voor een commissie aangewezen door het College voor Promoties in het openbaar te verdedigen op woensdag 30 mei 2012 om 16.00 uur

door

İsa Ertürk

geboren te Samsun, Turkije

Dit proefschrift is goedgekeurd door de promotor:

prof.dr.ir. M.G.D. Geers

Copromotor:

dr.ir. J.A.W. van Dommelen

Contents

Summary	vii
1 Introduction	1
2 Thermodynamical aspects of strain gradient crystal plasticity theories	5
2.1 Introduction	5
2.2 Strain gradient crystal plasticity frameworks	8
2.2.1 Physically motivated strain gradient crystal plasticity models of Evers et al. and Bayley et al.	8
2.2.2 A thermodynamically consistent strain gradient crystal plasticity theory by Gurtin	12
2.3 Thermodynamical aspects of Evers-Bayley models	16
2.3.1 Micro-stress vector from back stress definition	16
2.3.2 Defect energy function	18
2.3.3 Micro-boundary conditions	19
2.4 Discussion and concluding remarks	22
3 Multiphysical simulations with a gradient theory of crystal plasticity	25
3.1 Introduction	25
3.2 Strain gradient crystal plasticity formulation	28
3.3 Electro-mechanical transducer elements	30
3.4 Multiphysical simulations by using the SGCP theory	32
3.4.1 Thin film inelasticity	32
3.4.2 Simulation of electrostatic beam bending experiments	38
3.5 Summary and concluding remarks	42
3.6 Appendix: Modeling of electric domain and contact in the simulations	44
4 Modeling time and scale dependent phenomena in particle strengthened alloys	47
4.1 Introduction	48
4.2 Material background	50
4.3 Plastic flow in particle strengthened alloys	51
4.3.1 Interaction of dislocations with particles	52
4.3.2 Dislocation line tension	63
4.3.3 Velocity of dislocations	64
4.4 Strain gradient crystal plasticity model	69
4.5 Constitutive modeling of crystallographic slip	73
4.5.1 Flow rule for pure metals	74

4.5.2	Flow rule for particle strengthened alloys	77
4.6	Analysis of the new model for crystallographic slip	81
4.6.1	Pure metals	81
4.6.2	Alloys: without dislocation climb	81
4.6.3	Alloys: with dislocation climb	88
4.7	Application in strain gradient crystal plasticity framework	91
4.7.1	Thin film inelasticity	91
4.7.2	Simulation of micro-clamp beam bending experiment	98
4.8	Discussion	102
4.9	Summary and concluding remarks	106
5	Analysis of the time dependent behavior of a capacitive RF-MEMS switch	109
5.1	Introduction	109
5.2	A strain gradient crystal plasticity framework for particle hardened alloys	110
5.2.1	Strain gradient crystal plasticity formulation	111
5.2.2	Dislocation-dislocation interactions	114
5.2.3	Dislocation-particle interactions	116
5.3	Multiphysical simulations with the extended SGCP model	121
5.4	Discussion and concluding remarks	128
6	Conclusion and recommendations	131
	Bibliography	135
	Samenvatting	147
	Acknowledgments	149
	Curriculum Vitae	151

Summary

Modeling creep and anelasticity in particle strengthened alloys with strain gradient crystal plasticity

For small material volumes, size effects, e.g. due to the interface constraints or heterogeneous strain fields, may significantly affect the mechanical behavior of metals such that a deformation mechanism that is less important for the response in bulk form may become decisive for the performance of the material. Such second order effects were observed experimentally in the last two decades and form engineering challenges for the development and production of high-end modern technology. For example, creep and anelasticity observed in metallic thin film components of capacitive RF-MEMS switches may lead to time dependent deviations from the design specifications of the device. The characterization and understanding of the mechanical behavior of the material is indispensable to overcome the reliability issues of these switches which hinder their full commercialization. In this thesis, a numerical framework is presented for modeling the time dependent mechanical behavior of thin films made of particle strengthened fcc alloys as an extension of a previously developed strain gradient crystal plasticity (SGCP) model (here referred to as Evers-Bayley type model) for pure fcc metals. A physically based flow rule for crystallographic slip is developed based on the dislocation-dislocation and dislocation-particle interaction mechanisms. The extended SGCP framework is intrinsically able to capture the effect of an inhomogeneous distribution of geometrically necessary dislocation densities on the material behavior via the formulation of a back stress incorporating a material length scale.

In chapter 2, the physically based Evers-Bayley type model and a thermodynamically consistent strain gradient theory of crystal plasticity by Gurtin are compared by deriving micro-stresses for the Gurtin type formulation based on the energetic back stresses of the Evers-Bayley type models, incorporating dislocation-dislocation interactions. It is shown that the defect energy function for a micro-stress that contains the physical description of the interaction between dislocations of different slip systems has a more complicated form than those suggested in literature and is possibly non-convex. It is also shown that similar boundary conditions can be defined for the Evers-Bayley type and Gurtin type models despite their different additional field equations within the finite element context. Thereafter, in chapter 3, the SGCP model is employed in electromechanical finite element simulations of bending of polycrystalline thin beams made of a pure metal and a two phase alloy with a focus on the description of anelastic material behavior. Simulation results obtained with the SGCP model show a macroscopic strain recovery over time following the load removal. However, a detailed analysis demonstrates that the anelastic relaxation time and strength have no solid physical basis. A comparison of the results with experimental data implies that a single de-

formation mechanism may not be adequate for capturing the material response. Moreover, the slip law falls short in describing the behavior of a particle enhanced material.

Subsequently, an extension of the SGCP model for a more realistic description of the time dependent mechanical behavior of two phase alloys, i.e. creep and anelasticity, is given in chapter 4 and its application in multiphysical simulations of a capacitive RF-MEMS switch is presented in chapter 5. A new constitutive rule for crystallographic slip is developed by considering dislocation-dislocation interactions and three distinct dislocation-particle interactions: i) the Orowan process, ii) the Friedel process and iii) the climb of edge dislocations over particles. The new constitutive rule is obtained by the combination of separate slip laws for each type of interaction and is built based on the physically well-founded Orowan type rate equation. A flow rule for the slip rate of mobile dislocations governed by dislocation-dislocation interactions is written by taking into account the jerky and continuous glide regimes of dislocations. Slip laws corresponding to the Orowan and Friedel processes are constructed by considering thermally activated dislocation motion. The climb of edge dislocations is described via a thermal detachment model. Results of finite element simulations of bending of a single crystalline thin beam and a micro-clamp experiment with the extended SGCP model show that creep and anelastic behavior of a metallic thin film can be predicted with the extended SGCP framework. The amounts of the plastic deformation, anelastic recovery strength and associated relaxation times strongly rely on particle properties, the diffusional rate and the magnitude of internal stresses. The results of the simulations of the micro-clamp experiment imply that inhomogeneous material diffusion may play an important role in the anelastic behavior of polycrystalline thin films. The results also suggest that the internal stress formulation of the extended SGCP may need to be extended by considering additional sources of internal stresses. The extended SGCP framework is applied to analyse the behavior of a capacitive RF-MEMS switch in multiphysical simulations. The electrodes of the switch are considered to be made of a metal thin film with incoherent second phases and have a polycrystalline structure with columnar grains through the thickness and passivated surfaces. The variation of the gap between the electrodes over time is analyzed. First, the influences of particle size, volume fraction, surface constraints and film thickness on the performance of the switch after a loading and unloading cycle are studied. Then, the effects of cyclic loading and the duration of the unloaded state between sequential cycles are investigated. The results show that the residual changes in the gap and the amount and rate of time dependent recovery after the load removal are highly sensitive to the microstructure and the film thickness. The smallest amounts of permanent deformation and anelastic recovery are obtained with an upper electrode made of a relatively thin film which has a surface passivation and involves small incoherent particles with a relatively large volume fraction. Furthermore, the simulations revealed that the maximum residual change of the gap measured after completion of the unloading stage of each cycle saturates within a few cycles. A shorter duration of the unloaded state between successive loading-unloading cycles leads to a larger maximum residual gap change. Due to the decreasing gap, the pull-in voltage also decreases within a few cycles and shows a tendency to level off to a certain value. However, the release voltage does not seem to be as sensitive to the residual deformations as the pull-in voltage.

Finally, in chapter 6, the conclusions and recommendations for a future work are given.

Introduction

Microelectromechanical systems (MEMS) could be applied as switches in wireless networks, e.g. to satisfy the need for high performance at switching between the different operation bands in (next generation) smart phones [1]. RF-MEMS switches are superior to the currently used diode based solid state switches and macromechanical switches due to their small size, high linearity, high isolation, low insertion loss, low power consumption and ease of design [1]. Besides being still more expensive than their conventional and larger counterparts [1], one of the most important issues for the commercialization of RF-MEMS is currently their reliability, which is mainly dependent on the mechanical performance of their components.

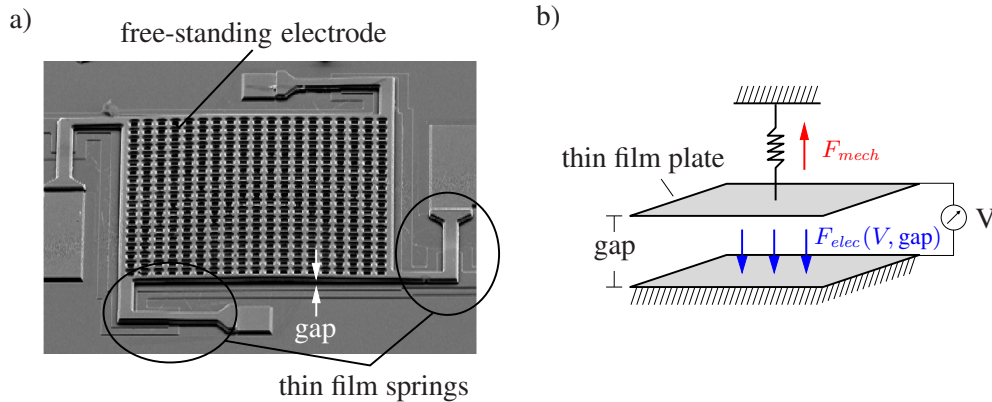


Figure 1.1: a) SEM picture of a capacitive RF-MEMS switch. Courtesy of Philips. b) Schematic representation of a capacitive RF-MEMS switch. $F_{elec}(V, gap)$ represents the electrostatic force acting on the plate, which is determined by the size of the gap and the potential difference between the plates. F_{mech} denotes the mechanical restoring force provided by the stiffness of the springs that hold the upper plate.

Capacitive RF-MEMS switches, see figure 1.1a, are one of the two common type of MEMS switches (the other is of Ohmic type). These switches have a structure that is similar to parallel plate capacitors and allow the modulation of signal transmission by large capacitance changes [1] created through the vertical motion of the free-standing upper plate under the electrostatic

forces emerging from the application of a potential difference to the plates, cf. figure 1.1b. The upper plate of the capacitive RF-MEMS switch is held in place by means of cantilever springs, see figure 1.1a, which are made of a metallic thin film with a few micrometers thickness in this particular case. A typical vertical displacement response of the free standing plate of a capacitive RF-MEMS switch with respect to the applied voltage is given in figure 1.2b as a function of time. As the voltage is increased, the upper plate starts to move downwards and the gap is decreased. At a device specific voltage, the pull-in voltage, the upper plate snaps on the dielectric layer covering the ground electrode and the switch is fully closed. The closed configuration of the switch is also illustrated in figure 1.2a. The dielectric layer ensures a small separation distance between the electrodes in the closed state, which allows the generation of a large capacitance, enabling to regulate the signal transmission. In the unloading stage, the upper plate is forced to return to its original position under the influence of the restoring forces provided by the elastic energy stored in the springs during the actuation. Upon opening a fully closed switch, another structural instability occurs at the release voltage at which the upper electrode springs back, leading to a sudden increase in the gap.

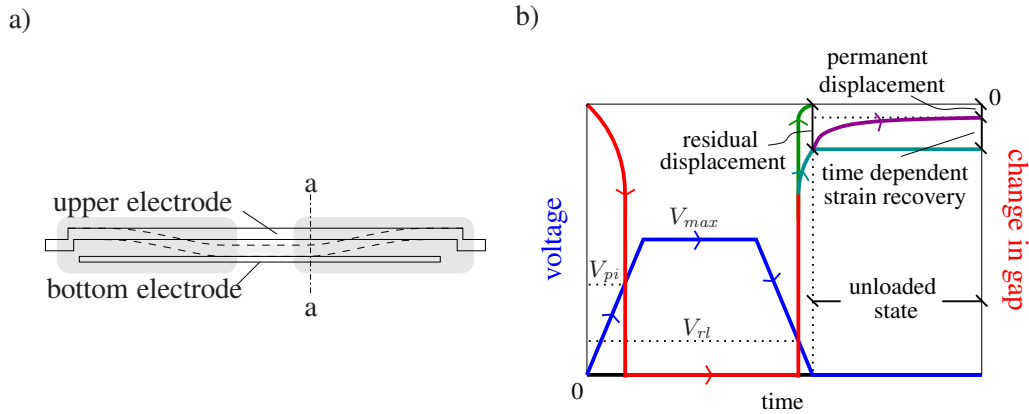


Figure 1.2: a) Depiction of vertical position of the upper plate of a capacitive RF-MEMS switch when the switch is "on" (solid line) and "off" (light shaded area with dashed line). Dark shaded areas highlight hinge regions subjected to relatively large stress levels. Hence residual deformations easily emerge in these regions, leading to malfunctioning of the switch. b) Illustration of the vertical displacement of a part of the upper electrode located along $a - a$ axis with respect to time and the applied potential difference during a loading-unloading cycle and afterwards. V_{pi} , V_{rl} and V_{max} stand for pull-in voltage, release voltage and the maximum applied voltage, respectively. Green and cyan colors show displacement for a completely elastic and an elasto-plastic behavior of the springs. In case of anelastic strain recovery, the residual change in the gap will decrease over time, denoted by magenta line.

The final gap between the electrodes in the unloaded state is largely controlled by the mechanical performance of the thin film components, see figure 1.2b. In the ideal case of the springs (and the plate) behaving fully elastic, the upper plate returns to its original position upon the load removal and the initial gap width is preserved. However, in practice, the relatively large stress levels in the springs (e.g. in the closed state, see figure 1.2a) in combination with prolonged actuation times and the effect of service conditions, such as high temperatures, may trigger plastic activity in the springs, leading to residual changes in the clearance between the plates when the switch is opened [2]. Although such a behavior closely resembles creep phenomena in bulk materials, experimental evidences [3–6] imply that size effects may be important for the mechanical

performance of the RF-MEMS switches. Moreover, it was found that in some cases, the residual deformation of free-standing thin films can be fully recovered over time [7], also observed in the form of an anelastic stress recovery following the load reduction [8]. Investigations [8–12] showed that above mentioned creep and anelastic behavior of metallic thin films are closely related to the (microstructural) composition of the material such as grain size, imperfections, size and type of particles involved in the matrix in case of alloys.

Permanent and evolving changes in the unloaded state of thin film components of capacitive RF-MEMS switches, see figures 1.2b and 1.3, pose additional challenges for the prediction of the effective service life of these devices. Therefore, the characterization and understanding of the mechanical behavior of the free-standing thin films for the service conditions of RF-MEMS devices is essential for their full commercialization.

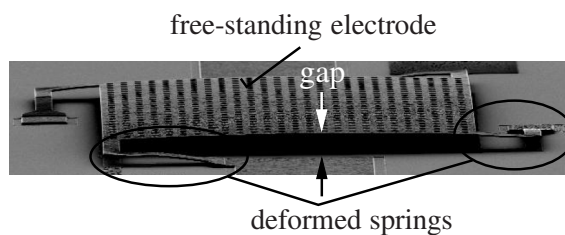


Figure 1.3: a) SEM picture of a deformed RF-MEMS switch. Courtesy of Philips. The excessive permanent deformation of the thin film springs may easily lead to device malfunctioning.

Scope and outline of the thesis

This thesis addresses the development of a physically motivated mathematical model for the time and scale dependent mechanical behavior of thin films made of precipitation strengthened fcc alloys and the application of it to study mechanical behavior of an RF-MEMS switch under operating conditions. A recently developed strain gradient crystal plasticity (SGCP) model (here referred to as Evers-Bayley type model) for pure fcc metals constituted the starting point of this work. Within this framework, the crystallographic slip is modeled by thermally activated dislocation glide and described via a modified, Arrhenius type rate equation. A back stress in terms of the gradients of geometrically necessary dislocation densities is employed to predict the corollaries of the size effect arising from strain gradients on the material behavior.

In the second chapter of this thesis, the thermodynamical aspects of the Evers-Bayley type model are discussed through a direct comparison with a thermodynamically consistent strain gradient theory of crystal plasticity by Gurtin. The similarities and differences between the energetic microstresses which are derived for the Gurtin type formulation based on the physical description of the back stresses of the Evers-Bayley type models and those suggested in literature are analyzed. Furthermore, the boundary conditions definable within the Evers-Bayley type and Gurtin type models are examined.

The third chapter deals with the investigation of the capabilities of the SGCP model for the description of anelastic material behavior in RF-MEMS structures. For this purpose, multiphysical simulations are conducted for electrostatic bending of thin beams of a pure metal and a two phase

alloy. The simulation results are studied in comparison with the experimentally available data for the implications for modeling of anelastic strain recovery in precipitation strengthened metallic thin films.

Next, in the fourth chapter, an extensive review of literature about the mechanisms of plastic slip in particle enhanced alloys is given. Then, the SGCP model is extended to obtain a more realistic description of time dependency in the mechanical behavior of two phase alloys, i.e. creep and anelasticity. The flow rule is replaced by the physically well-founded Orowan type rate equation. An expression is written for the velocity of mobile dislocations based on thermally activated dislocation glide and a viscous drag controlled motion. Three different particle overcoming mechanisms, i.e. the Orowan process, the Friedel process and a thermally activated detachment model for the climb of edge dislocations are incorporated into the new flow rule for dislocation-particle interactions. After analyzing the constitutive behavior described by the extended SGCP model at the material point level, finite element simulations of bending of a single crystalline beam and micro-clamp experiment on a polycrystalline beam are performed to evaluate the time dependent material behavior predicted at macro scale, including the influence of inhomogeneous material diffusion.

In the fifth chapter, the extended SGCP model is utilized to analyze how the time and scale dependent behavior of the thin film components of a capacitive RF-MEMS switch may influence the performance of the switch. In doing so, a numerical model of the device is generated by assuming that its free-standing electrode is made of a polycrystalline metal thin film with columnar grains through the thickness and containing incoherent second phases. Two sets of multi-physical finite element simulations of the switch are done. In the first set, the effects of particle size, volume fraction, surface constraints and film thickness on the mechanical behavior are investigated by referring to the residual changes in the gap between the plates and its variation over time after a loading and unloading cycle. In the second set of simulations, the mechanical behavior the switch under repeated loading-unloading cycles is examined with a focus on the duration of the unloaded state between sequential loading-unloading cycles.

In the last chapter, the main conclusions are summarized and recommendations are given for future work.

Thermodynamical aspects of strain gradient crystal plasticity theories

Abstract

This chapter focuses on the unification of two frequently used and apparently different strain gradient crystal plasticity frameworks: (i) the physically motivated strain gradient crystal plasticity models proposed by Evers et al. [13, 14] and Bayley et al. [15, 16] (here referred to as Evers-Bayley type models), where a physical back stress plays the most important role and which are further extended here to deal with truly large deformations, and (ii) the thermodynamically consistent strain gradient crystal plasticity model of Gurtin (2002-2008) (here referred to as the Gurtin type model), where the energetic part of a higher order micro-stress is derived from a non-standard free energy function. The energetic micro-stress vectors for the Gurtin type models are extracted from the definition of the back stresses of the improved Evers-Bayley type models. The possible defect energy forms that yield the derived physically-based micro-stresses are discussed. The duality of both type of formulations is shown further by a comparison of the micro-boundary conditions. As a result, this paper provides a direct physical interpretation of the different terms present in Gurtin's model.

2.1 Introduction

Continuous developments in the manufacturing of high-tech devices rely on the use of functional components, such as micro-electromechanical systems (MEMS). The prediction of service life (and reliability) of such devices depends on the fundamental understanding of the underlying material behavior. It has been experimentally shown [3–5] that on the scale of several micrometers and below, crystalline materials behave different from their bulk equivalent due to microstructural effects (e.g. grain size, lattice defects and impurities), gradient effects (e.g. lattice curvature due to a non-uniform deformation field) and surface constraints (e.g. hard coatings or free interfaces). These effects may lead to a stronger or weaker mechanical response depending on the size and the unique microstructure of a material [17]. For discussions and recent experimental analyses of the size dependent material behavior, one is referred to [18–25]. This scale dependent material

response can not be captured by standard continuum theories of plasticity since they are lacking material length scales in their formulations. One way to include a scale dependent mechanical response is the incorporation of strain gradients into the constitutive laws [26–29], which is the starting point of most strain gradient plasticity theories.

Strain gradient plasticity theories can be classified into two groups, i.e. higher and lower order theories, according to the method of incorporation of the strain gradients. The lower order theories include governing equations with the same order as those in standard continuum plasticity theories since no additional stresses arising from gradients of the deformation are taken into account; the strain gradients enter only into the hardening equations. Hence, no additional boundary conditions are necessary [30–36]. The higher order theories are based on the consideration of higher order stresses conjugate to strain gradients and their work (or power) contributions [3, 13–16, 37–47]. Therefore, higher order gradient theories require additional governing equations and boundary conditions.

Here, two types of higher order strain gradient theories of crystal plasticity with different formulations based on geometrically necessary dislocation (GND) densities are considered: (i) a physically based strain gradient crystal plasticity model, initially proposed by Evers et al. [13, 14] and extended by Bayley et al. [15, 16], here referred to as the Evers-Bayley type models, and (ii) the model derived based on thermodynamics by Gurtin [37, 43–45], further referred to as the Gurtin type model.

In the Gurtin type model, a higher order *micro-stress vector* that is intrinsically comprised of an energetic and a dissipative part and is conjugate to the gradient of slip rate per slip system is introduced in the formulation of the internal power expenditure in consistency with a *micro-force balance* equation for each slip system. The corresponding micro-traction, which is conjugate to the slip rate, appears in the definition of the external power. The model was implemented within a finite element framework by taking the slip rates on the slip system level as independent variables in addition to the displacements and using the micro-force balance equation as the additional governing equation.

In the Evers-Bayley type models, the *back stress* plays the main role, and originates from a physical description of the internal stress field resulting from the accumulation of the stress fields of individual dislocations due to the elastic distortion of the crystal lattice. In the model of Evers et al. [13, 14], it is formulated by considering the stress fields due to the GNDs of only the slip system itself, which is also called as the self-internal back stress formulation. This formulation is extended in the model of Bayley et al. [15, 16] by also including the contributions of the GNDs on other slip systems, so as to describe the energetic dislocation interactions more realistically, which is referred to as the full-internal back stress formulation. These models are implemented within a finite element context by considering the GND densities as the additional degrees of freedom and by employing the GND density balance equations as the extra field equations.

Recently, [46, 47] compared Gurtin’s framework to several physically based gradient crystal plasticity theories, including their own model that was derived from conventional single crystal plasticity for small deformations. It was shown that for the cases where the back stress relation for a slip system can be expressed as the divergence of a vector quantity, the micro-stress vector of the Evers-Bayley type models (there referred as non-work-conjugate formulations) can be recast into the form of Gurtin type models (there referred to as work-conjugate type formulations). Furthermore, the equivalence of the additional field equations, the micro-force balance law for work-conjugate and the GND density balance equation for the non-work-conjugate models, was trivially shown. When the micro-stresses resulting from the back stress relations are used together

with identical boundary conditions, both type of models capture the same material length scale effects, leading to the same results, which assures the thermodynamical consistency of the non-work-conjugate formulations. Their model was extended to finite deformations in [38]. However, their back stress definitions and therefore the micro-stresses derived from them do not include the energetic interactions between the GNDs of the different slip systems, which may be far from the description of the real dislocation mechanisms in metals. Hence, the model in [38] is comparable to the model of Evers et al. [13, 14], which omits the energetic interactions between slip planes in the definition of the back stress and also their micro-stress vector is similar to the micro-stress derived from the model of Evers et al. [13, 14] and to the one of Gurtin [37].

In the current study, an enhancement in the formulations of the Evers-Bayley type models is made by changing the domain with respect to which the gradient operators as used for crystallographic slip and dislocation densities, are defined from the reference to the intermediate configuration. Up to now, the Evers-Bayley type models were used for problems involving small plastic strains only. However, when the plastic deformations are large, spatial distances in this configuration are affected by the slip on multiple slip systems whereas the orientation of the lattice in the intermediate configuration remains unchanged. The enhancement allows to apply them for truly large plastic deformations as well. Then, as the main focus of interest of this work, the similarities and differences of the Gurtin type and the Evers-Bayley type models are discussed for the purpose of unification and at the end, for revealing the thermodynamical consistency of the latter type models. The starting point is the extraction of the energetic micro-stress vectors for the Gurtin type model from the *physical* back stress expressions of the Evers-Bayley type models and the discussion of the defect energy functions from which these micro-stresses can be derived. This is followed by a study on the additional (micro-)boundary conditions of these models. For the model of Evers et al. [13, 14], the derived micro-stress is directly comparable with the micro-stresses of Gurtin [37, 44, 45] (obtained from the uncoupled defect energy function) since these frameworks do not consider the latent back stress interaction between different glide systems and the accompanying defect energy potentials for these frameworks look the same, i.e. simple quadratic functions in terms of GND densities. However, successful continuum theories should preserve at least the accumulated effect of the influence of the discreteness, e.g. interactions between the dislocations of different slip systems since it affects the dislocation generation, annihilation and consequently the macroscopic material response [48, 49]. Therefore, for the complete unification of the work-conjugate and non-work-conjugate models, the consideration of a non-work-conjugate model is needed with a back stress form which properly includes the interactions between the dislocations of different slip systems, i.e. the model of Bayley et al. [15, 16] together the free energy form that may yield the micro-stress vector corresponding to that energetic back stress tensor. The micro-stress derived from the back stress of this model contains additional terms corresponding to the contribution to the internal stress state of a slip system by the GNDs of the other slip systems, which are ignored by Evers et al. [13, 14] and by Gurtin [44, 45]. These additional terms change the nature of the defect energy associated to this micro-stress, which may have a non-convex form. In Gurtin [37], a simple quadratic defect energy is suggested to couple the slip systems. However, in that model, the energetic interaction is defined in a phenomenological way and the resulting micro-stress vector is limited to lying in its slip plane, similar to the one derived from an uncoupled defect energy.

2.2 Strain gradient crystal plasticity frameworks

2.2.1 Physically motivated strain gradient crystal plasticity models of Evers et al. and Bayley et al.

Here, an enhanced version of the Evers-Bayley type models [13–16] is presented. Essentially, the gradient operators used for slip and dislocation densities, which were defined in the reference configuration in the original formulations of the Evers-Bayley type models are taken with respect to the intermediate configuration.

Constitutive framework

The Kröner-Lee decomposition [50, 51] of the deformation gradient tensor \mathbf{F} is the starting point for the models of Evers et al. [13, 14] and Bayley et al. [15, 16]:

$$\mathbf{F} = \mathbf{F}_e \cdot \mathbf{F}_p, \quad (2.1)$$

where \mathbf{F}_e is the elastic part of the deformation gradient, describing the stretch and the rotation of the lattice with respect to an intermediate stress free configuration (defined by the plastic deformation gradient \mathbf{F}_p with respect to the material configuration).

The second Piola-Kirchhoff stress tensor \mathbf{S}_* is given in terms of the elastic Green-Lagrange strain tensor \mathbf{E}_e in the intermediate configuration as:

$$\mathbf{S}_* = \mathbb{C} : \mathbf{E}_e \quad \text{with} \quad \mathbf{E}_e = \frac{1}{2} (\mathbf{F}_e^T \cdot \mathbf{F}_e - \mathbf{I}), \quad (2.2)$$

with \mathbf{I} the second order identity tensor and \mathbb{C} the fourth order elasticity tensor. \mathbf{S}_* is also defined as:

$$\mathbf{S}_* = \mathbf{F}_e^{-1} \cdot \boldsymbol{\tau} \cdot \mathbf{F}_e^{-T} \quad \text{with} \quad \boldsymbol{\tau} = J \boldsymbol{\sigma} \quad \text{and} \quad J = \det(\mathbf{F}_e) = \det(\mathbf{F}). \quad (2.3)$$

Here, $\boldsymbol{\tau}$ is the Kirchhoff stress tensor and $\boldsymbol{\sigma}$ the Cauchy stress tensor.

The resolved shear stress τ^α on slip system α is given by:

$$\tau^\alpha = \mathbf{S}_* : \mathbf{P}_*^\alpha \quad \text{with} \quad \mathbf{P}_*^\alpha = \mathbf{s}_*^\alpha \mathbf{n}_*^\alpha, \quad (2.4)$$

where \mathbf{P}_*^α is called the Schmid tensor, \mathbf{s}_*^α is the unit direction of the Burgers vector and \mathbf{n}_*^α is the unit normal of the slip plane of system α ¹.

The plastic velocity gradient tensor is defined as the summation of all contributions of n_s slip systems α , which are defined by their Schmid tensors and the plastic slip rates $\dot{\gamma}^\alpha$:

$$\mathbf{L}_p = \sum_{\alpha=1}^{n_s} \dot{\gamma}^\alpha \mathbf{P}_*^\alpha. \quad (2.5)$$

¹From here onwards, subscripts $_0$ and $_*$ are used to denote a quantity in the reference and intermediate configurations, respectively, while the quantities without any subscript are in the current configuration.

The material time derivative of the plastic deformation gradient tensor is obtained from:

$$\dot{\mathbf{F}}_p = \mathbf{L}_p \cdot \mathbf{F}_p. \quad (2.6)$$

The evolution of the plastic slip rate is governed by a viscoplastic power-law:

$$\dot{\gamma}^\alpha = \dot{\gamma}_0 \left(\frac{|\tau_{eff}^\alpha|}{s^\alpha} \right)^m \exp \left[-\frac{G_0}{kT} \left(1 - \frac{|\tau_{eff}^\alpha|}{s^\alpha} \right) \right] \text{sign}(\tau_{eff}^\alpha), \quad (2.7)$$

where $\dot{\gamma}_0$ and m are the reference slip rate and the rate sensitivity, respectively. Furthermore, s^α is the slip resistance, T is the absolute temperature and k is the Boltzmann constant. The material constant G_0 represents the thermal activation energy necessary for a dislocation to pass a barrier preventing crystallographic slip. The effective stress τ_{eff}^α drives the dislocation motion on the slip system considered. It is expressed by the difference between the externally applied resolved shear stress τ^α and the resolved back stress τ_b^α :

$$\tau_{eff}^\alpha = \tau^\alpha - \tau_b^\alpha. \quad (2.8)$$

One of the distinct features of this framework is the formulation of the back stress τ_b^α in terms of the gradients of the GNDs, which will be further elaborated in section 2.2.1.

The slip system resistance, s^α , is the resistance against the dislocation movement on the glide system α due to the short-range interactions between dislocations. It is formulated following [26] in terms of both statistically stored dislocation densities ρ_{SSD}^α and geometrically necessary dislocation densities ρ_{GND}^α as:

$$s^\alpha = cGb \sqrt{\sum_{\xi=1}^{12} A^{\alpha\xi} |\rho_{SSD}^\xi| + \sum_{\xi=1}^{18} A^{\alpha\xi} |\rho_{GND}^\xi|} \quad \text{for } \alpha = 1, 2, \dots, n_s, \quad (2.9)$$

where c is a material constant [52], G is the shear modulus, b the magnitude of the Burgers vector, and $A^{\alpha\xi}$ are the components of the interaction matrix which represents the strength of the interactions between slip systems as determined by [53]. It is composed of the six interaction coefficients corresponding to self hardening, coplanar hardening, Hirth lock, Glissile junction, Lomer-Cottrell lock, and cross slip [see 54].

Definition of back stress

The formulation of the back stress in the Evers-Bayley type models is based on a linearization of the GND distribution, whereby the stress fields of all dislocations are superposed, [55]. The stress fields of the individual dislocations emanate from the analytical solution within a distorted infinite lattice. The statistically stored dislocations (SSDs) represent the unsigned fraction of the total population of dislocations. Their contribution to the internal stress state is zero because of the cancellation of the individual contributions of SSDs. Hence, the back stress is induced only by the GNDs.

In Evers et al. [14], the back stress on slip system ξ is defined by considering only the contributions of the dislocations belonging to slip system ξ , also referred to as the *self-internal back stress* formulation. This formulation was later extended in Bayley et al. [15, 16] by incorporation of all stress contributions from all slip systems into the back stress, which is named the *full-internal back*

stress formulation.

Departing from Bayley et al. [16], the internal stress field induced by edge GNDs is given by:

$$\boldsymbol{\sigma}_e^{int} = \frac{GbR^2}{8(1-\nu)} \sum_{\xi=1}^{12} \nabla_*^\xi \rho_{GND,e}^\xi \cdot \left(\underline{3\mathbf{n}_*^\xi \mathbf{s}_*^\xi \mathbf{s}_*^\xi} + \underline{\mathbf{n}_*^\xi \mathbf{n}_*^\xi \mathbf{n}_*^\xi} + \underline{4\nu \mathbf{n}_*^\xi \mathbf{p}_*^\xi \mathbf{p}_*^\xi} - \underline{\mathbf{s}_*^\xi \mathbf{s}_*^\xi \mathbf{n}_*^\xi} - \underline{\mathbf{s}_*^\xi \mathbf{n}_*^\xi \mathbf{s}_*^\xi} \right), \quad (2.10)$$

and the screw GNDs part is:

$$\boldsymbol{\sigma}_s^{int} = \frac{GbR^2}{4} \sum_{\xi=13}^{18} \nabla_*^\xi \rho_{GND,s}^\xi \cdot \left(-\underline{\mathbf{n}_*^\xi \mathbf{s}_*^\xi \mathbf{p}_*^\xi} - \underline{\mathbf{n}_*^\xi \mathbf{p}_*^\xi \mathbf{s}_*^\xi} + \underline{\mathbf{p}_*^\xi \mathbf{s}_*^\xi \mathbf{n}_*^\xi} + \underline{\mathbf{p}_*^\xi \mathbf{n}_*^\xi \mathbf{s}_*^\xi} \right) \quad (2.11)$$

with $\mathbf{p}_*^\xi = \mathbf{s}_*^\xi \times \mathbf{n}_*^\xi$ associated with slip system ξ and R is the radius of the cylindrical integration volume. In the case of the self internal back stress formulation, $\alpha = \xi$ and consequently, the underlined terms vanish.

The back stress is opposite to the internal stress, which is given by the projection of the total stress field onto the slip system by the related Schmid tensor as:

$$\tau_b^\alpha = -(\boldsymbol{\sigma}_s^{int} + \boldsymbol{\sigma}_e^{int}) : \mathbf{P}_*^\alpha \quad \text{for } \alpha = 1, 2, \dots, n_s. \quad (2.12)$$

Dislocation density evolution

The evolution of *statistically stored dislocation* densities ρ_{SSD}^ξ on each slip system ξ , governing the slip resistance in equation (2.9), is given by:

$$\dot{\rho}_{SSD}^\xi = \frac{1}{b} \left(\frac{1}{L^\xi} - 2y_c \rho_{SSD}^\xi \right) |\dot{\gamma}^\xi| \quad \text{with} \quad \rho_{SSD}^\xi(t=0) = \rho_{SSD_0}^\xi, \quad (2.13)$$

which is the generalized form of the relation originally proposed by [56].

The first term within the parentheses in equation (2.13) describes the accumulation rate, where L^ξ denotes the average dislocation segment length calculated as:

$$L^\xi = \frac{K}{\sqrt{\sum_{\xi=1}^{12} H^{\alpha\xi} |\rho_{SSD}^\xi| + \sum_{\xi=1}^{18} H^{\alpha\xi} |\rho_{GND}^\xi|}}. \quad (2.14)$$

Here, $H^{\alpha\xi}$ represents the mutual interactions anticipated between the sliding SSDs and forest dislocations [13], built in a way similar to $A^{\alpha\xi}$ in equation (2.9).

The second term in the parentheses in equation (2.13) is the annihilation rate, which depends on the critical annihilation length y_c . This is the average distance between two oppositely signed dislocations, below which they annihilate.

Geometrically necessary dislocations represent the signed fraction of the total dislocation population, since they arise from the gradients of plastic slip and are necessary to preserve the lattice compatibility in the crystal. In accordance with [26], the slip gradients in the direction of the slip plane normal do not geometrically induce an excess of dislocations, whereas the slip gradient in

the direction of slip \mathbf{s}_*^α gives rise to edge dislocations and in the direction normal to slip \mathbf{p}_*^α induces screw dislocations. The densities of edge and screw GNDs are computed as:

$$\rho_{GND}^\xi = \rho_{GND_0}^\xi + \mathbf{d}_*^{\xi\beta} \cdot \nabla_* \gamma^\beta, \quad (2.15)$$

with

$$\mathbf{d}_*^{\xi\beta} = \begin{cases} -\frac{1}{b} \delta_{\beta\xi} \mathbf{s}_*^\xi & , \quad \xi, \beta = 1, 2, \dots, 12, \\ \frac{1}{b} (\delta_{\beta\alpha_1} \mathbf{p}_*^{\alpha_1} + \delta_{\beta\alpha_2} \mathbf{p}_*^{\alpha_2}) & , \quad \xi = 13, 14, \dots, 18. \end{cases} \quad (2.16)$$

Here, ξ runs over 1, 2, ..., 12 for edge GNDs and over 13, 14, ..., 18 for screw GNDs. $\rho_{GND_0}^\xi$ denotes the initial GND density present in the material, α_1 and α_2 indicate two slip systems with the same slip direction but different plane normals for each screw GND. A list of indices and vectors for dislocation densities and slip systems of FCC metals can be found in Evers et al. [13].

Note that, contrary to the original models of Evers et al. [13, 14] and Bayley et al. [15, 16], which were essentially used to resolve problems with small plastic strains, the gradients of GND densities in equations (2.10) and (2.11) and the gradient of slip in equation (2.15) are taken with respect to the intermediate configuration. This modification provides a more accurate calculation of the GND densities and, in turn, the back stresses, particularly when large strains and slip on multiple slip systems are concerned.

Variational formulation and boundary conditions

Implementation of the crystal plasticity framework outlined above in a finite element context uses 18 GND densities as the nodal degrees of freedom in addition to 3 nodal displacements. The set of governing field equations employed are the conventional stress equilibrium (neglecting the body forces):

$$\nabla_0 \cdot \mathbf{T}^T = \mathbf{0}, \quad (2.17)$$

(with \mathbf{T} being the first Piola-Kirchhoff stress tensor) and the dislocation density balance equation (2.15):

Weak forms of the governing field equations are obtained by multiplying (2.15) and (2.17) by weighting functions $\mathbf{w}_u(\mathbf{x}_0)$ and $w_\rho^\xi(\mathbf{x}_*)$, respectively and subsequently integrating the result over the volume V_0 in the intermediate configuration followed by application of the Gauss-divergence theorem:

$$\int_{V_0} (\nabla_0 \mathbf{w}_u)^T : \mathbf{T}^T dV_0 = \int_{A_0} \mathbf{w}_u \cdot \mathbf{t}_0 dA_0, \quad (2.18)$$

with A_0 the surface enclosing V_0 , \mathbf{t}_0 the surface traction associated with \mathbf{T} , and

$$\int_{V_*} \left(w_\rho^\xi \rho_{GND}^\xi + (\nabla_* w_\rho^\xi \cdot \mathbf{d}_*^{\xi\alpha}) \gamma^\alpha \right) dV_* = \int_{V_*} w_\rho^\xi \rho_{GND_*}^\xi dV_* + \int_{A_*} w_\rho^\xi \Gamma_*^\xi dA_*. \quad (2.19)$$

The last term in equation (2.19) represents an additional boundary condition where Γ_*^ξ is a crystallographic slip measure in surface normal direction \mathbf{n}_* along the boundary and is defined as

$\Gamma_*^\xi = \gamma^\beta (\mathbf{d}_*^{\xi\beta} \cdot \mathbf{n}_*)$. The additional boundary conditions are specified by setting either

$$\rho_{GND}^\xi = 0, \quad (2.20)$$

which means that the GNDs can escape at the surface, i.e. a *free surface* condition, or

$$\gamma^\beta (\mathbf{d}_*^{\xi\beta} \cdot \mathbf{n}_*) = 0, \quad (2.21)$$

which can be regarded as a non-slip condition (leading to GND accumulation on the boundary) on the surface with normal vector \mathbf{n}_* , i.e. a *hard interface*.

2.2.2 A thermodynamically consistent strain gradient crystal plasticity theory by Gurtin

Framework

Gurtin has introduced a higher order gradient theory of crystal plasticity in [37, 43–45]. The theory is based on the multiplicative decomposition of the deformation gradient tensor \mathbf{F} into its elastic part \mathbf{F}_e and the plastic part \mathbf{F}_p as in equation (2.1). It includes a set of micro-force balance laws derived from the principle of virtual power (omitting the body forces):

$$\underbrace{\int_A \mathbf{t} \cdot \tilde{\mathbf{v}} \, dA + \sum_\alpha \int_A \Xi^\alpha \tilde{\nu}^\alpha \, dA}_{P_{ext}} = \underbrace{\int_V \boldsymbol{\sigma} : \tilde{\mathbf{L}}_e \, dV + \sum_\alpha \int_V (\pi^\alpha \tilde{\nu}^\alpha + \boldsymbol{\xi}^\alpha \cdot \nabla \tilde{\nu}^\alpha) \, dV}_{P_{int}}. \quad (2.22)$$

Here, P_{ext} and P_{int} denote the external and internal virtual power expenditure in the current state V . In equation (2.22), α is the slip system index running over 1 to 12 for an FCC metal. $\tilde{\mathbf{v}}$ is the virtual velocity and $\tilde{\nu}^\alpha$ is a measure for the virtual slip rates in each individual slip systems. \mathbf{t} is the surface traction and $\boldsymbol{\sigma}$ the Cauchy stress tensor. $\Xi^\alpha = \boldsymbol{\xi}^\alpha \cdot \mathbf{n}$ is a scalar microscopic traction arising from the micro-stress vector $\boldsymbol{\xi}^\alpha$, which is assumed to be a Peach-Köhler force-like quantity in the present viscoplastic medium that is conjugate to the gradient of the slip rate and \mathbf{n} is the unit surface normal. π^α represents the scalar internal force that develops from the creation, annihilation and interaction of dislocations, which is conjugate to the slip rate.

The velocity gradient $(\nabla \mathbf{v})^T$ is defined as:

$$(\nabla \mathbf{v})^T = \mathbf{L}_e + \mathbf{F}_e \cdot \mathbf{L}_p \cdot \mathbf{F}_e^{-1} \quad (2.23)$$

where \mathbf{L}_e and \mathbf{L}_p are the elastic and plastic deformation rates, respectively, given by:

$$\mathbf{L}_e = \dot{\mathbf{F}}_e \cdot \mathbf{F}_e^{-1} \quad \text{and} \quad \mathbf{L}_p = \dot{\mathbf{F}}_p \cdot \mathbf{F}_p^{-1} = \sum_\alpha \nu^\alpha \mathbf{s}_*^\alpha \mathbf{n}_*^\alpha = \sum_\alpha \nu^\alpha \mathbf{P}_*^\alpha \quad (2.24)$$

and \mathbf{s}_*^α and \mathbf{n}_*^α are the unit lattice vectors in the intermediate configuration.

Next, macroscopic and microscopic force balances and traction conditions are derived. Choosing a virtual $\tilde{\mathbf{v}}$ and $\tilde{\nu}^\alpha = 0$ results in $\tilde{\mathbf{L}}^e = (\nabla \tilde{\mathbf{v}})^T$ according to equations (2.23) and (2.24). Subse-

quently, equation (2.22) turns into the conventional virtual power balance for the Cauchy stress:

$$\int_A \mathbf{t} \cdot \tilde{\mathbf{v}} \, dA = \int_V \boldsymbol{\sigma} : \tilde{\mathbf{L}}_e \, dV. \quad (2.25)$$

After some manipulations, equation (2.25) simplifies to the local (i.e. macroscopic) force balance

$$\nabla \cdot \boldsymbol{\sigma} = \mathbf{0} \quad (2.26)$$

and the traction condition $\mathbf{t} = \boldsymbol{\sigma} \cdot \mathbf{n}$.

For a virtual $\tilde{\nu}^\alpha$ and vanishing $\tilde{\mathbf{v}}$, the elastic distortion rate takes the form (cf. equations (2.23) and (2.24)):

$$\tilde{\mathbf{L}}_e = - \sum_{\alpha} \tilde{\nu}^\alpha \mathbf{P}^\alpha; \quad \mathbf{P}^\alpha = \mathbf{s}^\alpha \mathbf{n}^\alpha \quad \text{with} \quad \begin{cases} \mathbf{s}^\alpha = \mathbf{F}_e \cdot \mathbf{s}_*^\alpha, \\ \mathbf{n}^\alpha = \mathbf{F}_e^{-T} \cdot \mathbf{n}_*^\alpha. \end{cases} \quad (2.27)$$

Then, equation (2.22) reduces to the unconventional microscopic virtual power balance:

$$\int_V \boldsymbol{\sigma} : \tilde{\mathbf{L}}_e \, dV + \sum_{\alpha} \int_V (\pi^\alpha \tilde{\nu}^\alpha + \boldsymbol{\xi}^\alpha \cdot \nabla \tilde{\nu}^\alpha) \, dV = \int_A \Xi^\alpha \tilde{\nu}^\alpha \, dA. \quad (2.28)$$

Since $\tilde{\nu}^\alpha$ is arbitrary, equation (2.28) is further reduced to the micro-force balance law:

$$\pi^\alpha - \tau^\alpha - \nabla \cdot \boldsymbol{\xi}^\alpha = 0, \quad (2.29)$$

with an accompanying micro-traction condition $\Xi^\alpha = \boldsymbol{\xi}^\alpha \cdot \mathbf{n}$. Here, τ^α is the resolved shear stress which is defined as:

$$\tau^\alpha = \boldsymbol{\sigma} : \mathbf{P}^\alpha \quad (2.30)$$

which is conjugate to the slip rate.

The local free energy imbalance, which states that the rate of change of free energy can not be greater than the external power spent on the body V ,

$$\delta = -J^{-1} \dot{\psi} + J^{-1} \mathbf{S}_* : \dot{\mathbf{E}}_e + \sum_{\alpha} (\boldsymbol{\xi}^\alpha \cdot \nabla \nu^\alpha + \pi^\alpha \nu^\alpha) \geq 0, \quad (2.31)$$

is postulated for the derivation of the constitutive relations, assuming GND densities and the slip rate gradients to be the independent variables. In equation (2.31), δ represents the dissipation per unit volume in the current configuration, $J = \det(\mathbf{F}) = \det(\mathbf{F}_e)$, \mathbf{S}_* is the second Piola-Kirchhoff stress obtained from an elastic pull-back with $\mathbf{S}_* = J \mathbf{F}_e^{-1} \cdot \boldsymbol{\sigma} \cdot \mathbf{F}_e^{-T}$, \mathbf{E}_e is the elastic Green-Lagrange strain tensor and ψ is the free energy function in terms of GND densities per unit volume in the intermediate configuration which is invariant under all changes in the reference state.

Within the finite deformation formulation of [37], the free energy function ψ is formulated in terms of the geometrically necessary edge and screw dislocation densities $\hat{\rho}_{GND,e}^\alpha$ and $\hat{\rho}_{GND,s}^\alpha$, the rate

of change of which are given in the current configuration by²:

$$\dot{\hat{\rho}}_{GND,e}^\alpha = -\nabla \cdot \mathbf{q}_{GND,e}^\alpha + \sigma_{GND,e}^\alpha \quad \text{and} \quad \dot{\hat{\rho}}_{GND,s}^\alpha = -\nabla \cdot \mathbf{q}_{GND,s}^\alpha + \sigma_{GND,s}^\alpha, \quad (2.32)$$

where

$$\mathbf{q}_{GND,e}^\alpha = \nu^\alpha \mathbf{s}^\alpha \quad \text{and} \quad \mathbf{q}_{GND,s}^\alpha = -\nu^\alpha \mathbf{p}^\alpha \quad (2.33)$$

are respective fluxes of edge and screw GNDs and

$$\sigma_{GND,e}^\alpha = \nu^\alpha \nabla \cdot \mathbf{s}^\alpha \quad \text{and} \quad \sigma_{GND,s}^\alpha = -\nu^\alpha \nabla \cdot \mathbf{p}^\alpha \quad (2.34)$$

are spatial edge and screw GND supplies, respectively. \mathbf{p}^α is a push forward of lattice vector \mathbf{p}_*^α from the intermediate to the current configuration as $\mathbf{p}^\alpha = \mathbf{F}_e \cdot \mathbf{p}_*^\alpha$ with $\mathbf{p}_*^\alpha = -\mathbf{s}_*^\alpha \times \mathbf{n}_*^\alpha$. Hence, equations (2.32)-(2.34) result in:

$$\dot{\hat{\rho}}_{GND,e}^\alpha = -\nabla \nu^\alpha \cdot \mathbf{s}^\alpha \quad \text{and} \quad \dot{\hat{\rho}}_{GND,s}^\alpha = -\nabla \nu^\alpha \cdot \mathbf{p}^\alpha. \quad (2.35)$$

In Gurtin's model, the micro-stress $\boldsymbol{\xi}^\alpha$ is additively decomposed into an *energetic* part $\boldsymbol{\xi}_{en}^\alpha$ and a *dissipative* part $\boldsymbol{\xi}_{dis}^\alpha$. The constitutive equation for the energetic part of the micro-stress vector results from the exploitation of the free energy imbalance, equation (2.31), for a defect energy function $\psi_D = f(\hat{\rho}_{GND})$ together with equation (2.32) and reads:

$$\boldsymbol{\xi}_{en}^\alpha \equiv - \underbrace{J^{-1} \frac{\partial \psi_D}{\partial \hat{\rho}_{GND,e}^\alpha}}_{f_e^\alpha} \mathbf{s}^\alpha + J^{-1} \underbrace{\frac{\partial \psi_D}{\partial \hat{\rho}_{GND,s}^\alpha}}_{f_s^\alpha} \mathbf{p}^\alpha \quad (2.36)$$

with f_e^α and f_s^α energetic defect forces for the edge and screw GNDs in the slip system α , respectively.

For the derivation of the micro-stresses, defect energy forms have been proposed in [37] in terms of the net GND density (measured per unit volume in the reference configuration) :

$$\hat{\rho}_{net}^\alpha = \sqrt{|\hat{\rho}_{GND,e}^\alpha|^2 + |\hat{\rho}_{GND,s}^\alpha|^2}. \quad (2.37)$$

The simplest one proposed ignores the interactions between different slip systems and it is given by:

$$\psi_D = \frac{1}{2} S_0 L^2 \sum_{\alpha} (\hat{\rho}_{net}^\alpha)^2 \quad (2.38)$$

where L is an energetic length scale and S_0 is the initial slip resistance. By expressing the edge and screw GND density in the current configuration $\bar{\rho}_{GND,e}^\alpha$ and $\bar{\rho}_{GND,s}^\alpha$ as:

$$\bar{\rho}_{GND,e}^\alpha = J^{-1} \hat{\rho}_{GND,e}^\alpha \quad \text{and} \quad \bar{\rho}_{GND,s}^\alpha = J^{-1} \hat{\rho}_{GND,s}^\alpha \quad (2.39)$$

²GND densities in the models of Gurtin and Gurtin et al. (2000-2008) are consistently in units of inverse length (here indicated by $\hat{\rho}_{GND,e}^\alpha$ and $\hat{\rho}_{GND,s}^\alpha$) due to the absence of the magnitude of the Burgers vector in the decomposition of the Burgers tensor to the spatial distributions of the GNDs, for instance in equation (1.5) of [44], which also affects the form of the free energy function and the resulting micro-stress vectors. The definition of GND densities in the Evers-Bayley type models complies with the decomposition of the Burgers tensor in Sun et al. [57] and Arsenlis and Parks [58] with the dislocation length per unit of volume having the unit of inverse length squared.

and by following equation (2.36), the energetic defect forces and, hence, the micro-stresses are derived as:

$$\boldsymbol{\xi}_{en}^{\alpha} = S_0 L^2 (-\bar{\rho}_{GND,e}^{\alpha} \mathbf{s}^{\alpha} + \bar{\rho}_{GND,s}^{\alpha} \mathbf{P}^{\alpha}). \quad (2.40)$$

Another defect energy function which couples different slip systems is suggested in [37] as:

$$\psi_D = \left[\frac{1}{2} S_0 L^2 \sum_{\alpha} (\hat{\rho}_{net}^{\alpha})^2 + \lambda \sum_{\alpha, \beta, \alpha \neq \beta} \hat{\rho}_{net}^{\alpha} \hat{\rho}_{net}^{\beta} \right]. \quad (2.41)$$

where λ is a coupling coefficient. Having defined the dislocation concentrations $c_e^{\alpha} = \frac{\hat{\rho}_{GND,e}^{\alpha}}{\hat{\rho}_{net}^{\alpha}} = \frac{\bar{\rho}_{GND,e}^{\alpha}}{\hat{\rho}_{net}^{\alpha}}$ and $c_s^{\alpha} = \frac{\hat{\rho}_{GND,s}^{\alpha}}{\hat{\rho}_{net}^{\alpha}} = \frac{\bar{\rho}_{GND,s}^{\alpha}}{\hat{\rho}_{net}^{\alpha}}$, the energetic defect forces are derived and resulting micro-stress vector is:

$$\boldsymbol{\xi}_{en}^{\alpha} = S_0 L^2 (c_e^{\alpha} \mathbf{s}^{\alpha} + c_s^{\alpha} \mathbf{P}^{\alpha}) \left[\bar{\rho}_{net}^{\alpha} + \lambda \sum_{\beta, \beta \neq \alpha} \bar{\rho}_{net}^{\beta} \right]. \quad (2.42)$$

With the definition of the energetic micro-stress, the dissipation inequality in (2.31) reduces to:

$$\delta = \sum_{\alpha} (\boldsymbol{\xi}_{dis}^{\alpha} \cdot \nabla \nu^{\alpha} + \pi^{\alpha} \nu^{\alpha}) \geq 0. \quad (2.43)$$

This reduced dissipation inequality provides the inspiration for the constitutive equation forms for the dissipative part of the micro-stresses $\boldsymbol{\xi}_{dis}$ through the definition of the dissipative scalar force π^{α} from standard crystal plasticity theories. In [37], π^{α} is given by:

$$\pi^{\alpha} = S^{\alpha} R(d^{\alpha}) \frac{\nu^{\alpha}}{d^{\alpha}} \quad (2.44)$$

where S^{α} is the slip resistance, $d^{\alpha} = \sqrt{|\nu^{\alpha}|^2 + l^2 |\nabla \nu^{\alpha}|^2}$ is an effective flow rate, l is a dissipative length scale and $R(d^{\alpha})$ is a sensitivity rate function and $|\nabla \nu^{\alpha}|^2 = \nabla \nu^{\alpha} \cdot \nabla \nu^{\alpha}$. The suggested constitutive relation for $\boldsymbol{\xi}_{dis}^{\alpha}$ reads:

$$\boldsymbol{\xi}_{dis}^{\alpha} = S^{\alpha} R(d^{\alpha}) l^2 \frac{\nabla \nu^{\alpha}}{d^{\alpha}}. \quad (2.45)$$

The flow rule is obtained by inserting the micro-stress $\boldsymbol{\xi}^{\alpha}$ and the internal force π^{α} into the micro-force balance law (2.29). For the complete framework, see [37, 43–45].

Boundary conditions

The local macro-force balance law (2.26) and the non-local micro-force balance law (2.29) were used as the governing field equations within a finite element context, taking the nodal displacements and the slip rates of all slip systems as the degrees of freedom.

The external power expended on a slip system α on surface A with the normal vector \mathbf{n} by the micro-stress vector is given by

$$W_{ext} = \int_A (\boldsymbol{\xi}^{\alpha} \cdot \mathbf{n}) \nu^{\alpha} dA. \quad (2.46)$$

For a zero external power on the surface, i.e. $W_{ext} = 0$, the necessary boundary conditions can be derived by taking either

$$\boldsymbol{\xi}^\alpha \cdot \mathbf{n} = 0 \quad (2.47)$$

which is the definition of a *micro-stress free boundary* or

$$\nu^\alpha = 0 \quad (2.48)$$

which defines a *hard boundary*, i.e. a non-slip condition.

2.3 Thermodynamical aspects of Evers-Bayley models

2.3.1 Micro-stress vector from back stress definition

The aim of this section is the derivation of the micro-stress vectors $\boldsymbol{\xi}_*^\alpha$ based on the physical definition of the back stress in the Evers-Bayley type models which is given in section 2.2.1. To do so, consider the dissipative effects in the Evers-Bayley type models which are included through the slip resistance s^α in the flow rule, equation (2.7). When its definition in equation (2.9) is considered, it can be seen that these models are dissipative in the slip γ^α via SSD densities ρ_{SSD}^ξ (equation (2.13)) and dissipative in the slip gradient $\nabla_* \gamma^\alpha$ via GND densities ρ_{GND}^ξ . These models are energetic in $\nabla_* \gamma^\alpha$ through the definition of back stresses (equation (2.12)) via GND densities. In the present paper, the contribution of GND densities to the slip resistance is ignored. Hence, the Evers-Bayley type models become fully dissipative in γ^α and fully energetic in $\nabla_* \gamma^\alpha$. Consequently, the micro-stress $\boldsymbol{\xi}_*^\alpha$, which is conjugate to $\nabla_* \gamma^\alpha$, will be fully energetic, i.e. $\boldsymbol{\xi}_*^\alpha = \boldsymbol{\xi}_{en*}^\alpha$ and $\boldsymbol{\xi}_{dis*}^\alpha = \mathbf{0}$.

Now, consider the definition of the effective shear stress on a slip plane α :

$$\tau_{eff}^\alpha = \tau^\alpha - \tau_b^\alpha. \quad (2.49)$$

Setting up a relation between the back stresses τ_b^α of the Evers-Bayley type models and the micro-stress vector $\boldsymbol{\xi}_*^\alpha$ (in the intermediate configuration) of [43] such that³

$$\tau_b^\alpha = -\nabla_* \cdot \boldsymbol{\xi}_*^\alpha \quad (2.50)$$

is the key step [38, 46, 47] for the unification of the phenomenological model of Gurtin and the models by Evers et al. and Bayley et al., which, in turn, will also validate the thermodynamical consistency of the latter type models.

With the definition (2.50), it can be shown through equation (2.49) that the effective resolved shear stress τ_{eff}^α of the Evers-Bayley type models is the same as the scalar internal stress π_*^α of

³Gurtin's framework in section 2.2.2 is in the spatial configuration, whereas from section 2.3 onwards, all formulations are presented in the intermediate configuration. This enables a consistent comparison with the Evers-Bayley type models without loss of generality.

Gurtin's model (in the intermediate configuration)⁴, and consequently equation (2.49) is identical to the micro-force balance law (in the intermediate configuration) defined by Gurtin (cf. equation (2.29)):

$$\tau_{eff}^\alpha = \pi_*^\alpha \Leftrightarrow \pi_*^\alpha - \tau^\alpha - \nabla_* \cdot \xi_*^\alpha = 0, \quad (2.51)$$

yielding the physical interpretation of the micro-force balance law⁵. Then, by equation (2.51), the reduced dissipation inequality for the Evers-Bayley type models can be written as

$$\delta = \sum_{\alpha} \tau_{eff}^\alpha \dot{\gamma}^\alpha \geq 0, \quad (2.52)$$

cf. equation (2.43). Based on the flow rule used in the Evers-Bayley type models in equation (2.7), or in a recast form in footnote (4), τ_{eff}^α and $\dot{\gamma}^\alpha$ always have the same sign, the multiplication of which results in a positive dissipation, confirming the thermodynamical consistency of the Evers-Bayley type models.

The micro-stress vector ξ_*^α for the model of Evers et al. [14] is derived through equation (2.50) based on the quantification of a back stress given by equations (2.10)-(2.12):

$$\xi_*^\alpha = -\frac{GbR^2}{8(1-\nu)} \rho_{GND,e}^\alpha \mathbf{s}_*^\alpha + \frac{GbR^2}{4} \rho_{GND,s}^\alpha \mathbf{P}_*^\alpha. \quad (2.53)$$

Note that this micro-stress vector does not include the influence of the other slip systems on system α (i.e. the latent hardening) since only the effects of GNDs belonging to slip system α are considered in the definition of internal stress fields in Evers et al. [14]. Equation (2.53) clearly shows that ξ_*^α lies in its slip plane. From these aspects, ξ_*^α compares to the micro-stresses proposed by [37, 38, 43–47]. In particular, keeping in mind the relation between the GND densities $\rho_{GND,e,s}^\alpha$ defined in Gurtin's model and $\rho_{GND,e,s}^\alpha$ in Evers' and Bayley's model $\rho_{GND,e,s}^\alpha \sim \frac{1}{b} \rho_{GND,e,s}^\alpha$, ξ_*^α becomes the identical counterpart of the energetic micro-stress (equation (2.40)) that is derived from a simple quadratic defect energy function when the energetic length scale of Gurtin's model, L , is set equal to that of the Evers-Bayley type models, R , and S_0 to $\frac{G}{8(1-\nu)}$ for edge and S_0 to $\frac{G}{4}$ for screw GNDs. It should be mentioned that contrary to the energetic length scale L , which is phenomenologically introduced in Gurtin's model, the energetic length scale R in the Evers-Bayley type models has a physical meaning: it is the radius of a circular region around a material point in which GNDs are considered and their individual contributions to the back stress are superposed. One may refer to Geers et al. [55] for a detailed discussion on the energetic length scales involved in the Evers-Bayley type models. Note that the Gurtin framework contains one more length-scale measure, which is phenomenologically introduced as a dissipative length scale l in equations (2.44) and (2.45) to take into account the gradient of slip in the dissipative processes and to define the dissipative micro-stress. It cannot be compared to any scale measure in the Evers-Bayley type

⁴ The original flow rule in equation (2.7), which is used in the models of Evers et al. and Bayley et al. has an exponential term to account for the thermal activation of the crystallographic slip. Here, for convenience, isothermal conditions are considered, allowing the omission of the term related to thermal activation. The inverse formulation of the flow rule then is $\tau_{eff}^\alpha = \pi_*^\alpha = s^\alpha \text{sign}(\dot{\gamma}^\alpha) \left(\frac{|\dot{\gamma}^\alpha|}{\dot{\gamma}_0^\alpha} \right)^m$.

⁵ In the derivation of equation (2.51), one should note that there exists a difference in the definition of GND density rate between the Evers-Bayley type models and the Gurtin type models. For the former type model, the time derivative of equation (2.15) involves a term, $\overline{\nabla_* \dot{\gamma}^\beta} = -\mathbf{L}_p^T \cdot \nabla_* \dot{\gamma}^\beta + \nabla_* \dot{\gamma}^\beta$. In the latter type models, this term is denoted by $\nabla_* \nu^\beta$, cf. equation (2.35). Here, for the purpose of comparison of the Evers-Bayley type and Gurtin type models, $\nabla_* \dot{\gamma}^\beta$ is used instead of $\nabla_* \nu^\beta$ to represent the rate of the gradient of slip, which is in line with Gurtin's formulation.

models since the effect of gradient of slip on the dissipative processes and the dissipative part of the micro-stress in these models are omitted here. Moreover, while the initial slip resistance S_0 is considered as the same for both edge and screw GNDs in Gurtin's models, its counterpart in the Evers-Bayley type models, which comes from the definition of the internal stress due to the distortion in an elastic continuum by GNDs, is different for the different types of GNDs, i.e. $\frac{G}{8(1-\nu)}$ for an edge and $\frac{G}{4}$ for a screw GND. For further details, one may refer to [13–16, 49, 55].

The micro-stress vector for the model of Bayley et al. [16] has a more complicated form compared to the one for the model of Evers et al. in equation (2.53) because in the internal stress field formulation of Bayley's model (see equations (2.10) and (2.11)), not only the contributions by the GNDs of the related slip system but also the contributions by the GNDs of the other slip systems are considered. First, the third order tensors \mathbf{A}_*^ξ and \mathbf{B}_*^ξ are introduced for the sake of compactness:

$$\mathbf{A}_*^\xi = 3\mathbf{n}_*^\xi \mathbf{s}_*^\xi \mathbf{s}_*^\xi + \mathbf{n}_*^\xi \mathbf{n}_*^\xi \mathbf{n}_*^\xi + 4\nu \mathbf{n}_*^\xi \mathbf{p}_*^\xi \mathbf{p}_*^\xi - \mathbf{s}_*^\xi \mathbf{s}_*^\xi \mathbf{n}_*^\xi - \mathbf{s}_*^\xi \mathbf{n}_*^\xi \mathbf{s}_*^\xi, \quad (2.54)$$

$$\mathbf{B}_*^\xi = -\mathbf{n}_*^\xi \mathbf{s}_*^\xi \mathbf{p}_*^\xi - \mathbf{n}_*^\xi \mathbf{p}_*^\xi \mathbf{s}_*^\xi + \mathbf{p}_*^\xi \mathbf{s}_*^\xi \mathbf{n}_*^\xi + \mathbf{p}_*^\xi \mathbf{n}_*^\xi \mathbf{s}_*^\xi. \quad (2.55)$$

Then, the micro-stress vector for Bayley's model can be written using equations (2.10)-(2.12) and (2.50):

$$\boldsymbol{\xi}_*^\alpha = \left(\frac{GbR^2}{8(1-\nu)} \sum_{\xi=1}^{12} \rho_{GND,e}^\xi \mathbf{A}_*^\xi + \frac{GbR^2}{4} \sum_{\xi=13}^{18} \rho_{GND,s}^\xi \mathbf{B}_*^\xi \right) : \mathbf{P}_*^\alpha. \quad (2.56)$$

Such a complex micro-stress vector, which takes the interactions between individual slip systems into account within its physical basis, is not present in the models of [43–45] and [38, 46, 47].

In [37], a micro-stress vector that is derived from a defect energy which couples the individual slip systems is given (cf. equation (2.42)). The coupling in the corresponding defect energy, equation (2.41) is phenomenological and the derived micro-stress still lies in the plane of the slip system to which it belongs whereas the micro-stress vector in equation (2.56) does not necessarily lie in the corresponding slip plane. An out-of-plane micro-stress vector may be physically explained by the defect forces with their direction out of the slip plane that may arise as a result of the interaction with a second glide system whose slip plane is not parallel to the slip plane considered.

2.3.2 Defect energy function

The constitutive equation for an energetic micro-stress of a slip system α is defined in terms of a defect energy function $\psi_D = f(\rho_{GND})$ in the current configuration by equation (2.36), or its equivalent in the intermediate configuration as:

$$\boldsymbol{\xi}_*^\alpha = \frac{\partial \psi_D}{\partial \nabla_* \gamma^\alpha}. \quad (2.57)$$

A defect energy function that gives the micro-stress vector (2.53) for the framework of Evers et al. through equation (2.57) can be defined as:

$$\psi_D = \frac{Gb^2 R^2}{16(1-\nu)} \sum_{\alpha=1}^{12} (\rho_{GND,e}^\alpha)^2 + \frac{Gb^2 R^2}{8} \sum_{\alpha=13}^{18} (\rho_{GND,s}^\alpha)^2 \quad (2.58)$$

which is a convex function similar to the defect energies suggested by Gurtin et al. and Gurtin

[37, 45] (see equation (2.38)) and [38, 47], in which the coupling between different slip systems is omitted. Such a quadratic function means that the energy will monotonically increase with the dislocation density, e.g. as the dislocation density increases or decreases, the energy also increases or decreases, respectively.

From a physical perspective, a quadratic energy function does not suffice to capture the real energetic dislocation interactions across different glide systems, where the total energy may decrease even though, for instance, the same amount of GND density is preserved in the volume considered. In fact, this directly affects the form of the defect energy function, as in the case for the model of Bayley et al. [15, 16]. For this model, the influence of the dislocation interactions from different slip systems on the micro-stress in equation (2.56) is associated with a defect energy function that is considerably more complex than the one for the model of Evers et al. [13, 14]. The required defect energy function is expected to be *non-convex* in contrast to the one in equation (2.58).

A convex defect energy function that couples the individual slip systems proposed by [37] is given in equation (2.41). Still, this type of energy form does not allow for a physically based micro-stress vector of the type identified in equation (2.56) because of its out of plane components, consistent with a non-convex nature of a defect energy function. Apparently, the incorporation of the energetic interactions between different slip systems into the Gurtin type models via a defect energy function (which is ultimately required for a realistic description of the material behavior) may not be a straightforward task to be handled in a phenomenological approach.

2.3.3 Micro-boundary conditions

The counterpart of the external power expended on the boundaries by the micro-stress ξ^α in the current configuration (equation (2.46)) corresponding to its equivalent ξ_*^α in the intermediate configuration can be defined as $\int_{A_*} (\xi_*^\alpha \cdot \mathbf{n}_*) \dot{\gamma}^\alpha dA_*$. Then, the integral terms from which the additional (micro-)boundary conditions for the physically based models are obtained by substitution of equation (2.53) and obtain for the formulation of Evers et al.:

$$W_{ext} = \sum_{\alpha} \int_{A_*} \left[\left(-\frac{GbR^2}{8(1-\nu)} \rho_{GND,e}^\alpha \mathbf{s}_*^\alpha + \frac{GbR^2}{4} \rho_{GND,s}^\alpha \mathbf{p}_*^\alpha \right) \cdot \mathbf{n}_* \right] \dot{\gamma}^\alpha dA_*, \quad (2.59)$$

and by inserting equation (2.56) for the model proposed by Bayley et al.:

$$W_{ext} = \sum_{\alpha} \int_{A_*} \left[\left(-\frac{GbR^2}{8(1-\nu)} \sum_{\xi=1}^{12} \rho_{GND,e}^\xi \mathbf{A}_*^\xi + \frac{GbR^2}{4} \sum_{\xi=13}^{18} \rho_{GND,s}^\xi \mathbf{B}_*^\xi \right) : \mathbf{P}_*^\alpha \right] \cdot \mathbf{n}_* \dot{\gamma}^\alpha dA_*. \quad (2.60)$$

Subsequently, two different boundary conditions can be identified, which assure that equations (2.59) and (2.60) vanish. The first condition reads:

$$\dot{\gamma}^\alpha = 0, \quad (2.61)$$

which implies that the dislocations are trapped at the surface, i.e. a *hard boundary layer* exists.

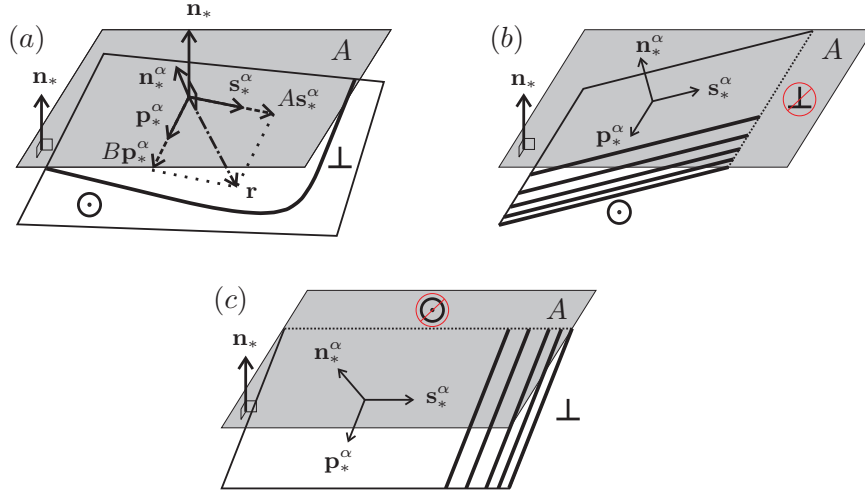


Figure 2.1: Free boundary layers: (a) non-zero edge (\perp) and screw (\odot) GND densities, (b) edge GNDs escape through the surface, (c) screw GNDs escape through the surface.

For the model of Evers et al. [14], the second condition is given by:

$$\left(-\frac{GbR^2}{8(1-\nu)} \rho_{GND,e}^\alpha \mathbf{s}_*^\alpha + \frac{GbR^2}{4} \rho_{GND,s}^\alpha \mathbf{p}_*^\alpha \right) \cdot \mathbf{n}_* = 0, \quad (2.62)$$

whereas for the model of Bayley et al. [16] this reads:

$$\left[\left(-\frac{GbR^2}{8(1-\nu)} \sum_{\xi=1}^{12} \rho_{GND,e}^\xi \mathbf{A}_*^\xi + \frac{GbR^2}{4} \sum_{\xi=13}^{18} \rho_{GND,s}^\xi \mathbf{B}_*^\xi \right) : \mathbf{P}_*^\alpha \right] \cdot \mathbf{n}_* = 0, \quad (2.63)$$

which means that the dislocations freely escape from the surface, i.e. a *micro-stress free boundary*.

Whereas Kuroda and Tvergaard investigated the interpretation of the boundary conditions for a case similar to Evers et al. [13, 14], here the confrontation of Gurtin's model with the models of Evers et al. and Bayley et al. is treated in a more general setting. For the former model, equations (2.20) and (2.21) are considered and the physically based micro-stress vectors in the original external power description, i.e. equations (2.59), (2.61) and (2.62), are used for the latter type model for the unification purpose of the two model types, which is not a necessity for the proof of the thermodynamical consistency of the former type models.

Free surface: Within the original framework of the Evers-Bayley type models, a micro-stress free boundary was defined by dislocation densities that vanish on the surface, e.g. $\rho_{GND}^\xi = 0$ (cf. equation (2.20)) whereas it has a more complex definition (equation (2.62)) within the Gurtin type formulation. Several special cases in which equation (2.62) is fulfilled (except for the trivial solution of $\rho_{GND,e}^\alpha = \rho_{GND,s}^\alpha = 0$) are depicted in figure 2.1 and can be explained as:

- The resultant vector \mathbf{r} of the orthogonal vectors $A \mathbf{s}_*^\alpha$ and $B \mathbf{p}_*^\alpha$ (where A and B are scalar coefficients defined by $A = -\frac{GbR^2}{8(1-\nu)} \rho_{GND,e}^\alpha$ and $B = \frac{GbR^2}{4} \rho_{GND,s}^\alpha$) is perpendicular to the unit normal vector \mathbf{n}_* of the surface (i.e. lies in the slip plane) and none of the GND densities have to vanish.
- $\mathbf{s}_*^\alpha \cdot \mathbf{n}_* \neq 0$ and $\mathbf{p}_*^\alpha \cdot \mathbf{n}_* = 0$. In this case, edge GNDs can escape through the surface. Therefore, $\rho_{GND,e}^\alpha = 0$.

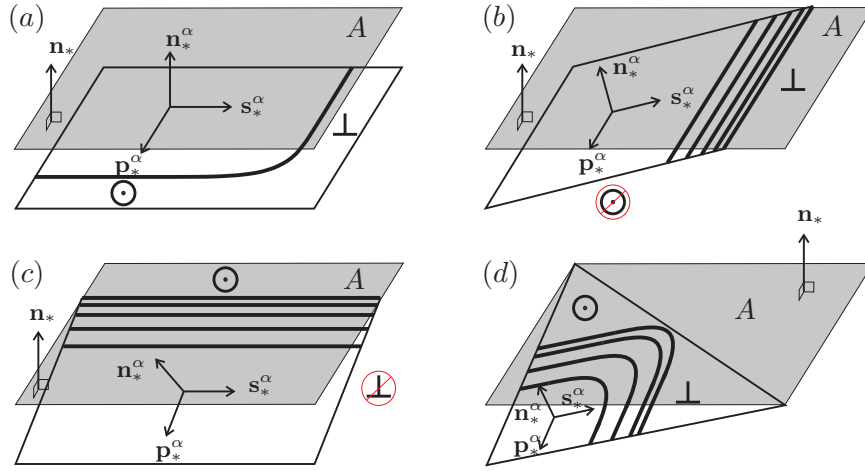


Figure 2.2: Hard boundary layers: (a) a non-zero slip parallel to the surface, (b) non-zero edge (\perp) and zero screw (\odot) GND densities, (c) zero edge and non-zero screw GND densities, (d) non-zero GND densities.

c) $\mathbf{s}_*^\alpha \cdot \mathbf{n}_* = 0$ and $\mathbf{p}_*^\alpha \cdot \mathbf{n}_* \neq 0$. In this case, screw GNDs can escape through the surface. Therefore, $\rho_{GND,s}^\alpha = 0$.

Notice that for case (a), the free surface definition depends on the orientation of the slip system and GND densities are not zero whereas in the model of Evers et al., GND densities are explicitly assumed to vanish. For the cases (b) and (c), both type of formulations are equivalent to each other.

Hard boundary: Obstructing slip at the surface, for example by a passivation layer, yields a hard boundary condition. In the Gurtin type model, this type of boundary condition is defined by vanishing crystallographic slip on the surface, e.g. $\dot{\gamma}^\alpha = 0$ (cf. equation (2.48)). The hard boundary condition in the Evers-Bayley type formulation is given by equation (2.21). Special cases satisfying equation (2.21) can be distinguished (see figure 2.2):

- a) $\mathbf{s}_*^\alpha \cdot \mathbf{n}_* = 0$ and $\mathbf{p}_*^\alpha \cdot \mathbf{n}_* = 0$. In this case, γ^α does not have to be zero on A_* .
- b) $\mathbf{s}_*^\alpha \cdot \mathbf{n}_* \neq 0$ and $\mathbf{p}_*^\alpha \cdot \mathbf{n}_* = 0$. Then, mandatorily $\gamma^\alpha = 0$, $\rho_{GND,e}^\alpha \neq 0$ and $\rho_{GND,s}^\alpha = 0$ on A_* .
- c) $\mathbf{s}_*^\alpha \cdot \mathbf{n}_* = 0$ and $\mathbf{p}_*^\alpha \cdot \mathbf{n}_* \neq 0$. Then, mandatorily $\gamma^\alpha = 0$, $\rho_{GND,e}^\alpha = 0$ and $\rho_{GND,s}^\alpha \neq 0$ on A_* .
- d) $\mathbf{s}_*^\alpha \cdot \mathbf{n}_* \neq 0$ and $\mathbf{p}_*^\alpha \cdot \mathbf{n}_* \neq 0$, then $\gamma^\alpha = 0$ is required.

Hence, it can be concluded that the Gurtin type formulation misses case (a) (cf. figure 2.2) where the definition of a hard boundary is still valid. For the cases (b), (c) and (d), both models give the same results. Note that, even though for the model of Bayley et al. [15, 16], it is not possible to visualize boundary conditions as it is done above, the study of the micro-boundary conditions for Evers's formulation demonstrates that similar micro-boundary conditions can be established for the Gurtin type model and the Evers-Bayley type models.

2.4 Discussion and concluding remarks

In this study, the thermodynamical consistency of a physically based strain gradient crystal plasticity theory, as proposed in Evers et al. [13, 14, 33] and Bayley et al. [15, 16], has been demonstrated through a direct comparison with a thermodynamically consistent strain gradient theory of crystal plasticity by Gurtin and Gurtin et al. [37, 43–45]. Evers-Bayley type models, which have been used for problems with small plastic strains so far, were enhanced by altering the state of the gradient operator in the internal stress and the dislocation density definitions from the reference configuration to the intermediate configuration in order to deal with truly large plastic strains. Then, energetic micro-stresses for the Gurtin type formulation were written based on the physical description of the back stresses of the Evers-Bayley type models, which provides a physical interpretation for the micro-stresses and shows that the micro-force balance law for a slip system corresponds to the definition of the effective resolved shear stress acting on that slip plane.

It has been shown for the model of Evers et al., which is a self-internal back stress formulation where only the dislocations that belong to the slip system itself contribute to the internal stress state, that the derived micro-stress is similar to the one given in [37] for an uncoupled defect energy function and to those in [38, 46, 47]. It lies in the plane of its slip system and the defect energy function that gives the constitutive equation for this micro-stress vector is a simple quadratic function in terms of GND densities.

For the full-internal back stress formulation of Bayley et al., which involves the energetic interactions between different slip systems, the derived physical micro-stress has a more complex form than the one for the formulation of Evers et al. [13, 14]. This micro-stress no longer resides in the plane of its slip system, which is believed to be a result of the defect forces exerted by the other slip systems with non-parallel slip planes. Hence, this micro-stress vector is different from those of Evers et al., Gurtin and Kuroda and Tvergaard where the energetic coupling of the different slip systems is not included and even from the micro-stress which is derived from a quadratic defect energy that couples different glide systems in a phenomenological way in Gurtin [37] since with a constitutive equation of the type as given in equation (2.36), a micro-stress vector of a slip system with out of plane components can not be handled. The defect energy function associated to the micro-stress resulting from Bayley et al. implicitly takes a more complex form, which is expected to be non-convex. As demonstrated in [48, 49] and similar publications, the contribution of GNDs of the same slip plane to the macroscopic material behavior may be described, at least qualitatively, by averaging the total effect over the related plane. However, this is not the case for the contribution arising from the interactions between the GNDs of different slip planes. The discrete-energetic interactions between different slip planes should be ensured in the definitions of back stresses for the Evers-Bayley type formulations, e.g. as in [15, 16] and in the definition of energetic micro-stresses and the associated defect energy functions of the Gurtin type models for a more realistic description of the material behavior from a physical perspective, which apparently requires more than simple quadratic energy functions. Furthermore, although apparently completely different additional field equations (GND density balance equations vs. the micro-force balance law) are used within the finite element context, it is shown that similar boundary conditions can be defined for both types of models. Note that the boundary conditions in between the free surface and hard interfaces, which can be important for the interfaces like penetrable surface coating or grain boundaries, can also be incorporated into these models. However, a physical interpretation of these in-between boundary conditions would require a separate constitutive model for these boundary conditions, see, for instance, [59].

This work discusses the thermodynamical consistency of the models by Evers et al. and Bayley et

al. and the unification with the model of Gurtin. However, the discussions here do not apply only to the three models considered, i.e. Evers et al., Bayley et al. and Gurtin, but also to other strain gradient crystal plasticity theories which follow a phenomenological approach.

Multiphysical simulations with a gradient theory of crystal plasticity

Abstract

The micro and sub-micro scale dimensions of the components of modern high-tech products pose challenging engineering problems that require advanced tools to tackle them. An example hereof is time dependent strain recovery, here referred to as anelasticity, which is observed in metallic thin film components of RF-MEMS switches. Moreover, it is now well known that the properties of a thin film material strongly depend on its geometrical dimensions through so-called size effects. A strain gradient crystal plasticity formulation (SGCP) is hereby required as recently proposed [13–16], involving a back stress in terms of strain gradients capturing the lattice curvature effect. In the present work, the SGCP model is used in a realistic simulation of electrostatic bending of a free standing thin film beam made of either a pure fcc metal or a particle strengthened Al-Cu alloy. The model capabilities to describe the anelastic and plastic behavior of metallic thin films in comparison with experimentally available data are thereby assessed. Simulation results show that the SGCP model is able to predict a macroscopic strain recovery over time following the load removal. The amount of the anelastic relaxation and the accompanying relaxation times results from the rate dependent modeling approach, the basis of which is phenomenological only. The SGCP model is not capable of describing the permanent deformations in an alloy thin beam as observed in electrostatic experiments. Hence, to incorporate realistic time constants and the influence of the microstructure into the mechanical behavior of the thin film material, an improved constitutive law for crystallographic slip is necessary within the SGCP formulation.

3.1 Introduction

Capacitive radio-frequency microelectromechanical systems (RF-MEMS) possess a high potential for being applied in the next generation of wireless network applications (e.g. GPS systems, radars or mobile phones). This is due to their high Q factor, low power consumption, low insertion loss, high isolation and many other superior characteristics compared to their functional equivalents such as diode based solid state relays [1, 60]. A schematic representation of a capacitive RF-

MEMS is given in figure 3.1. Its working principle is similar to that of parallel plate capacitors: there exist two electrodes, one of which is suspended over the other by means of springs. The position of the free-standing electrode is adjusted by application of a voltage. This makes the device reconfigurable, making it fully operational over a wide range of frequencies.

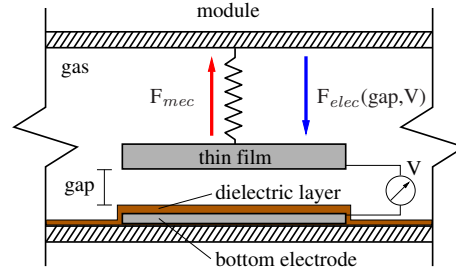


Figure 3.1: Schematic representation of a capacitive RF-MEMS device. At pull-in voltage, the electrostatic force F_{elec} , a function of the gap between the electrodes and the applied potential difference (V), becomes larger than the elastic restoring force F_{mec} and the upper electrode snaps on the bottom electrode. The dielectric layer covering the bottom electrode provides a small clearance between the electrodes in this configuration, making the generation of a high capacitance possible.

Reliability is one of the important concerns related to RF-MEMS devices. As discussed in [61], typical reasons for the degradation of MEMS properties during service life are wear, fatigue, creep, excessive plastic/anelastic deformations, delamination in multi-layered structures and dielectric charging or residual stresses due to, for instance, the manufacturing processes. The reader is referred to [61] and the references therein for additional information on the failure modes of MEMS devices. Most of the mentioned failure types are in one way or another associated to the mechanical behavior of the materials used, such as the behavior of the springs holding the free-standing electrode in a capacitive RF-MEMS switch. Hence, an accurate description of the material behavior is necessary for the development of reliable products with a predictable service life.

The springs of the RF-MEMS device considered in this work are polycrystalline thin film components that are made of an Al-Cu alloy containing small second phase particles. In the last two decades, it has been shown [3–5] that the mechanical properties of metallic thin films are clearly influenced by so-called size effects, e.g. invoked by the distribution of the densities of geometrically necessary dislocations or by surface constraints like passivation layers [17]. Thin film materials are also reported to be prone to time dependent deformations such as creep [6, 9–12] and anelasticity [6–8, 62–65]. Creep, accumulating plastic deformation under a constant load over time, is also observed in bulk materials, where it is a relatively well studied phenomenon, see [66, 67] and the references therein. On the contrary, the anelastic time dependent strain recovery of metal thin films after load removal has recently attracted attention since it appears to be more pronounced in small material volumes. Time dependent deformation of thin film components in RF-MEMS may easily lead to malfunctioning of the device. For instance, creep can cause irreversible deformations that permanently reduce the gap between the electrodes and, in turn, the opening and closing voltages of the switch. Anelasticity may induce uncontrollable evolving changes in device properties as the gap height will change over time.

Burg et al. [68] performed micro-beam bending experiments on polycrystalline thin beams of different lengths and thicknesses. The beams were made of an Al-Cu [1 wt%] alloy with second phase θ particles. For long beams, the experiments yielded a Young's modulus and a yield stress

of around 69 GPa (a value close to that of the bulk material) and 150 MPa, respectively, whereas these quantities showed large spread for shorter beams. They were not able to identify the effect of beam thickness on the Young's modulus and the yield stress. In another study [2], the effect of creep on a capacitive RF-MEMS switch with polycrystalline thin film electrodes was investigated by electrostatic experiments and numerical simulations. The material used in the experiments was considered to be the same as that in [68]. The test structures showed no permanent deformation after full relaxation at room temperature, whereas at 75°C and 100°C, an increasing permanent deformation was observed with increasing temperature. Additionally, finite element simulations were done for the reproduction of the experimental results, using a phenomenological constitutive equation for the plastic strain rate based on dislocation glide [10–12]. However, the simulation results showed that the employed constitutive law is incapable of predicting the material response. In [7], experiments were conducted on Al-Cu [1 wt%] free-standing polycrystalline thin films by using a micro clamp tool to mechanically bend the specimens. In these experiments, it was observed that after an initial elastic spring back upon unloading, an additional strain recovery occurs over time and almost no permanent deformation remains. The bulge tests and stress dip tests by [6] on free-standing polycrystalline Al films with thicknesses between 220 and 550 nm showed that thinner beams are more resistant to creep deformations. Moreover, at about the same stress levels, creep strains in thin film samples were at least three orders of magnitude smaller than that of the material in bulk form. Additionally, some anelasticity was observed in the response, which was attributed to grain boundary sliding. After a correction for the anelastic relaxation, the experimental results were reproduced reasonably well by a material model based on dislocation glide [6]. Quasi-static micro-tensile stress relaxation tests on free-standing Al and Al-Ti thin films at stress levels below the yield strength were performed by [8, 62]. It was found that the anelastic recovery depends on the average grain size: relaxation time and strength decrease with increasing grain size. In case of Al-Ti films that have precipitates along grain boundaries, a smaller amount of relaxation with larger time constants was observed, suggesting that grain boundary sliding may be the rate controlling mechanism for the observed relaxations. Similar creep and anelasticity phenomena were also reported for free-standing gold films in plane strain membrane bulge tests [63, 65].

In addition to the material non-linearities, the geometry of a capacitive RF-MEMS switch introduces another source of non-linearity. At a device specific voltage, pull-in voltage, the free-floating electrode snaps onto the dielectric layer covering the bottom electrode. Additionally, the interaction between the thin film surfaces and the inert gas trapped within a device module may provide additional damping during transient loads.

In this work, the predictive capabilities of a previously developed strain gradient crystal plasticity (SGCP) model [16] for the description of anelastic material behavior in RF-MEMS structures are assessed. A higher order description is used since standard continuum theories fail to describe the scale dependency observed in metal thin films, lacking an internal length scales. Multi-physical simulations are performed to describe electrostatic bending of thin beams of a pure metal and a two phase alloy by considering i) the mechanical behavior of the thin film, represented by the SGCP theory, and ii) electrostatic forces generated by voltage application [69]. The combined effect of the crystallographic micro-structure of the thin film and distributed electrostatic loads on the overall structural response is evaluated and compared with available experimental data. The results show that the SGCP model is able to yield a macroscopic strain recovery over time following the load removal. However, a detailed analysis demonstrates that the anelastic relaxation time and strength originate from the rate dependent nature of the model only.

3.2 Strain gradient crystal plasticity formulation

In the present work, the mechanical behavior of the material is described with the strain gradient crystal plasticity theory of [13–16]. The model is based on a multiplicative decomposition [50, 51] of the deformation gradient tensor \mathbf{F} into its elastic and plastic parts:

$$\mathbf{F} = \mathbf{F}_e \cdot \mathbf{F}_p, \quad (3.1)$$

where the elastic part \mathbf{F}_e describes the stretch and the rotation of the lattice with respect to an intermediate configuration defined by the plastic part \mathbf{F}_p .

The elastic second Piola-Kirchhoff stress tensor \mathbf{S} is given in the intermediate configuration via the linear Hookean relation

$$\mathbf{S} = \mathbb{C} : \mathbf{E}_e \quad \text{with} \quad \mathbf{E}_e = \frac{1}{2} (\mathbf{F}_e^T \cdot \mathbf{F}_e - \mathbf{I}), \quad (3.2)$$

with the fourth order elasticity tensor \mathbb{C} , the elastic Green-Lagrange strain tensor \mathbf{E}_e and the second order identity tensor \mathbf{I} . \mathbf{S} is defined by the pull-back of the Kirchhoff stress $\boldsymbol{\tau}$ to the intermediate configuration as

$$\mathbf{S} = \mathbf{F}_e^{-1} \cdot \boldsymbol{\tau} \cdot \mathbf{F}_e^{-T}. \quad (3.3)$$

The rate of the plastic deformation gradient is determined by

$$\dot{\mathbf{F}}_p = \mathbf{L}_p \cdot \mathbf{F}_p, \quad (3.4)$$

where \mathbf{L}_p is the plastic velocity gradient and is rendered from the crystallographic slip rates of 12 octahedral slip systems for an fcc metal as

$$\mathbf{L}_p = \sum_{\alpha=1}^{12} \dot{\gamma}^\alpha \mathbf{P}_0^\alpha. \quad (3.5)$$

Here, $\dot{\gamma}^\alpha$ is the plastic slip rate of system α and $\mathbf{P}_0^\alpha = \mathbf{s}_0^\alpha \mathbf{n}_0^\alpha$ is the Schmid tensor with \mathbf{s}_0^α the unit direction of the Burgers vector and \mathbf{n}_0^α the unit normal of the slip plane of system α defined in the intermediate configuration.

The flow rule is given by a modified Arrhenius type rate equation:

$$\dot{\gamma}^\alpha = \dot{\gamma}_0 \left(\frac{|\tau_{eff}^\alpha|}{s^\alpha} \right)^m \exp \left[-\frac{\Delta F_0}{kT} \left(1 - \frac{|\tau_{eff}^\alpha|}{s^\alpha} \right) \right] \text{sign}(\tau_{eff}^\alpha), \quad (3.6)$$

where $\dot{\gamma}_0$ is the reference slip rate, m is the rate sensitivity, s^α is the slip resistance, T is the absolute temperature and k is the Boltzmann constant. ΔF_0 is the energy necessary to overcome the crystallographic slip resistance at zero stress. The effective resolved shear stress acting in a slip system is given by the difference between the applied resolved shear stress τ^α and the resolved back stress τ_b^α

$$\tau_{eff}^\alpha = \tau^\alpha - \tau_b^\alpha \quad \text{with} \quad \tau^\alpha = \mathbf{S} : \mathbf{P}_0^\alpha. \quad (3.7)$$

The back stress is the key ingredient of the SGCP model, through which the influence of the lattice curvature on the material behavior is incorporated into the framework. It is calculated in a material

point by the integration of stress fields of non-uniformly distributed densities of geometrically necessary dislocations (GNDs) in a cylindrical volume. The back stress of a slip system was initially formulated by [13, 14] in terms of contributions of the GNDs of that slip system only. In [15, 16], it was extended further by considering the contributions of all slip systems. The internal stress field due to edge GNDs is given by [15, 16] as

$$\boldsymbol{\sigma}_e^{int} = \frac{GbR^2}{8(1-\nu)} \sum_{\xi=1}^{12} \nabla_0 \rho_{GND,e}^{\xi} \cdot \left(3\mathbf{n}_0^{\xi} \mathbf{s}_0^{\xi} \mathbf{s}_0^{\xi} + \mathbf{n}_0^{\xi} \mathbf{n}_0^{\xi} \mathbf{n}_0^{\xi} + 4\nu \mathbf{n}_0^{\xi} \mathbf{p}_0^{\xi} \mathbf{p}_0^{\xi} - \mathbf{s}_0^{\xi} \mathbf{s}_0^{\xi} \mathbf{n}_0^{\xi} - \mathbf{s}_0^{\xi} \mathbf{n}_0^{\xi} \mathbf{s}_0^{\xi} \right), \quad (3.8)$$

and for screw GNDs, it reads:

$$\boldsymbol{\sigma}_s^{int} = \frac{GbR^2}{4} \sum_{\xi=13}^{18} \nabla_0 \rho_{GND,s}^{\xi} \cdot \left(-\mathbf{n}_0^{\xi} \mathbf{s}_0^{\xi} \mathbf{p}_0^{\xi} - \mathbf{n}_0^{\xi} \mathbf{p}_0^{\xi} \mathbf{s}_0^{\xi} + \mathbf{p}_0^{\xi} \mathbf{s}_0^{\xi} \mathbf{n}_0^{\xi} + \mathbf{p}_0^{\xi} \mathbf{n}_0^{\xi} \mathbf{s}_0^{\xi} \right), \quad (3.9)$$

with $\mathbf{p}_0^{\xi} = \mathbf{s}_0^{\xi} \times \mathbf{n}_0^{\xi}$ associated with slip system ξ and R the radius of the cylindrical integration volume, which is also a length scale. In [13–16], two screw dislocations with the same direction of the Burgers vector are coupled into one set, leading to 6 slip systems for screw GNDs whereas the number of slip systems for edge GNDs is 12. Hence, index ξ runs over 1...12 in case of edge dislocations and 13...18 for screw dislocations. The back stress is then given by the opposite of the internal stress that is resolved onto the slip system by the related Schmid tensor:

$$\tau_b^{\alpha} = - \left(\boldsymbol{\sigma}_e^{int} + \boldsymbol{\sigma}_s^{int} \right) : \mathbf{P}_0^{\alpha} \quad \text{for } \alpha = 1, 2, \dots, 12. \quad (3.10)$$

Note that although statistically stored dislocations (SSDs) are also involved in the framework, they do not contribute to the internal stress state as they are randomly distributed. However, together with GNDs, they determine the resistance, s^{α} , against dislocation glide. The slip resistance of a slip system is provided by the short-range dislocation-dislocation interactions. Following [26], it is formulated in terms of both ρ_{SSD}^{α} and ρ_{GND}^{α} as:

$$s^{\alpha} = cGb \sqrt{ \sum_{\xi=1}^{12} A^{\alpha\xi} |\rho_{SSD}^{\xi}| + \sum_{\xi=1}^{18} A^{\alpha\xi} |\rho_{GND}^{\xi}| } \quad \text{for } \alpha = 1, 2, \dots, 12, \quad (3.11)$$

where c is a material constant [52], G is the shear modulus, b the magnitude of the Burgers vector, and $A^{\alpha\xi}$ are the components of the matrix that defines the strength of the interactions between different slip systems [53]. It is composed of six interaction coefficients corresponding to self hardening, coplanar hardening, Hirth lock, Glissile junction, Lomer-Cottrell lock, and cross slip [70].

The evolution of SSD densities on each slip system ξ is described by

$$\dot{\rho}_{SSD}^{\xi} = \frac{1}{b} \left(\frac{1}{L^{\xi}} - 2y_c \rho_{SSD}^{\xi} \right) |\dot{\gamma}^{\xi}| \quad \text{with } \rho_{SSD}^{\xi}(t=0) = \rho_{SSD_0}^{\xi} \quad \text{for } \xi = 1, 2, \dots, 12, \quad (3.12)$$

which is the generalized form of the relation originally suggested by [56]. In this equation, the first term within the parentheses denotes the accumulation, where L^{ξ} is the average dislocation

segment length defined by

$$L^\xi = \frac{K}{\sqrt{\sum_{\alpha=1}^{12} H^{\xi\alpha} |\rho_{SSD}^\alpha| + \sum_{\alpha=1}^{18} H^{\xi\alpha} |\rho_{GND}^\alpha|}}. \quad (3.13)$$

Here, K is a material parameter. $H^{\xi\alpha}$ are the components of an interaction matrix that is similar to $A^{\alpha\xi}$ and represents the mutual interactions between the dislocations [13]. The second term in the parentheses is the annihilation rate where y_c stands for the critical annihilation length, which is the average distance between two oppositely signed dislocations, below which they annihilate.

The GNDs represent the signed fraction of the total dislocation population and are necessary to preserve the lattice compatibility in a crystal. The gradient of slip in the slip direction \mathbf{s}_0^α gives the density of edge GNDs whereas the slip gradient in the direction of \mathbf{p}_0^α yields the density of screw GNDs. The gradient of slip in the direction of the slip plane normal \mathbf{n}_0^α does not introduce any GNDs [26]. A balance equation for the densities of the GNDs can be written as

$$\rho_{GND,e}^\xi = \rho_{GND,e0}^\xi - \frac{1}{b} \mathbf{s}_0^\xi \cdot \nabla_0 \gamma^\xi, \quad (3.14)$$

$$\rho_{GND,s}^\xi = \rho_{GND,s0}^\xi + \frac{1}{b} \left(\mathbf{p}_0^{\alpha_1(\xi)} \cdot \nabla_0 \gamma^{\alpha_1(\xi)} + \mathbf{p}_0^{\alpha_2(\xi)} \cdot \nabla_0 \gamma^{\alpha_2(\xi)} \right). \quad (3.15)$$

Here, ξ runs over 1, 2, ..., 12 for edge GNDs and over 13, 14, ..., 18 for screw GNDs. $\rho_{GND,e0}^\xi$ and $\rho_{GND,s0}^\xi$ denote the densities of edge and screw GNDs that are initially present in the material, $\alpha_1(\xi)$ and $\alpha_2(\xi)$ represent two slip systems with the same slip direction but different plane normals for each screw GND. Note that equation (3.15) differ slightly from [16].

The SGCP model is implemented in a finite element framework in the commercial software ANSYS by using two governing field equations: the momentum balance equation and the GND density balance equations (3.14) and (3.15). Degrees of freedom are the displacements and densities of GNDs. 20 noded hexagonal elements are used for the discretization of the displacement domain with 3 translational displacement degrees of freedom for each node, whereas 8 noded hexagonal elements are employed for the dislocation density domain with 18 GND densities (12 for edge and 6 for screw dislocations) as degrees of freedom for each node. Hence, there are 21 degrees of freedom at the corner nodes of the element and 3 degrees of freedom at the mid-nodes. The two problems are solved in a strongly coupled manner. The associated variational formulation can be found in [13–16].

3.3 Electro-mechanical transducer elements

The electrostatic pull down of a cantilever thin beam is next studied using multiphysical simulations. The beam is loaded by means of the attractive forces generated by a voltage difference between the beam and a ground plate. This phenomenon is modeled by using transducer elements as existing in the element library of ANSYS. Electro-mechanical transducers are one dimensional line elements developed by [69], based on the concept of an electrical transducer element with a variable geometry. The relative position between the plates of the transducer can be changed by the application of an electric potential to the plates, cf. figure 3.2. A transducer element has two degrees of freedom per node, a voltage and an axial displacement, and strongly couples the

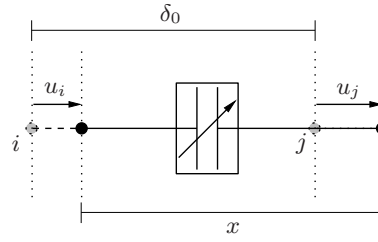


Figure 3.2: Representation of a transducer element. i and j are indices for the nodes, x quantifies the distance between the nodes (plates) and is given by $x = \delta_0 + u_j - u_i$ where u denotes nodal displacement and δ_0 is the initial separation distance.

structural finite element domain with the electric domain. The electrostatic force f is defined as [69]

$$f = \frac{d}{dx} \left[\frac{C(x)}{2} V^2 \right] \quad (3.16)$$

where $C(x)$ is the capacitance as a function of the relative displacement x of the plates and V is the electrical potential difference. Within the electrical domain, the electric current i is given by

$$i = \frac{d}{dt} [C(x)V] \quad (3.17)$$

An important input for transducer elements is the relationship between capacitance and relative displacement. This relationship can be provided either by defining the coefficients of a polynomial that defines the capacitance versus displacement response, e.g.

$$C(x) = C_0/x + C_1 + C_2x + C_3x^2 + C_4x^3, \quad (3.18)$$

or in the form of data that should be generated by running an initial set of electrostatic simulations. A typical capacitance versus gap curve is given in figure 3.3a. In this figure δ_{min} represents the minimum distance between the plates, after which the transducer element starts working as a linear contact element. Figure 3.3b shows the change in the net force acting on the plates with respect to the gap. When the relative distance between the electrodes are small and the surface areas of electrodes are large, e.g. in case of RF-MEMS switches, the nodal capacitance can be approximated by

$$C(x) = \epsilon_0 A_N / x, \quad (3.19)$$

based on the parallel plate assumption where ϵ_0 is the free-space permittivity and A_N is the nodal area. In this work, equation (3.19) is used for the calculation of the nodal capacitance in the electrostatic simulations in the next sections. For additional information on the modeling of the electrical domain, see appendix A.

Further information on the theory of transducer elements may be found in [69, 71, 72].

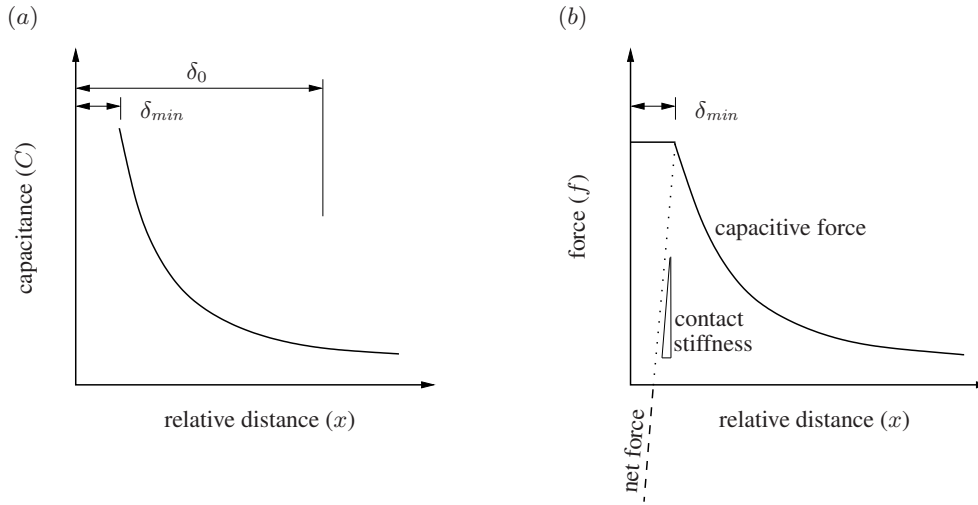


Figure 3.3: Variation of the capacitance (a) and the net force on the plates (b) with respect to the separation distance between the plates of a transducer element [71].

3.4 Multiphysical simulations by using the SGCP theory

The electrostatic actuated bending of a cantilever thin beam is studied as a representative case for the solution of the full capacitive switch problem. Several electrostatic beam bending simulations are performed which are classified in two sets. In the first set, the focus is on the investigation of the capabilities of the SGCP model to predict an anelastic response for a free-standing pure metal film. In the second set, multiphysical simulations are done to reproduce the results of an electrostatic beam bending experiment on a Al-Cu thin film.

3.4.1 Thin film inelasticity

The electrostatic bending of a cantilever thin beam is numerically analyzed for two different surface conditions: a free surface, through which dislocations can escape, and a passivated surface, which fully hinders the motion of dislocations. A discussion about boundary conditions that can be imposed within the SGCP framework can be found in [73]. The dimensions of the finite element model and the boundary conditions used in the simulations are given in figure 3.4a. The beam is made of a pure fcc metal having in plane randomly oriented grains, with their [111] axis parallel to the film surface normal. The mechanical behavior of the thin film material is described by using the SGCP model while for the electric domain, transducer elements are used, cf. figure 3.4b. Additionally, non-linear springs are employed to take into account the roughness of the metallic surfaces inducing contact with the dielectric layer on the bottom electrode. Further information about the modeling of electric domain and the contact between the beam and the dielectric layer can be found in appendix section of this chapter. The material parameters associated with the SGCP formulation are provided in table 3.1. The remaining parameters are taken from literature [13–16]. Dielectric charging is ignored in the simulations. The loading scheme is depicted in figure 3.5. A potential difference is applied to the beam and the bottom electrode and is increased until the pull-in voltage V_{pi} at t_1 . At V_{pi} , the cantilever beam becomes unstable and snaps to the bottom electrode. Since the pull-in of the beam imposes convergence issues, this instability is passed by a custom solution algorithm: At time t_1 at pull-in voltage, the vertical displacements, u_z , of some of the nodes on the bottom surface of the beam which are located in the contact region shown in

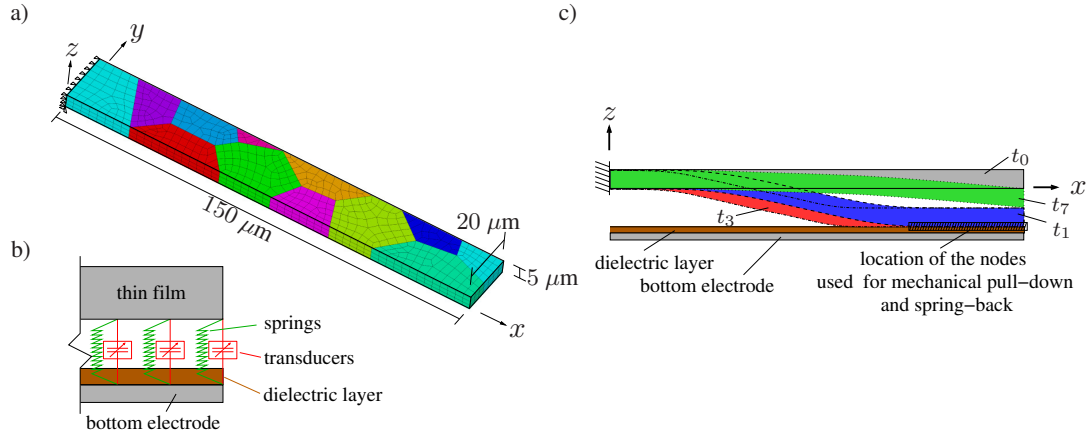


Figure 3.4: a) Finite element model of a polycrystalline cantilever thin beam. b) A $y - z$ cross-section of the numerical model. The clearance between the bottom surface of the beam and the top surface of the dielectric layer is about $3.2 \mu\text{m}$. The bottom electrode is located fully c) The instabilities at pull-in and release voltages are overcome by a custom solution algorithm which uses the nodes on the bottom surface of the beam in the region of contact with the dielectric layer. The deformed shape of the beam expected to occur at times $t = t_0$ (initial state), $t = t_3$ (just after the pull-in), $t = t_5$ (at the maximum voltage) and $t = t_7$ (after unloading, by assuming that the beam shows residual deformations) are also shown in dark gray, blue, red and green colors, respectively.

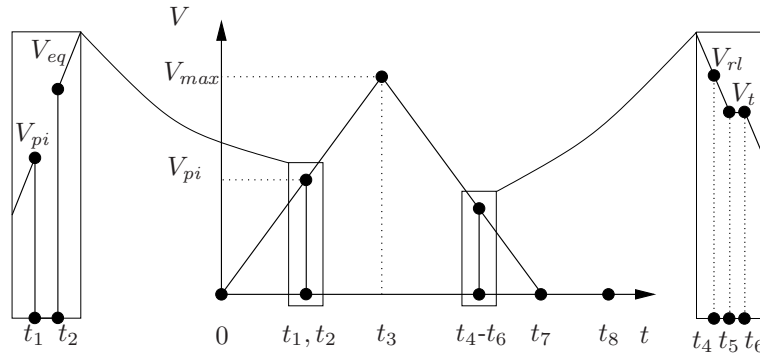


Figure 3.5: A loading-unloading cycle in the multiphysical simulations. Corresponding time and voltage values are given in table 3.2.

figure 3.4c are constrained and the potential difference is reset to zero. Between t_1 and t_2 , the beam is pulled down by the application of a prescribed displacement to these constrained nodes until contact with the bottom electrode is reached. After t_2 , the electric potential is increased at a relatively fast rate to V_{eq} , the voltage at which force equilibrium is achieved at the nodes used for pulling down the beam. At V_{eq} , these constrained nodes are released and the voltage is increased further to the maximum voltage V_{max} at the same rate as in time period $[0, t_1]$. A similar approach is used during the unloading phase to handle the spring back of the beam at the release voltage, V_{rl} , at which the mechanical restoring forces are larger than the electrostatic forces. However, this time the voltage is reduced to a value (V_t) slightly lower than the release voltage at t_5 following the constraining of some of the nodes in the contact region at t_4 . Then, the forced equilibrium position is searched for at these constrained nodes by reducing the gap at the constant voltage until t_6 . The beam is fully unloaded between $[t_6, t_7]$ and the variation of the vertical displacement of the beam is traced until t_8 for possible anelastic relaxation.

Table 3.1: Material parameters for the SGCP model.

Parameter	Meaning	Value	Unit
C_{11}	Elastic constant	95230	MPa
C_{12}	Elastic constant	40400	MPa
C_{44}	Elastic constant	53840	MPa
ν	Poisson's ratio	0.37	-
m	Strain rate sensitivity	10	-
G_0	Activation energy	$30 \cdot 10^{-8}$	pJ
T	Temperature	293	K
b	Burgers vector length	$2.86 \cdot 10^{-4}$	μm
K	Material constant	10	-
y_c	Critical annihilation length	$1.6 \cdot 10^{-3}$	μm
c	Material constant	0.3	-
ρ_{SSD_0}	Initial SSD density	7	μm^{-2}
$\dot{\gamma}_0$	Reference plastic strain rate	$1 \cdot 10^{-3}$	s^{-1}
R	Length scale	1	μm

Table 3.2: Time and voltage data associated with figure 3.5.

Time [s]	Voltage [V]
$t_1 = 1.3$	$V_{pi} = 130^\dagger, 135^\ddagger$
$t_2 - t_1 \approx 0.1$	$V = 0, V_{eq} \approx 60$
$t_3 = 1.8$	$V_{max} = 180$
$t_4 = 3$	$V_{rl} \approx 60$
$t_6 - t_4 \approx 0.1$	$V_t \approx 57$
$t_7 = 3.6$	$V_{min} = 0$
$t_8 = 10$	$V_{min} = 0$

[†] For free surface condition.

[‡] For passivated surface condition.

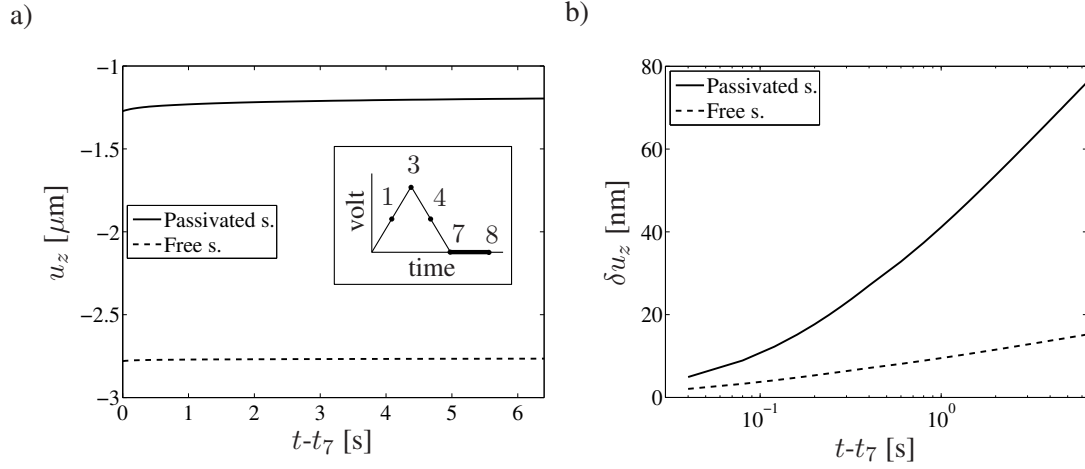


Figure 3.6: a) Position of a node at the tip of the beam after t_7 for free surface and passivated surface conditions. b) Displacement of the node after t_7 vs. time on a logarithmic scale.

Figure 3.6 shows the time dependent displacement of a node located at the beam tip for the simulations with two different surface conditions, i.e. free and passivated surfaces, starting from the moment when the voltage was just decreased to zero at $t = t_7$, where elastic recovery already started. At $t = t_7$, the vertical location of the control node reads $z = -2.78 \mu\text{m}$ and $z = -1.27 \mu\text{m}$ for free and passivated surface conditions, respectively. This result is in line with the beam with passivated surfaces having a larger resistance against the plastic deformation because the prevention of slip through surfaces will lead to larger GND densities, the inhomogeneous distribution of which causes larger internal stresses, i.e. larger back stresses. As seen in figure 3.6a, the amount of time dependent recovery is also larger for the passivated surface condition than for the free surface condition, reflecting the role of the internal stresses on the recovery process. Moreover, the difference in the slopes of the curves in figure 3.6b, which shows the recovery versus time, demonstrates that the time constants related to recovery are different for the two different surface conditions.

Additional information acquired from the simulations revealing details on the observed anelastic recovery is presented in figure 3.7. In this figure, (a) and (b) show the vertical displacement profile of the beam along the z axis at different instants of time for free and passivated surface conditions. The presence of a passivation layer on the surfaces leads to an extended range, in which the beam behaves elastically. The results shows that the beam with surface passivation has also a larger pull-in voltage, cf. table 3.2. This results from an increase in GND density due to the trapping of dislocations at surfaces. As seen in figures 3.7c and d, the average GND density¹ in case of a passivated surface condition reaches values that are about twice as large as that in case of a free surface condition. GNDs are typically produced at locations with a large curvature. Moreover, for the passivated surface condition, the GND density significantly drops in the time period $[t_3, t_8]$ while no noticeable change occurs in the GND density for the beam with free surfaces. In fact, the decrease of the GND densities is related to the recovery of plastic strains. Figure 3.7d reveals

¹The average GND density over the length of beam is given by $\bar{\rho}_{GND}^{x_{i-1}, x_i} = \left[\sum_{n=1}^N (\rho_{GND}^n) / N \right]_{x_{i-1}}^{x_i}$ where x_{i-1} and x_i are two successive points along the length, N is the number of nodes involved in the volume, the borders of which are set by x_{i-1} and x_i . ρ_{GND}^n is the average GND density at a node and given by $\rho_{GND}^n = \sqrt{\sum_{i=1}^{12} (\rho_{GND,e}^i)^2 + 0.5 \sum_{i=13}^{18} (\rho_{GND,s}^i)^2}$.

Table 3.3: Material parameters used for the identification of the parameter governing the relaxation time during anelastic deformation recovery. Unspecified values are the same as those in the reference set.

c [-]	ρ_{SSD_0} [μm^{-2}]	m [-]	ΔF_0 [pJ]
0.3	7	10	$30 \cdot 10^{-8}$
0.4	-	-	-
0.5	-	-	-
-	10	-	-
-	20	-	-
-	-	20	-
-	-	50	-
-	-	-	$10 \cdot 10^{-8}$
-	-	-	$20 \cdot 10^{-8}$

that the density of GNDs is already being reduced during the unloading stage $[t_3, t_7]$. The back stress developed during the loading is large enough to change the sign (or direction) of the effective resolved shear stress during the unloading phase, cf. figure 3.7f and h. A change of the sign of the effective resolved shear stress causes a reversal of the direction of crystallographic slip. Figures 3.7d, f and h suggest that in case of a passivated surface condition, the reverse glide continues, particularly in the regions close to the fixed end of the beam, during $[t_7, t_8]$, i.e. after the beams are fully unloaded. Within this period of time, the effective resolved shear stress is mainly composed of the back stress. During the reverse glide of dislocations, the plastic strain and the density of the GNDs are reduced (see equations (3.8) and (3.9)). As a result, the back stress decreases (figure 3.7h) and, accordingly, the driving force for the reverse slip shrinks. The recovery goes on until the effective resolved shear stress will be reduced to a value that does not trigger any significant crystallographic slip.

Additional simulations are performed to identify the governing time constants for the recovery of the beam. The material parameter c , initial SSD density ρ_{SSD} , stress sensitivity constant m and activation energy ΔF_0 control the anelastic behavior of the material at a constant temperature through equation (3.6). Note that the reference slip rate, $\dot{\gamma}_0$, is considered to have the same effect as the parameters above. The bending of a single crystalline beam with passivated surfaces and having the same geometry as the beam in figure 3.4a is simulated by using several values for these parameters, as summarized in table 3.3. The results are presented in figure 3.8. The vertical displacement of a node at the tip of the beam starting from $t = t_7$ (after the elastic recovery upon the removal of the load) is given in the left column of the figure. Figures 3.8a, c, e and g show that the amount of the strain recovery largely relies on parameters c , ρ_{SSD_0} and ΔF_0 , controlling the overall crystallographic slip resistance. The influence of different values of m in a physical range on the amount of the anelastic recovery and the relaxation times is negligible compared to the remaining parameters, i.e. c , ρ_{SSD_0} and ΔF_0 . It can be inferred from the slope of the curves in figures 3.8a, c, e and g that these three parameters also determine the relaxation times generated by the SGCP model. Their influence can be interpreted as follows: a larger c or ρ_{SSD_0} results in a larger slip resistance. A larger slip resistance reduces the crystallographic slip activity, i.e. the amount of plastic slip is decreased, which generates less GNDs and, hence a lower internal stress for the driving force in reverse slip. Moreover, a large slip resistance will also preclude reverse slip when the magnitude of the effective resolved shear stress is relatively low with respect to the

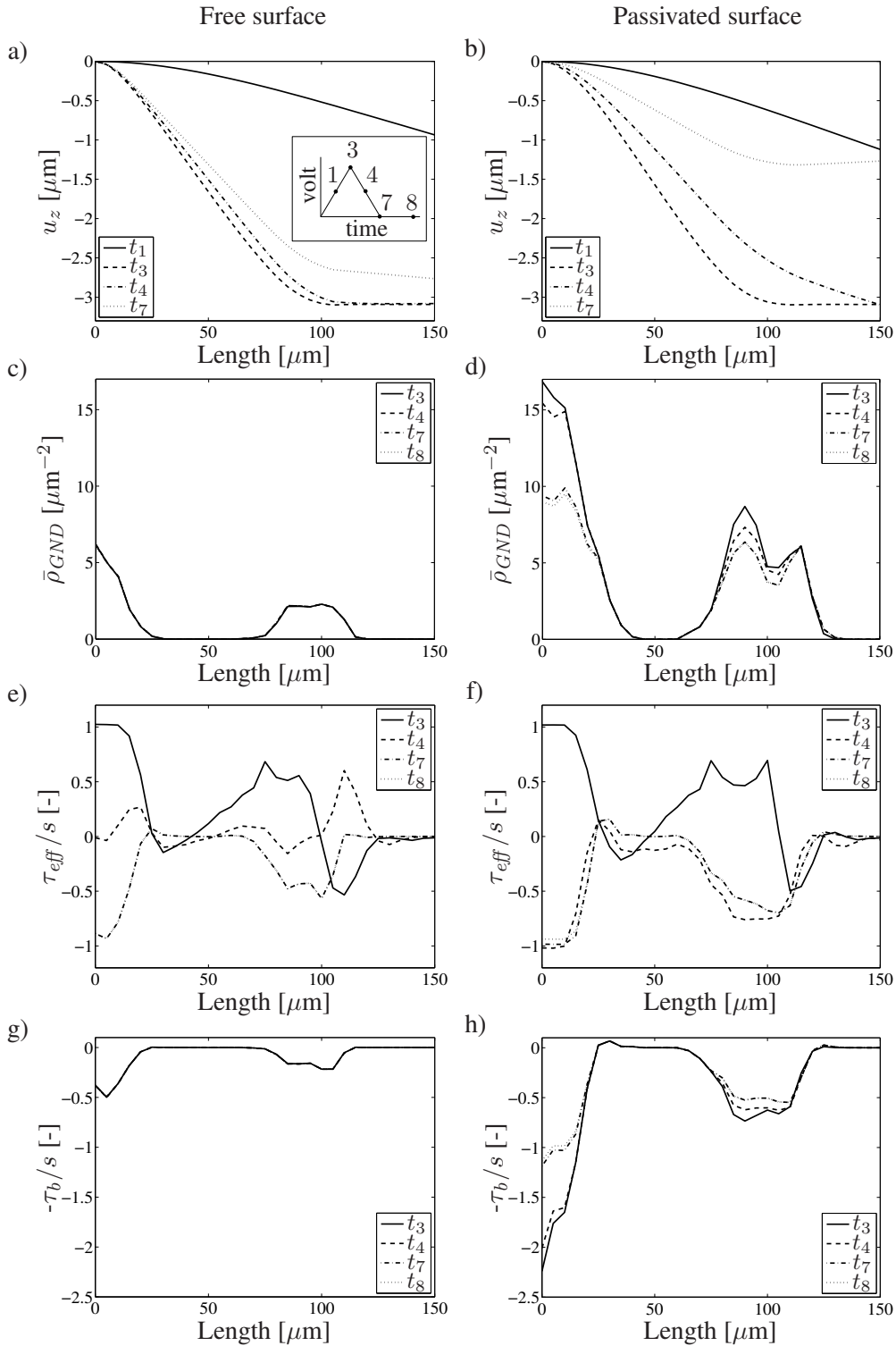


Figure 3.7: Simulation results at various instants of time: deflection profile (a-b), average GND density $\bar{\rho}_{GND}$ (c-d), and the ratios of the effective resolved shear stress (e-f) and the back stress (g-h) to the slip resistance. The results on the left and right side are obtained with free surface and passivated surface conditions, respectively. The data plotted in (e)-(h) belong to the slip system with the largest crystallographic slip rate.

slip resistance. A similar interpretation also applies to figure 3.8g. ΔF_0 is an activation energy for both forward and reverse slip, and hence, a smaller activation energy favors anelastic recovery.

The right column of figure 3.8 shows the rate of the deformation recovery, which decays with time. Note that the smallest recovery rates occur for the largest values of c and ρ_{SSD_0} . Due to the large slip resistance, the slip rate by reverse glide is so small that it would not induce a fast reduction in the GND density and the back stress. Consequently, the rate of recovery may be either very small as in figure 3.8d or nearly zero for short observation times, cf. figure 3.8b, but the recovery will be still noticeable at longer times.

Although the anelastic recovery observed in these simulations is physically explainable based on a dislocation glide mechanism, the associated relaxation times are not considered to realistic. The SGCP model does not incorporate a physically justified parameter for the precise characterization of the time dependency. Simulation results show that the rate of recovery predicted by the SGCP model is sensitive to the parameters governing the flow rule even though these parameters are introduced for different purposes. The observed anelasticity is a simple consequence of the rate dependent modeling of crystal plasticity.

3.4.2 Simulation of electrostatic beam bending experiments

Experiments

Electrostatically actuated bending experiments were conducted by [74] on a thin polycrystalline cantilever beam in order to characterize the mechanical behavior of the material. The beam was made of an Al-Cu [1 wt%] alloy, including very small second phase particles. See figure 3.9a for its geometrical properties. Experiments consisted of successive loading-unloading cycles under isothermal conditions at 75°C in order to minimize the effect of humidity and charging of the dielectric layer. In each cycle, the applied voltage was increased from 0 to a specific value within about $t_1 = 1$ s. The vertical displacement profile of the beam was measured at that specific voltage level within $t_2 - t_1 \approx 7$ s. Then, the voltage was decreased to zero within $t_3 - t_2 = 1$ s and the beam profile was re-measured. A schematic representation of a loading cycle is given in figure 3.10.

The experimental results are presented in figure 3.11. It turned out that the beam had an initial curvature at the beginning of the experiment which suggests the presence of a residual stress or strain, due to the thin film processing. The beam develops a small but noticeable plastic deformation during the loading-unloading cycle at a loading voltage of 89 V. Displacement profiles for loading cycles at voltage levels lower than 89 V are not shown in figure 3.11. Above 89 V, the residual deformation increases with increasing maximum voltage levels. No information is available about whether or not any anelastic recovery occurred in the experiment after the removal of the voltage at time $t = t_3$ in each loading cycle.

Simulations

The electrostatic experiments are simulated using the SGCP formulation for the loading cycles at 89 V and 135 V. Note that there is only one beam tested in the experiment. In other words, the sample is exposed to 9 loading-unloading cycles before the loading cycle to 89 V is started and 14 cycles before the cycle with 135 V. However, two individual simulations are performed for these two loading cycles, i.e. the voltage is directly increased from 0 to 89 V and 135 V in each

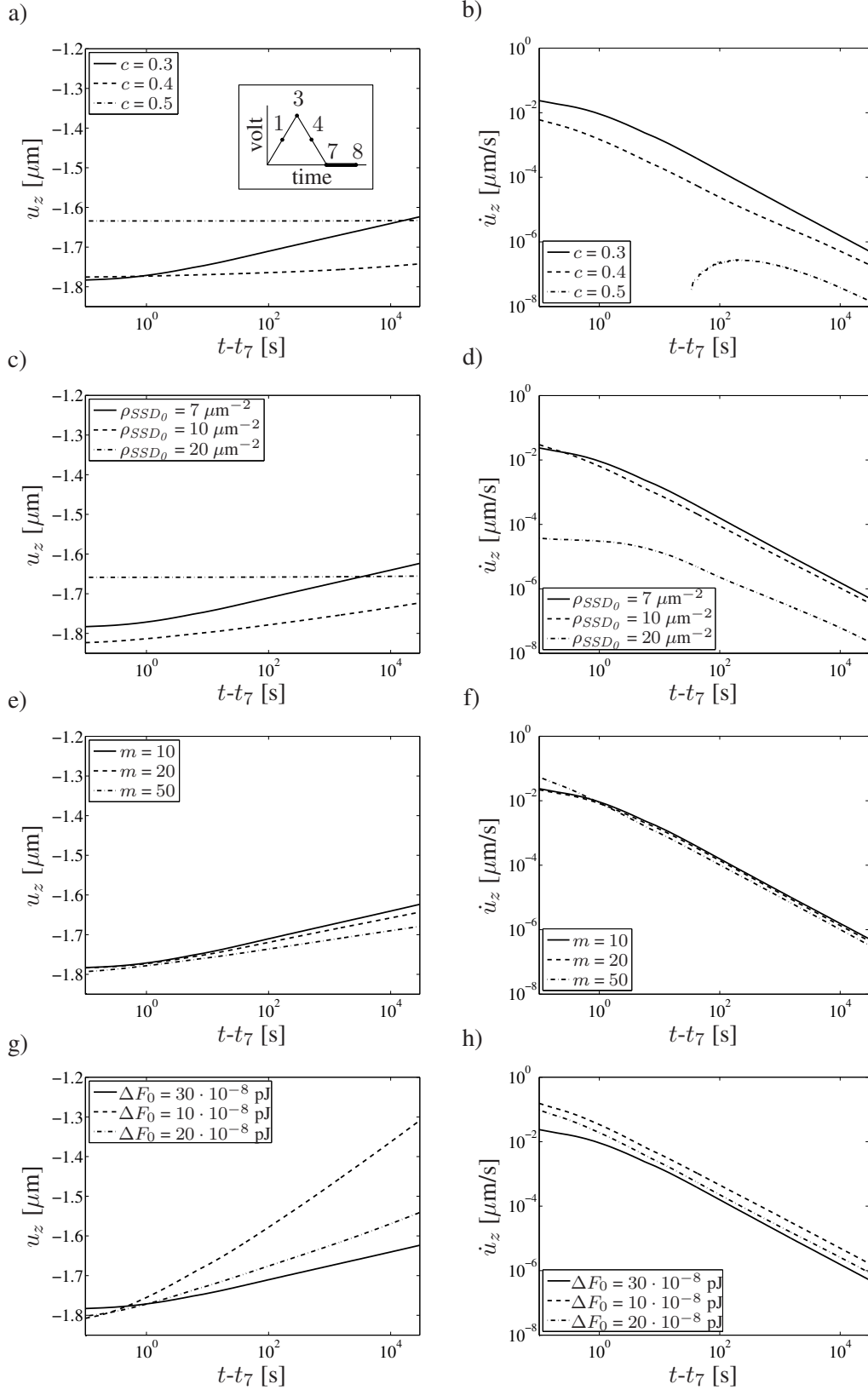


Figure 3.8: Anelastic recovery during $[t_7, t_8]$ obtained by using different values of a) the material parameter c , c) initial SSD density ρ_{SSD_0} , e) stress sensitivity constant m and g) activation energy ΔF_0 . Figures b, d, f and h involve the rate of the recovery that is plotted in figures a, c, e and g, respectively. The rates are calculated by $\dot{u}_{z_t} = (u_{z_t} - u_{z_{t-1}})/\Delta t$.

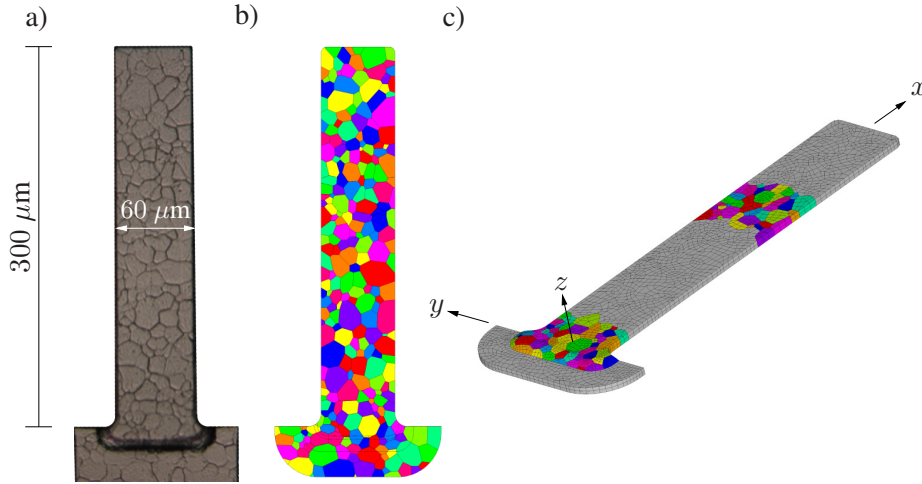


Figure 3.9: a) Polycrystalline Al-Cu cantilever beam with $5 \mu\text{m}$ thickness used in the electrostatic experiments. b) The numerical model of the beam used in multiphysical simulations. Different colors show the orientations of grains. c) The SGCP model is used in the colored grains. The less deformed gray parts are modeled as a transversely isotropic elastic medium.

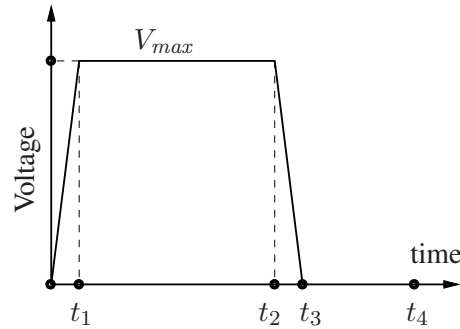


Figure 3.10: Schematic representation of a loading-unloading cycle for the electrostatic experiments: $t_1 = 1 \text{ s}$, $t_2 = 8 \text{ s}$ and $t_3 = 9 \text{ s}$. Since the time dependent strain recovery was not considered in the electrostatic experiments, time t_3 constitutes the last measurement time in the experiments. Time $t_4 = 15 \text{ s}$ is used only in the multiphysical simulations in the forthcoming section to track possible time dependent changes in the deformed state of the beam.

simulation. The finite element model of the beam [75] used in the simulations is shown in figure 3.9b. The grains have in plane random orientations with the $[111]$ direction parallel to z axis. To reduce computational time, the SGCP model is only employed in regions where sufficiently large plastic strains are anticipated based on the deformed shape of the beam in figure 3.11. These regions are located near the fixed end of the beam and in the region of high deformation at a distance of about one third of the beam length from the tip, as shown in figure 3.9c. The rest of the material is modeled as a transversely isotropic elastic medium. The gap between the bottom surface of the beam and the ground is about $3.2 \mu\text{m}$. The beam is deformed via the application of a voltage difference to the transducer elements between the beam and the ground according to the loading scheme in figure 3.10. Three material parameters are considered to be important for the description of the plastic behavior of the beam: the activation energy ΔF_0 , material parameter c and the initial dislocation density ρ_{SSD_0} . The activation energy is taken from the work of [12] which involved

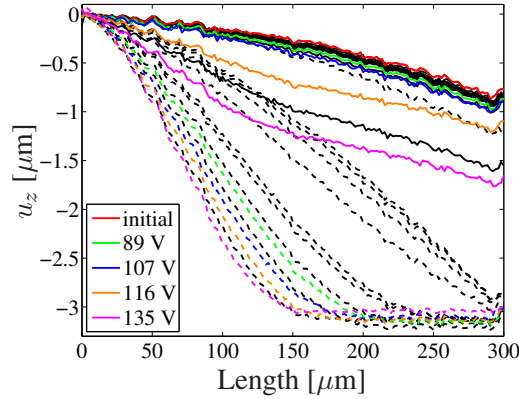


Figure 3.11: Experimental vertical displacement profile of the beam measured for loading-unloading cycles to 8, 17, 26, 36, 47, 60, 66, 70, 80, 89, 97, 107, 116, 125 and 135 V [74]. The dashed and continuous lines show the completely loaded and unload states. Colored lines demonstrates the loading cycles considered in the simulations with the SGCP model.

creep measurements on a thin film of an Al-Cu alloy with a composition similar to the material in this work. The value of material constant c was determined in previous studies [13–16] for a crystallographic slip resistance originating from short range dislocation-dislocation interactions in pure fcc metals. In literature, the material parameter c is reported to depend on several factors [52] such as deformation rate, dislocation distribution, temperature and the composition of the material. Given the existence of impurities in the thin film material considered here (e.g. solute atoms or small precipitates), c must be adequately large values to take into account the additional strength provided by the interaction between dislocations and impurities. [52] presented values of c that are larger than 1 for single crystalline Cu alloys and polycrystalline Fe alloys. Therefore, the value of c is estimated as 1. The remaining parameter, the initial SSD density, is adjusted for capturing the permanent deformation profile after the load cycle with a maximum voltage of 89 V. The rest of the material parameters used in the simulations can be found in table 3.4 and elsewhere [13–16].

The simulation results are compared to the experimental data in figure 3.12. The figure shows that the deformed shape of the beam in the unloaded state at $t = t_3$ after the loading to 89 V can be well captured by the finite element simulations with the SGCP model. In the loaded state at $t = t_2$, the deformed shape obtained from the simulation is still close to the experiment but the accuracy is not as high as that for the unloaded state. No anelastic recovery is noticed in the simulations with the current material parameter set, which is in line with the results of subsection 3.4.1. Hence, the state of the material (e.g. residual stress and microstructural quantities such as the density of edge GNDs) at $t = t_3$ is considered to remain constant until $t = t_4$. Figure 3.12 also contains the deformed shapes calculated in another simulation by using the same material parameters and loading scheme but with a larger voltage level, i.e. 135 V. This time, the deformed shape estimated by the simulation differs significantly from the experiments in the unloaded state ($t = t_3$) whereas the difference in the loaded state ($t = t_2$) is small. The dependence of the permanent deformation in the beam on the maximum voltage of the loading cycles in the electrostatic experiment is given in figure 3.13 for two control points located at different positions along the beam length. It is seen that the residual deformation grows rapidly with the increasing voltage in the experiment. This might result from the accumulation of plastic deformation over the repeated loading cycles and can be identified only by means of dedicated experiments. It is also seen that with the parameters given in table 3.4, the experimental results belonging to the cases with low voltage levels (e.g. 89 V, 107 V and 116 V for the point close to the beam tip, figure 3.13a) can be reproduced fairly

Table 3.4: Material parameters used in the electrostatic simulations with the SGCP model.

Parameter	Meaning	Value	Unit	Reference
C_{11}	Elastic constant	108000	MPa	[70, 76, 77]
C_{12}	Elastic constant	61300	MPa	[70, 76, 77]
C_{44}	Elastic constant	28500	MPa	[70, 76, 77]
ν	Poisson's ratio	0.347	-	[78]
m	Strain rate sensitivity	20	-	-
G_0	Activation energy	$64 \cdot 10^{-8}$	pJ	[12]
T	Temperature	348	K	-
b	Burgers vector length	$2.86 \cdot 10^{-4}$	μm	-
K	Material constant	10	-	[13–16]
y_c	Critical annihilation length	$1.6 \cdot 10^{-3}$	μm	[13–16]
c	Material constant	1	-	[52]
ρ_{SSD_0}	Initial SSD density	0.4	μm^{-2}	-
$\dot{\gamma}_0$	Reference plastic strain rate	$1 \cdot 10^{-3}$	s^{-1}	[13–16]
R	Length scale	1.5	μm	-

well using the SGCP formulation. However, for higher voltage levels, e.g. 135 V in figure 3.13b, the SGCP formulation falls short in capturing the material behavior: the simulations yield much smaller residual deformations than those in the experiment, meaning that the beam behaves more elastically in the simulations. An additional set of simulations is conducted with a reduced length scale of $R = 1 \mu\text{m}$ in order to decrease the level of back stress which will lead to an increased plastic activity. The result of these simulations are shown in figure 3.13 as well. The lower R value causes larger permanent deformations at higher voltages and brings the simulation results closer to those from the experiments. However, the plastic deformation at low voltage levels is increased as well, hence, therefore not providing a real improvement of the results.

It should be mentioned that the influence of successive loading is assumed to be negligible in the simulations. The results of another study which involves two sequential load cycles with a voltage amplitude of 135 V (the largest voltage level considered in the experiment) has shown the negligible influence of the cycle repetition on the results presented in figures 3.12 and 3.13. The most significant change in the permanent vertical displacement of the beam over its length due to the plastic strain accumulation after the second loading cycle to 135 V is about 15 nm, see figure 3.14.

3.5 Summary and concluding remarks

In this study, it is shown by means of multiphysical finite element simulations of the bending of cantilever thin metallic beams that the SGCP formulation is able to describe a time dependent deformation recovery following the unloading of the material, which can be mechanistically explained by the reverse glide of dislocations driven by the residual internal stresses due to the inhomogeneous distribution of the density of GNDs. It is observed that a larger amount of recovery occurs in the presence of larger internal stresses, which decay with the recovery as the GND densities decrease. A systematic investigation of the anelastic recovery produced by the SGCP

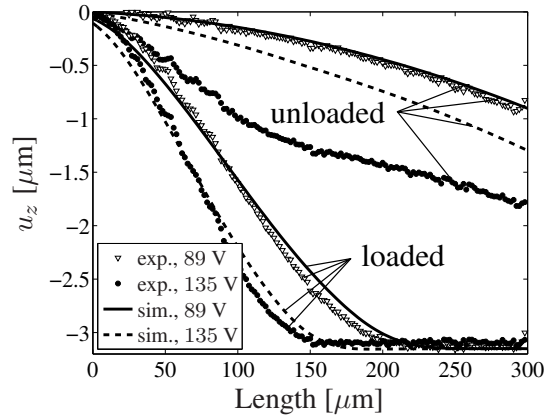


Figure 3.12: The vertical displacement profile of the beam evaluated from the finite element simulations with the SGCP model in comparison with the results from the electrostatic beam bending experiments.

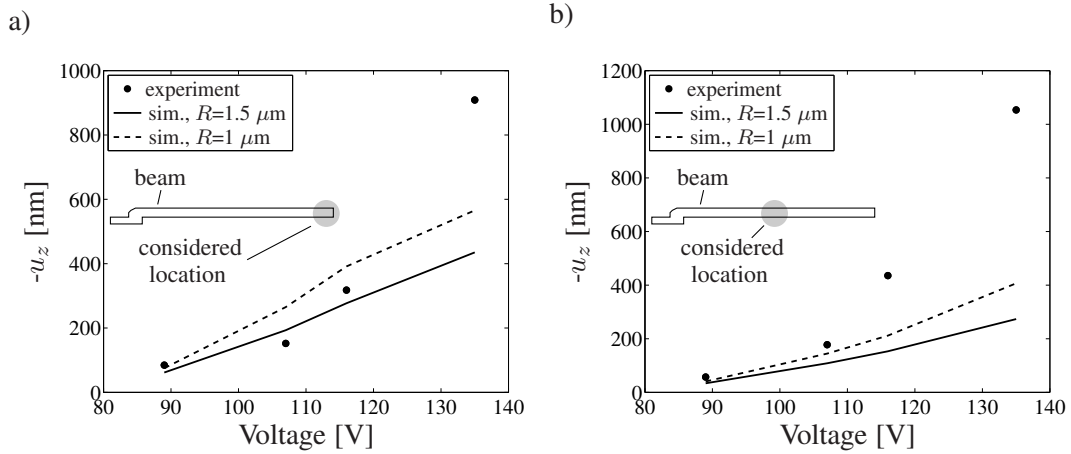


Figure 3.13: Permanent displacements at two different locations of the beam after loading cycles with maximum voltage levels of 89 V, 107 V, 116 V and 135 V: a) at about $x=290 \mu\text{m}$ and b) at about $x=156 \mu\text{m}$.

model reveals that the amount of the time dependent strain recovery and the related time constants are significantly dependent on the terms entering the constitutive law for crystallographic slip: c , ρ_{SSD_0} and ΔF_0 . Because of the fact that these parameters serve for the definition of the overall slip resistance and are not directly linked to the time scale of the dislocation glide mechanism, it is concluded that the observed anelasticity is an artifact of the rate dependent modeling of crystal plasticity.

The SGCP model is also used for the simulation of electrostatic beam bending experiments conducted on a thin Al-Cu [1 wt%], involving several loading-unloading cycles to the different voltage levels. The simulation results indicate that it is not trivial to accurately describe the material behavior in the experiment with the SGCP formulation with a unique set of material parameters. One reason for this could be the effect of the repeated loading cycles in the experiment, which may not be properly handled by the SGCP formulation. The results of the simulations involving two successive loading cycles to the maximum voltage show that the accumulated deformation through these sequential cycles are significantly smaller compared to the difference between the permanent deformations from the experiment and the simulations. Another reason would be the nature of the

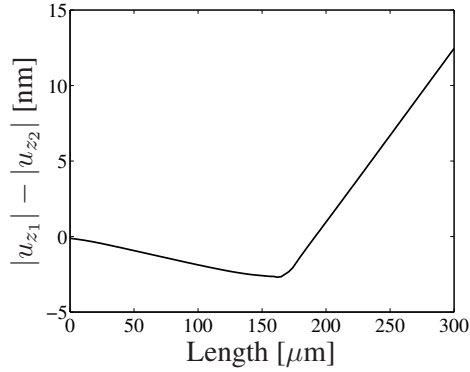


Figure 3.14: The difference in permanent deformations of the beam along its length due to two sequential loading cycles to 135 V in the finite element simulations with the SGCP model.

flow rule for crystallographic slip in the SGCP formulation: it was originally developed for pure fcc metals by assuming that only dislocation-dislocation interactions provide the slip resistance. On the contrary, the thin film tested is made of a metallic alloy which contains solute atoms and small second phase particles. In this study, the relevant material parameters, i.e. c and ΔF_0 , are adjusted to take into account the additional strength that may be provided, for instance, by particles. However, increasing resistance against crystallographic slip extends the elastic range of the material described by the SGCP model, and thereby lowers the accuracy to predict the large permanent deformations remaining after the loading cycles to larger voltage levels. A larger slip resistance also leads to the vanishing of the anelastic recovery in the simulations since it will hinder the reverse slip of mobile dislocation driven by the back stresses despite the fact that the time dependent deformation recovery in the simulations using the SGCP model is a consequence of the rate dependent nature of the SGCP. Note, however that time dependent recovery has been observed in some experiments on thin films of a similar alloy.

The presence of particles and solute atoms in a metal would necessitate the consideration of additional forms of interactions such as particle shearing or looping (Orowan and Friedel effects) with their specific characteristics (e.g. strength, time scales). Additionally, the relatively large anelastic recovery times observed in the experiments on Al-Cu thin films point to a diffusional process through which the internal stresses residing in the material after a loading-unloading cycle are relaxed. This study showed that the development of a new crystallographic slip law which explicitly takes into account the dislocation-particle (and/or dislocation-solute atoms) interactions is essential for a proper description of the mechanical behavior of an alloy with the SGCP formulation. The development of such a constitutive law based on physical mechanisms may also give rise to the introduction of realistic time scales into the material behavior observed in finite element simulations which is a requirement for capturing the anelastic recovery accurately.

3.6 Appendix: Modeling of electric domain and contact in the simulations

A further information about the modeling of the electric domain and the contact between the free-standing beam and the dielectric layer in the multiphysical simulations is provided below.

Modeling of electric domain

The electric domain is idealized by the use of transducer elements. In table 3.5, some of the parameters that are used for the definition of transducer elements in the simulations of subsection 3.4.1 are listed.

Table 3.5: Some of the parameters for the electric domain in the multiphysical simulations.

Parameter	Meaning	Value	Unit
δ_{air}	Gap between thin film and dielectric layer	3.2	μm
δ_{rough}	Average surface roughness of beam	$0.15^\dagger, 0.06^\ddagger$	μm
t_{diel}	Thickness of dielectric layer	$0.425^\dagger, 1.5^\ddagger$	μm
t_{beam}	Thickness of beam	$5^\dagger, 4.75^\ddagger$	μm
ϵ_{diel}	Dielectric permittivity	$7.3^\dagger, 4^\ddagger$	$\text{pF}/\mu\text{m}$

[†] For the simulations in section 3.4.1.

[‡] For the simulations in section 3.4.2.

The initial air gap between the beam and the bottom electrode, δ_0 , is an input for transducer elements and is calculated via

$$\delta_0 = \delta_{air} + \frac{t_{diel}}{\epsilon_{diel}}. \quad (3.20)$$

Another input for a transducer element is the minimum gap, δ_{min} here given by

$$\delta_{min} = \frac{t_{diel}}{\epsilon_{diel}}. \quad (3.21)$$

When the gap between the plates (i.e. the thin beam and the bottom electrode in the present case) falls below δ_{min} , the transducer starts to behave as a linear contact element. In addition to this, a non-linear contact formulation is adopted for the contact between the dielectric layer and the thin beam and is modeled by gasket elements and non-linear springs, discussed in the forthcoming part.

Note that the use of transducers is justified in case of structures with one dimension relatively small compared to the other two, as is the case for MEMS devices. Nevertheless, the fringe electric fields may noticeably affect the device behavior. In the simulations of subsection 3.4.1, such fringe field effects are neglected for simplicity. On the contrary, in the simulations of the electrostatic experiment in subsection 3.4.2, the influence of the fringe fields is taken into account by additional transducer elements along the periphery of the beam [75]. The contribution of the fringe field transducers to the overall capacitance is calculated by the following analytical expression [75, 79]:

$$C = \frac{\epsilon_0}{\pi} \left(\ln \left[\frac{1 + \sqrt{\delta^*}}{2(1 - \sqrt{\delta^*})} \right] + 2 \right) \quad \text{with} \quad \delta^* = \left[1 - \frac{1}{(t_{beam}/\delta + 1)^2} \right]^{1/2} \quad (3.22)$$

where δ is the vertical position of the beam with a thickness of t_{beam} and varies between δ_{rough} and δ_{air} .

Modeling of contact between beam and dielectric

The contact between the surface of the beam and the dielectric layer on the bottom electrode is modeled in the simulations of section 3.4.1 by gasket elements with the following loading curve [75]

$$g_f(z) = g_{f_0} \exp(K_g \Delta\delta(z)), \quad (3.23)$$

$g_f(z)$ is the contact stress in terms of position of the beam along the z axis, g_{f_0} is a pre-exponential factor and K_g is the gasket stiffness. $\Delta\delta(z)$ is the amount of penetration into the dielectric layer as a function of z and has values in the range of $[0, 2\delta_{rough}]$. For section 3.4.1, $\delta_{rough} = 0.15 \mu\text{m}$, g_{f_0} and K_g are given as $1 \cdot 10^{-3} \mu\text{m}^{-1}$ and 200 MPa, respectively.

In the simulations of section 3.4.2, the contact is modeled by using non-linear springs, which is different from section 3.4.1. The contact stress is defined by [75]

$$g_f(z) = 2.5K_g \left[1 - \left(1 - \exp \left[- \frac{\frac{4}{\pi} + \frac{a}{2} \left(\frac{\Delta\delta(z)}{\sigma_r} \right)^2}{a + 2 \left(\frac{\sigma_r}{\Delta\delta(z)} \right)^2} \right] \right)^{1/2} \right]. \quad (3.24)$$

Here, σ_r and a are defined by

$$\sigma_r = \delta_{rough}/5 \quad \text{and} \quad a = -8(\pi - 3)/(3\pi(\pi - 4)). \quad (3.25)$$

In equation (3.25), K_g is 1500 MPa and $\delta_{rough} = 0.06 \mu\text{m}$.

Modeling time and scale dependent phenomena in particle strengthened alloys

Abstract

A proper description of the mechanical behavior of metal thin film components of capacitive RF-MEMS switches is essential for the development of more reliable devices since the main failure mechanisms are directly related to the behavior of the free-standing electrode of these switches. It is now a well known phenomenon that thin films are susceptible to size effects, which can be captured successfully by gradient plasticity theories. Besides the scale dependency, metal thin films also exhibit time dependent behavior: anelasticity (which is the deformation recovery over time following elastic spring back upon load removal) and creep (permanent deformation developed over time at constant loads). This work focuses on the extension of a strain gradient crystal plasticity (SGCP) model [13–16], previously developed for the scale dependent behavior of pure fcc metals, so that it can be exploited for the description of the scale and time dependent mechanical behavior of thin films that are made of metal alloys with second phase particles. For this purpose, an extended physically based slip law is developed for crystallographic slip in fcc metals by considering the deformation mechanisms that are active within the grains. In doing so, the interaction of dislocations with other dislocations and with second phase particles is taken into account. Three dislocation-particle interactions which may contribute to the overall material resistance are considered: i) the Orowan mechanism, ii) the Friedel mechanism, and iii) climb over particles. Moreover, the dynamic nature of the RF-MEMS' service conditions is expected to lead to an influence of additional interaction mechanisms such as the interaction of dislocations with phonons and electrons, which usually governs dislocation motion at high strain rates and which may be encountered during transient loading of the device and pull-in of the suspended electrode. Separate slip rate equations are written for these interaction mechanisms and are then combined into a new constitutive model for crystallographic slip which covers both, so-called, thermal activation and viscous drag regimes. The new constitutive equation is incorporated into the SGCP model and implemented in a finite element framework. Simulations of the bending of a single crystalline beam show that within the presented model, the strength of a material with semicoherent second

phases is determined by the resistance against the slip of screw dislocations at low to moderate stress levels when dislocation climb is omitted. When dislocation climb is incorporated into the formulation, its rate controls the plastic slip at low stresses. Provided that a considerable lattice diffusion occurs and sufficiently large back stresses exist in the material, the extended SGCP model predicts that a noticeable fraction of the residual deformation remaining after unloading will be recovered over time. The magnitude and the characteristic time scale of the anelastic recovery is controlled by dislocation glide limited by climb. Simulations of the micro-clamp experiment on a polycrystalline thin beam reveals that the use of an inhomogeneous diffusion constant which is characteristic for grain boundary diffusion in the close neighborhood of grain boundaries and close to the coefficient for lattice diffusion within grain interiors provides a material behavior that is much closer to that observed in the micro-clamp experiment on a polycrystalline thin beam. Simulation results also suggest that the internal stress formulation may need to be modified by incorporation of additional sources of internal stresses.

4.1 Introduction

Capacitive radio frequency micro-electro-mechanical systems (RF-MEMS) switches are a class of MEMS with radio frequency functionality that have recently become commercialized in wireless networks applications. Similar to parallel plate capacitors, these switches are composed of two electrodes, which are made of thin metal films of a few micrometers thickness. One of them is suspended above the other with springs and is able to move vertically under the effect of electrostatic forces generated by the application of a voltage difference between the electrodes. The elastic energy stored in the springs during the actuation of the switch provides the restoring force to increase the gap between the electrodes when the voltage is reduced or to open the switch at zero voltage. This reconfigurability of RF-MEMS allows them to operate over a wide range of frequencies. Because of this working principle, the reliability of RF-MEMS devices becomes strongly dependent on the mechanical behavior of the free standing electrode (i.e. the metal thin film). Therefore, the characterization and understanding of the mechanical behavior of the free standing thin film for the service conditions of RF-MEMS devices is essential for the development of more reliable devices.

The mechanical properties of metallic thin films at micron and sub-micron scales vary with changes in dimensions [3–5], which is referred to as *scale dependent* behavior or *size effects*. Size effects are closely related to the material's specific microstructure and the boundary constraints and usually result in a stronger mechanical response. Scale dependent behavior can only be described by continuum theories that involve characteristic length scales of the material in the corresponding formulations. Several models that make use of strain gradients [26–29] in order to capture specific aspects of this scale dependency exist in literature [13, 16, 30–42].

Thin films are reported to show *time dependent* behavior of two types upon unloading after long loading times: i) *creep*, the irreversible deformation developed under constant loads [6, 9, 12, 80] (possibly with accompanying permanent plastic deformations, e.g. due to instantaneous loading), and ii) *anelasticity*, a deformation recovery over time (following the elastic spring back) [7, 8, 62–65, 81]. Creep and anelasticity of thin films are attributed in literature to different deformation mechanisms such as dislocation glide [6, 80, 82–84], grain boundary sliding [62, 81, 85–89], or a combination of grain boundary sliding and dislocation glide [64].

Besides the aforementioned nonlinearities in the mechanical behavior, which originate from the material, an additional nonlinearity adds to the mechanical response during the *pull-in* of the free standing electrode due to the structure of the device. Around a certain voltage level, which is

named the *pull-in voltage* and is device specific, the free standing thin film loses its stability and is instantly pulled down to the bottom electrode, leading to a deformation at high strain rates. At high strain rates, the rate of deformation (or dislocation motion) has only a limited dependence on dislocation interactions with obstacles. The resistance against dislocation motion then originates from the viscous drag of phonons, electrons and the relativistic effects on the dislocations and increases with temperature contrary to the Arrhenius type of temperature dependence at ordinary strain rates. Impact shear tests on Al single crystals [90] revealed that at stress levels larger than the thermal activation range, the shear rate varies linearly with the stress and is temperature dependent within 20-500 K and the observed viscous material behavior can be described by phonon and electron drag models [91, 92]. The findings of [93] also supports that a linear viscous drag acts on mobile dislocations in Al. Impact shear tests on Al, prestrained Al and Al-Cu [4 at%] alloy with θ'' and θ' particles at 10-293 K were conducted by [94], and yielded results in line with the conclusions of [90]. It was shown in the same work that prestressing (i.e. introduction of initial dislocations) and alloying of the material gave rise to an offset in the measured stresses in Al, below which relatively little shear strain was observed, which is attributed to the interaction of gliding dislocations with forest dislocations and the particles.

A strain gradient crystal plasticity (SGCP) model in terms of statistically stored dislocation (SSD) and geometrically necessary dislocation (GND) densities was previously published by Evers et al. [13] for the scale dependent behavior of fcc pure metals induced by a lattice curvature effect. Therein, the size dependency is captured via a back stress, which is calculated for each slip system in a material point by the analytical integration of the stress fields due to GND density gradients over a cylindrical volume with a radius as the length scale. In [13], the back stress of a slip system is defined by considering the interaction of dislocations that belong only to that slip system. In follow-up work by Bayley et al. [15, 16], this definition was extended in order to incorporate the influence of the dislocations on the other slip systems.

This study starts with an extensive review about the processes of plastic flow in particle strengthened alloys and corresponding models to capture them. Next, an extension of the SGCP framework [15] is presented for the description of time and scale dependent mechanical behavior of fcc based alloys with second phase particles, particularly for the creep and anelastic behavior of Al-Cu [1 wt%] thin films. A physically motivated rate equation for slip is presented in terms of the microstructural quantities. In deriving this equation, it is assumed that the material consists of second phase particles, more specifically coherent θ'' , incoherent θ or semicoherent θ' particles, which are randomly distributed in the Al matrix. It is assumed that the deformation occurs through dislocation glide on multiple slip systems within the grain interior. The rate of dislocation glide, i.e. the dislocation velocity, is controlled by the thermally activated release of dislocations from obstacles at stress levels below the strength provided by the interaction of dislocations with other dislocations and the particles. Four different interaction processes are considered to constitute the rate governing mechanisms: i) the dislocation-dislocation interaction, ii) the Friedel process, iii) the Orowan process and iv) dislocation climb over particles. Separate constitutive equations are written for the crystallographic slip rates of each process and are combined in a physically motivated manner. For the slip rate governed by the resistance due to dislocation-dislocation interactions, the viscous glide of dislocations is also taken into account at stresses larger than the resistance provided by the dislocation-dislocation interactions. The new constitutive law for crystallographic slip is integrated into the strain gradient crystal plasticity framework of [16] and implemented in a finite element method. A boundary value problem involving the displacement controlled bending of an Al-Cu cantilever beam is solved to study the effect of the dislocation-particle interactions on the mechanical behavior of the material.

4.2 Material background

The thin films considered in this study are polycrystalline cantilever beams with columnar grains of about $20\ \mu\text{m}$ and made of an Al-Cu [1 wt%] alloy. Alloying Al with Cu leads to a material which has a reduced lattice dimension decreasing linearly with the Cu content to a value of $0.4038\ \text{nm}$ [95] at the equilibrium solubility of Cu, 5.70%. By alloying with Cu, the Debye temperature of Al increases to about $517\ \text{K}$ [95]. The solid-solid interfacial energy between the matrix and CuAl_2 is $130 - 170\ \text{mJ/m}^2$ in the eutectic state, in which the phase registry is minimum while in the random boundaries, the interfacial energy may reach $400 - 600\ \text{mJ/m}^2$ [95]. For the case of equiaxed and evenly distributed CuAl_2 , the strength of the matrix depends on the mean free path between the particles. The material hardness within the grain is as high as that in grain boundary regions. By increasing the Cu content, the damping capacity of Al is reduced while its strength at high temperature is increased and the creep rate is decreased by a factor of 2-10. The activation energy for creep in the range of $500 - 600\ \text{K}$ is around $1.5\ \text{eV}$ [95]. The addition of copper also increases the fatigue strength of Al. The equilibrium vacancy concentration of Al-Cu alloys is close to that of pure metal, which is around $10^{-4} - 10^{-5}$ vacancies per atom in case of rapid quenching [95].

Typical microstructural features that can be expected in thin films, such as the type of precipitates, their size, density and the distribution of the solute atoms, are obtained from literature on bulk Al-Cu alloys and Al-Cu alloy thin films. In bulk Al-Cu alloys, the firstly observed precipitates are disk shaped, fully coherent Guinier-Preston zones (G-PI) which are rapidly formed on defects such as dislocations [95], with thicknesses of about 2 atomic layers and diameters of $10\text{-}30\ \text{nm}$ with a separation of $25\text{-}30b$ with b the magnitude of the Burgers vector [96]. A G-PI zone is composed of one or two Cu layers lying between $\{100\}$ planes of Al. As aging continues, coherent G-P-II zones emerge at a much slower rate than G-PI [95]. These are also called θ'' precipitates and involve several layers of Cu atoms. They have larger diameters (about $10 - 100\ \text{nm}$ [95]) and thicknesses (about $10\ \text{nm}$) than G-PI zones [97] and have a tetragonal structure with lattice parameters $a = 0.404\ \text{nm}$ and $c = 0.790\text{-}0.768\ \text{nm}$ [98] with a lattice misfit in the c direction. Usually, optimal mechanical properties are achieved in the presence of θ'' precipitates as the stress fields around the different zones almost overlap [95]. Next, θ' phase particles with an Al_2Cu composition are formed. It is a semi-coherent phase with broad faces that are coherent (the (001) plane) with the Al matrix and other incoherent faces (the (100) and (010) planes) and has a tetragonal structure with lattice parameters $a = 0.404\ \text{nm}$ and $c = 0.580\ \text{nm}$ [97, 98]. Depending on the nucleation time and temperature, this phase may attain diameters of $10\text{-}600\ \text{nm}$ and thicknesses of $10\text{-}150\ \text{nm}$ [95]. Dislocations and low and high angle boundaries are preferential nucleation sites for this phase and its nucleation does not depend on the existence of GP zones [97]. The interface energy between the θ' phase and the matrix is in the order of $1530\ \text{mJ/m}^2$. Finally, the thermodynamically stable θ precipitates are formed, which are fully non-coherent particles. This phase has an I4/mcm (C16) structure with the same composition as θ' and having lattice parameters $a = 0.6030\text{-}0.6066\ \text{nm}$ and $c = 0.4860\text{-}0.4874\ \text{nm}$ [95, 98–100]. A further discussion on the bulk Al-Cu alloy can be found in [97] and the references therein.

In case of thin films, the knowledge on precipitation based on bulk materials is questionable due to the large surface-to-volume ratio. Information available in literature on thin films is limited in comparison with bulk materials. Mondolfo [95] mentions that G-PI zones form slowly in thin Al-Cu films while the stable phase θ nucleates rapidly. There are some other papers [101–103] in literature confirming that θ is usually the only phase present in Al-Cu thin films, sometimes accompanied by θ' . Mader and Herd [104] studied Al-Cu thin films with $100\text{-}200\ \text{nm}$ thickness

by a heat treatment of the solid solution alloy between 100-300°C. They observed that nucleation of GP zones is retarded. A high density of θ' phase particles forms at lower temperatures than in the bulk form. They are also smaller in size, about 10 nm and nucleate in the absence of θ'' . θ are precipitated at the same time with θ' in similar quantities again at lower temperatures than in the bulk form. At 300°C, only large θ precipitates exist as the second phase particles. The distribution of the Cu atoms in Al-Cu polycrystalline thin films of 500 nm thicknesses with up to 1 at% Cu was examined by [105] via thermal cycling between 323 K and 773 K. It has been found that the density of Al_2Cu particles (the θ phase) is similar for free-standing thin films and films on a substrate. The Cu concentration does not influence the amount of particles but does affect their size: the lower the Cu concentration, the smaller the particles.

4.3 Plastic flow in particle strengthened alloys

Plastic deformation of a metallic material at the macro scale is the cumulative result of different mechanisms at the atomic scale, such as dislocation glide, climb or atomic diffusion. The mechanism that dominates the rate of plastic flow depends on factors such as temperature, strain rate and the applied stress. At low homologous temperatures, i.e. at temperatures below half of the melting temperature of the material, plastic deformation of polycrystalline materials in bulk form usually occurs via dislocation glide mechanisms, the rate of which is limited by the obstructions on the glide plane, for instance discrete obstacles (e.g. particles) at ordinary strain rates and a viscous drag force on gliding dislocations, e.g. due to phonons and electrons, at high strain rates. At increasing temperatures, diffusive processes start to dominate the rate of plastic deformation, as in the case of climb controlled dislocation glide, diffusional creep (e.g. Nabarro Herring, Coble creep) or grain boundary sliding [106]. Also, the contribution of the grain interior and the grain boundaries varies depending on the stress levels. At low stresses (and high temperatures), strain is accumulated in the grain boundary regions while at large stresses, a large part of the deformation is accommodated within the grain interior, mainly via dislocation creep and grain boundary strengthening [66, 107–110].

In a general sense, it can be stated that depending on the lattice structure and the composition of the material, the type of the obstacle that provides the most significant portion of the resistance against dislocation glide may be different. For instance, in case of pure aluminum, which has an fcc structure, the main slip resistance is due to the interaction of the dislocations, whereby the contribution of the lattice resistance is negligible, while for a material with a bcc structure, it is the lattice resistance that gives the main strength of the material. Moreover, for alloys, the presence of solute atoms (in case of solid solution alloys) and/or second phase particles (particle strengthened alloys) may significantly increase the strength.

In the following sections, the main focus is on the mechanisms that take place in the grain interior. Particular deformation mechanisms at grain boundaries, such as grain boundary sliding, are neglected. It is assumed that the plastic deformation essentially results from dislocation glide. A slip law is proposed for the description of the mechanical behavior of thin metal films that are made of Al-Cu [1 wt%] alloy. Relying on the available literature, it is assumed that the material consists of θ'' or θ' phase particles with an average radius of 10-30 nm. In setting up the constitutive rule, the rate of slip is considered to be restricted by the cooperation of the following processes:

- i. dislocation-dislocation interaction,
- ii. viscous drag (at high strain rates),

- iii. dislocation-particle interaction,
- iv. climb of dislocations over particles.

Furthermore, the particles are idealized as spherical in shape, with a constant volume fraction and size (i.e. they do not evolve during deformation). Possibly, the individual Cu atoms that are dissolved in the Al matrix also add to the material resistance. However, since the total solute amount is 1% by weight and since small precipitates are present, this contribution is not taken into account. Moreover, because of the high stacking fault energy of Al, the dislocations are regarded as undissociated.

The dislocation-dislocation interactions in fcc pure metals are treated in [13–16, 33]. In the next section, the dislocation-particle interactions are discussed.

4.3.1 Interaction of dislocations with particles

In fcc pure metals and alloys, the strength against plastic deformation principally originates from the interaction of mobile dislocations with obstacles on their slip planes, such as other dislocations or precipitates. For a dislocation that is forced to glide through an array of particles on its plane under an applied stress, the sampling of the obstacles, i.e. how often and where the dislocation can encounter an obstruction with what size, is a statistical process.

Following the assumption of spherical particles, an average planar radius r_s , cf. figure 4.1, of a random circular section of a particle on a glide plane is defined as [111, 112]

$$r_s = \frac{\pi r}{4}, \quad (4.1)$$

where r is the average particle radius. The number of particles, N_v , per unit volume can be determined by

$$N_v = \frac{3f}{4\pi r^3}, \quad (4.2)$$

with f the particle volume fraction. The number of intersections of slip planes with particles of uniform size, N_s , is related to N_v via

$$N_s = 2rN_v. \quad (4.3)$$

By making use of equation (4.3), the spacing of particles that are distributed in a regular square array, L_{cc} , is given by [111, 113, 114]

$$L_{cc} = \frac{1}{N_s^{1/2}} = \left(\frac{2\pi}{3f}\right)^{1/2} r. \quad (4.4)$$

The average center-to-center spacing between a particle and its closest neighbor intersected by a random plane for a random particle arrangement is given by [115]

$$L'_{cc} = 0.5L_{cc}. \quad (4.5)$$

However, the consideration of multiple nearest neighbors is a more correct estimate for the particle

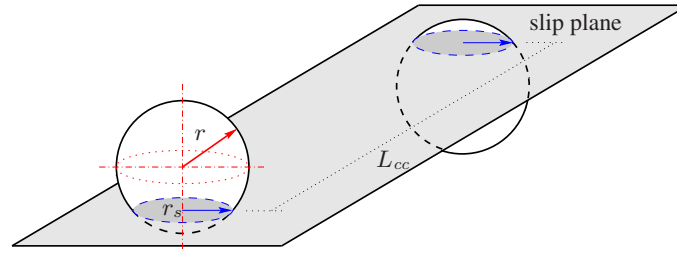


Figure 4.1: Schematic representation of geometrical properties of a particle with respect to a cutting slip plane.

spacing, which then reads [111, 115, 116] as

$$L''_{cc} = 1.25L_{cc}. \quad (4.6)$$

In the rest of this work, equation (4.4) is used to calculate the mean planar center-to-center particle spacing since the equations used in the following sections are derived based on a square array particle arrangement and contain coefficients to take the randomness of the particle distribution into account. If L_{cc} and r_s are comparable, the interparticle spacing must be corrected as $L = L_{cc} - 2r_s$, which is then the surface-to-surface spacing.

The dislocation-particle interaction may be of influence in two ways [111, 112, 117, 118]:

- i. Dislocations feel a resistance upon passing through the individual particles, which can occur only if the slip planes of these dislocations cut the particles. This type of resistance can be considered as the accumulation of discrete *localized forces*.
- ii. Dislocations interact with the stress fields around the particles. Such particles have, for instance, a size, lattice or modulus misfit with the matrix. In this case, dislocations experience *diffuse forces*. The range of the diffuse forces can be larger than the size of the particles and, hence, for the interaction with dislocations to occur, their slip planes are not necessarily required to intersect the particles.

Dislocations can overcome the particles by different processes depending on the strength of the obstruction. Under a sufficiently large effective resolved shear stress, the dislocations may pass the particles by bowing in between if the particles are strong enough, e.g. in case of large coherent (overaged) particles or incoherent particles. This process is referred to as the *Orowan mechanism*. If the particles are weak, as in the case of underaged or aged coherent particles, dislocations can shear them, referred to as the *Friedel mechanism*. When the applied stress is relatively low for the Orowan or Friedel mechanisms, edge dislocations can still overcome the obstacles by *climb* (for which may require higher temperatures) whereas screw dislocations can pass by them via *cross-slip*.

The Orowan, Friedel and climb mechanisms are discussed in the following sections. The cross-slip phenomenon is omitted within this study.

Friedel mechanism

Under a sufficiently large effective resolved shear stress (τ_{eff}), a dislocation glides on its slip plane until it is hindered by particles, see figure 4.2. As the applied load is increased, the dislocation bows

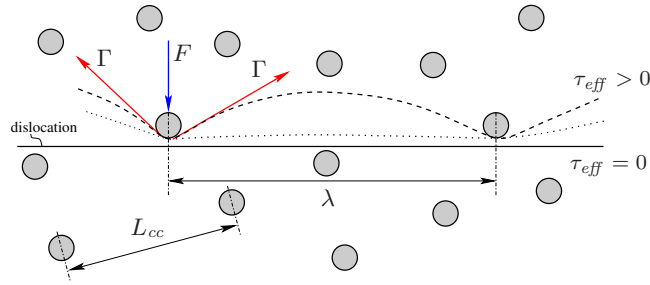


Figure 4.2: A dislocation passing through a random array of localized particles in a sub-critical state, [112].

out between them until a critical dislocation configuration is achieved, i.e. when the force exerted on the particle by the dislocation through its line tension becomes equal to the particles' shear strength, cf. figure 4.3. There, ϕ_c denotes the cusp angle, Γ_c is the line tension of the dislocation,

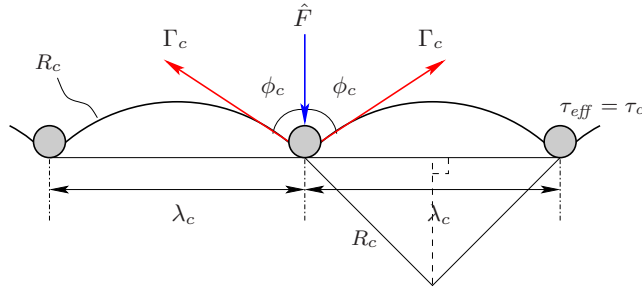


Figure 4.3: Dislocation configuration at the critical state.

\hat{F} is the maximum shear force that can be sustained by the particle, λ_c is the critical sampling length along the dislocation line and R_c is the radius of curvature in the critical configuration. Then, the force balance for a particle can be written as

$$\hat{F} = 2\Gamma_c \cos \phi_c \quad \text{at} \quad \tau_{eff} = \tau_c. \quad (4.7)$$

A rough estimate of the particle strength can be made based on $\cos \phi_c = \beta_c$. For $\beta_c < 0.5$ particles can be considered *weak* while for strong particles β_c gets closer to 1 [119]. When $\phi_c = 0$, particles behave as impenetrable and the gliding dislocations escape from them by the Orowan mechanism. $\phi_c > 0$ means that the gliding dislocations overcome the particles by shearing them, i.e. via the Friedel mechanism. Using equation (4.7), the critical stress τ_c results from the expression for the radius of curvature of the bowing dislocation

$$R_c = \frac{\Gamma_c}{\tau_c b}, \quad (4.8)$$

and the cusp angle from figure 4.3

$$\cos \phi_c = \frac{\lambda_c}{2R_c}, \quad (4.9)$$

leading to

$$\tau_c = \frac{2\Gamma_c}{b\lambda_c} \cos \phi_c = \frac{\hat{F}}{b\lambda_c}. \quad (4.10)$$

The critical sampling length is limited [119] by

$$\lambda_{min} \leq \lambda_c \leq \lambda_{max}, \quad (4.11)$$

where λ_{min} is equal to the distance between particles in a uniform square lattice arrangement L_{cc} (which means $\Gamma \rightarrow 0$, i.e. an infinitely flexible dislocation) and $\lambda_{max} = \frac{4r}{3f}$ corresponds to the particle separation along a straight dislocation line ($\Gamma \rightarrow \infty$, i.e. a rigid dislocation). The upper and lower limits for τ_c can be obtained by using these limits together with equation (4.10) [119]:

$$\tau_u = \frac{\hat{F}}{b\lambda_{min}} = \frac{2\Gamma_c}{b\lambda_{min}} \cos \phi_c \quad \text{and} \quad \tau_l = \frac{\hat{F}}{b\lambda_{max}} = \frac{2\Gamma_c}{b\lambda_{max}} \cos \phi_c. \quad (4.12)$$

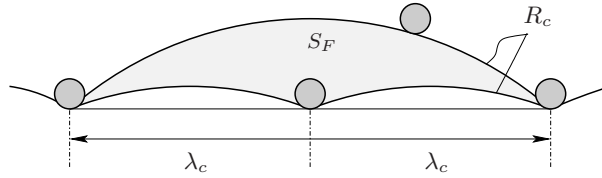


Figure 4.4: Steady state unzipping.

Friedel [96] and Fleischer and Hibbard [120] derived an approximation for λ_c based on the following assumptions:

- i. uniform particle arrangement,
- ii. point-like treatment of particles,
- iii. small bowing-out of dislocations.

Their approach is referred to as *Friedel-Fleischer (FF) statistics*. It is based on the *steady state unzipping condition*, that is when a dislocation escapes from a particle, it moves until it encounters a new particle by increasing its line length with the same radius of curvature [111–115, 117]. Physically, this implies [111, 117] that with increasing particle strength, dislocations will bow more (where the natural upper bound is the Orowan process), increasing the probability of probing new obstacles. The dislocation will escape from a particle in the critical configuration and glide until it is caught by another particle. The area swept during this process, shaded in figure (4.4), is equal to the glide plane area of an obstacle [117], which is L_{cc}^2 . Then, for $\lambda_c \ll R_c$ and small bending of dislocation, L_{cc} , λ_c and the cusp angle ϕ_c are related to each other as

$$L_{cc}^2 = \frac{\lambda_c^3}{2R_c} = \lambda_c^2 \cos \phi_c. \quad (4.13)$$

Finally, the critical shear stress can be obtained through equations (4.7)-(4.13):

$$\tau_c = \frac{2\Gamma_c}{bL_{cc}} \left(\frac{\hat{F}}{2\Gamma_c} \right)^{\frac{3}{2}}. \quad (4.14)$$

For $\frac{\hat{F}}{2\Gamma_c} < 1$, dislocations shear the particles by the Friedel mechanism, and $\tau_c = \tau_{FR}$ while for $\frac{\hat{F}}{2\Gamma_c}$ equal to 1, the Orowan mechanism becomes active, and $\tau_c = \tau_{OR}$. It has been shown by computer simulations [116, 121] that as $\frac{\hat{F}}{2\Gamma_c}$ gets larger than 0.5, dislocations find paths through which the penetration is easier at the cost of significant deviation from a straight line and the resistance falls below the values of those calculated by equation (4.14) [112].

When λ_c is calculated by using equation (4.13), it may exceed λ_{max} in equation (4.12) for very small \hat{F} and β_c . Therefore, an explicit limit for the Friedel stress should be set as $\tau_F \leq \tau_u$ [119]. Also, to satisfy assumption (iii), a bottom limit for the critical sampling length should be introduced such that $\lambda_c \geq \sqrt{2}L_{cc}$, [119].

The effect of a random particle arrangement was studied by [116, 121, 122] via different statistical methods where the steady state unzipping condition of FF statistics is dropped but assumption (iii) is still kept. The equation proposed in [122] for the critical shear stress,

$$\tau_c = 0.85 \frac{2\Gamma_c}{bL_{cc}}, \quad (4.15)$$

was shown to be more accurate in describing the results of the computer simulations [116] for $\beta_c > 0.5$ while the Friedel equation (4.14) is still the best fit for $\beta_c < 0.5$, [111]. Another suggestion for the calculation of τ_c is [114]:

$$\tau_c = 0.8 \frac{2\Gamma_c}{bL_{cc}} \cos \phi_c \quad \text{for } \phi_c < 50^\circ, \quad (4.16)$$

$$\tau_c = \frac{2\Gamma_c}{bL_{cc}} (\cos \phi_c)^{3/2} \quad \text{for } \phi_c > 50^\circ. \quad (4.17)$$

Other empirical equations exist in literature to fit computational results, e.g.

$$\tau_c = \frac{2\Gamma_c}{bL_{cc}} \left(\frac{\hat{F}}{2\Gamma_c} \right)^{\frac{3}{2}} \left(0.8 + \frac{\phi_c}{5\pi} \right). \quad (4.18)$$

This equation gives similar results to those from equation (4.14) for large ϕ_c values. However, for $\phi_c \rightarrow 0^\circ$, this equation is not strictly correct due to its finite slope at $\phi_c = 0^\circ$ [114], even though it is still preferable over equations (4.16)-(4.17) since it covers the entire range of ϕ_c [119]. A similar empirical equation proposed by [111] reads:

$$\tau_c = 0.956 \frac{2\Gamma_c}{bL_{cc}} \left(\frac{\hat{F}}{2\Gamma_c} \right)^{\frac{3}{2}} \left[1 - \frac{1}{8} \left(\frac{\hat{F}}{2\Gamma_c} \right)^2 \right]. \quad (4.19)$$

The equations derived based on FF statistics are valid for localized obstacles, i.e. the case where dislocations are pinned by point-like obstacles (assumption (ii)). However, a particle has finite dimensions in reality. Also, in some cases, such as for a modulus mismatch, the effective interaction range of the particle with dislocations could be larger than its physical dimensions. These subjects were investigated numerically by [123], whereby a parameter η_0 is introduced

$$\eta_0 = \frac{y_0}{L_{cc}} \frac{1}{(\hat{F}/2\Gamma_c)^{1/2}} \quad (4.20)$$

with y_0 being the range of the interaction force. It is proposed that for $\eta_0 \ll 1$, FF statistics can

still be used to predict the critical shear stress. As $\eta_0 \gtrsim 0.5$, FF statistics is insufficient and should be modified as

$$\tau_{SL} = C_1(1 + C_2\eta_0)^{C_3}\tau_{FF}. \quad (4.21)$$

τ_{FF} is the critical shear stress calculated by equation (4.14). In this work, $C_1 = 0.94$, $C_2 = 2.5$ and $C_3 = 0.33$ are taken for elastically interacting particles with $0 \leq \eta_0 \leq 4$ and $C_1 = 0.94$, $C_2 = 0.82$, and $C_3 = 1$ for energy storing particles with $0 \leq \eta_0 \leq 1.2$ [112, 119]. The coefficient C_1 allows to include the effect of the randomness of the particle distribution [119]. When $\eta_0 \gg 1$, the dislocation-particle interaction becomes similar to that in solid-solution alloys, in which partly overlapping particles are sampled and the interaction forces are relatively weak but more numerous. Such cases are well presented by *Mott-Labusch (ML) statistics*, [124–126]. It is stated in [111] that the applicability of equation (4.21) is limited to cases with small $\frac{F}{2\Gamma}$ (< 0.3) and cannot be safely applied to strong particles with a small y_0 . For a detailed discussion, the reader is referred to [111, 123].

The particle strength \hat{F} considered in equations (4.7)-(4.21) can be of different origins, which are studied and reviewed by many authors in literature [111, 112, 114, 115, 117, 127, 128] and are summarized below:

- a) *Chemical strengthening* is the result of the generation of additional interfaces during the shearing of energy storing coherent particles. The maximum resistance force experienced by a screw dislocation during this process is given by [111, 112, 114, 115, 119, 129]

$$\hat{F} = 2\chi_s b, \quad (4.22)$$

with χ_s the specific energy of the particle-matrix interface. The resistance force for an edge dislocation can be approximated by the one of a screw dislocation [114, 115, 119, 129]. The specific energy of the particle-matrix interface of a coherent particle is relatively small. For semicoherent particles, χ_s is greater than 200 mJ/m^2 [130] ($< 500 \text{ mJ/m}^2$ for Al_2Cu , [96]) and they are usually unshearable. Incoherent particles cannot be sheared.

The description of the energy barrier (i.e. the activation energy) corresponding to \hat{F} depends on the force-displacement profile of the associated strengthening mechanism. In figure 4.5, typical force-displacement profiles for particle-dislocation interactions are depicted. The energy barrier corresponding to chemical strengthening can be described by [112]

$$\Delta G_{CHE} = 2\hat{F}r \left[1 - \left(\frac{|\tau_{eff}|}{\tau_{FR}} \right)^{2/3} \right]. \quad (4.23)$$

Note that equation (4.22) is independent of the particle size. Therefore, the critical shear stress estimated by equation (4.14) decreases with increasing particle size at constant volume fraction, which makes chemical strengthening important only for very small particles (e.g. underaged). Based on this fact, it can be said that chemical strengthening can be considered as an assisting mechanism to other strengthening mechanisms during particle shearing [111, 112, 114, 119].

Chemical hardening can be important for Al rich alloys such as Al-Cu or Al-Ag alloys [111].

- b) *Stacking fault (SF) strengthening* originates from the difference in the SF energies of the matrix and particles ($\Delta\chi$). In SF strengthening, the dislocations-particle interaction is considered as elastic [119]. A lower SF energy of the particles will generate an attractive interaction, which leads to a local reduction of the dislocation line energy within the precipitate.

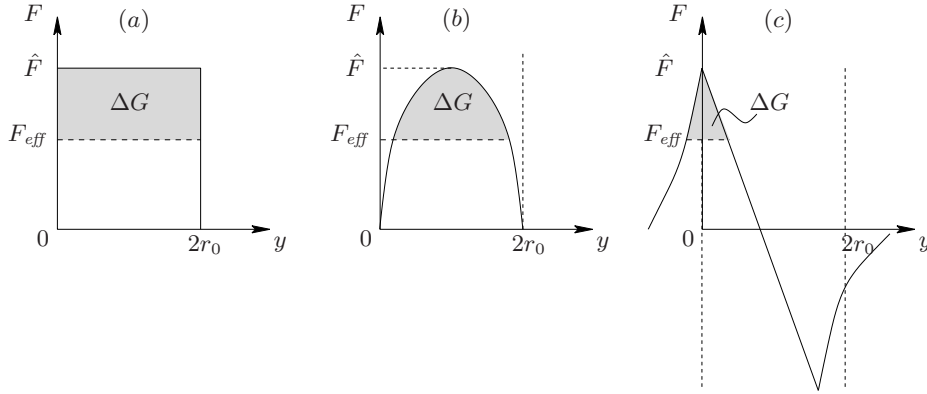


Figure 4.5: Typical force (F)-distance (y) profiles for dislocation-obstacle interactions: a) chemical interaction, b) a localized obstacle with internal friction or fault (energy storing type obstacles), c) soft contact obstacle (energy storing or elastically interacting obstacle). \hat{F} and F_{eff} are forces corresponding to the peak resistance stress $\hat{\tau}$ and the effective resolved shear stress τ_{eff} . ΔG is the energy barrier for thermally assisted overcoming of particles. After [112].

A number of papers regarding SF strengthening [111, 112, 119, 131–133] are available in literature. Here, the approach in [131] is adopted due to its simplicity. Therein, the additional drag force experienced by a straight dislocation due to the mismatch in stacking fault energies is given as

$$\hat{F} = 2(2\hat{d}r_s - \hat{d}^2)^{1/2}|\Delta\chi|, \quad (4.24)$$

where $\hat{d} = \min(w_m, r_s)$. w_m is the equilibrium distance between Shockley partial dislocations in a material matrix given by¹ [132]

$$w_m = \frac{G_m b^2}{24\pi\chi} \frac{2 - 3\nu}{1 - \nu} \left[1 + \frac{4\nu}{2 - 3\nu} \sin^2 \beta \right] \quad (4.25)$$

where β is the angle between the total Burgers vector and the dislocation line. It has been shown by [134] that equation (4.24) yields larger values than when the dislocation flexibility is taken into account and it can be corrected by the introduction of a constant factor in front of it.

The SF hardening model [131] is here formulated through an interaction force versus displacement profile that belongs to the class of elastic dislocation particle interactions, which is close to the profile depicted in figure 4.5c. The corresponding activation energy is given by [112] and reads:

$$\Delta G_{SFS} = r\hat{F} \left[1 - \frac{3}{2} \left(\frac{|\tau_{eff}|}{\tau_{FR}} \right)^{4/9} + \frac{1}{2} \left(\frac{|\tau_{eff}|}{\tau_{FR}} \right)^{4/3} \right]. \quad (4.26)$$

This type of hardening can be important in Al rich alloys due to the high stacking fault energy of Al.

- c) *Coherency hardening* occurs due to the stress fields that arise from the lattice misfit (ε) between the coherent particles and the matrix. This hardening type is important for equiaxed particles

¹From here onwards, the subscripts m and p are for matrix and particle, respectively.

with a misfit larger than $\approx 1\%$, while its significance reduces with decreasing misfit, or for plate-like particles, [114].

The interaction of the dislocations with the strain field due to the lattice mismatch is of an elastic and diffuse type [131]. For an infinitely long straight screw dislocation, the interaction vanishes. Because of that, mainly the interaction with edge dislocations is studied in literature. Also, when the slip plane contains the center of the particle, there is no interaction. Moreover, once a dislocation penetrates into a particle, the resistance due to coherency vanishes.

The maximum resistance force that an edge dislocation may experience reads [111, 129, 135–138]

$$\hat{F} = 4G|\varepsilon|br, \quad (4.27)$$

which is achieved when the slip plane cuts the particle at a distance $h = r/\sqrt{2}$ from its center.

Since the particle-dislocation interaction considered here is of the diffuse type, a dislocation moving on a slip plane that does not intersect the coherent particle may still feel the influence of that particle. Hence, in contrast to the other strengthening sources mentioned earlier, an averaging procedure is necessary to describe the overall influence of all particles [111]. In literature, several equations [111, 114, 129, 135–138] are suggested for the critical resolved shear stress necessary to shear coherent spherical particles. Many of them take a form similar to

$$\tau_{COH} = C_4(G_m\varepsilon)^{\frac{3}{2}} \left[\frac{f r b}{2\Gamma} \right]^{\frac{1}{2}} \quad \text{and} \quad \varepsilon = \frac{a_p - a_m}{a_m} \left[1 + \frac{2G_m(1 - 2\nu_p)}{G_p(1 + \nu_p)} \right], \quad (4.28)$$

where a is the lattice parameter of the matrix and C_4 is a constant between 2 and 4 depending on the averaging procedures used [111, 119].

By making use of equations (4.27) and (4.28), it is inherently assumed that the particles considered are *small* and *weak* enough so that the dislocations are not bent around the particles at large angles, since these equations are formulated by assuming rigid dislocations [111]. Hence, these equations are valid for $\frac{Gbr|\varepsilon|}{\Gamma} < 0.25$, i.e. $\frac{\hat{F}}{2\Gamma} < 0.5$. In other cases, the flexibility of the dislocation must be taken into account [137].

Depending on the force-distance profile of this type of interactions, an activation energy form is proposed by [112] as

$$\Delta G_{COH} = r\hat{F} \left[1 - \frac{3}{2} \left(\frac{|\tau_{eff}|}{\tau_{FR}} \right)^{4/9} + \frac{1}{2} \left(\frac{|\tau_{eff}|}{\tau_{FR}} \right)^{4/3} \right]. \quad (4.29)$$

When the coherent particles are large enough, the dislocations interacting with those particles may be exposed to large resistance forces such that they are bent into large angles [114]. An optimum particle radius, at which dislocations are bent to large angles, can then be defined by considering $\beta_c = 1$, which can also be used to calculate the maximum resistance stress due to the lattice mismatch [111, 114] as

$$\tau_{COH,max} = 1.84G|\varepsilon|f^{1/2}. \quad (4.30)$$

In this work, equation (4.28) is used to estimate the additional strength provided by the lattice mismatch between the particles and the matrix by taking $C_4 = 3.9$, which results from the substitution of equation (4.27) into equation (4.14).

- d) *Modulus hardening* occurs due the difference in elastic moduli of the matrix and particles (ΔG). In modulus hardening [131], the matrix dislocations interact elastically with the particles. A number of papers exist, in which this topic is particularly investigated. The reader is referred to [111, 119] for a rigorous elaboration on the subject.

In the present case, the study of [139] is used for the incorporation of the effect of a modulus mismatch. In [139], an empirical equation is derived for the maximum force that can be experienced by an edge dislocation:

$$\hat{F} = C_5 \Delta G b^2 \left(\frac{r}{b} \right)^{C_6}, \quad (4.31)$$

where $C_5 \approx 0.05$ and $C_6 \approx 0.85$ are constants [111]. It should be noted that equation (4.31) is valid for particle sizes in the range of $8b < r < 50b$ [139]. Since in its derivation, the assumption of a straight dislocation is used, any influence of the particle-dislocation interaction on the line tension is ignored. Moreover, the particles are intersected by the slip planes at their centers and maximum forces always occur approximately at the particle interface.

For a screw dislocation, \hat{F} is lower than for an edge dislocation. However, an expression for screw dislocations is not explicitly provided in [139]. Therefore, equation (4.31) is also used for screw dislocations in this work together with an artificial reduction by 25%, which is qualitatively in line with the calculation results in [139] for screw type dislocations.

Following [112], an expression for the energy barrier for overcoming the resistance can be written as

$$\Delta G_{MOD} = r \hat{F} \left[1 - \frac{3}{2} \left(\frac{|\tau_{eff}|}{\tau_{FR}} \right)^{4/9} + \frac{1}{2} \left(\frac{|\tau_{eff}|}{\tau_{FR}} \right)^{4/3} \right], \quad (4.32)$$

which is similar to equation (4.29) due to the similarity between the interactions due to size and modulus mismatches.

The effect of modulus mismatch may be important for Al alloys since Al has a relatively low shear modulus.

- e) *Order strengthening* originates from the generation of an anti-phase boundary in the slip plane of an ordered precipitate during shearing by the dislocations moving in groups. It is presumed that this kind of particle-dislocation interaction is not observed for the material (Al-Cu [1 wt%] alloy) considered here.
- f) A *difference in the Peierls-Nabarro (P-N) stresses* [140, 141] of the matrix and the particles leads to additional strengthening. A modified expression for P-N stress at 0 K is given by [142, 143]

$$\tau_{PN_{m,p}} \approx \frac{G_{m,p}}{1 - \nu_{m,p}} \exp \left(-\frac{4\pi\zeta_{m,p}}{b_{m,p}} \right) \quad \text{with} \quad \zeta_{m,p} = \frac{a_{m,p}}{2(1 - \nu_{m,p})} \quad (4.33)$$

for an edge dislocation whereas for a screw dislocation, the terms $(1 - \nu_{m,p})$ are to be replaced by unity. The additional resistance force is then calculated by [112]

$$\hat{F} = 2rb\Delta\tau_{PN} \quad \text{with} \quad \tau_{PN} = \tau_{PN_p} - \tau_{PN_m}. \quad (4.34)$$

It is observed that the contribution to the strength of the material due to the difference in PN stresses is ignorably small, which is not surprising for fcc metals. Keeping in mind that equation

(4.33) and its equivalent forms estimate Peiers-Nabarro stresses at absolute zero temperature, the magnitude of this additional strengthening will be even smaller with increasing temperatures. Therefore, it will be omitted in the rest of this work.

Orowan mechanism

The Orowan mechanism is the circumvention process that occurs when the particles involved in the materials are non-shearable due to full incoherency or very large strength. In this case, dislocations are bent around the particles until the critical angle ϕ_c in figure 4.3 becomes zero. Then, the wrapping parts of the dislocation collapse on each other and the dislocation escapes from the particle, leaving behind a dislocation loop around the particle. Referring to equation (4.7), this process occurs when

$$\frac{\hat{F}}{2\Gamma_c} = \cos \phi_c = 1 \quad (4.35)$$

at the stress equal to the *Orowan stress* τ_{OR} . An expression for τ_{OR} for spherical particles is given by [119]

$$\tau_{OR} = 0.93 \frac{G_m b}{2\pi\sqrt{1-\nu} w_l r} \ln \left(\frac{2w_d r}{b} \right) \left[\frac{\ln(2w_d r/b)}{\ln(w_l r/b)} \right]^{1/2} \quad (4.36)$$

with G_m and b the shear modulus and the magnitude of the Burgers vector of the matrix, respectively. w_r , w_q , w_l and w_d are statistical parameters given by

$$w_r = \frac{\pi}{4}, \quad w_q = \frac{2}{3}, \quad w_l = \sqrt{\frac{\pi w_q}{f}} - 2w_r \quad \text{and} \quad w_d = (w_l^{-1} + (2w_r)^{-1})^{-1}. \quad (4.37)$$

Note that $w_r r$ gives the mean planar particle radius r_s . For small particles, $w_d \approx w_r$ and $w_l r$ is equal to L_{cc} , the mean separation distance between the obstacles in a square lattice array. In equation (4.36), the factor 0.93 accounts for the random distribution of the obstacles, in line with equation (4.21). In this work, it is assumed that the Orowan stresses for edge and screw dislocations are identical.

For non-shearable particles, the process for overcoming the obstacles via the Orowan mechanism is almost temperature independent. Such a property can be described using a relatively large activation energy such as $\Delta G_O > 2Gb^3$ following [106]. Hence, a stress dependent energy barrier for the Orowan process is proposed here as

$$\Delta G_O = 3Gb^3 \left(1 - \frac{|\tau_{eff}|}{\tau_{OR}} \right), \quad (4.38)$$

which is used in the forthcoming sections.

Dislocation climb over particles

In the absence of an applied stress that is large enough for the Friedel or Orowan processes, dislocations can still overcome particles by diffusion, i.e. by means of *climb*. The early modeling approaches for dislocation climb over particles were based on so-called *local climb* [114, 144, 145], in which dislocations are assumed to profile the surface of the particles. In order for such a climb

mechanism to be accomplished, the length of the climbing dislocation has to increase and the diffusion involved in the process is very small. The local climb resulting in sharp dislocation bends, which requires additional energy, is believed to be the source of athermal threshold stresses observed in creep experiments of particle strengthened alloys, above which significant deformation occurs. However, these sharp bends are unstable and can be quickly relaxed by diffusion, which may significantly reduce the threshold stress of local climb [114, 146–149]. In such a case, so-called *general climb*, the required increase in the line length is small but a relatively large vacancy diffusion is required. This suggests the existence of other mechanisms for the explanation of the experimentally observed threshold stresses, such as *attractive particle-dislocation interaction* [150]. Due to this interaction, the line tension of a climbing dislocation is relaxed at the particle-matrix interface. Hence, an additional energy must be supplied so that the dislocation attains the energy level required to detach from the particle. Therefore, two energy barriers for the completion of the climbing process over a particle exist: i) a climb barrier (for the increase of the line length) and ii) a detachment barrier (due to the reduction of the line energy). Arzt and Wilkinson [145] introduced an empirical fit for the critical value of the degree of the line tension relaxation at the interface, k_r , in terms of the particle size (r_s) and separation (λ) as:

$$k_c = 0.94 \left(1 - \frac{r_s}{\lambda}\right)^{0.073}. \quad (4.39)$$

For $k_r < k_c$, the detachment barrier governs the climbing process and otherwise, the climb barrier. In reality, $k_r > 0.7$ and it attains its lowest values for incoherent particles [151].

In this work, based on the assumption of the existence of sufficiently strong attractive particle-dislocation interaction, thermally activated detachment [152] is considered as the rate limiting process for climb. The attempt frequency v of a dislocation involved in this climb mechanism is given by [152] as

$$v = v_v \exp\left(-\frac{E_d}{kT}\right) \quad \text{with} \quad v_v = \frac{n}{2} \nu_D \exp\left(-\frac{Q_f + Q_m}{kT}\right) = \frac{3D_l}{b^2}, \quad (4.40)$$

where v_v is frequency of vacancy absorption, $D_l = \frac{1}{6} n b^2 \nu_D \exp\left(-\frac{Q_l}{kT}\right)$ is the lattice diffusivity, ν_D is the Debye frequency, Q_f and Q_m are the activation energies for vacancy nucleation and migration, Q_l is the activation energy for self diffusion, and E_d is the detachment energy given by

$$E_d = 2\Gamma r \left[(1 - k_r) \left(1 - \frac{|\tau_{eff}|}{\tau_d} \right) \right]^{\frac{3}{2}} \quad (4.41)$$

for spherical particles of average radius r where

$$\tau_d = \sqrt{1 - k_r^2} \tau_{OR} \quad (4.42)$$

is the detachment threshold stress [146].

Another expression for the detachment threshold stress was suggested by [153]

$$\tau_d \approx \left(1 + \frac{1}{\sqrt{1 - k_r^2}} \right)^{3/2} \tau_{OR}, \quad (4.43)$$

by considering a rather weak behavior of dispersions during the thermal detachment which contradicts the strong obstacle approximation by [146]. Equation (4.43) provided a lower threshold

stress for the detachment than the original formulation by [146]. Moreover, equation (4.43) also leads to a shift of the critical relaxation parameter from 0.94 to 0.96, which is the limit between detachment controlled slip and climb controlled slip.

The consideration of the attractive dislocation-particle interaction in the climb process stabilizes the local climb and leads to a detachment threshold stress τ_d , which vanishes with increasing particle size as the Orowan stress is reduced [146, 151, 152]. For small particles, the probability of the thermally activated detachment becomes larger since the detachment energy is proportional to the particle size.

4.3.2 Dislocation line tension

There are several approaches for the calculation of the line tension in the equations above. The simplest one is the fixed line tension approximation which is given by

$$\Gamma = \frac{Gb^2}{2}, \quad (4.44)$$

which is the same for both edge and screw dislocations.

Another approach is using de Wit-Koehler model

$$\Gamma = \frac{W_s}{L} + \frac{\partial^2(W_s/L)}{\partial\beta^2}, \quad (4.45)$$

where $\frac{W_s}{L}$ is the elastic energy per length of a straight dislocation in an isotropic crystal with the definition [78, 114, 154]

$$\frac{W_s}{L} = \frac{Gb^2}{4\pi} \left(\frac{1 - \nu \cos^2 \beta}{1 - \nu} \right) \ln \frac{R_o}{R_i}, \quad (4.46)$$

with inner and outer cutoff-radii R_i and R_o . Hence, equation (4.45) becomes

$$\Gamma = \frac{Gb^2}{4\pi} \left(\frac{1 + \nu - 3\nu \sin^2 \beta}{1 - \nu} \right) \ln \frac{R_o}{R_i}. \quad (4.47)$$

Equations (4.45) and (4.46) lead to a smaller radius of curvature for edge dislocations. Hence, a complete dislocation loop has a shape elongated in the direction of the Burgers vector. This is in contradiction with equation (4.8) which assumes that a dislocation loop is circular. Ardell [111] suggested to use the following equations for the improvement of accuracy:

$$\Gamma_e = \frac{Gb^2}{4\pi} \left[1 + \nu - 3\nu \left(1 - \frac{\cos^2 \phi_c}{3} \right) \right] \ln \frac{R_o}{R_i}, \quad (4.48)$$

$$\Gamma_s = \frac{Gb^2}{4\pi} [1 + \nu - \nu \cos^2 \phi_c] \ln \frac{R_o}{R_i}, \quad (4.49)$$

which are derived by [155] by calculating the average line tension along the length of an arc that is assumed to be circular [111].

The line tension of a dislocation derived through equations (4.45)-(4.49) does not contain the effect of the self-interaction of the dislocation and its configuration (i.e. whether the dislocation bow is large or small), which may influence the calculated values by a factor of two [156]. The following

set of equations for the line tensions of an edge (Γ_e) and a screw (Γ_s) dislocation is therefore proposed in [156]:

$$\Gamma_e = \frac{Gb^2}{4\pi(1-\nu)} \left[(1-2\nu) \ln \frac{eR}{R_i} + 4.78\nu - 2.89 \right], \quad (4.50)$$

$$\Gamma_s = \frac{Gb^2}{4\pi(1-\nu)} \left[(1+\nu) \ln \frac{eR}{R_i} - 1.89\nu - 2.89 \right], \quad (4.51)$$

with the Euler number e . Equations (4.50) and (4.51) are derived by using the self-energies of a small bow-out configuration of straight dislocations involving self-interaction effects [78, 156, 157].

In the subsequent sections, equations (4.48) and (4.49) are used for the calculation of the line tension. The magnitude of the line tension is highly sensitive to the selected value of R_0 . Different quantities were substituted for R_0 by various authors [111] such as using a constant value justified for a matrix with peak aged precipitates or using the Friedel sampling length λ_c . A discussion on the choice of R_0 can be found in [158]. In this work, the surface-to-surface spacing of the obstacles that are arranged in a square lattice array, L , is used as a reasonable estimate for the outer cut-off radius.

4.3.3 Velocity of dislocations

Dislocation motion can be roughly classified into two mechanisms: jerky glide and viscous (continuous) glide. In case of jerky glide, the applied stress is below the mechanical threshold $\hat{\tau}$, cf. figure 4.6, at some locations and the gliding dislocations are trapped at obstacles. Therefore, the dislocation velocity is controlled by the rate at which the dislocations escape from these obstacles, which is a statistical process that is assisted through thermal fluctuations, i.e. by thermal activation. When the applied stress reaches values that are larger than the mechanical threshold stress everywhere, dislocations move in a continuous manner under the effect of viscous drag forces. In this regime, the velocity of dislocations depends linearly on the applied stress. Further increase of the applied stress towards the ideal shear strength τ_{ideal} activates additional dissipative processes that set upper limits for the maximum velocity attainable by the dislocations.

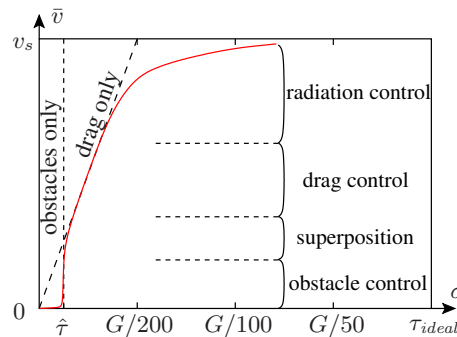


Figure 4.6: Schematic representation of the kinetics of dislocation motion with average dislocation velocity \bar{v} , after [159].

In the forthcoming subsections, a theoretical background is provided on the kinetics of jerky glide

and viscous glide of dislocations in the presence of discrete obstacles, mainly based on the work of Kocks et al. [159].

Viscous glide of dislocations

In a configuration where a dislocation moves at constant velocity v_{dr} along axis y (and where inertial effects are negligible) under a local driving force $b(\tau - \tilde{\tau}(y))$, the force equilibrium equation can be written as [159, 160]

$$Bv_{dr}(y) = b(\tau - \tilde{\tau}(y)) \quad (4.52)$$

with drag coefficient B , the magnitude of the Burgers vector b , applied resolved shear stress τ and glide resistance $\tilde{\tau}$. The average velocity \bar{v}_{dr} of the dislocations between two obstacles is then defined by the ratio of the distance covered, λ_2 , over the total time spent during the viscous glide:

$$\bar{v}_{dr} = \frac{\lambda_2}{\int_0^{\lambda_2} \frac{dy}{v_{dr}(y)}}. \quad (4.53)$$

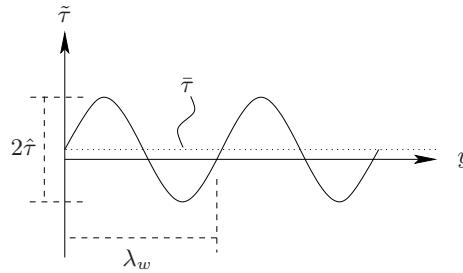


Figure 4.7: Sinusoidal glide resistance.

In case of a glide resistance with a sinusoidal variation, as shown in figure 4.7, $\tilde{\tau}(y)$ can be approximated by [159]

$$\tilde{\tau}(y) = \bar{\tau} + \hat{\tau} \sin\left(\frac{2\pi}{\lambda_w}y\right). \quad (4.54)$$

Here, $\bar{\tau}$ is the mean resistance, $\hat{\tau}$ is the amplitude and λ_w is the wavelength of the periodic slip resistance.

For a glide resistance that originates from the stress fields of the dislocations within a square lattice arrangement, a simple expression can be written by using equation (4.54) [159] via

$$\bar{\tau} = 0 \quad \text{and} \quad \hat{\tau} = s = \frac{Gb}{\lambda_w}. \quad (4.55)$$

Then, the average velocity is calculated by substituting equation (4.55) into equation (4.53) [159, 160]:

$$\bar{v}_{dr} = \frac{b}{B} \sqrt{\tau^2 - s^2}. \quad (4.56)$$

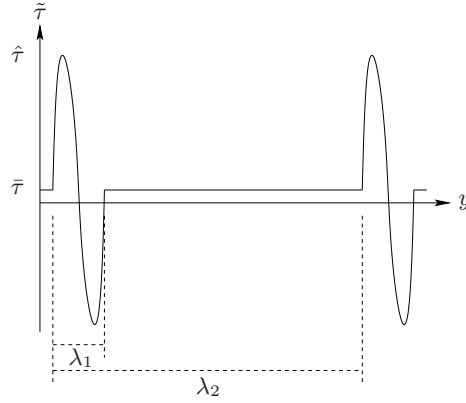


Figure 4.8: Schematic representation of the flow resistance profile on a slip plane.

For a glide resistance with sinusoidal variation as in figure 4.7, the separation between the particles is the same as their width, i.e. $\lambda_w = \lambda_1 = \lambda_2$ in figure 4.8. However, in cases where dislocations are treated as the source of glide resistances, width λ_1 is in the order of a few Burgers vectors [160] and relatively small in comparison with the separation distance λ_2 , cf. figure 4.8. Hence, equation (4.56) needs to be modified to take into the account the time spent in between the particles. The description of the average velocity for such cases is given by [159] and with the conditions given in equation (4.55), it reads as

$$\bar{v}_{dr} = \frac{\frac{b}{B} \sqrt{\tau^2 - s^2}}{\frac{\lambda_1}{\lambda_2} + \frac{\sqrt{\tau^2 - s^2}}{\tau} \frac{\lambda_2 - \lambda_1}{\lambda_2}}. \quad (4.57)$$

Note that for larger values of $\frac{\lambda_1}{\lambda_2}$, equation (4.57) reduces to

$$\bar{v}_{dr} = \frac{b}{B} \tau. \quad (4.58)$$

The viscous drag B controlling the dislocation motion can originate from different sources depending on the material. For instance, in crystals with a large Peierls resistance like bcc metals, B is dominated by the lattice friction. For materials with negligible lattice friction, as in case of fcc metals such as Al, the drag on the dislocations is linear and B is determined by the interaction of the gliding dislocations with phonons and at very low temperatures, with electrons. A detailed overview of the various types of interactions can be found in [159] and references therein. As the velocity of dislocations gets closer to the speed of sound, the magnitude of the drag force increases due to highly nonlinear interactions between the mobile dislocations and phonons and electrons [159]. Besides, the relativistic contraction of the dislocations at high velocities leads to an increased line energy, which, in turn, increases the weight of the other drag mechanisms that are safely neglected at a lower velocities. In summary, above half the speed of sound, the rate of the energy dissipation increases significantly [159].

A general drag coefficient for temperatures above the Debye temperature resulting from phonon interactions reads as

$$B \simeq \frac{kT}{\Omega \omega_A}, \quad (4.59)$$

Table 4.1: Material parameters for Al.

G	25.1	GPa
v_S	3.06	km/s
ω_A	$1.07 \cdot 10^{13}$	1/s
T_D	428	K
B	$1.8 \cdot 10^{-5}$	Pa s
Ω	16.50	\AA^3

which leads to a maximum velocity

$$v_{dr} = \frac{\Omega\tau}{kT}v_S, \quad (4.60)$$

at the steady state. As mentioned above, the upper bound for the dislocation velocity is set by the speed of sound. For the satisfaction of this constraint by equation (4.59), the upper bound for the effective resolved shear stress should be defined as

$$\tau \ll \frac{kT}{\Omega}, \quad (4.61)$$

which is around 245 MPa for Al at room temperature for the parameters given in table 4.1.

In the following sections, the slip resistance is considered as a result of dislocation-dislocation interaction and treated as a short range interaction due to large values of $\frac{\lambda_1}{\lambda_2}$. Hence, equation (4.58) is used to define the average velocity of mobile dislocations in the viscous drag regime. The drag coefficient B is calculated by equation (4.59).

Jerky glide of dislocations

At low levels of the applied stresses, i.e. less than the mechanical threshold stress, the dislocation motion is at some locations prevented by the obstacles. In such circumstances, the motion can be continued provided that the energy supplied to the dislocation by the thermal fluctuations is sufficient to overcome the obstruction, which is referred to as *thermal activation*. In the thermally activated slip, dislocations move in a jerky manner, namely, the rate of the motion is governed by the waiting times spent at the obstacles and the time needed to move between obstacles is negligible.

A general rate equation for the net rate of the thermally activated release of dislocations at constant stress, denoted by P , is provided by [159]

$$P = v_G \left[\exp\left(-\frac{\Delta G_f}{kT}\right) - \exp\left(-\frac{\Delta G_r}{kT}\right) \right] = \frac{1}{t_w}, \quad (4.62)$$

with ΔG_f and ΔG_r the forward and backward activation energies, respectively. The inverse of equation (4.62) yields the waiting time, t_w , of the trapped dislocations at an obstacle, which is needed for the calculation of the average dislocation velocity [160].

The forward activation energies used in this work are defined by [112] in terms of the obstacle

radius r_0^2 , the maximum force \hat{F} and stress $\hat{\tau}$ that can be sustained by the obstacles with different resistance-displacement profiles are given in figure 4.5. The activation energy ΔG_r (cf. figure 4.9) for the reverse jumps can be approximated by [159]

$$\Delta G_r \simeq \Delta G_f + |\tau_{eff}|b(L + 2r_0)(2\lambda_c) \quad (4.63)$$

for weak particles that can be treated within FF statistics. When the forward and reverse work done by τ_{eff} are equal but with opposite signs, as the case for rectangular waves with $L = 0$, equation (4.62) boils down to a hyperbolic form which is often used in the literature, even though it is only a special case [159].

The term $(L + 2r_0)$ in equation (4.63) stands for the jumping distance or slip distance between two successive activations. One can approximately calculate this distance by the steady unzipping condition of FF statistics as

$$\lambda_2 = (L + 2r_0) \simeq \frac{L_{cc}^2}{2\lambda_c}, \quad (4.64)$$

where L_{cc} is the center-to-center planar spacing of obstacles and λ_c is the critical obstacle sampling length by dislocations. Then, the average velocity of dislocations in a thermally activated slip can

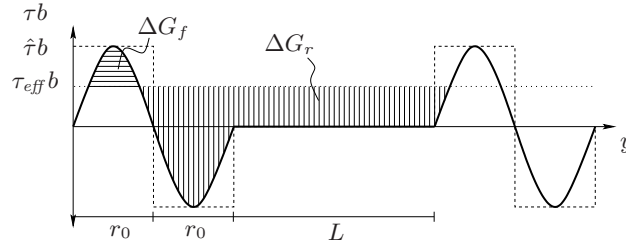


Figure 4.9: Horizontal and vertical shaded areas denote the activation energies for forward and reverse slip, respectively, for a system with two identical obstacles with a sine-like resistance profile.

be written as

$$\bar{v}_{th} = \frac{\lambda_2}{t_w}. \quad (4.65)$$

By the substitution of equations (4.62)-(4.64) into equation (4.65), \bar{v}_{th} reads³

$$\bar{v}_{th} = \frac{1}{2}L_{cc} \left(\frac{L_{cc}}{\lambda_c} \right) v_G \exp \left(-\frac{\Delta G_f}{kT} \right) \left[1 - \exp \left(-\frac{|\tau_{eff}|bL_{cc}^2}{kT} \right) \right] \text{sign}(\tau_{eff}). \quad (4.66)$$

The backbone assumption of FF statistics, i.e. at the critical configuration,

$$\left(\frac{L_{cc}}{\lambda_c} \right)^2 = \cos \phi_C = \frac{\hat{F}}{2\Gamma_c} \quad (4.67)$$

²Note that r_0 covers also the effective range of the resistance force, cf. figure 4.9

³Equation (4.65) is formulated such that the dislocation moves in the direction of the effective stress.

is used to replace the term $\frac{L_{cc}}{\lambda_c}$, which finally leads to

$$\bar{v}_{th} = \frac{1}{2} L_{cc} \left(\frac{\hat{F}}{2\Gamma_c} \right)^{1/2} v_G \exp \left(-\frac{\Delta G_f}{kT} \right) \left[1 - \exp \left(-\frac{|\tau_{eff}| b L_{cc}^2}{kT} \right) \right] \text{sign}(\tau_{eff}). \quad (4.68)$$

A closer look at equation (4.68) reveals that in a material with shearable obstructions with constant properties and by assuming that they can be overcome by the help of thermal fluctuations, the maximum velocity attainable by the dislocations (i.e. when $|\tau_{eff}| = \hat{\tau}$) is given by the constant pre-exponential term and depends on the obstacle properties such as particle size, volume fraction, strength and line tension. Additionally, an equation for the velocity of dislocations in a material with *non-shearable* particles is derived in a way similar to equation (4.68) based on the following justifications:

- i. for non-shearable particles

$$\cos \phi_c = \frac{\hat{F}}{2\Gamma_c} = 1, \quad (4.69)$$

- ii. assuming that the steady state unzipping condition is also valid for the Orowan mechanism, the dislocation sampling length becomes equal to the mean planar separation distance of particles, L_{cc} . Then, the effective slip distance also becomes L_{cc} .

The dislocation velocity can then be approximated as

$$\bar{v}_{ns} = L_{cc} v_G \exp \left(-\frac{\Delta G_f}{kT} \right) \left[1 - \exp \left(-\frac{|\tau_{eff}| b L_{cc}^2}{kT} \right) \right] \text{sign}(\tau_{eff}). \quad (4.70)$$

4.4 Strain gradient crystal plasticity model

A strain gradient crystal plasticity framework (SGCP) was recently developed by [13–16] to capture the scale dependent behavior of fcc pure metals due to the lattice curvature effect. Therein, the size effect is modeled with a back stress, which is obtained by resolving the internal stress fields due to the non-uniform distribution of geometrically necessary dislocations (GND) onto individual slip systems. The GNDs represent the signed fraction of the total dislocation population in the material and are necessary to preserve the lattice compatibility in the crystal. The SGCP framework involves also statistically stored dislocations (SSD), however, they do not contribute to the back stresses due to their random orientation, whereas they do play a role in the isotropic hardening process.

The framework is based on the multiplicative decomposition [50, 51] of the deformation gradient tensor \mathbf{F} into its elastic, \mathbf{F}_e , and plastic, \mathbf{F}_p , components

$$\mathbf{F} = \mathbf{F}_e \cdot \mathbf{F}_p, \quad (4.71)$$

where \mathbf{F}_e describes the stretch and the rotation of the lattice with respect to an intermediate configuration that is defined by \mathbf{F}_p with respect to the reference configuration.

The second elastic Piola-Kirchhoff stress tensor \mathbf{S} is given in terms of the elastic Green-Lagrange

strain tensor \mathbf{E}_e in the intermediate configuration as:

$$\mathbf{S} = \mathbb{C} : \mathbf{E}_e \quad \text{with} \quad \mathbf{E}_e = \frac{1}{2} (\mathbf{F}_e^T \cdot \mathbf{F}_e - \mathbf{I}), \quad (4.72)$$

with \mathbb{C} the fourth order elasticity tensor and \mathbf{I} the second order identity tensor. \mathbf{S} is defined by the pull-back of the Kirchhoff stress $\boldsymbol{\tau}$ to the intermediate configuration as

$$\mathbf{S} = \mathbf{F}_e^{-1} \cdot \boldsymbol{\tau} \cdot \mathbf{F}_e^{-T}. \quad (4.73)$$

The rate of the plastic deformation gradient is obtained from

$$\dot{\mathbf{F}}_p = \mathbf{L}_p \cdot \mathbf{F}_p, \quad (4.74)$$

where \mathbf{L}_p is the plastic velocity gradient tensor and is resolved from the plastic slips at the slip system level (here 12 octahedral slip systems for an fcc metal):

$$\mathbf{L}_p = \sum_{\alpha=1}^{12} \dot{\gamma}^\alpha \mathbf{P}_0^\alpha. \quad (4.75)$$

In this equation, $\dot{\gamma}^\alpha$ denotes the plastic slip rate of system α and $\mathbf{P}_0^\alpha = \mathbf{s}_0^\alpha \mathbf{n}_0^\alpha$ is the Schmid tensor with \mathbf{s}_0^α the unit direction of the Burgers vector and \mathbf{n}_0^α the unit normal of the slip plane of system α , both in the intermediate configuration.

The evolution of the plastic slip was described in the previous versions of the model [13–16] by a power-law type relation:

$$\dot{\gamma}^\alpha = \dot{\gamma}_0 \left(\frac{|\tau_{eff}^\alpha|}{s^\alpha} \right)^m \exp \left[-\frac{\Delta F_0}{kT} \left(1 - \frac{|\tau_{eff}^\alpha|}{s^\alpha} \right) \right] \text{sign}(\tau_{eff}^\alpha), \quad (4.76)$$

where $\dot{\gamma}_0$ and m are the reference slip rate and the rate sensitivity, respectively. Furthermore, s^α is the slip resistance, T is the absolute temperature and k is the Boltzmann constant. The material constant ΔF_0 represents the energy barrier to be supplied by the thermal fluctuations for overcoming the slip resistance at vanishing stress levels. τ_{eff}^α is the effective stress which is given by the difference between the applied resolved shear stress τ^α and the resolved back stress τ_b^α :

$$\tau_{eff}^\alpha = \tau^\alpha - \tau_b^\alpha \quad \text{with} \quad \tau^\alpha = \mathbf{S} : \mathbf{P}_0^\alpha. \quad (4.77)$$

The back stress of a slip system in the SGCP model is calculated at a material point by integration of the stress fields of a distribution of GNDs in a cylindrical volume, the dimension of which represents a *length scale*. The definition of τ_b^α was initially given by [13, 14] in terms of contributions of the GNDs of that slip system only. Later on, it was extended by [15, 16] taking into account the contributions of all slip systems. The definition of the internal stress field due to edge dislocations is given by [15, 16] as:

$$\boldsymbol{\sigma}_e^{int} = \frac{GbR^2}{8(1-\nu)} \sum_{\xi=1}^{12} \nabla_0 \rho_{GND,e}^\xi \cdot \left(3\mathbf{n}_0^\xi \mathbf{s}_0^\xi \mathbf{s}_0^\xi + \mathbf{n}_0^\xi \mathbf{n}_0^\xi \mathbf{n}_0^\xi + 4\nu \mathbf{n}_0^\xi \mathbf{p}_0^\xi \mathbf{p}_0^\xi - \mathbf{s}_0^\xi \mathbf{s}_0^\xi \mathbf{n}_0^\xi - \mathbf{s}_0^\xi \mathbf{n}_0^\xi \mathbf{s}_0^\xi \right), \quad (4.78)$$

and for the screw GNDs, it is:

$$\boldsymbol{\sigma}_s^{int} = \frac{GbR^2}{4} \sum_{\xi=13}^{18} \nabla_0 \rho_{GND,s}^{\xi} \cdot \left(-\mathbf{n}_0^{\xi} \mathbf{s}_0^{\xi} \mathbf{p}_0^{\xi} - \mathbf{n}_0^{\xi} \mathbf{p}_0^{\xi} \mathbf{s}_0^{\xi} + \mathbf{p}_0^{\xi} \mathbf{s}_0^{\xi} \mathbf{n}_0^{\xi} + \mathbf{p}_0^{\xi} \mathbf{n}_0^{\xi} \mathbf{s}_0^{\xi} \right) \quad (4.79)$$

with $\mathbf{p}_0^{\xi} = \mathbf{s}_0^{\xi} \times \mathbf{n}_0^{\xi}$ associated with slip system ξ and R the radius of the cylindrical integration volume. In [13–16], two of the screw dislocations with the same Burgers vector are coupled into one set, leading to 6 screw dislocations while the number of slip systems for edge dislocations is kept constant. Hence, index ξ runs over 1...12 in case of edge dislocations and 13...18 for the screw dislocations. The back stress on a slip system α is then calculated by:

$$\tau_b^{\alpha} = - \left(\boldsymbol{\sigma}_e^{int} + \boldsymbol{\sigma}_s^{int} \right) : \mathbf{P}_0^{\alpha} \quad \text{for } \alpha = 1, 2, \dots, 12. \quad (4.80)$$

The slip resistance on the glide system, s^{α} , is provided by the short-range dislocation-dislocation interactions. It is formulated following [26] in terms of both ρ_{SSD}^{α} and ρ_{GND}^{α} as:

$$s^{\alpha} = cGb \sqrt{\sum_{\xi=1}^{12} A^{\alpha\xi} |\rho_{SSD}^{\xi}| + \sum_{\xi=1}^{18} A^{\alpha\xi} |\rho_{GND}^{\xi}|} \quad \text{for } \alpha = 1, 2, \dots, 12, \quad (4.81)$$

where c is a material constant [52], G is the shear modulus, b the magnitude of the Burgers vector, and $A^{\alpha\xi}$ are the components of the interaction matrix that quantifies the strength of the interactions between slip systems [53]. It is composed of the six interaction coefficients corresponding to self hardening, coplanar hardening, Hirth lock, Glissile junction, Lomer-Cottrell lock, and cross slip [70].

The evolution of SSD densities on each slip system ξ is described by the generalized form of the relation originally proposed by [56]:

$$\dot{\rho}_{SSD}^{\xi} = \frac{1}{b} \left(\frac{1}{L^{\xi}} - 2y_c \rho_{SSD}^{\xi} \right) |\dot{\gamma}^{\xi}| \quad \text{with } \rho_{SSD}^{\xi}(t=0) = \rho_{SSD_0}^{\xi} \quad \text{for } \xi = 1, 2, \dots, 12. \quad (4.82)$$

In this equation, the first term within the parentheses represents the accumulation rate where L^{ξ} denotes the average dislocation segment length given by:

$$L^{\xi} = \frac{K}{\sqrt{\sum_{\alpha=1}^{12} H^{\xi\alpha} |\rho_{SSD}^{\alpha}| + \sum_{\alpha=1}^{18} H^{\xi\alpha} |\rho_{GND}^{\alpha}|}}. \quad (4.83)$$

Here, $H^{\xi\alpha}$ are the components of an interaction matrix similar to $A^{\alpha\xi}$, representing the mutual interactions anticipated between the dislocations [13]. The second term in the parentheses is the annihilation rate in terms of the critical annihilation length y_c , the average distance between two oppositely signed dislocations, below which they annihilate.

The densities of GNDs are calculated via the gradients of the crystallographic slips. The slip gradients in the direction of slip \mathbf{s}_0^{α} yield the densities of edge GNDs while the gradients in the direction of \mathbf{p}_0^{α} give screw GND densities. A gradient of slip in the direction of the slip plane normal \mathbf{n}_0^{α} does not introduce any GNDs [26]. Hence, a balance equation for the densities of the

GNDs can be written as

$$\rho_{GND,e}^{\xi} = \rho_{GND,e_0}^{\xi} - \frac{1}{b} \mathbf{s}_0^{\xi} \cdot \nabla_0 \gamma^{\xi}, \quad (4.84)$$

$$\rho_{GND,s}^{\xi} = \rho_{GND,s_0}^{\xi} + \frac{1}{b} \left(\mathbf{p}_0^{\alpha_1(\xi)} \cdot \nabla_0 \gamma^{\alpha_1(\xi)} + \mathbf{p}_0^{\alpha_2(\xi)} \cdot \nabla_0 \gamma^{\alpha_2(\xi)} \right). \quad (4.85)$$

Here, ξ runs over 1, 2, ..., 12 for edge GNDs and over 13, 14, ..., 18 for screw GNDs. ρ_{GND,e_0}^{ξ} and ρ_{GND,s_0}^{ξ} denote the initial densities of edge and screw GNDs. The superscripts $\alpha_1(\xi)$ and $\alpha_2(\xi)$ represent two slip systems with the same slip direction but different plane normals for each screw GND. Note that equation (4.85) differs slightly from the implementation by [16].

Scale dependency of the material response due to the lattice curvature effect is well captured by the current framework [13–16]. However, for a proper description and analysis of the time dependency observed in the material behavior of the metallic thin film components of RF-MEMS devices, several aspects should be considered:

- i. Incorporation of physically justified time constants into the constitutive equations, e.g. in the slip rate equation (4.76), is necessary, which is lacking in the current formulation. Although $\dot{\gamma}_0$ in equation (4.76) seems to be such a parameter, it is simply a reference slip rate.
- ii. The current flow rule considers only the dislocation-dislocation interactions as the source of the slip resistance, which is treated as a short range obstruction that is overcome by thermal activation. In this respect, equation (4.76) can be safely used for effective stress levels below the slip resistance, i.e. within the thermal activation regime. At larger stresses, which can also be interpreted as high strain rates, the dislocation motion falls into the viscous drag regime and equation (4.76) becomes invalid. Regarding the dynamical working environment of the capacitive RF-MEMS switches considered here, it is expected that high strain rates are achieved, especially during the pull-in of the free standing top electrodes.
- iii. As mentioned before, equation (4.76) is designed for pure fcc metals, whereas the material considered in this work is a metal alloy, more specifically Al-Cu [1 wt%] with second phase particles. Hence, together with the dislocation-dislocation interactions, the influence of the interaction of dislocations with the solute atoms and the particles on the material behavior needs to be taken into account.
- iv. The slip rate equation (4.76) applies to pure metals and is essentially phenomenological despite the parameters entering into it, such as the effective resolved shear stress and slip resistance, having some physical basis.

In the following sections, based on these justifications, firstly an extended flow rule, which covers both the thermal activation and viscous drag regimes, is formulated for pure fcc metals based on the Orowan type slip rate equation. Thereafter, the new flow rule is extended to materials with second phase particles by involving three additional mechanisms of dislocation-particle interactions contributing to the resistance against crystallographic slip : i) the Friedel mechanism, ii) the Orowan mechanism and iii) dislocation climb over particles. Separate slip rate equations are written for each mechanism, which are then combined in a physically motivated manner. All four mechanisms (one from dislocation-dislocation interaction and three from the dislocation-particle interaction) inherently involve real time scales via the Granato frequency v_G , but more importantly, the rate equation for climb includes terms originating from *diffusion*, being important for creep and

anelasticity. The new flow rule for alloys is incorporated into the SGCP model to substitute equation (4.76).

4.5 Constitutive modeling of crystallographic slip

When a straight dislocation shears a crystal fully, as depicted in figure 4.10a, the size of the step generated is given by b , the magnitude of the Burgers vector. When it shears the crystal partially

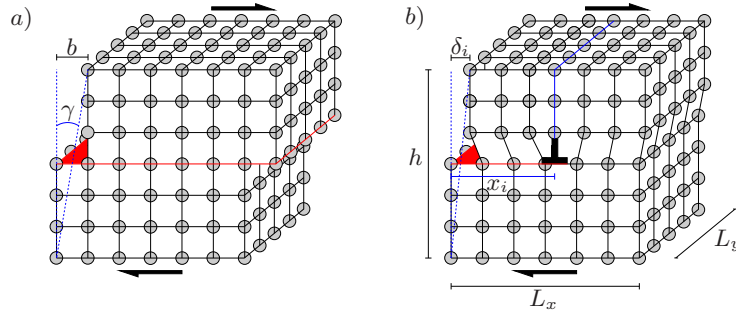


Figure 4.10: Illustration of shear strain due to the slip of an edge dislocation after: a) partial shearing, b) full shearing.

for a distance of x_i , as in figure 4.10b, the resulting relative displacement δ_i can be expressed in terms of the dimensions of the crystal and the Burgers vector such that

$$\delta_i = \frac{b}{L_x} x_i. \quad (4.86)$$

If there are N sliding dislocations, the resulting overall displacement Δ will be given by the summation of their individual contributions:

$$\Delta = \sum_i^N \delta_i = \sum_i^N \frac{b}{L_x} x_i. \quad (4.87)$$

The shear strain is then calculated by

$$\gamma = \frac{\Delta}{h} = \frac{b}{hL_x} \sum_i^N x_i. \quad (4.88)$$

By defining an average slipping distance \bar{x}

$$\bar{x} = \frac{1}{N} \sum_i^N x_i, \quad (4.89)$$

and the density of the gliding dislocations ρ_m , as the total length of dislocations per volume, such that

$$\rho_m = \frac{NL_y}{hL_xL_y}, \quad (4.90)$$

the shear strain can be rewritten as

$$\gamma = \rho_m b \bar{x}. \quad (4.91)$$

The shear rate then reads [119, 128],

$$\dot{\gamma} = \dot{\rho}_m b \bar{x} + \rho_m b \dot{\bar{x}}. \quad (4.92)$$

Based on the assumptions that

- i. the total length of the mobile dislocations is large,
- ii. in some parts of the crystal, the dislocation length will increase while in some other parts it decreases,

it is assumed here that the variation in the strains with respect to time is mainly driven by the variation in the displacements. Hence, equation (4.92) is reduced to the form

$$\dot{\gamma} = \rho_m b \bar{v}. \quad (4.93)$$

In this equation, $\bar{v} = \dot{\bar{x}}$ denotes the average dislocation velocity. It is highly sensitive to the stress acting on the gliding dislocations, temperature and the microstructural properties of the material, such as the obstruction type, the volume fraction of precipitates (if any exist) and their distribution. Equation (4.93) is the well known Orowan type flow rule, which is a physically based kinematic equation for the plastic slip rate $\dot{\gamma}$.

4.5.1 Flow rule for pure metals

In this section, a constitutive equation for the slip rate in fcc pure metals such as Al is constructed in a way analogous to [159, 160] by considering two regimes of dislocation motion: thermally activated glide and viscous glide. It is considered here that the resistance against plastic slip is only due to the dislocation-dislocation interactions as treated in [13–16].

Average velocity of dislocations

The average velocity of dislocations in viscous motion is given by equation (4.58) as

$$\bar{v}_{dr}^{\alpha} = \frac{b}{B} \tau_{eff}^{\alpha}. \quad (4.94)$$

Here, α is an index referring to the slip system to which the dislocation belongs. The average time spent to span a distance L^{α} in viscous motion can be estimated by the gliding time

$$t_r^{\alpha} = \frac{L^{\alpha}}{\bar{v}_{dr}^{\alpha}}. \quad (4.95)$$

For the jerky glide of dislocations in a material with shearable obstacles, the average velocity \bar{v}_{th}^{α} is given by equation (4.68). Note that for the type of the slip resistance considered here, the mean planar particle spacing L_{cc} in equation (4.68) is to be replaced by L_d^{α} , which is the effective mean planar distance between the obstructing dislocations on plane α as defined in the forthcoming subsections. In the thermally activated dislocation motion regime, the running time over a distance

L^α is negligible with respect to the waiting time that dislocations spend at the obstacles until their release. Hence, the average time passed is almost equal to the waiting time and it reads

$$t_w^\alpha = \frac{L^\alpha}{\bar{v}_{th}^\alpha}. \quad (4.96)$$

Then, in a plastic flow where viscous and jerky motion are considered together, the average total time spent to slip a distance of L^α is given by the summation of equations (4.95) and (4.96)

$$t_{tot}^\alpha = t_r^\alpha + t_w^\alpha. \quad (4.97)$$

Finally, the average dislocation velocity is given by the ratio of total distance covered and the total time spent as [160]

$$\bar{v}_{av}^\alpha = \frac{L^\alpha}{t_{tot}^\alpha} = \left(\frac{1}{\bar{v}_{dr}^\alpha} + \frac{1}{\bar{v}_{th}^\alpha} \right)^{-1}. \quad (4.98)$$

At stress levels below the slip resistance, equation (4.98) yields a velocity that is determined by the thermal activation while at stresses larger than the slip resistance, the velocity is governed by the viscous drag on the dislocations. A transition regime occurs for a stress level around the slip resistance where the effects of both the thermal fluctuations and the viscous drag are superposed.

Slip rate of dislocations

The behavior of the material can be described within the crystal plasticity framework by setting up a relation between the dislocation motion due to an effective resolved shear stress τ_{eff}^α and the net resulting slip rate $\dot{\gamma}^\alpha$ for each slip system. Such a constitutive relation is proposed based on the Orowan type equation (4.93):

$$\dot{\gamma}^\alpha = \rho_m^\alpha b \bar{v}_{av}^\alpha, \quad (4.99)$$

where $\dot{\gamma}^\alpha$ and ρ_m^α denote the slip rate and the density of mobile dislocations on slip system α , respectively. In this work, the total slip rate $\dot{\gamma}^\alpha$ is decomposed into two components, cf. figure 4.11:

- i. the contribution from edge dislocations, $\dot{\gamma}_e^\alpha$,
- ii. the contribution from screw dislocations, $\dot{\gamma}_s^\alpha$,

such that

$$\dot{\gamma}^\alpha = \dot{\gamma}_e^\alpha + \dot{\gamma}_s^\alpha. \quad (4.100)$$

This directly implies that the quantities ρ_m^α and \bar{v}_{av}^α are defined separately for the edge and screw type dislocations.

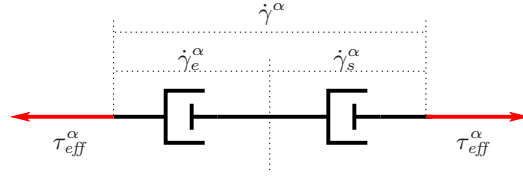


Figure 4.11: Mechanical analogue of the slip rate equation (4.100).

Slip rate of edge dislocations

The contribution of edge dislocations to the evolution of plastic slip is quantified via

$$\dot{\gamma}_e^{\alpha} = \rho_{m,e}^{\alpha} b \bar{v}_{av,e}^{\alpha}, \quad (4.101)$$

where the mobile edge dislocation density $\rho_{m,e}^{\alpha}$ is defined here as

$$\rho_{m,e}^{\alpha} = \Phi \left(|\rho_{GND,e}^{\alpha}| + |\rho_{SSD,e}^{\alpha}| \right), \quad (4.102)$$

with Φ a scalar constant that gives the mobile fraction of all edge dislocations in slip system α . In a way slightly different than the SGCP model by [13–16], the SSD densities (ρ_{SSD}^{α}) calculated by using equation (4.82) are equally split into edge and screw SSDs in the framework presented here, denoted by $\rho_{SSD,e}^{\alpha}$ and $\rho_{SSD,s}^{\alpha}$, respectively. The average velocity of the mobile edge dislocations, $\bar{v}_{av,e}^{\alpha}$, is given by equation (4.98). Within the current framework, the viscous drag controlled velocity, \bar{v}_{dr}^{α} , is used for both edge and screw type dislocations as defined by equation (4.58), where τ_{eff} is replaced by τ_{eff}^{α} . The average velocity of edge dislocations in the thermal activation regime, $\bar{v}_{th,e}^{\alpha}$, is calculated by equation (4.68), in which τ and L_{cc} are replaced by τ_{eff}^{α} and L_d^{α} , respectively. Here, L_d^{α} is the *effective* mean planar distance between the dislocations on plane α given by

$$L_d^{\alpha} = \left[\sum_{\xi=1}^{12} A^{\alpha\xi} \left(|\rho_{SSD,e}^{\xi}| + |\rho_{SSD,s}^{\xi}| \right) + \sum_{\xi=1}^{18} A^{\alpha\xi} |\rho_{GND}^{\xi}| \right]^{-1/2}, \quad (4.103)$$

where $A^{\alpha\xi}$ are the components of the interaction matrix representing the strength of the interactions between slip systems as determined by [53]. It is composed of six interaction coefficients corresponding to self hardening, coplanar hardening, Hirth lock, Glissile junction, Lomer-Cottrell lock, and cross slip, cf. [70]. In this study, L_d^{α} is taken identical for both edge and screw dislocations. The forward activation energy ΔG_f is given by [13–16]

$$\Delta G_f = \Delta F_0 \left(1 - \frac{|\tau_{eff}^{\alpha}|}{s^{\alpha}} \right). \quad (4.104)$$

In this equation, ΔF_0 represents the energy required to overcome particles at zero stress and s^{α} stands for the resistance against glide provided by the short-range interactions between dislocations [13–16] and given by

$$s^{\alpha} = c \frac{Gb}{L_d^{\alpha}}, \quad (4.105)$$

where c is a material constant [52]. Note that the slip resistance in equation (4.105) involves screw SSDs via L_d^{α} in contrast to [13, 14]. By considering the analogy between equations (4.14)

and (4.105), an estimation for the maximum resistance force \hat{F}_e of edge dislocations, used to calculate $\bar{v}_{th,e}^\alpha$ (cf. equation (4.68)), can be obtained from $c = (\hat{F}_e/2\Gamma_c)^{3/2}$ if the line tension is approximated by equation (4.44).

Slip rate of screw dislocations

The slip rate due to mobile screw dislocations is calculated in a way similar to that for mobile edge dislocations by using

$$\dot{\gamma}_s^\alpha = \rho_{m,s}^\alpha b \bar{v}_{av,s}^\alpha, \quad (4.106)$$

where the density of the mobile screw dislocations⁴ $\rho_{m,s}^\alpha$ reads

$$\rho_{m,s}^\alpha = \Phi (|\rho_{GND,s}^\alpha| + |\rho_{SSD,s}^\alpha|). \quad (4.107)$$

The average velocity of the mobile screw dislocations is also given by equations (4.58), (4.68) and (4.98). L_d^α , c and s^α are taken as the same for both edge and screw dislocation types.

4.5.2 Flow rule for particle strengthened alloys

In section 4.5.1, a constitutive law was formulated for crystallographic slip in pure metals by considering two different regimes of dislocation motion, i.e. thermally activated dislocation glide and viscous drag. For alloys, additional obstructions to dislocation glide exist, such as solute atoms in case of solid-solution alloys or precipitates and/or dispersions in particle strengthened alloys. In order for plastic slip to occur, dislocations have to overcome the particles via different processes. The three mechanisms that are listed below are presumed to play an important role in the deformation of the material studied here (Al-Cu [1 wt%]):

- i. the Friedel process,
- ii. the Orowan process,
- iii. dislocation climb over particles.

These mechanisms were discussed in the previous sections and are used in the formulation of a physically based constitutive law for the description of crystallographic slip. In doing so, several assumptions are made:

- i. The constitutive law for slip systems aims at capturing the mechanical behavior of the material *within a grain*. Hence, any deformation mechanisms occurring at/along grain boundaries are ignored⁵.
- ii. Only one type of particle phase exists in the matrix phase. Possible effects of the solute atoms in the matrix are not considered to be significant.

⁴In equation (4.107), 12 screw dislocation densities are needed. Hence, it is assumed here that the available screw GND density is equally distributed between the associated slip systems.

⁵Grain boundary strengthening due the pile-up of dislocations can still be captured by the introduction of impenetrable boundaries into the material.

- iii. Upon the completion of the Orowan process, dislocation loops are left around the particles, the pile up of which may lead to an additional hardening. This secondary effect is not considered in the present formulation.
- iv. It is assumed that an *attractive interaction* exists between the particles and the dislocations. Based on this assumption, it is assumed further that the climb process is dominated by the thermal detachment of dislocations from the particles. This assumption can be justified by the existence of semicoherent and incoherent particles, which is commonly observed in thin films made of Al-Cu alloy (cf. section 4.2).
- v. At low stress levels, the overall slip rate is controlled by the climb of edge dislocations over the particles.
- vi. The geometrical evolution of the particles may be ignored, i.e. the average size and the volume fraction of particles are constant.
- vii. In a material point of the crystal plasticity model, all particles are sampled simultaneously by the dislocations at the same rate.

Then, the multiple dashpot configuration in figure 4.12 is used to incorporate the effect of particles into the matrix material, which is treated as pure Al here due to assumption (ii). The dashpot arrangement in figure 4.12 can be motivated as follows: When the material is loaded, the external resolved shear stress (τ^α) must overcome firstly the back stress (τ_b^α) so that a non-zero effective resolved shear stress (τ_{eff}^α) can drive mobile dislocations. In order to move a dislocation from one position to another, τ_{eff}^α has to simultaneously overcome the crystallographic slip resistance by dislocation-dislocation interactions and dislocation-particle interactions. Dislocation-dislocation interactions and dislocation-particle interactions are therefore connected in parallel in the first and second branch, respectively. If τ_{eff}^α is sufficiently large, dislocations can pass by obstacles via the Friedel or/and Orowan processes. These two mechanisms are incorporated separately in the dislocation-particle branch. If τ_{eff}^α is low, dislocations cannot cut through obstacles or bow around (meaning that the dashpots connected in parallel yield zero or negligible slip rates). However, dislocation glide may still occur via diffusional processes. It is assumed in the current formulation that the climb of dislocations over particles is the only rate limiting diffusional mechanism. A dashpot representing the dislocation climb is added into the main branch so that finite strain rates are produced even if the effective resolved shear stress levels are insufficient for the Orowan and Friedel mechanisms.

As shown in figure 4.12, the constitutive law is characterized by these dashpot systems, governing the contribution to the total plastic slip rate $\dot{\gamma}^\alpha$ of the edge dislocations, $\dot{\gamma}_e^\alpha$, and the screw dislocations, $\dot{\gamma}_s^\alpha$. The total plastic slip rate is obtained by equation (4.100). Each dashpot in figure 4.12 has its own unique slip law that relates the stress in the branch to the slip rate it delivers. Based on the combination presented in the figure, the slip rates of individual dashpots and the overall slip rate are connected to each other by

$$\dot{\gamma}_e^\alpha = \dot{\gamma}_{R,e}^\alpha + \dot{\gamma}_{C,e}^\alpha = \dot{\gamma}_{O,e}^\alpha + \dot{\gamma}_{F,e}^\alpha + \dot{\gamma}_{C,e}^\alpha, \quad (4.108)$$

$$\dot{\gamma}_s^\alpha = \dot{\gamma}_{R,s}^\alpha = \dot{\gamma}_{O,s}^\alpha + \dot{\gamma}_{F,s}^\alpha. \quad (4.109)$$

The dashpot systems for the edge and screw dislocations experience the same stress, τ_{eff}^α , which is then divided between their underlying branches. This can be formulated as

$$\tau_{eff}^\alpha = \tau_{1,e}^\alpha + \tau_{2,e}^\alpha = \tau_{1,s}^\alpha + \tau_{2,s}^\alpha. \quad (4.110)$$

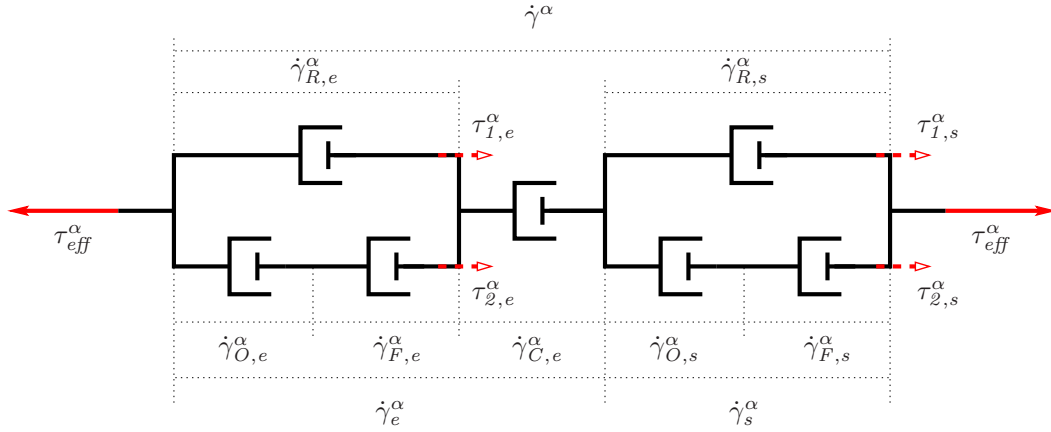


Figure 4.12: Mechanical analogue of the constitutive law for a slip system in a particle strengthened alloy. In the figure, α denotes slip plane and runs over 1..12 for fcc metals, τ^α is the effective resolved shear stress, $\dot{\gamma}^\alpha$ is the total slip rate corresponding to τ_{eff}^α , τ_I^α and τ_Σ^α are the stresses in the first and second branches. $\dot{\gamma}_R^\alpha$, $\dot{\gamma}_O^\alpha$, $\dot{\gamma}_F^\alpha$ and $\dot{\gamma}_C^\alpha$ are the slip rates of the dislocation-dislocation interaction dashpot, the Orowan, the Friedel and the climb dashpots, respectively. Subscripts $(\cdot)_e$ and $(\cdot)_s$ represent the quantities for edge and screw dislocations.

The dashpot in the *first branch* of each of the parallel dashpot groups in figure 4.12 represents the slip resistance provided by the dislocation-dislocation interaction, which is given by equation (4.105). The slip rate for the edge dislocations controlled by the dislocation-dislocation interactions is given by equation (4.101) and for the screw dislocations, it is given by equation (4.106).

The *second branch* of the parallel dashpot groups takes into account the effect of the particles. As an important difference with the first branch, the dashpots in this branch work within the thermally activated slip regime only. As soon as the stress in the branch exceeds the threshold stress of a dashpot, that dashpot becomes active, and hence the stress in the branch hardly increases further with an increase in the applied stress and the dashpot of the first branch sustains the further loading alone. The first dashpot in the second branch denotes the particles that are overcome by the *Orowan process*. The stress required for the activation of this process is calculated with equation (4.36). The velocity of the edge dislocations involved in the process is estimated by using equation (4.70):

$$\bar{v}_{O,e}^\alpha = L_{cc} v_G \exp\left(-\frac{\Delta G_{O,e}^\alpha}{kT}\right) \left[1 - \exp\left(-\frac{|\tau_{\Sigma,e}^\alpha| b L_{cc}^2}{kT}\right)\right] \text{sign}(\tau_{\Sigma,e}^\alpha). \quad (4.111)$$

The corresponding slip rate is defined in a way similar to equation (4.101):

$$\dot{\gamma}_{O,e}^\alpha = \rho_{m,e}^\alpha b \bar{v}_{O,e}^\alpha. \quad (4.112)$$

Equations similar to equations (4.111) and (4.112) are used to calculate the average velocities and the slip rates for the screw dislocations.

The second dashpot of the branch represents the *Friedel process*. The threshold of this dashpot, the Friedel stress τ_{FR} , is determined by selecting the largest of the additional stresses that can be provided by the potential strengthening sources discussed in section 4.3.1. These stresses are calculated via equations (4.14) and (4.21) by the substitution of the maximum resistance forces (equations (4.22), (4.24), (4.27) and (4.31)) that a dislocation can experience during particle shearing. The critical line tension in equation (4.14) is calculated by equations (4.48) and (4.49), which

are the modified version of De Wit-Koehler model with outer cut-off radii equal to the mean planar particle spacing L_{cc} . The forward activation energy of the process is also determined by the strengthening source that determines τ_{FR} . Now, the average velocity of the edge dislocations between two successive arrests at particles can be defined via equation (4.68):

$$\bar{v}_{F,e}^{\alpha} = L_{cc} v_G \left(\frac{\hat{F}_e}{8\Gamma_{c,e}} \right)^{1/2} \exp \left(-\frac{\Delta G_{F,e}^{\alpha}}{kT} \right) \left[1 - \exp \left(-\frac{|\tau_{2,e}^{\alpha}| b L_{cc}^2}{kT} \right) \right] \text{sign}(\tau_{2,e}^{\alpha}). \quad (4.113)$$

Having defined the average velocity of the edge dislocations, the slip rate by the Friedel dashpot for edge dislocations can be calculated by the same formulation as equation (4.112). The same procedure is repeated for the screw dislocations as well.

The dashpot system for the edge dislocations, cf. figure 4.12, contains an additional dashpot in series with the parallel groups of dashpot for the incorporation of the *climb* of dislocations over particles, described here by the thermally activated detachment model [152]. The detachment energy and the detachment threshold stress are given by equations (4.41) and (4.42), respectively. The average velocity of the edge dislocations which is governed by the thermal detachment is calculated by

$$\bar{v}_{C,e}^{\alpha} = L_J \frac{3D_l}{b^2} \exp \left(-\frac{E_{d,e}^{\alpha}}{kT} \right) \left[1 - \exp \left(-\frac{|\tau_{eff,e}^{\alpha}| b L_{cc}^2}{kT} \right) \right] \text{sign}(\tau_{eff,e}^{\alpha}). \quad (4.114)$$

Note that this equation slightly differs from the slip law proposed by [152]. L_J , the average distance to be traveled after the detachment from a particle until the next encounter with another particle, is approximated by an effective travel distance L_{cc}^2/λ_c if $\tau_{FR} < \tau_{OR}$. Otherwise, it is taken as equal to L_{cc} . The contribution of the climb dashpot to the slip rate of the second branch is then calculated via

$$\dot{\gamma}_{C,e}^{\alpha} = \rho_{m,e}^{\alpha} b \bar{v}_{C,e}^{\alpha}. \quad (4.115)$$

For screw dislocations, the motion out of the slip plane is referred to as *cross-slip* and is omitted here. Note that climb of the edge dislocations over the particles is a diffusional process, which introduces a real time dependency into the constitutive rule through the diffusion constant and is assumed to determine the overall crystallographic slip rate of a slip system at low stress levels.

In the proposed constitutive model, the rate of each individual process, as represented by the dashpots in figure 4.12, is governed by the thermal activation at the level of the branch stresses (i.e. τ_1^{α} and τ_2^{α}) that are lower than the dashpot resistances. At such low stress levels, the total slip rate is controlled by the slip rate of the climb dashpot. When τ_2^{α} is larger than the particle resistance (namely τ_{OR} or τ_{FR}), the slip behavior becomes similar to that in a particle-free material and a further increase in the applied stress is carried only by the resistance arising from the dislocation-dislocation interactions. As τ_1^{α} exceeds s^{α} , the dislocation motion falls into the so-called *viscous drag* regime and τ_{eff}^{α} does work against the viscous drag forces only.

4.6 Analysis of the new model for crystallographic slip

4.6.1 Pure metals

Two different constitutive formulations for slip systems in pure fcc metals, one of which is equation (4.76) proposed by [13–16] and the other is suggested in this work through equations (4.100), (4.101) and (4.106), are compared at a single slip system level in figure 4.13 for the material parameters given in tables 4.2 and 4.3. Clearly equation (4.76) has no upper bound for the slip rate. This contradicts the fact that the speed of sound limits the maximum velocity that dislocations may attain and thereby imposes an upper bound on the shear rate. At stress levels above the slip resistance, which is set to 15 MPa in this example, the stress sensitivity of the shear rate is large, which deviates from the linear stress-strain rate relation found in the viscous drag regime (assuming the changes in the dislocation density have a negligible effect on the shear rate). Contrarily, the new flow rule which is developed by considering the influence of viscous drag forces on the mobility of dislocations does have an upper bound as seen in figure 4.13 and is also valid at stress levels that are larger than the crystallographic slip resistance provided by dislocation-dislocation interactions.

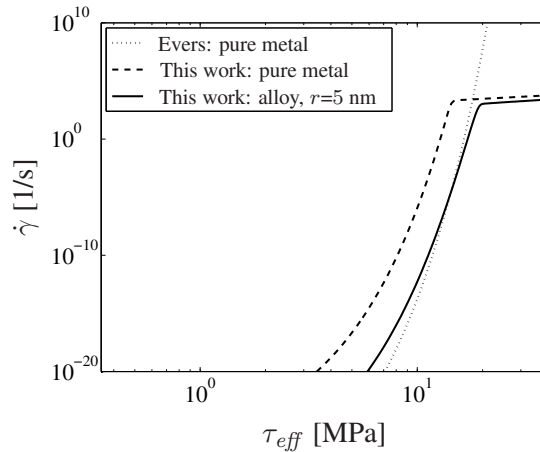


Figure 4.13: Comparison of the slip laws proposed by [13–16] and in this work.

4.6.2 Alloys: without dislocation climb

The thin films considered in this work are composed of an Al-Cu alloy. As mentioned in section 4.2, the material essentially contains incoherent θ phases, possibly accompanied by semicoherent θ' particles. It is next assumed that the material contains only semicoherent particles with an average radius of 5 nm, which have coherent and fully incoherent interfaces. The incoherent interfaces can have a lattice misfit with the matrix that is large enough to accommodate dislocations, while along the coherent surfaces a stress field can exist due to the elastic distortions of the matrix triggered by the in-plane lattice misfit. The surface energy of the incoherent faces is so high that shearing of the particle is possible only at large stresses, before which the Orowan process intervenes. The contributions of the chemical hardening and the coherency strains to the particle strength $\hat{\tau}$ are calculated over a range of particle radii at a constant volume fraction by using equations (4.21), (4.22) and (4.27) and plotted in figure 4.14a for edge dislocations and in figure 4.14c

Table 4.2: Parameters used to study the typical behavior of flow rules for a single slip system.

r	5	nm
f	1.2	%
$\dot{\gamma}_0$	$1 \cdot 10^{-3}$	1/s
y_0	$2r_s$	nm
s	15	MPa
$\rho_{GND,e}$	1	$1/\mu\text{m}^2$
$\rho_{GND,s}$	1	$1/\mu\text{m}^2$
$\rho_{SSD,e}$	1	$1/\mu\text{m}^2$
$\rho_{SSD,s}$	1	$1/\mu\text{m}^2$
Φ	$1 \cdot 10^{-2}$	-
m	10	-

Table 4.3: Material parameters used in this work.

Parameter	Meaning	Value	Unit	Reference
r	Average particle radius	5, 20	nm	-
f	Volume fraction	1.2%	-	-
v_G	Granato frequency	$1 \cdot 10^{11}$	s^{-1}	-
G_m	Shear modulus	26000	MPa	[70, 76]
G_p	Shear modulus	40000	MPa	[161–163]
ν_m	Poisson's ratio	0.347	-	[78]
ν_p	Poisson's ratio	0.34	-	[161, 162]
b	Burgers vector length	$2.86 \cdot 10^{-4}$	μm	[70]
b_p	Burgers vector length	$2.65 \cdot 10^{-4}$	μm	-
χ	Stacking fault energy	$166 - 200 \cdot 10^{-3}$	$\text{pJ}/\mu\text{m}^2$	[164, 165]
χ_p	Stacking fault energy	$92 \cdot 10^{-3}$	$\text{pJ}/\mu\text{m}^2$	[164, 165]
a_m	Lattice constant	$4.0417 \cdot 10^{-4}$	μm	[102]
a_p	Lattice constant	$4.04 \cdot 10^{-4}$	μm	-
$ \varepsilon $	Lattice constant	0.57 – 5.1	%	[166, 167]
χ_s	Surface energy	$190 - 600 \cdot 10^{-3}$	$\text{pJ}/\mu\text{m}^2$	[130, 163, 167]
C_4	A constant for coherency hard.	3.9	-	-
C_5	A constant for modulus hard.	0.05	-	[119, 139]
C_6	A constant for modulus hard.	0.85	-	[119, 139]
ΔF_0	Activation energy	$30 \cdot 10^{-8}$	pJ	[159, 168]
k	Boltzmann constant	$1.38054 \cdot 10^{-11}$	pJ/K	-
T	Absolute temperature	293	K	-
k_r	Relaxation coefficient	0.94	-	-
ρ_{SSD0}	Initial SSD density	7 – 20	μm^{-2}	-
R	Disl. capture radius	1	μm	-
ϕ	Mobile frac of dislocations	$1 \cdot 10^{-2}$	-	-

for screw dislocations. Note that the lattice mismatch between the particle and the matrix does not add to the resistance against the slip of screw dislocations within the presented framework due to the straight dislocation assumption in the derivation of equation (4.27). The Orowan stress, given by equation (4.36), is also included in the figure as a reference. Two values of 190 mJ/m^2 and 600 mJ/m^2 are assigned for the surface energy χ_s and for the lattice misfit 0.57% and 5.1% are used following [167] and the references therein, with the larger values belonging to the incoherent interfaces. Figure 4.14a shows that the use of the mismatch parameter of the incoherent particle to define the Friedel stress τ_{FR} leads to very large stresses (dash-dotted curve), exceeding the Orowan stress over the whole particle size range and the upper bound τ_u (the largest stress attainable for the given particle size and volume fraction by equation (4.12)) for a particle radius larger than about 1 nm . Because of this, it can be expected that gliding dislocations on a slip plane that intersects a θ' particle at its incoherent faces cannot shear the particle but can pass it by the Orowan process.

For mobile edge dislocations penetrating into a semicoherent particle through its coherent face, figure 4.14a-b shows that the lattice misfit induces a larger shear resistance than chemical hardening. The Orowan stress is smaller than the Friedel stress for particles with a radius r larger than about 12 nm (for which $\hat{F}/2\Gamma_c$ is about 1 in figure 4.14b). For screw dislocations, the shear resistance provided by chemical hardening is always smaller than the Orowan stress and $\hat{F}/2\Gamma_c$ is less than 1, cf. figure 4.14c-d. The additional strength against particle shearing offered by chemical hard-

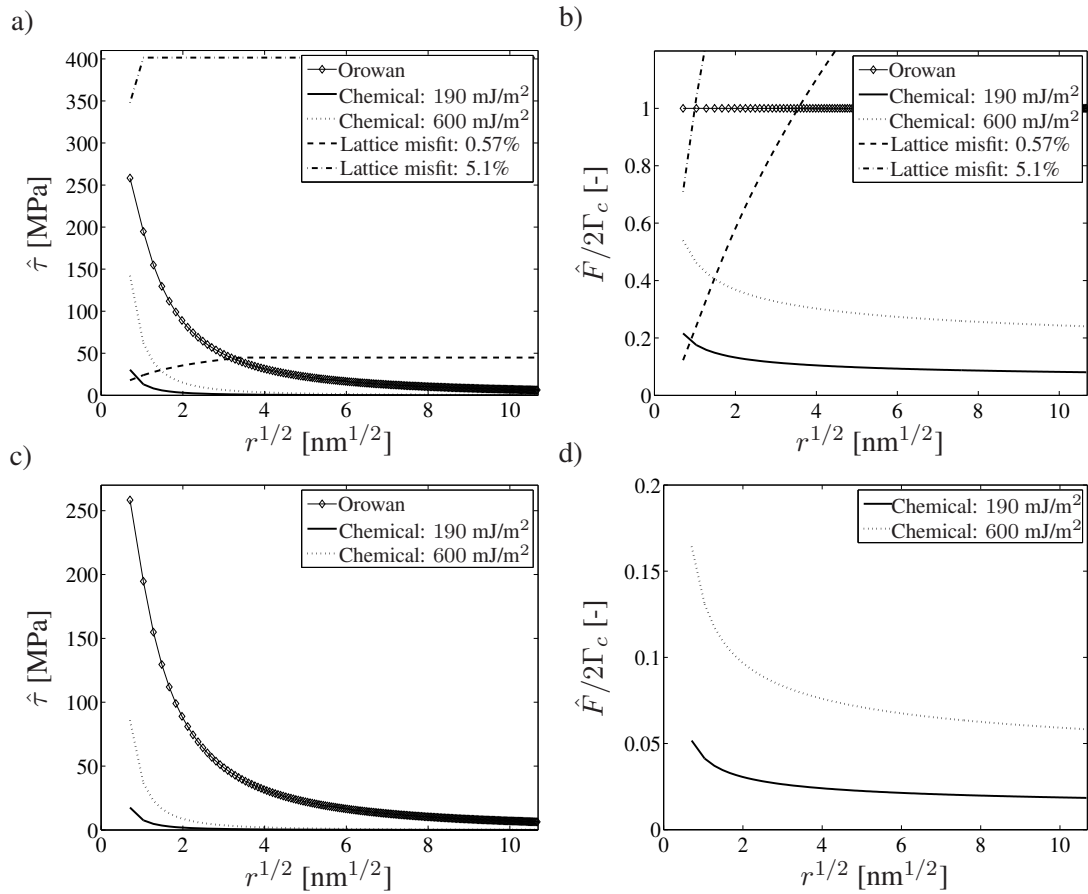


Figure 4.14: The particle resistance $\hat{\tau}$ and the corresponding strength measure $\hat{F}/2\Gamma_c$ due to chemical hardening and lattice mismatch: (a)-(b) for edge dislocations and (c)-(d) for screw dislocations. The Orowan stress is taken equal for edge and screw dislocations.

ening, stacking fault hardening, hardening due to the modulus mismatch and the lattice mismatch between the matrix and the particle are calculated via equations (4.21), (4.22), (4.24), (4.27) and (4.31) by using the properties of coherent particles (i.e. chemical energy and lattice mismatch), see figure 4.15a. It is found that the lattice mismatch constitutes the largest contribution to the shear resistance of particles in case of edge dislocations for particle radii above about 1 nm. Hence, it controls the Friedel stress $\tau_{FR,e}$ of coherent particles for edge dislocations. The particle size corresponding to the peak aged condition is visible in figure 4.15b at around 12 nm, after which the Orowan mechanism starts to operate. For mobile screw dislocations, the Friedel stress $\tau_{FR,s}$ originates alternatively from the stacking fault strengthening and the modulus mismatch depending on the particle size. Yet, $\tau_{FR,s}$ is always smaller than the Orowan stress and $\hat{F}/2\Gamma_c$ is always smaller than 1, see figure 4.15c-d. Therefore, one may conclude that the additional strength provided by semicoherent particles levels between the strengthening due to small coherent particles (which are overcome by the Friedel process) and the strengthening due to large coherent particles or incoherent particles (which are passed by the Orowan mechanism).

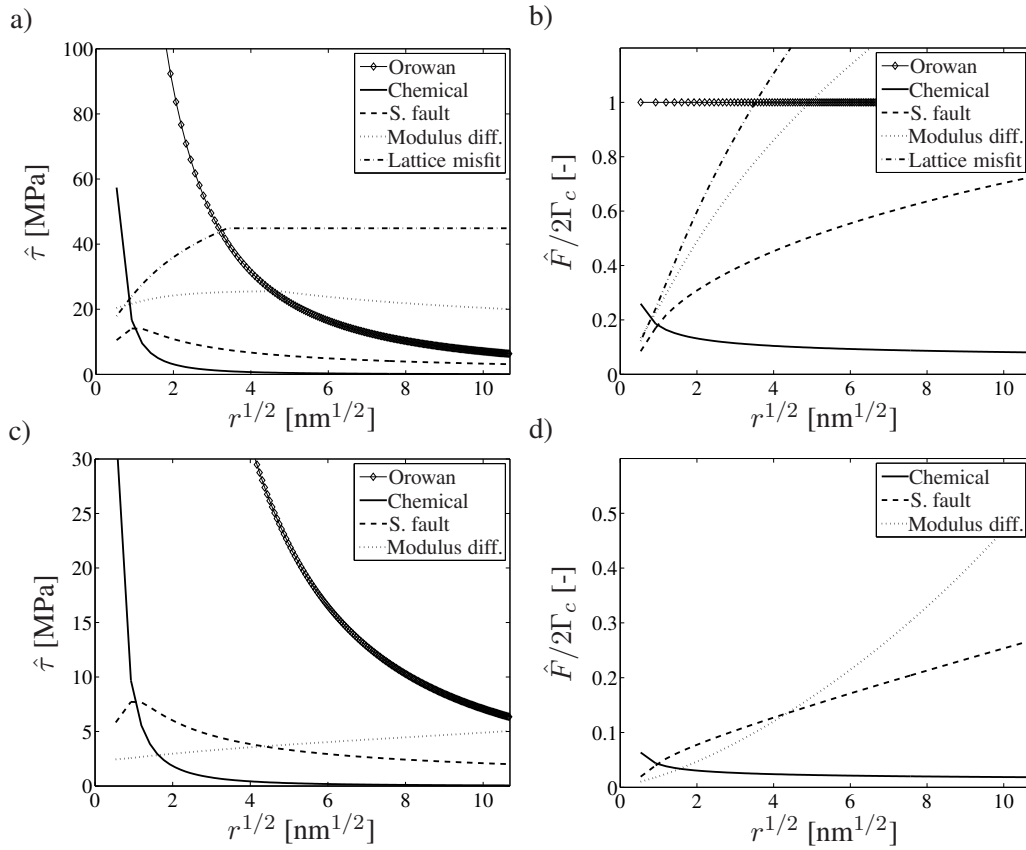


Figure 4.15: The particle resistance $\hat{\tau}$ and the corresponding strength measure $\hat{F}/2\Gamma_c$ due to chemical hardening, stacking fault hardening and mismatches in the lattice constant and shear modulus of the particle and the matrix: (a)-(b) for edge dislocations and (c)-(d) for screw dislocations. The Orowan stress is taken equal for edge and screw dislocations.

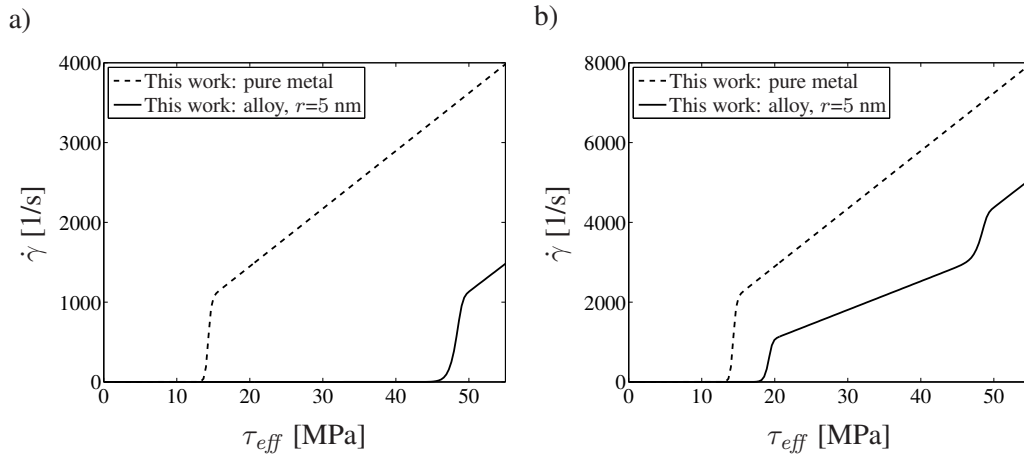
Crystallographic slip rates are calculated via equations (4.100)-(4.107) for a pure metal and via equations (4.100), (4.108)-(4.115) for an alloy having coherent particles with $r = 5$ nm, see figure 4.16. The material parameters used in the calculations are given in tables 4.2 and 4.3. Some

Table 4.4: Several parameters that are calculated and used in the slip rate equations for $r = 5$ nm.

	Edge dislocations	Screw dislocations	
\hat{F}	$8.48 \cdot 10^{-4}$	$3.11 \cdot 10^{-4}$	μN
Γ_c	$6.35 \cdot 10^{-4}$	$1.85 \cdot 10^{-3}$	μN
$\hat{F}/2\Gamma_c$	0.67	0.08	-
η_0	0.15	0.41	-
τ_{FR}	37.82	5.62	MPa
τ_{OR}	75.05	75.05	MPa
τ_d	12.47 [†]	-	MPa

[†] Calculated by equation (4.43). The description of the detachment threshold (equation (4.42)) in the original work [152] yields a larger value, 25.61 MPa.

resulting quantities necessary to interpret figure 4.16 are listed in table 4.4. The Friedel stress τ_{FR} for edge dislocations, which originates from the stress fields due to the lattice misfit (cf. figure 4.15a), equals about 37.82 MPa, which is smaller than the Orowan stress $\tau_{OR} = 75$ MPa, cf. table 4.4. The Friedel stress τ_{FR} for screw dislocations is provided by the stacking fault strengthening (see figure 4.15c) and is about 5.62 MPa, smaller than τ_{OR} . Thus, dislocations overcome the particles via the Friedel mechanism. η_0 is smaller than 0.4 for edge dislocations and around 0.4 for screw dislocations, which justifies the use of FF statistics, i.e. the treatment of the particles as point-like obstacles.

**Figure 4.16:** Comparison of constitutive laws for slip systems in pure metals and particle strengthened alloys ($r = 5$ nm): a) Edge dislocations only. b) Edge and screw dislocations.

In figure 4.16a, the slip rates of the edge dislocations are plotted. For pure metals, there is a transition from thermally activated dislocation glide to viscous glide around 15 MPa, which is the value assigned to the slip resistance arising from dislocation-dislocation interactions, s . For alloys, this transition shifts to larger stresses by an amount about equal to the Friedel stress for the edge dislocations. In figure 4.16b, the total slip rate is plotted. Note that there is still one transition of the dislocation glide regime around s for pure materials since the resistance provided by dislocation-dislocation interactions is taken equal for edge and screw dislocations while for alloys, there are

two transition regions. The first transition, which occurs around 20 MPa is attributed to the screw dislocations, for which the Friedel stress $\tau_{FR,s}$ ($= 5.62$ MPa) is relatively small. As the effective stress is increased further, the velocity of the mobile screw dislocations will be limited by the viscous drag force while the mobile edge dislocations are still in the jerky glide regime. Around $\tau_{eff} = s + \tau_{FR,e}$, the second transition occurs, after which all mobile dislocations slip in the viscous glide regime.

The slip rates of edge and screw dislocations and the total slip rate are shown in figure 4.17 for two different particle sizes. For $r = 5$ nm, both edge and screw dislocations overcome the particles by the Friedel mechanism since the Friedel stress is less than the Orowan stress, cf. table 4.4. Because the Friedel stress is considerably less for screw dislocations and the climb of edge dislocations is not considered, the screw dislocations are more mobile than the edge dislocations, which allows them to accommodate almost all of the total slip rate at low and moderate stress levels. The contribution of the edge dislocations to the total slip rate becomes significant only at high stresses, at which the screw dislocations move already in the viscous drag regime. Note that below 20 MPa, the contribution of the edge dislocations is almost zero. For $r = 20$ nm, edge dislocations can pass the particles only by bowing around them, i.e. via the Orowan mechanism since $\tau_{OR,e} < \tau_{FR,e}$, see table 4.5. For screw dislocations, the Friedel stress is still smaller than the Orowan stress, hence they continue gliding by shearing the particles on their slip path. Since $\tau_{FR,s}$ is much less than the Orowan stress for the edge dislocations, the total slip rate still mainly results from the screw dislocations.

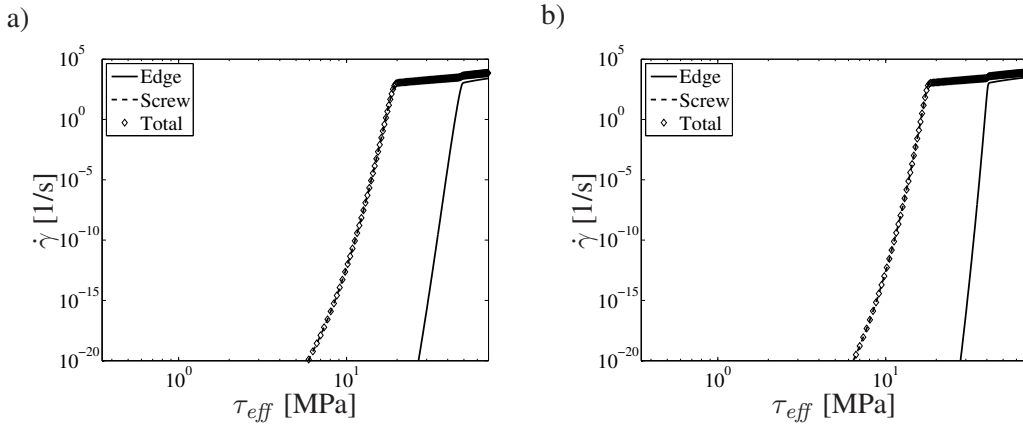


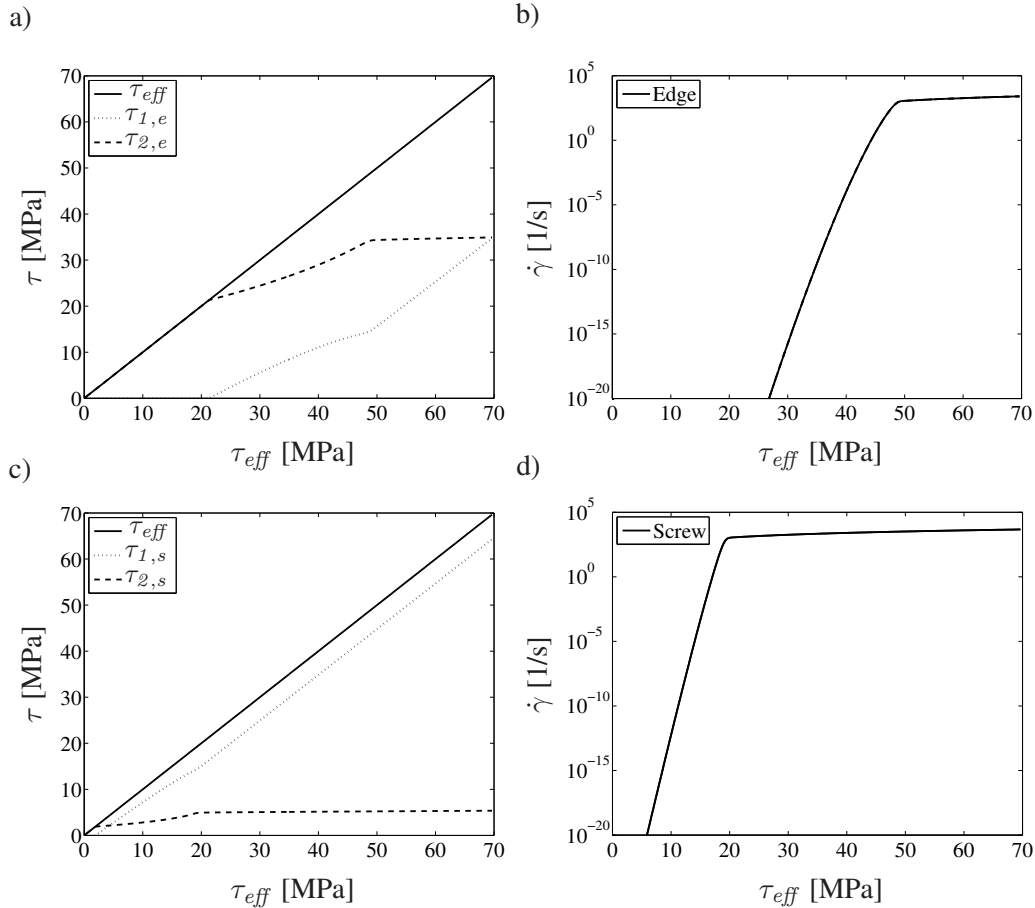
Figure 4.17: Slip rate ($\dot{\gamma}$) versus the effective resolved shear stress (τ_{eff}) for edge dislocations and screw dislocations for particle sizes (a) $r = 5$ nm and (b) $r = 20$ nm. Dislocation climb is not considered.

Figure 4.18 shows the distribution of the effective resolved shear stress between the branches of the dashpot system in figure 4.12 and the resulting slip rates of the dashpots, representative for the individual overcoming mechanisms discussed in the previous sections. It is seen in figure 4.18a that for edge dislocations, up to about 20 MPa, the effective stress is fully sustained by the particles, i.e. the second branch. Meanwhile, since the stress in the first branch, $\tau_{1,e}$ is almost zero (and also climb of edge dislocations is ignored), the total slip rate of edge dislocations is also negligible, cf. figure 4.18b. As the effective stress is further increased, the first branch also starts carrying load. The dashpots in both branches yield slip rates in a compatible manner so that the net total slip rate increases. At a sufficiently large stress level, i.e. equal to $\tau_{2,e}$ for edge dislocations (for $r = 5$ nm), in the second branch, the Friedel dashpot is saturated and the additional increase in the load

Table 4.5: Several parameters that are calculated and used in slip rate equations for $r = 20$ nm.

	Edge dislocations	Screw dislocations	
\hat{F}	$3.39 \cdot 10^{-3}$	$6.55 \cdot 10^{-4}$	μN
Γ_c	$1.41 \cdot 10^{-3}$	$2.33 \cdot 10^{-3}$	μN
$\hat{F}/2\Gamma_c$	1.21	0.14	-
η_0	0.1	0.32	-
τ_{FR}	44.87	3.67	MPa
τ_{OR}	26.43	26.43	MPa
τ_d	4.39^\dagger	-	MPa

[†] Calculated by equation (4.43). The description of the detachment threshold (equation (4.42)) in the original work [152] yields a larger value, 9.02 MPa.

**Figure 4.18:** Branch stresses and the individual contributions of different processes to the slip rate of edge and screw dislocations for $r = 5$ nm.

will be carried only by the dashpot representing the dislocation-dislocation interactions. A similar explanation holds for the screw dislocations in figures 4.18c-d. Note that for screw dislocations, the fraction of the stress carried by the second branch is noticeably smaller than that for edge dislocations, since $\tau_{FR,s}$ is relatively small.

Figures 4.18a-d show the behavior of a slip system for particles of 5 nm radius. Similar curves can be obtained for different particle sizes (e.g. figure 4.17b), for which the type of the particle overcoming mechanism (i.e. the Orowan or Friedel mechanism) and the main source of the strength in case of the Friedel mechanism can be determined from figures 4.15a-d. For larger and stronger coherent particles, the Orowan mechanism will become active. In case of incoherent particles, the Orowan process will be the only particle overcoming mechanism (in the absence of dislocation climb).

This study showed that when the second phase particles are considered to be of coherent type and dislocation climb is ignored, the total slip rate of a crystallographic system is mainly dictated by the screw dislocations within the presented framework. For screw dislocations, the set of equations used to calculate the threshold stress for the Friedel mechanism always lead to values smaller than that of the Orowan stress. Hence, they always overcome coherent particles by shearing them regardless of the properties of particles, i.e. their size and volume fraction. Moreover, the magnitudes of the Friedel stress for screw dislocations are low compared to those for edge dislocations and the slip resistance due to the dislocation-dislocation interaction. Therefore, it may be stated through equation (4.100) that coherent particles do not provoke a noticeable strengthening according to the presented framework. On the contrary, in case of incoherent particles, the stress barrier for the particle circumvention is the same for both type of dislocations and is determined by the Orowan stress, which is highly sensitive to particle properties and can assume values up to hundreds of MPa.

4.6.3 Alloys: with dislocation climb

Within the current framework, the rate of climb of edge dislocations is limited by the thermally activated detachment from the attractive particles. An important parameter herein is the relaxation constant k_r and it determines the detachment threshold stress as well as the activation energy for the thermal detachment. In figure 4.19, the threshold stress (τ_d) and the activation energy (E_d) at zero effective shear stress are plotted for three different values of k_r for a range of particle sizes. Note that τ_d decreases with particle size following the reduction of the Orowan stress while E_d increases. At a constant particle size and volume fraction, the detachment stress and the detachment energy at zero stress decrease with increasing k_r in line with equations (4.41) and (4.42).

The total slip rates that are calculated at slip system level incorporating the contribution of the climb of edge dislocations are shown in figure 4.20a-b for two size of coherent particles (with a finite degree of attractive interaction). In these figures, the slip rates of the parallel dashpot groups for edge and screw dislocations are also explicitly shown. Figure 4.20a shows that the slip rate of the climb dashpot adds to the crystallographic slip rate at low stress levels depending on τ_d and k_r , leading to values of the total slip rate that are larger than when the dislocation climb is neglected (cf. figure 4.17). Note that the slip rate controlled by the thermally activated detachment is highly sensitive to k_r values: the lower k_r , the smaller the slip rate limited by climb since the detachment barrier increases with decreasing k_r . Rösler and Arzt [152] studied the creep of an Al alloy with oxide dispersions over a temperature range of 573-773 K by using the thermally activated detachment model with an estimated k_r value of 0.74. However, such small k_r values will lead to a negligible contribution of the dislocation climb to the overall slip rate due to the large threshold stress and the detachment energy, particularly at low temperatures considered in this work. In the rest of this work, k_r is set equal to 0.94, the value determined by [145] as the critical value marking the change of the rate limiting barrier from the thermally activated detachment from particles to the energy barrier related to the climbing process or vice versa. The effect of particle

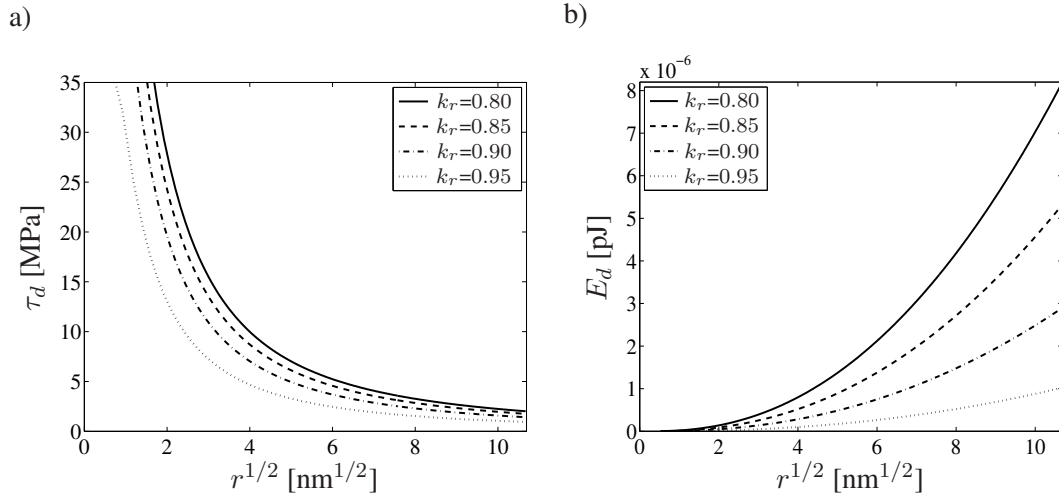


Figure 4.19: Variation of the detachment stress (a) and the detachment energy at zero stress (b) with particle radius for three different values of the relaxation parameter k_r at constant volume fraction.

size on the slip rate limited by climb is presented in figure 4.20. Although the detachment threshold is reduced with increasing particle size, the rate of dislocation climb noticeably decreases due to increasing detachment energy, see figure 4.19.

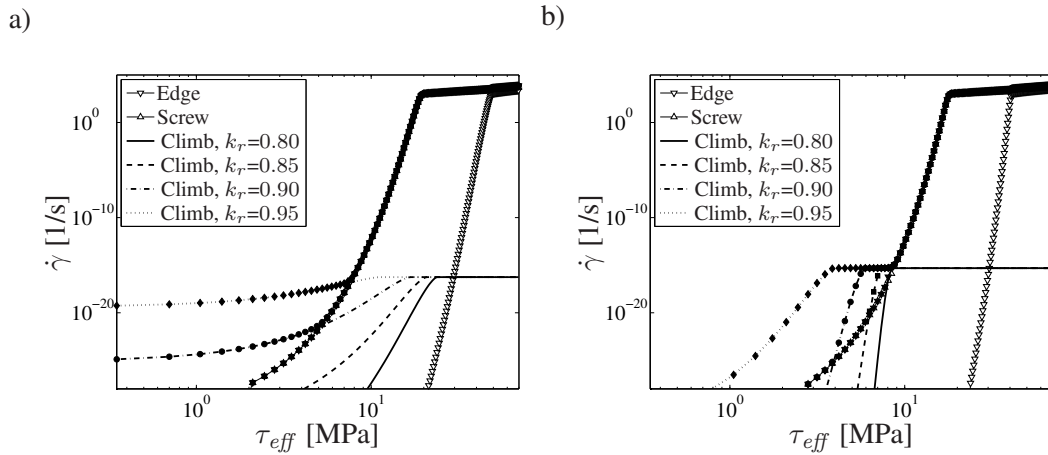


Figure 4.20: Slip rate versus effective shear stress: a) $r = 5$ nm. b) $r = 20$ nm. *Edge* and *Screw* denote the parallel dashpot groups for edge and screw dislocations, respectively, while *Climb* stands for the climb of edge dislocations for different values of k_r . The closed markers denote the overall slip rates.

Another important parameter that controls the climb rate is the diffusion rate of vacancies. The original work on the detachment controlled dislocation climb [152] focuses on a range of temperatures that can be considered as elevated temperatures. At high temperatures, the diffusion of vacancies occurs mainly through the lattice and the rate of the diffusion can be described by an Arrhenius type equation as $D_{eff,l} = D_{0,l} \exp(-Q_l/kT)$ where $D_{eff,l}$ is the coefficient of effective lattice diffusion, $D_{0,l}$ is a pre-exponential coefficient and Q_l is the activation energy. At low temperatures, however, lattice diffusion is rather slow: with the pre-exponential coefficient and activation energy for pure Al [106] given in table 4.6, $D_{eff,l} \approx 8.2 \cdot 10^{-18} \mu\text{m}^2/\text{s}$ at room tem-

Table 4.6: Pre-exponential coefficients and activation energies for different diffusion mechanisms.

Diffusion type	D_0	Q [eV] #	Reference
Lattice*, Al	$1.7 \cdot 10^8$	1.48	[106]
	$1.1 \cdot 10^7$	1.26	[169]
	$5 \cdot 10^7$	$1.47 \cdot 10^{-3} T_m$	[170, 171]
	$7.5 \cdot 10^6$	1.32	[172]
	-	1.48	[173]
	-	1.26 – 1.48	[174]
Lattice*, Al-Cu	$6 \cdot 10^2$	1.04	[172]
	-	1.22 – 1.31	[174]
Core†, Al	$7 \cdot 10^{-1}$	0.85	[106]
	53	$1.08 \cdot 10^{-3} T_m$	[170, 171]
	-	0.8 – 0.9	[173]
Grain boundary‡, Al	$5 \cdot 10^4$	0.87	[106]
	$1.5 \cdot 10^4$	$7.7 \cdot 10^{-4} T_m$	[170, 171]
	-	0.5 – 0.7	[173]
Interface, Al-Al ₂ O ₃	-	0.9 – 1	[173]

* For lattice diffusion, $D_{0,l}$ is in $\mu\text{m}^2/\text{s}$.

† For core diffusion, $D_{0,c} = A_c D_{0,l}$ (in $\mu\text{m}^4/\text{s}$) with the effective core diffusion area $A_c = 4b^2$.

‡ For grain boundary diffusion, $D_{0,g} \approx \delta_g D_{0,l}$ (in $\mu\text{m}^3/\text{s}$) with the effective width of the grain boundary $\delta_g = b$.

T_m is the melting temperature.

perature. Consequently, little material transport occurs via lattice diffusion. Therefore, based on the hypothesis that the anelastic deformation recovery observed over a longer period of time is the cumulative result of the diffusional processes occurring at the micro level, i.e. through dislocation climb, a considerably larger effective diffusion constant is necessary.

At low temperatures, the diffusion rates may be effectively enhanced via the so-called *short-circuit paths*, especially in case of small material dimensions. These paths can be the surfaces, interfaces, grain boundaries or dislocations available in the material [171, 173, 175] depending on the temperature and properties such as grain size and geometrical dimensions, e.g. the thickness. Self diffusion through the core of dislocations (pipe diffusion) is much faster than diffusion through the lattice due to its lower activation energy, around 0.85 eV [106, 173, 176], and it can remarkably improve the rate of mass transport within the material. The core diffusion coefficient is coupled to the dislocation density and its simplest form is given by $D_{eff,c} = D_{0,c} \exp(-Q_c/kT) \rho_c$ where $D_{eff,c}$ is the effective core diffusivity, $D_{0,c}$ is a pre-exponential coefficient, Q_c is the activation energy and ρ_c is the density of dislocations contributing to core diffusion. Reasonable values for the dislocation densities for thin films are reported to be typically less than $100 \mu\text{m}^{-2}$ for thin film conductors [177]. Hence, although the core diffusion coefficient ($1.7 \cdot 10^{-15} \mu\text{m}^2/\text{s}$, see table 4.7) at room temperature is larger than the coefficient for lattice diffusion by many orders of magnitude, it is not large enough to produce slip rates that may cause noticeable changes in the macroscopic deformation state of the material. Grain boundaries can also serve as fast diffusion paths. The coefficient of grain boundary diffusion is related to the grain size by $D_{g,eff} = D_{0,g} \exp(-Q_g/kT)/L_g$, where $D_{g,eff}$ is the coefficient of effective grain boundary diffusion, $D_{0,g}$ is the pre-exponential

Table 4.7: Effective diffusion coefficients for different mechanisms at room temperature.

Diffusion type	D_{eff} [$\mu\text{m}^2/\text{s}$]	Reference
Lattice, Al	$8.2 \cdot 10^{-18}$	[106]
Lattice, Al-Cu	$8.9 \cdot 10^{-16}$	[172]
Core*, Al	$1.7 \cdot 10^{-15}$	[106]
Grain boundary [†] , Al	$1.4 \cdot 10^{-9}$	[170, 171]
Interface [‡] , Al-Al ₂ O ₃	$7.5 \cdot 10^{-12}$	[173]

* For $\rho_c = 1 \mu\text{m}^{-2}$.

[†] For $L_g = 10 \mu\text{m}$ and $Q_g = 0.7 \text{ eV}$.

[‡] $D_{0,i}$ is approximated by $\delta_i D_{0,l}$ with the width of interface $\delta_i \approx 1 - 2 \text{ nm}$. The diffusion coefficient is given by $D_{eff,i} = 2(1/w + 1/t)D_{0,i} \exp(-Q_i/kT)$ for a structure with a rectangular cross-section with width $w = 25 \mu\text{m}$ and thickness $t = 5 \mu\text{m}$.

coefficient, Q_c is the activation energy and L_g is the average grain size. Grain boundary diffusion is a fast process with an activation energy of 0.60 eV [106, 171, 173, 175, 176]. Similarly, interfaces, e.g. between the matrix and the oxide layer in case of Al alloys, may constitute preferential paths for diffusion with an activation energy around 0.85 eV [173]. However, grain boundaries and interfaces cannot contribute directly to the dislocation climb mechanism considered in this work unless the average grain size or the thickness is relatively small. Nonetheless, the estimated values for the coefficients of grain boundary diffusion and interface diffusion are given in table 4.7 for comparative purposes.

The solute atoms may also lead to an enhanced lattice diffusivity. The activation energy for lattice diffusion observed in Al-Cu alloys can be as low as about 1 eV [169, 172], which is much smaller than the value reported by [106] for pure Al of about 1.48 eV, cf. table 4.7. The slip rates delivered by the climb dashpot with the diffusion constants corresponding to lattice diffusion and core diffusion in pure Al and lattice diffusion in Al-Cu alloy (see table 4.7) are plotted in figure 4.21a. As will be shown in the next section, the total slip rates obtained by these three diffusion mechanisms are too low to produce any noticeable changes in the macroscopic strain state of a material.

4.7 Application in strain gradient crystal plasticity framework

The new constitutive model for crystallographic slip in particle strengthened fcc alloys is implemented in the strain gradient crystal plasticity framework of section 4.4 in the commercial finite element analysis software ANSYS. In the forthcoming sections, firstly, the capabilities of the extended model in describing creep and anelasticity in thin films are investigated by finite element simulations of a boundary value problem. Secondly, the new model is employed for the analysis of a micro-clamp beam bending experiments [7].

4.7.1 Thin film inelasticity

The effect of the climb dashpot on the macroscopic behavior of a material is investigated by simulating the displacement controlled bending of a thin cantilever beam that is made of a single

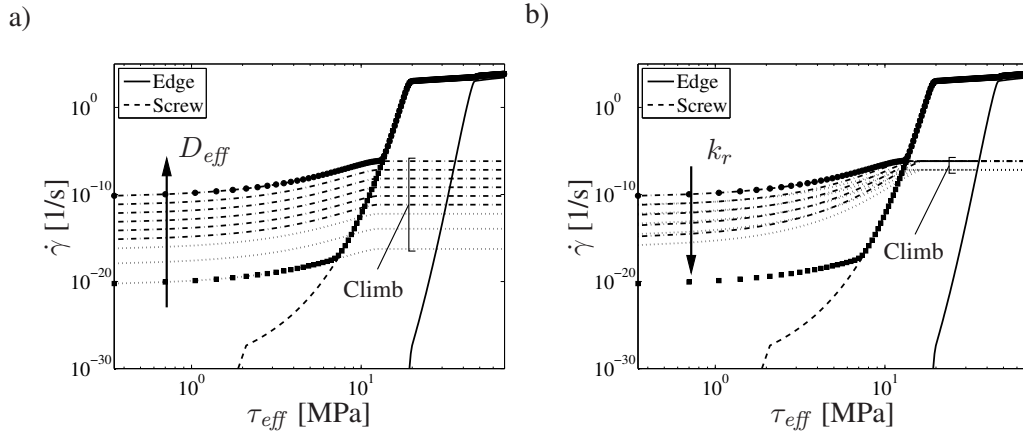


Figure 4.21: Total slip rate as a function of diffusion coefficient for $r = 5$ nm. a) Continuous and dashed curves represent the slip rate of the parallel dashpot groups for edge and screw dislocations, respectively. The dotted curves show the slip rate of the dislocation climb dashpot using lattice diffusion and core diffusion in pure Al and lattice diffusion in an Al-Cu alloy (see table 4.7). Dash-dotted curves of are climb controlled for a range of diffusion constants (10^{-12} , 10^{-11} , 10^{-10} , 10^{-9} , 10^{-8} and 10^{-7} $\mu\text{m}^2/\text{s}$) for $k_r = 0.94$. The vertical arrow shows the effect of increasing diffusion constants. The closed circle and square markers denote the upper and lower bounds of the total slip rate with the considered values of diffusion constants, respectively. b) Similar curves as those plotted in (a) can be effectively obtained by changing k_r values for the same diffusion coefficient. The dash-dotted and dotted climb curves are obtained for the diffusion constants of 10^{-7} and 10^{-8} $\mu\text{m}^2/\text{s}$, respectively, for a range of k_r : 0.90, 0.91, 0.92, 0.93 and 0.94. The vertical arrow shows the effect of increasing k_r values at a fixed diffusion constant. Upper and lower bounds for the total slip rate are the same for (a) and (b).

crystalline material oriented with its [111] direction parallel to the loading direction z , see figure 4.22a. The material is assumed to have semicoherent second phase particles with a radius of 5 nm. The initial dislocation density is $\rho_{SSD} = 1 \mu\text{m}^{-2}$ and $k_r = 0.90$. The rest of the material parameters used in the simulations are given in table 4.3. It is further assumed that the surface of the beam is passivated by an oxide layer, which is modeled as an impenetrable layer in the current formulation where dislocations are trapped at the surface. For a discussion on the boundary conditions in the SGCP framework, the reader is referred to [73]. The dimensions of the beam are given in figure 4.22a. The beam is meshed with hexagonal elements with 15, 3 and 3 elements in x , y and z directions, respectively. Detailed information on the element technology used in the present work can be found in [13–16]. The loading diagram is given in figure 4.22b. The beam is pulled down at the nodes located along the a - a' axis by an amount of $\delta_z = 1 \mu\text{m}$ in $-z$ direction within $t_1 = 1$ s. Then, the beam is kept loaded until the load is removed at $t_2 = 2$ days. Subsequently, the vertical displacement of a control node located on the tip of the beam is traced until $t_4 = 4$ days. Six simulations are conducted with a different diffusion constant each time (10^{-12} , 10^{-11} , 10^{-10} , 10^{-9} , 10^{-8} , 10^{-7} $\mu\text{m}^2/\text{s}$), leading to different slip rates of the climb dashpot (see figure 4.21a). Similar changes in the slip rate would occur by varying k_r as shown in figure 4.21b.

Simulation results are presented in figures 4.23-4.27. The time dependent displacement of the tip between t_3 and t_4 is given in figure 4.23. It is shown that the residual plastic deformation after the elastic recovery at time $t = t_3$ gets larger with increasing diffusion constant, i.e. the largest plastic deformation at $t = t_3$ grows with $D_{eff} = 10^{-7}$ $\mu\text{m}^2/\text{s}$ and is $\delta_z \approx -0.563 \mu\text{m}$ whereas the lowest value $-0.358 \mu\text{m}$ results for $D_{eff} = 10^{-12}$ $\mu\text{m}^2/\text{s}$. The amount of the anelastic recovery

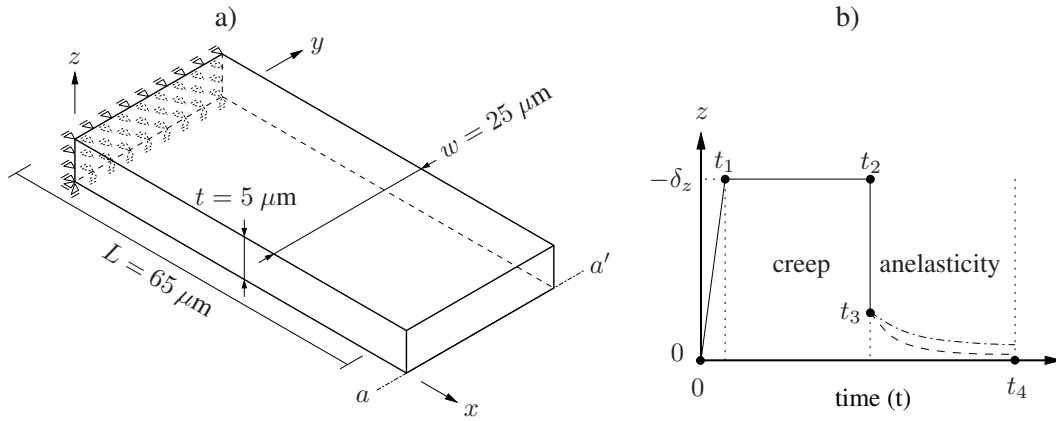


Figure 4.22: a) Dimensions and boundary conditions of the numerical model. b) Loading diagram: $\delta_z = 1 \mu\text{m}$, $t_1 = 1 \text{ s}$, $t_2 = 2 \text{ days}$ and $t_4 = 4 \text{ days}$.

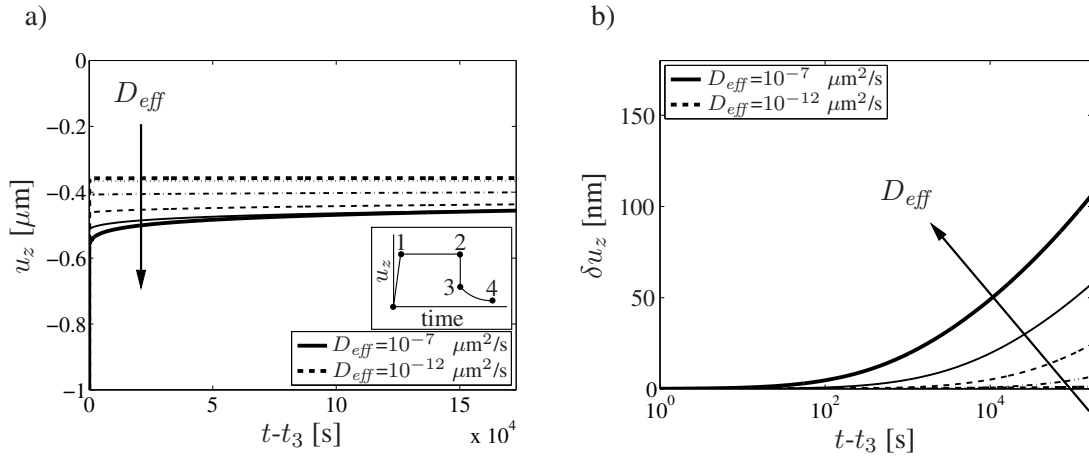


Figure 4.23: a) Tip displacement following the elastic recovery after the load removal. b) Anelastic recovery relative to the position at $t = t_3$). The arrow shows the effect of an increasing diffusion constant.

that occurs between t_3 and t_4 and the associated time constants drastically depend on the rate of the slip controlled by dislocation climb. No noticeable recovery is observed in the simulations with the smallest diffusion constant. The first visible recovery, around 1 nm , occurs for $D_{eff} = 10^{-11} \mu\text{m}^2/\text{s}$. The largest amount of recovery is found for the largest diffusion constant, yielding about $0.107 \mu\text{m}$.

Figure 4.24 shows the variation of the maximum Von Mises stress. It is seen that material starts to develop plastic strains when the maximum stress level reaches about 40 MPa . As expected, different diffusion constants have no effect on the stress during this a short loading time. In figure 4.24b, the maximum Von Mises stress is plotted over the complete time span $[0, t_4]$. During the creep over $[t_1, t_2]$, a stress relaxation occurs for all values of the diffusion constants. However, the magnitude of the relaxation is the largest for the largest diffusion constant, $D_{eff} = 10^{-7} \mu\text{m}^2/\text{s}$. During the anelastic recovery, hardly any relaxation occurs for diffusion constants smaller than $10^{-10} \mu\text{m}^2/\text{s}$ and the drop in the stress is again the largest for $D_{eff} = 10^{-7} \mu\text{m}^2/\text{s}$.

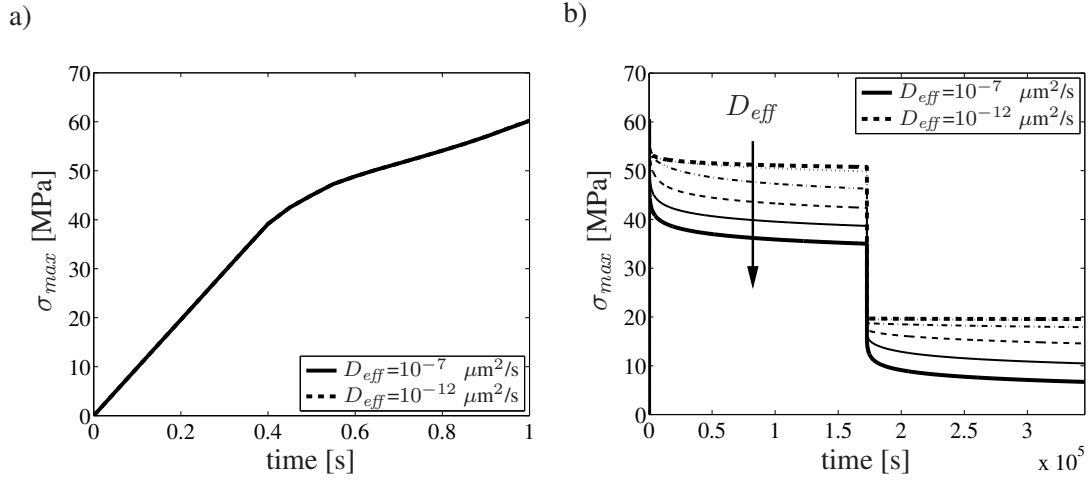


Figure 4.24: Maximum Von Mises stress: (a) during the loading, $[0, t_1]$, (b) complete time period, $[0, t_4]$. The arrow shows the effect of increasing diffusion constant.

The change in the maximum of the nodal norm of the edge and screw GNDs⁶ over time is given in figure 4.25. It shows that the density of edge GNDs is larger than that of the screw type. The vast portion of the density of GNDs is created during the loading where the effect of the diffusion constant is limited. The dislocation density increases during creep and the maximum value achieved increases with the rate of dislocation climb. The GND densities have a tendency to decrease during the anelastic recovery due to reverse slip and the magnitude of the reduction increases with the climb rate.

The overall mechanical behavior of the material during load application, creep and anelastic recovery can be clarified at the level of a single material point. In figure 4.26a, the effective resolved shear stress τ_{eff} , the elastic resolved shear stress τ_{el} and the back stress τ_b are plotted for $[0, t_4]$ on the slip system having a slip direction $1/\sqrt{2}[\bar{1}11]$ and slip plane $1/\sqrt{3}(111)$ in an integration point that is located in the region close to the fixed end of the beam. The figure shows that τ_{eff} reaches its maximum value during the loading period, in which τ_{el} and τ_b also increase significantly. During the creep between t_1 and t_2 , the back stress continues to increase due to the accumulation of plastic strains. Consequently, the elastic resolved shear stress decreases and so does the effective resolved shear stress. Figure 4.26b shows that the effective resolved shear stress and its components, e.g. τ_{el} and τ_b , hardly vary between t_3 and t_4 after the release of the beam at time t_2 . The total slip rate and its components, i.e. the contributions to the total slip rate by the parallel dashpot groups for the edge and screw dislocations and the climb dashpot, are plotted in figure 4.26c. The parallel dashpot group for the edge dislocations does not contribute to the slip rate for the given loading condition and material parameters since the Friedel stress is larger than the stress available for cutting of particles. The slip rate of the screw dislocations is relatively large and in the same order of magnitude as that of the climb dashpot for $D_{eff} = 10^{-12} \mu\text{m}^2/\text{s}$ during some fractions of the total simulation time. The total slip rate, which is the sum of the slip rates delivered by the parallel dashpot group for screw dislocations and the climb dashpot, increases with loading, achieving its maximum value in the positive direction and decreasing during the loading stage $[0, t_1]$ (the effective resolved shear stress starts to decrease because of the increasing back stress). During the creep within $[t_1, t_2]$, the total slip rate is mainly determined by the climb dashpot and

⁶ $\max ({}^n \rho_{GND,e}) = \max \left(\sqrt{\sum_{i=1}^{12} ({}^n \rho_{GND,e}^i)^2} \right)$ and $\max ({}^n \rho_{GND,s}) = \max \left(\sqrt{0.5 \sum_{i=13}^{18} ({}^n \rho_{GND,s}^i)^2} \right)$.

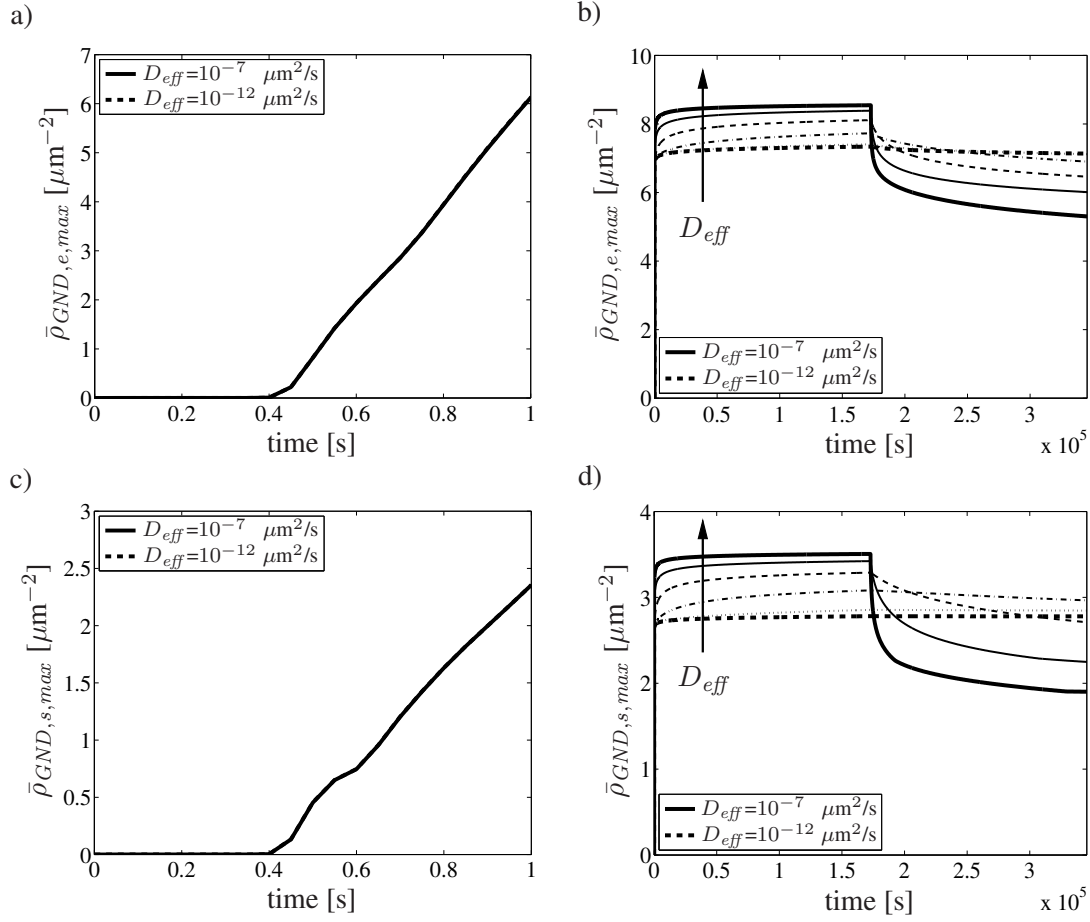


Figure 4.25: Maximum of the norm of GNDs during the loading and the total time span for edge dislocations (a,b) and for screw dislocations (c,d). The arrow shows the effect of increasing diffusion constant.

decreases. During the period $[t_3, t_4]$, since τ_{eff} is almost constant, the total slip rate also stays about the same. Figure 4.26c-d demonstrates that the slip rate of the climb dashpot calculated by using $D_{eff} = 10^{-12} \mu\text{m}^2/\text{s}$ does not significantly contribute to the overall slip rate on that slip system. The order of magnitude of the slip rate is so low that it does not allow any internal stress relaxation after the release of the beam. The same observation holds for the other slip systems in the same integration point, having sufficiently large effective resolved shear stresses. Since this also applies to the other material points, no visible deformation recovery occurs between t_3 and t_4 for $D_{eff} = 10^{-12} \mu\text{m}^2/\text{s}$.

Similarly, the variation of the effective resolved shear stress and the total slip rate over time is plotted in figure 4.27 for the same slip system in the same integration point for $D_{eff} = 10^{-7} \mu\text{m}^2/\text{s}$. The change in the resolved shear stress and its components during the loading is similar to that of the case with $D_{eff} = 10^{-12} \mu\text{m}^2/\text{s}$. However, the total slip rate is determined only by the climb dashpot and is significantly higher. During creep, the total slip rate is higher as well, and hence, τ_b attains larger values than for $D_{eff} = 10^{-12} \mu\text{m}^2/\text{s}$. Meanwhile, τ_{eff} changes its sign and so does the total slip rate. The most significant effect of the rate of the climb dashpot occurs after the release of the beam. After t_2 , a stress redistribution occurs so that the effective resolved shear stress decays to zero, cf. figure 4.27b. This is realized by the reduction of the back stress at a rate controlled by dislocation climb. Within the current formulation, the back stress can only be

reduced by decreasing the GND densities, the signed portion of the dislocations. This occurs by reverse glide of the dislocations. This phenomenon is illustrated best in figure 4.27. The reversal of the direction of the effective resolved stress by the release of the beam (such as in figure 4.27b) leads to reverse glide of the dislocations at the slip system level. If the glide rate is sufficiently large (cf. figure 4.27c), the GND densities will be reduced (see figure 4.25b), which, in turn, will lower the back stress. Together with the back stress, the elastic shear stress must also decrease so that the effective resolved shear stress vanishes, as seen in figure 4.27b. This process continues until a stress equilibrium is reached. Consequently, the macroscopic time dependent recovery will have a decreasing rate (which is controlled by the slip rate of the climb dashpot) and will cease when the total slip rate at the individual slip systems becomes too small to bring about noticeable variations in the GND densities.

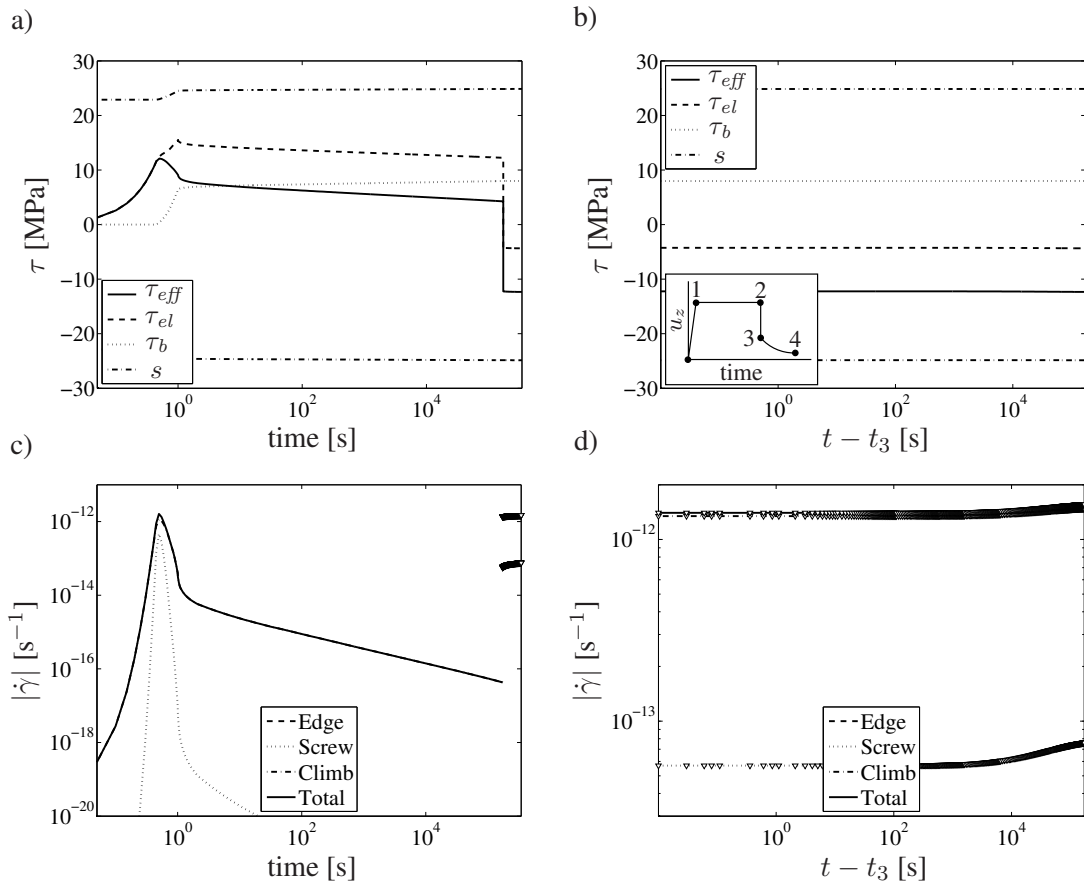


Figure 4.26: The slip resistance, effective resolved shear stress, elastic resolved shear stress and the back stress for a slip system having a slip direction $1/\sqrt{2}[\bar{1}11]$ and slip plane $1/\sqrt{3}(111)$ in an integration point located at the fixed end of the beam for $D_{eff} = 10^{-12} \mu\text{m}^2/\text{s}$: (a) over the whole time span, (b) during the anelastic recovery. The total slip rate and the individual contributions by the climb dashpot and the parallel dashpot groups for edge and screw dislocations are given in (c) and (d) corresponding to the effective resolved shear stress plotted in (a) and (b), respectively, where ∇ marks the negative values of the slip rates. Note that only the anelastic recovery period $[t_3, t_4]$ is shown in (b) and (d). The slip rate of edge dislocations are about zero and outside the figure. The total slip rate is mainly governed by the rate of dislocation climb.

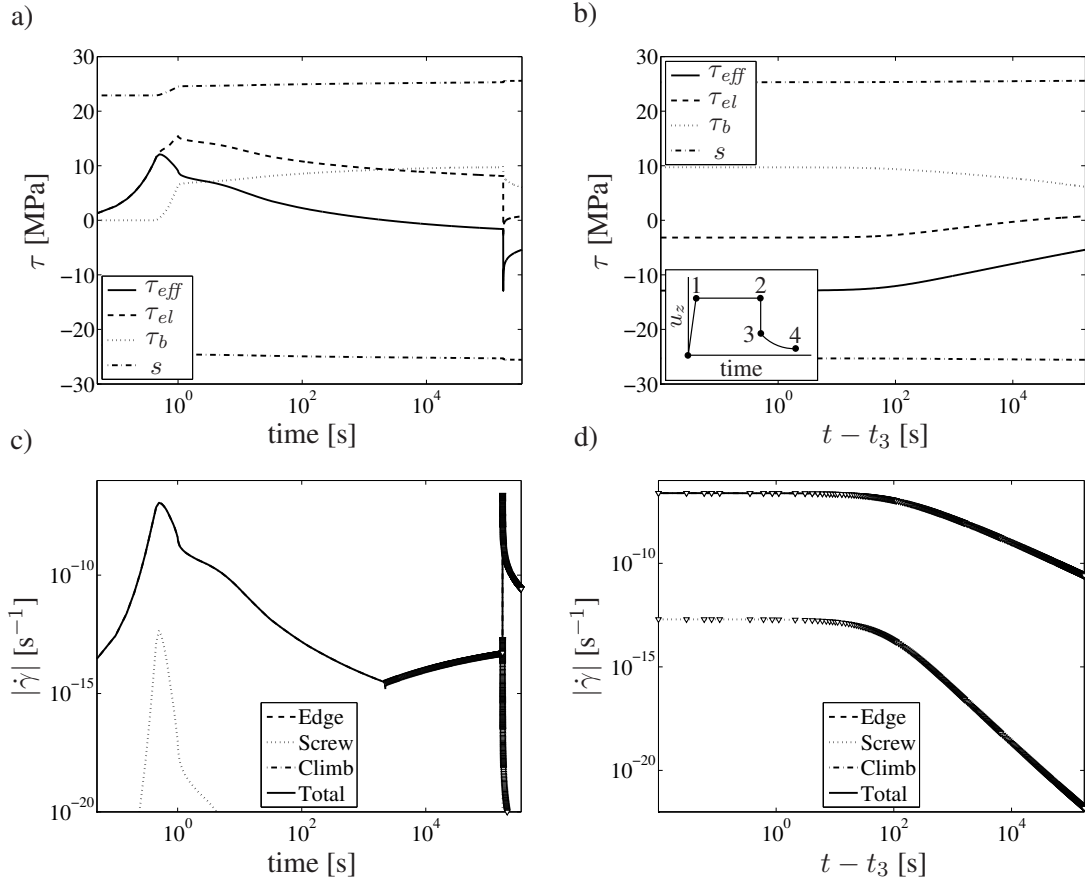


Figure 4.27: The slip resistance, effective resolved shear stress, elastic resolved shear stress and the back stress for a slip system having a slip direction $1/\sqrt{2}[\bar{1}11]$ and slip plane $1/\sqrt{3}(111)$ in an integration point located at the fixed end of the beam for $D_{eff} = 10^{-7} \mu\text{m}^2/\text{s}$: (a) over the whole time span, (b) during the anelastic recovery. The total slip rate and the individual contributions by the climb dashpot and the parallel dashpot groups for edge and screw dislocations are given in (c) and (d) corresponding to the effective resolved shear stress plotted in (a) and (b), respectively, where ∇ marks the negative values of the slip rates. Note that only the anelastic recovery period $[t_3, t_4]$ is shown in (b) and (d). The slip rate of edge dislocations are about zero and outside the figure. The total slip rate is mainly governed by the rate of dislocation climb.

During the loading, creep and anelastic recovery, the slip resistance in the slip system considered in figures 4.26a and 4.27a either stays constant or increases whereas GND densities decrease significantly during the time dependent recovery. This is because the SSD density, the unsigned fraction of dislocations in the related material point continues to increase as shown in figure 4.28.

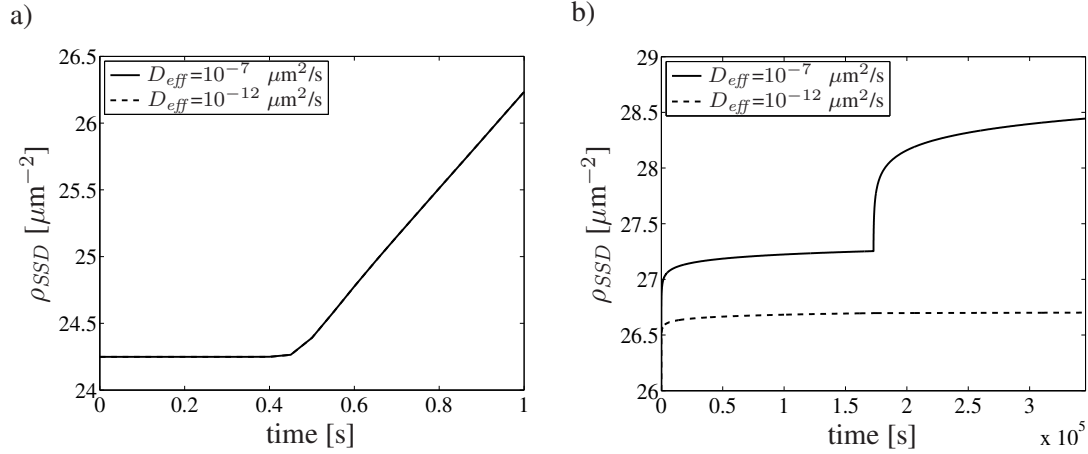


Figure 4.28: L2 norm of the SSD densities in an integration point at the fixed end of the cantilever beam: a) during the loading phase only $[0, t_1]$, b) total time span $[0, t_4]$.

4.7.2 Simulation of micro-clamp beam bending experiment

Experiment

A dedicated beam bending experiment was conducted by [7] for the measurement of anelastic strain recovery in a cantilever thin beam, see figure 4.29a. The beam was made of a polycrystalline Al-Cu [1 wt%] alloy with a thickness of about $5 \mu\text{m}$. The loading scheme is given in figure 4.29b. It was mechanically bent via a knife edge until the tip deflection reached an amount of $-\delta z = 0.875 \mu\text{m}$ within $t_1 = 10 \text{ ms}$. The magnitude of the prescribed deflection was chosen such that the stress levels will be lower than the yield strength of the material that is estimated as 180 MPa. After $t_2 = 2$ days of loading, the beam was released and the vertical position of the beam tip was recorded for $t_4 - t_2 = 6 \text{ h}$. The experimental result is shown in figure 4.30a and b. The beam showed a residual deformation of about 25 nm at t_3 , which was completely recovered between t_3 and t_4 following the release of the beam.

Simulations

The micro-clamp experiment [7] is numerically analyzed with the extended SGCP model. Figure 4.29d shows the finite element model of the beam, where different colors represent individual grains with different orientations determined from OIM measurements, cf. figure 4.29c. The hinge part of the sample is approximated by three large grains due to lack of available information. It is assumed that the material involves incoherent particles. It is assumed further that the beam surface is covered by an oxide layer, i.e. a passivated surface condition is applied. A parameter sensitivity study is done by using different values of particle radius r , relaxation parameter k_r and effective diffusion coefficient D_{eff} given in table 4.8. These are the parameters that significantly characterize the material behavior. The simulations are performed for three different values of the characteristic length scale R , i.e. $R = 1.5, 3$ and $5 \mu\text{m}$. The rest of the parameters are given in table 4.3 and elsewhere in literature [13–16]. The loading of the beam via a knife edge is idealized as a prescribed displacement as shown by arrows in figure 4.29d.

Figure 4.30a shows the residual displacement of the beam tip at about 100s after the beam release ($u_{z,r}$), since the first 100 s following the load removal was not measured in the experiment [7], and

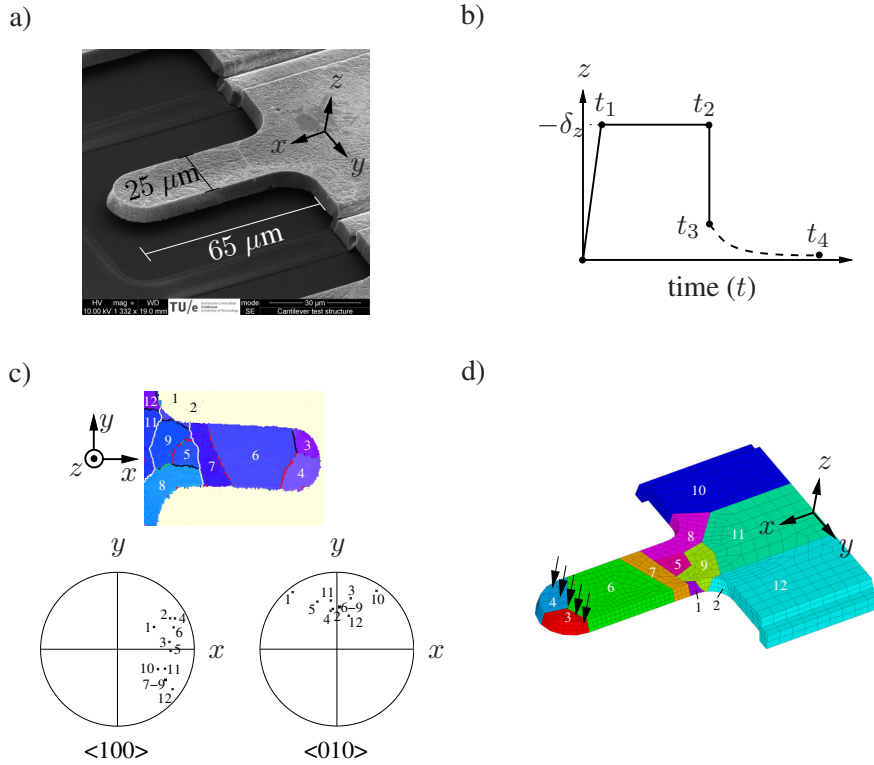


Figure 4.29: a) SEM picture of the cantilever beam used in the micro-clamp experiment [7]. b) Loading scheme: $t_1 = 10$ ms, $t_2 \approx t_3 \approx 2$ days and $t_4 - t_3 = 6$ h. c) OIM picture of the tested beam. Different colors shows individual grains with the orientations given in the pole diagrams. d) Numerical model of the beam used in the finite element simulations. Arrows show the location and the direction of the applied displacement.

the anelastic recovery (δu_z) within 6 h obtained from the simulations. As expected, the amount of the residual deformation increases with increasing k_r and D_{eff} since increasing k_r reduces the activation energy and the threshold stress for the detachment and D_{eff} is a direct multiplier for the crystallographic slip rate, see equations (4.40)-(4.43) and (4.115). The anelastic recovery is affected by k_r and D_{eff} in two ways. The reverse climb rate increases with k_r and D_{eff} . Increasing residual deformation with k_r and D_{eff} also implies larger densities of GNDs which leads to larger internal stresses provided that they are inhomogeneously distributed. Since reverse glide is

Table 4.8: Material parameters used in the simulations of figure 4.30a. "-" denotes the same value as in the first row of the table.

Set	r [nm]	k_r [-]	D_{eff} [$\mu\text{m}^2/\text{s}$]
i	5	0.93	$5 \cdot 10^{-8}$
ii	-	-	$5 \cdot 10^{-9}$
iii	-	-	$5 \cdot 10^{-7}$
iv	-	0.92	-
v	-	0.94	-
vi	3	-	-
vii	8	-	-

sustained by internal stresses, the larger the internal stresses, the larger the amount of anelastic recovery. Note that increasing particle size (r) has an opposite effect on $u_{z,r}$ and δu_z compared to increasing k_r and D_{eff} since in equation (4.41), the detachment energy at zero effective resolved shear stress depends on r . In addition, figure 4.30a shows that for a given set of material parameters, larger values of R brings the simulation results closer to the experiment result, pointing at the necessity of a back stress that is sufficiently large not only to limit the accumulation of excessive plastic strains during creep but also to provide a driving force that is large enough for strain recovery via reverse glide of dislocations.

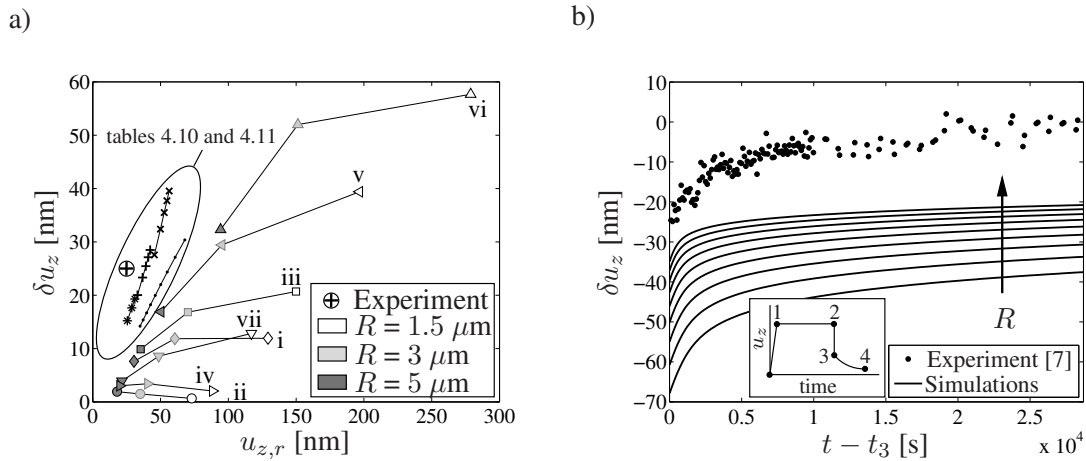


Figure 4.30: a) Parameter sensitivity study showing the anelastic displacement of the beam tip (δu_z) and the residual deformation after the beam release ($u_{z,r}$) described by the extended SGCP model. White, light gray and dark gray colors show three different sets of simulations with $R = 1.5, 3$ and $5 \mu\text{m}$, respectively. \oplus marks the experimental result [7]. See tables 4.8, 4.10 and 4.11 for the rest of markers. Lines connect the simulation results obtained by the same set of material parameters but with different R . b) The comparison of the simulation and experimental results. R takes values of $5.5, 6, 6.5, 7, 7.5, 8, 8.5, 9$ and $9.5 \mu\text{m}$. The arrow shows the effect of increasing R . See table 4.9 for the rest of material parameters.

The effect of the back stress on the time dependent material behavior is studied further by performing additional simulations with larger values of R , i.e. $R = 5.5, 6, 6.5, 7, 7.5, 8, 8.5, 9$ and $9.5 \mu\text{m}$ where r , k_r and D_{eff} are constant and given in table 4.9. The volume fraction of particles, f , is also reduced from 1.2% to 0.4% by assuming that the amount of θ phase particles are lower than what would be anticipated based on the phase diagram for Al-Cu alloys (due to different cooling rates, leading to different microstructures that are not in thermodynamical equilibrium). At a constant particle size r , a lower volume fraction leads to a lower detachment threshold stress. The difference between the Cu contents of these two volume fractions are stored in the matrix as solute atoms and/or amorphous phases which can provide additional obstructions for gliding dislocations. The simulation results are compared with the experiment in figure 4.30b. As seen in the figure, increasing R leads to a reduction of the residual deformation at the start of the anelastic recovery. However, it does not enhance the deformation recovery. Table 4.10 shows that the maximum percentage of the residual deformation that is recovered over time is around 45% and decreases with increasing R . Increasing R reduces by lowering the gradients of GND densities. This explains why even with the values of R that are outside a justifiable range, there is relatively little improvement in capturing the anelastic recovery by the SGCP model with the material parameters given in table

Table 4.9: Material parameters used in the simulations of figure 4.30b.

Parameter	Meaning	Value	Unit
r	Particle radius	4	nm
f	Particle volume fraction	0.4	%
D_{eff}	Effective diffusion constant	$5 \cdot 10^{-10}$	$\mu\text{m}^2/\text{s}$
k_r	Relaxation parameter	0.94	-
Φ	Mobile fraction of dislocation density	$5 \cdot 10^{-3}$	-
$\rho_{SSD,e}$	Initial density of edge SSDs	1	$1/\mu\text{m}^2$
$\rho_{SSD,s}$	Initial density of screw SSDs	1	$1/\mu\text{m}^2$
R	Dislocation capture radius	5.5-9.5	μm

Table 4.10: Residual displacement of the beam tip at t_3 after the release of the beam ($u_{z,r}$) and the subsequent anelastic displacement of the tip in 6 h (δu_z) for simulations with a large homogeneous diffusion constant, plotted in figures 4.30a (with marker ".") and 4.30b.

D_{eff} [$\mu\text{m}^2/\text{s}$]	R [μm]	$\bar{\rho}_{GND,max}$ [$1/\mu\text{m}^2$]	$u_{z,r}$ [nm]	δu_z [nm]	$\delta u_z/u_{z,r}$ [%]
$5 \cdot 10^{-10}$	5.5	0.49	-67.90	30.36	44.71
	6.0	0.44	-60.81	27.11	44.58
	6.5	0.40	-55.00	24.35	44.27
	7.0	0.36	-50.16	21.99	43.84
	7.5	0.33	-46.10	19.96	43.30
	8.0	0.31	-42.66	18.21	42.69
	8.5	0.28	-39.72	16.69	42.02
	9.0	0.26	-37.17	15.36	41.32
	9.5	0.25	-34.95	14.19	40.60

4.9.

The results presented in subsection 4.7.1 and in figure 4.30 show that two key ingredients are required for the prediction of the creep and anelastic behavior of the material that is comparable to the experiment result: i) a diffusion coefficient that is considerably larger than the coefficient for lattice diffusion and; ii) the storage of sufficiently large internal stresses. However, as seen in figure 4.30, the relatively large amount of dissipation of energy in each simulation prevents the recovery of a significant fraction (e.g 60%) of the residual deformation after the load removal. One way to limit the energy dissipation is the partial restraining of the plastic activity in the material. By doing so, the residual deformation of the material after the unloading can be decreased, and, more importantly, elastic energy can be conserved. In the simulations so far, a homogeneous diffusion coefficient is used for the whole material with magnitudes up to those characteristic for grain boundary diffusion. Considering that the creep behavior of the material is governed by the diffusional climb process, the use of an inhomogeneous diffusion coefficient, i.e. values that are in the order of lattice diffusion for grain interiors and of grain boundary diffusion for the regions in the vicinity of grain boundaries, would reduce the total amount of dissipated energy since grain

interiors will behave more elastically at low stress levels than for a large homogeneous diffusion constant. In this manner, additional simulations are performed to study the effect of inhomogeneous diffusion coefficients on the creep and anelastic behavior of the beam structure by using the lattice diffusion coefficient $D_{eff} = 8.9 \cdot 10^{-16} \mu\text{m}^2/\text{s}$ given in table 4.7 for grain interiors and diffusion coefficients ($D_{eff,gb}$) of $1 \cdot 10^{-9}$, $2 \cdot 10^{-9}$, $3 \cdot 10^{-9}$, $4 \cdot 10^{-9}$ and $5 \cdot 10^{-9} \mu\text{m}^2/\text{s}$ for grain boundary zones⁷ with $R = 4, 5$ and $6^8 \mu\text{m}$. The remaining parameters are given in table 4.9. The simulation results are presented in figure 4.31. It is seen in figure 4.31a that for comparable values of the residual displacements at t_3 , the amount of recovery in the simulations with $R = 4 \mu\text{m}$ is considerably increased by using an inhomogeneous diffusion constant. As shown in table 4.11, the percentages of the residual deformation that is recovered with time become as large as 70%. Furthermore, figure 4.31b indicates that the relaxation times obtained from the simulations with inhomogeneous diffusion constants are closer to the experimental result in comparison with the simulation results presented in figure 4.30b. However, a noticeable amount of permanent deformation still remains at t_4 . It can be seen in table 4.11 that the maximum of the norm of the GND densities⁹ generated in the simulations with inhomogeneous diffusion constants are larger than those of simulations with comparable residual deformations at $t = t_3$ listed in table 4.10. Hence, the magnitude of the internal stresses calculated in the simulations with inhomogeneous diffusion constants are significantly larger than those from the simulations presented in figure 4.30, since the gradients are calculated in the initial configuration. Figures 4.30a and 4.31 involve also the results of the simulations with $R = 5$ and $6 \mu\text{m}$ (with markers "+" and "*", respectively, in figure 4.30a). A larger R brings the residual deformations calculated in the simulations closer to that from the experiment. The permanent deformations at $t = t_4$ are also smaller for larger R . However, the deformation recovery proceeds at a slower rate, which is possibly due to the smaller back stresses due to the lower GND densities.

4.8 Discussion

An enhanced physically based constitutive formulation for crystallographic slip in pure fcc metals and particle strengthened fcc metals has been presented in sections 4.5.1 and 4.5.2. In figure 4.13, two distinct regimes of dislocation motion (i.e. jerky glide of dislocations and viscous glide of dislocations), obtained by the new formulation, were shown, providing a more realistic description of the material behavior, especially at high stress levels by the introduction of an upper bound for the velocity of mobile dislocations. On the contrary, the phenomenological slip law used in the original SGCP model [13–16] may lead to unrealistic crystallographic slip rates since it lacks an upper bound.

Incorporation of particles into the constitutive equations shifts the critical effective resolved shear stress by an amount equal to the particle strength, see figure 4.16. The threshold stresses for the Friedel, Orowan and climb processes determine the resistance of the individual dashpots of the

⁷In these simulations, grain boundary zones are approximated such that they extend from boundaries towards grain interiors about $1 \mu\text{m}$. The width of grain boundary zones is important as the larger the width, the larger the material volume in which there is a high plastic slip activity. However, the zones cannot be too small since the validity of the SGCP formulation becomes questionable very near the grain boundaries.

⁸Only with $D_{eff,gb}$ of $1 \cdot 10^{-9}$, $2 \cdot 10^{-9}$ and $3 \cdot 10^{-9} \mu\text{m}^2/\text{s}$ due to the convergence issues that occur when $D_{eff,gb}$ is increased further.

⁹Note that $\bar{\rho}_{GND,max}$ is a local quantity as it belongs to a node. However, it still clarifies the difference generated in the mechanical response of the beam by the use of an inhomogeneous diffusion constant.

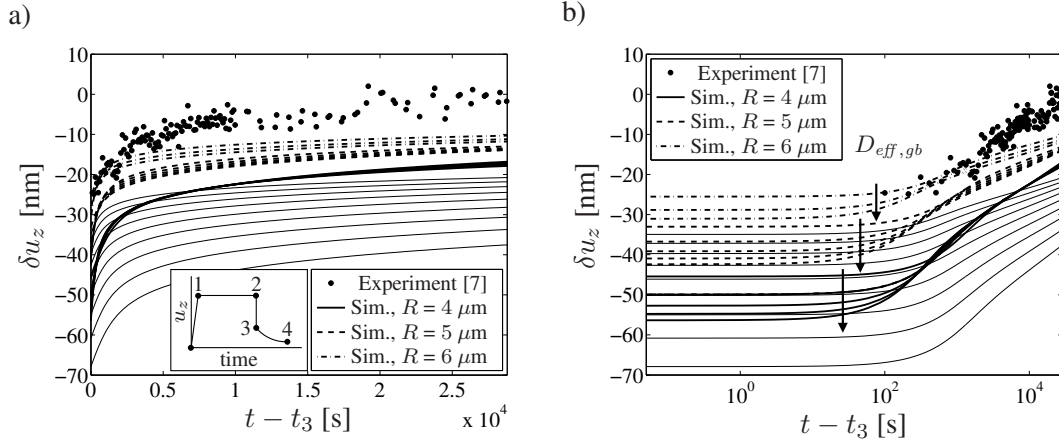


Figure 4.31: Comparison of the simulation and experimental results. $D_{eff,gb}$ assumes values of $1 \cdot 10^{-9}$, $2 \cdot 10^{-9}$, $3 \cdot 10^{-9}$, $4 \cdot 10^{-9}$ and $5 \cdot 10^{-9} \mu\text{m}^2/\text{s}$ with time on a) linear scale and b) logarithmic scale. Thin continuous lines are the simulation results plotted in figure 4.30b. The arrow shows the effect of increasing $D_{eff,gb}$.

system shown in figure 4.12 and are calculated separately for edge and screw dislocations. For screw dislocations, the present framework yields threshold stresses for the Friedel process that are *always* smaller than the Orowan stress for the whole range of relevant particle sizes, which is not the case for edge dislocations. The Friedel stress for screw dislocations is also always smaller than the threshold stresses for the Orowan and Friedel processes for edge dislocations. Therefore, since the slip resistance originating from the dislocation-dislocation interactions is the same for both dislocation types, screw dislocations govern the total crystallographic slip rate at low and moderate stress levels according to the current coupling of the slip rates of edge and screw dislocations when dislocation climb is omitted, see figure 4.17. When dislocation climb is included, at low stresses, the total slip rate is controlled by the climb of edge dislocations or by the Friedel process for screw dislocations depending on the slip rate generated.

The results of the *single crystalline* beam bending simulations show that the rate of dislocation climb affects the evolution of plastic strains in the material. As the slip rate of the climb dashpot increases, the overall crystallographic slip rate is also increased, which leads to the generation of larger densities of GNDs and, therefore, larger back stresses especially during creep. The influence of the climb rate becomes more prominent in the form of a time dependent deformation recovery following the elastic recovery after the removal of the external load. The amount of the recovery and the characteristic time scales depend on the climb rate: larger climb rates result in larger rates of reverse slip, which lead to faster degradation of GND densities and the back stress. Hence, not only a faster recovery but also a faster decay of the effective resolved shear stress occurs. The relaxation parameter k_r and the diffusion constant are important since they determine the extreme values of the climb rate for a given particle size, cf. figures 4.20 and 4.21. The relaxation parameter controls the size of the energy barrier and the threshold stress for the detachment, and hence it defines the slip rate versus τ_{eff} at stresses below τ_d , while the diffusion constant directly influences the maximum value that can be reached, see (4.114) and (4.115). Because of the lack of sufficient information about the degree of interaction between the climbing dislocations and the particles present in the material considered, k_r is fixed to a value of 0.94 and the diffusion constant is adjusted to alter the rate of climb in the finite element simulations. In the simulations, significant anelastic recovery is observed for values of the diffusion constants larger than $10^{-11} \mu\text{m}^2/\text{s}$. Compared to the given values for several diffusion paths in table 4.7, this value is considerably larger than the lattice diffusion and the core diffusion constants but close to the values that are

Table 4.11: The maximum of the norm of the GND densities ($\bar{\rho}_{GND,max}$) and the residual displacement of the beam tip ($u_{z,r}$) at t_3 and the subsequent anelastic displacement of the tip (δu_z) in 6 h that belong to the results of the simulations with inhomogeneous diffusion constants, which are plotted in figures 4.30a and 4.31.

D_{eff} [$\mu\text{m}^2/\text{s}$]	R [μm]	$D_{eff,gb}$ [$\mu\text{m}^2/\text{s}$]	$\bar{\rho}_{GND,max}$ [$1/\mu\text{m}^2$]	$u_{z,r}$ [nm]	δu_z [nm]	$\delta u_z/u_{z,r}$ [%]	Marker in figure 4.30a
$8.9 \cdot 10^{-16}$	4	$1 \cdot 10^{-9}$	0.86	-45.43	27.56	60.66	×
		$2 \cdot 10^{-9}$	1.01	-49.94	32.39	64.86	
		$3 \cdot 10^{-9}$	1.17	-52.72	35.49	67.32	
		$4 \cdot 10^{-9}$	1.33	-54.76	37.71	68.86	
		$5 \cdot 10^{-9}$	1.51	-56.35	39.54	70.17	
	5	$1 \cdot 10^{-9}$	0.66	-33.01	20.02	60.65	+
		$2 \cdot 10^{-9}$	0.80	-36.75	23.31	63.43	
		$3 \cdot 10^{-9}$	0.98	-39.16	25.45	64.99	
		$4 \cdot 10^{-9}$	1.21	-40.96	27.11	66.19	
		$5 \cdot 10^{-9}$	1.56	-42.40	28.49	67.19	
	6	$1 \cdot 10^{-9}$	0.53	-25.52	15.20	59.56	*
		$2 \cdot 10^{-9}$	0.69	-28.83	17.63	61.15	
		$3 \cdot 10^{-9}$	0.96	-31.04	19.28	62.11	

characteristic for grain boundary diffusion and interface diffusion. Although one would expect faster diffusion in a thin film material because of the microscale dimensions, the explicit incorporation of grain boundary diffusion and interface diffusion was omitted since the beam is considered to be made of a single crystalline with a relatively large width and thickness. If a high diffusion constant would have a physical meaning, it points to a diffusion mechanism that gives rise to rates in the order of those achieved in grain boundary diffusion or interface diffusion. In literature, it is reported that the existence of second phase particles in a material matrix may increase the rate of the diffusion [174]. Moreover, in case of semicoherent and incoherent particles, the particle-matrix interfaces may act as vacancy sources, from which vacancies then migrate into the matrix. Such a diffusion mechanism closely resembles the motion of vacancies from grain boundaries and lattice defects into the bulk as described in [175] with activation energies as low as 0.62 eV. Such a mechanism would lead to larger diffusion rates and amplify the slip rate controlled by the climb of edge dislocations over particles since the diffusion during the climb over a particle occurs only in the region surrounding that particle.

The results of the finite element simulations of the micro-clamp experiment on a *polycrystalline* thin beam [7] with the extended SGCP model show that the use of an inhomogeneous diffusion coefficient, which takes values in the order of grain boundary diffusion within grain boundary regions and relatively small values that are comparable to lattice diffusion within grain interiors, may be more reasonable than a large homogeneous diffusion coefficient leading to an excessive energy dissipation. By using an inhomogeneous diffusion constant, plastic slip activity is mainly confined to grain boundary regions. Since the prescribed displacement is small, the stress levels achieved with the application of the load and during the creep are relatively low. Consequently, only the dislocation glide mechanism of which the rate is limited by climb is active. Therefore, the grain interiors deform almost fully elastically due to the small lattice diffusion constant. When the load is removed, the beam is enforced to return to its original position under the combined

effect of the internal stresses developed within the grain boundary regions and the large elastic energy stored within grain interiors. The relaxation of the internal stresses by the reverse glide of dislocations within the grain boundary regions determines the time scale of the recovery process.

The simulations of the micro-clamp experiment with the extended SGCP model result in permanent deformations in contrast to the full recovery of the residual deformations stated in [7]. Simulation results are highly sensitive to the grain texture of the considered specimen. The incomplete approximation of the grain structure of the hinge part due to lack of experimental details constitutes a source of noticeable inaccuracy for the simulation results. Moreover, the information about the microstructure of the material is limited; the properties of (intermetallic) phases present in the material, such as their type, size and volume fraction, are not exactly known. The input parameters of the extended SGCP model are chosen such that they are within the margins reported in literature, yielding a mechanical behavior that is relatively close to the experimental data.

The simulation results reveals further that the back stresses that are calculated by the current internal stress formulation with acceptable values of the length scale R is not sufficient to capture the anelastic strain recovery observed in the micro-clamp experiment. In the simulations, R is varied to increase the magnitude of internal stresses for the given loading scheme even though the use of large values for R may not be justified from a physical perspective [55]. However, larger values of R also do not significantly improve the accuracy of the simulation results at predicting the material behavior observed in the experiment because the internal stresses are proportional to the gradients of GNDs densities and the amount of GNDs are reduced with increasing values of R . Hence, provided that the internal stresses are responsible for the full recovery of strains in the micro-clamp experiment [7], the simulation results presented in this work suggest that the current internal stress formulation needs to be extended to account for additional sources of internal stresses. This would induce large back stresses at low stress levels, as expected to be the case for the experiment [7].

In the present case, several factors, which are also discussed in detail by [178], may contribute to the internal stress state of the material. For instance, subgrains (if existing) can store energy when they are elastically bowed under the applied stress. Following the reduction or removal of the applied load, they can unbow due to this stored energy, driving back the piled-up dislocations in front of them. Similarly, the line tension in bowed dislocations under loading can act as a back stress on the dislocations themselves and may cause them to glide in reverse direction once the load is removed. Additionally, the local pile up of dislocations such as the Orowan rings left around the particles may locally create internal stress fields. A dislocation which is balanced between such an internal stress field and the applied external stress may be forced to glide back under the effect of the local internal stress field when the external stress is removed. Dislocation pile-ups may also contribute to the recovery process by acting as dislocation sources. Load reductions may lead to the dispersion of pile-ups and a consequent increase in the amount of mobile dislocations. As a result, the rate of reverse crystallographic slip per available driving force goes up, which will help to recover a larger amount of strain. Besides, residual stresses that are present in the material prior to loading would also be important for the observed anelastic behavior. For instance, the stress fields due to coherency strains can provide long range back stresses¹⁰ and may contribute to the driving forces for reverse slip of dislocations.

¹⁰The additional resistance due to coherency strains around particles is treated as short range interactions within the extended SGCP model.

4.9 Summary and concluding remarks

In this work, a physically based constitutive formulation in terms of microstructural quantities is proposed for time and scale dependent crystallographic slip in precipitate strengthened fcc alloys. The presented model covers both thermally activated and viscous drag controlled regimes of dislocation motion, which extends its applicability to cases where high strain rates are relevant.

Within the presented formulation, the overall material strength is provided by a combination of dislocation-dislocation and dislocation-particle interactions. The particle-dislocation interaction is modeled by considering three distinct processes: i) the Friedel process, i.e. particle shearing, ii) the Orowan process, i.e. circumvention via looping and iii) dislocation climb. The long range interaction is modeled via a back stress which is derived from the gradients of geometrically necessary dislocation densities.

The new model is integrated within a strain gradient crystal plasticity theory and implemented in a finite element method and its capabilities are investigated by simulations of the bending of a single crystalline cantilever beam and the simulations of a micro-clamp experiment. Analyses of the simulation results showed that:

- i. When the climb of edge dislocations is neglected, the overall slip rate at slip system level is dominated by the slip rate of mobile screw dislocations at low and moderate stress levels for shearable particles.
- ii. When dislocation climb is involved, the total slip rate at low stresses is governed by the climb of edge dislocations, independent of the type of particles (i.e. coherent or incoherent).
- iii. The dislocation climb rate, which is determined by the relaxation constant and the diffusion constant together with size and volume fraction of particles, controls the amount of residual deformation that remains after the load removal. Residual deformations are developed during load transients and creep and tend to be larger with increasing rate of dislocation climb.
- iv. At low stress levels, the rate of dislocation climb determines also the rate of the reverse slip that occurs after the removal of applied loads. The reverse crystallographic slip is driven by the internal stresses (i.e. back stresses), which originate from the inhomogeneous distribution of GND densities within the extended SGCP model. Therefore, the climb also controls the amount and the characteristic time scales of anelastic deformation recovery.
- v. The magnitude of the time dependent recovery depends not only on the magnitude of the existing back stress, but also on how easy the dislocations can glide back, in other words, the magnitude of the rate of reverse crystallographic slip attainable at that stress level. If the dislocation climb leads to slip rates that are sufficiently large to generate changes, i.e. reduction, in the GND densities, a stress redistribution will occur: absolute values of the elastic resolved shear stress and the back stress will be reduced, and hence, the effective resolved shear stress will decay to zero. A larger climb rate will also result in a faster strain recovery in parallel to the decay in the GND densities.
- vi. The rate of dislocation glide limited by climb strongly relies on the diffusion coefficient at constant particle properties (i.e. size, volume fraction and relaxation parameter). Results of single crystalline beam bending simulations show that deformation recovery becomes macroscopically visible only with diffusion constants that are considerably larger than that of lattice diffusion.

- vii. The simulations of the micro-clamp experiment demonstrates that in case of a polycrystalline material, the use of a large overall diffusion constant leads to an excessive amount of energy dissipation, which limits the percentage of the residual deformation that is recovered over time. Instead of a large homogeneous deformation constant, the use of an inhomogeneous diffusion constant which assumes values that are close to grain boundary diffusion in the vicinity of grain boundaries and values close to lattice diffusion within grain interiors seems justified. The percentages of recovered deformation are noticeably increased when an inhomogeneous diffusion constant is utilized due to the storage of a larger amount of elastic energy within grains and larger back stresses in grain boundary zones. As plastic slip activity occurs within grain boundary regions, it can be expected that residual deformations will increase with decreasing grain size. It may also be expected that time constants associated with deformation recovery in case of finer grains will be larger because of a larger amount of GNDs which results in larger internal stresses.
- viii. The simulation of micro-clamp experiments also show that the magnitudes of the back stresses calculated by the current formulation of internal stresses are not sufficient for the full recovery of the residual deformations in the simulations. This is due to the low GND densities resulting from the small prescribed displacement. Employing an inhomogeneous diffusion constant lead to larger GND densities since plastic strains are localized in grain boundary zones. Consequently, the magnitude of the back stresses gets larger, ensuring a larger and faster deformation recovery. However, a plastic deformation still remains at the end of simulations whereas the residual deformation in the micro-clamp experiment fully recovered. Hence, by assuming that the experimental result is sufficiently reliable and precise, the results of this work suggest that the current formulation of internal stress may need to be extended by considering additional sources of internal stresses which can help to recover the whole residual deformation.
- ix. In cases where high levels of back stress are developed during the loading times, the anelastic recovery will be controlled both by the Friedel process (or Orowan process depending on the properties of the particle) and dislocation climb. The recovery, during which the crystallographic slip rates will be governed by the slip rate of the parallel dashpot group, will be relatively fast. As soon as the effective resolved shear stress drops to a level at which it is not possible to cut the obstacles (or loop around them), the rate of recovery will start to be controlled by dislocation climb, i.e. by diffusion which is a slower process.

Analysis of the time dependent behavior of a capacitive RF-MEMS switch

Abstract

Size effects are responsible for scale dependent variations in the global mechanical behavior of metallic materials with submillimeter dimensions. Such variations may range from a change of material strength to the activation of new phenomena that are not common at larger scales, such as anelastic recovery that is observed in polycrystalline thin films [7]. These fine scale phenomenon can be predicted only by theories that incorporate internal length scales in their formulations. In this work, multiphysical finite element simulations are performed by using a strain gradient crystal plasticity model [179] in order to analyze the mechanical performance of a capacitive RF-MEMS switch containing a free-floating polycrystalline thin film electrode under (cyclic) creep loading. Simulation results show that the switch is prone to residual changes in the gap between the electrodes following the load removal, a fraction of which is recovered over time in the unloaded state. The extended SGCP model predicts that the magnitude of the residual deformation and the amount and rate of anelastic recovery can be controlled by the modification of the microstructure and the thickness of the film. Under cyclic loading, the residual deflection of the electrode saturates within a few loading cycles and the pull-in voltage drops together with the increasing residual deformation. The saturation magnitude of the residual deformation and the pull-in voltage depend on the hold time in the unloaded state between sequential cycles.

5.1 Introduction

It is experimentally observed that at sub-millimeter scales, mechanical properties of metallic materials rely strongly on the material dimensions [3–5] as a result of the increased influence of the microstructure of the material. Among these, grain orientations, dislocation distributions, and the boundary constraints, e.g. surface passivation alter the mechanical behavior [17], which is referred to as scale dependent behavior. These size effects may also result in well known typical material characteristics that turn out to be markedly different than what is commonly observed in metals at large scales. Time dependent strain recovery, referred to as anelastic recovery in this work, was ob-

served by [7] in micro-clamp bending experiments on Al-Cu [1 wt%] free-standing polycrystalline thin beams. It was reported in [7] that the residual deformation that developed within 2 days of creep loading at stress levels below the yield strength of the material almost fully recovered within about 6 h following the unloading.

The combined action of size effects and relatively well studied time dependent phenomena, such as creep [66, 67], can pose additional reliability issues for advanced engineering products that involve (sub)micron sized components, such as capacitive RF-MEMS switches with metallic thin film plates. This type of switches generally has an electrode that is suspended by means of springs, which are also made of thin metal films. The free-standing electrode is able to move vertically under the effect of electrostatic forces generated by the application of a voltage difference between the electrodes. The elastic energy stored in the springs during the actuation of the switch provides the restoring force to increase the gap between the electrodes when the voltage is reduced or to open the switch when the voltage drops to zero. Hence, the reliability of these switches mainly depends on the mechanical performance of the free standing electrode and the springs (i.e. the metal thin film). For instance, creep can cause irreversible deformations in the springs which will permanently reduce the gap between the electrodes and, in turn, the opening and closing voltages of the switch. Anelasticity may lead to temporary changes in device properties as the gap height will change over time.

Scale dependent behavior of a material can only be described by theories that involve characteristic length scales of the material in the underlying formulation. A higher order crystal plasticity (SGCP) model that involves statistically stored dislocation (SSD) and geometrically necessary dislocation (GND) densities was previously proposed by Evers et al. [13] for scale dependent behavior of pure fcc metals. In this model, a back stress in terms of the gradients of crystallographic slip was employed to capture the lattice curvature effect. The back stress on a slip system is described by the interaction between the dislocations of that slip system [13], or as extended by Bayley et al. [15, 16] by considering the interaction between different slip systems. The SGCP model is further extended by [179] for modeling creep and anelasticity of fcc alloys containing small second phase particles. A physically based constitutive law for crystallographic slip was developed based on thermally activated dislocation glide limited by different mechanisms of dislocation-particle interactions together with dislocation-dislocation interaction. This extension was incorporated into the SGCP framework.

Here, the results of electro-mechanical finite element simulations of an RF-MEMS device are presented. In these simulations, the extended SGCP model [179] is utilized for the description of the mechanical behavior of a thin film component that is made of an Al-Cu [1 wt%] alloy. Two sets of simulations are performed. In the first set, the effect of various quantities, i.e. particle size and volume fraction, surface constraints and film thickness, on the mechanical response of the switch to a loading-unloading cycle is investigated. In the second set, the mechanical performance of the switch under multiple loading-unloading cycles is studied with a focus on the duration of the unloaded state between successive cycles.

5.2 A strain gradient crystal plasticity framework for particle hardened alloys

A strain gradient single crystal plasticity framework (SGCP) was recently developed by [13–16] for the prediction of scale dependent behavior of fcc pure metals. Therein, a phenomenological power law relationship was employed as the viscoplastic flow rule for crystallographic slip. Three

different types of dislocation-particle interactions were incorporated into the enhanced flow rule:

- i. the Friedel process, i.e. the shearing of particles,
- ii. the Orowan process, i.e. the particle by-passing by bowing around them,
- iii. the climb of edge dislocations over particles.

5.2.1 Strain gradient crystal plasticity formulation

Within the extended SGCP framework, the deformation gradient \mathbf{F} is multiplicatively decomposed into its elastic, \mathbf{F}_e , and plastic, \mathbf{F}_p , components [50, 51]:

$$\mathbf{F} = \mathbf{F}_e \cdot \mathbf{F}_p, \quad (5.1)$$

where \mathbf{F}_e describes the stretch and the rotation of the lattice with respect to an intermediate configuration which is defined by \mathbf{F}_p with respect to the reference configuration.

The second elastic Piola-Kirchhoff stress tensor \mathbf{S} is defined in terms of the elastic Green-Lagrange strain tensor \mathbf{E}_e in the intermediate configuration as:

$$\mathbf{S} = \mathbb{C} : \mathbf{E}_e \quad \text{with} \quad \mathbf{E}_e = \frac{1}{2} (\mathbf{F}_e^T \cdot \mathbf{F}_e - \mathbf{I}), \quad (5.2)$$

where \mathbb{C} is the fourth order elasticity tensor and \mathbf{I} is the second order identity tensor. \mathbf{S} is given by the pull-back of the Kirchhoff stress $\boldsymbol{\tau}$ to the intermediate configuration

$$\mathbf{S} = \mathbf{F}_e^{-1} \cdot \boldsymbol{\tau} \cdot \mathbf{F}_e^{-T}. \quad (5.3)$$

The rate of the plastic deformation gradient is calculated by

$$\dot{\mathbf{F}}_p = \mathbf{L}_p \cdot \mathbf{F}_p. \quad (5.4)$$

Here, \mathbf{L}_p is the plastic velocity gradient tensor and is resolved from the plastic slips at the slip system level (12 octahedral slip systems for an fcc metal):

$$\mathbf{L}_p = \sum_{\alpha=1}^{12} \dot{\gamma}^\alpha \mathbf{P}_0^\alpha. \quad (5.5)$$

In this equation, $\dot{\gamma}^\alpha$ represents the plastic slip rate of system α . $\mathbf{P}_0^\alpha = \mathbf{s}_0^\alpha \mathbf{n}_0^\alpha$ is the Schmid tensor with \mathbf{s}_0^α the unit direction of the Burgers vector and \mathbf{n}_0^α the unit normal of the slip plane of system α , both defined in the intermediate configuration.

The total crystallographic slip rate $\dot{\gamma}^\alpha$ of a slip system α is decomposed into the slip rates due to mobile edge and screw dislocations reading

$$\dot{\gamma}^\alpha = \dot{\gamma}_e^\alpha + \dot{\gamma}_s^\alpha, \quad (5.6)$$

where subscripts $(\cdot)_e$ and $(\cdot)_s$ denote edge and screw types, respectively. Note that the dislocation-particle interactions (i) and (ii) occur for both edge and screw type of mobile dislocations whereas only edge dislocations can climb. $\dot{\gamma}^\alpha$ results from the sum of both flow rules, which are constructed for each of dislocation-particle and dislocation-dislocation interaction mechanisms and combined

in the way demonstrated by figure 5.1. The slip rates due to edge and screw dislocations are given

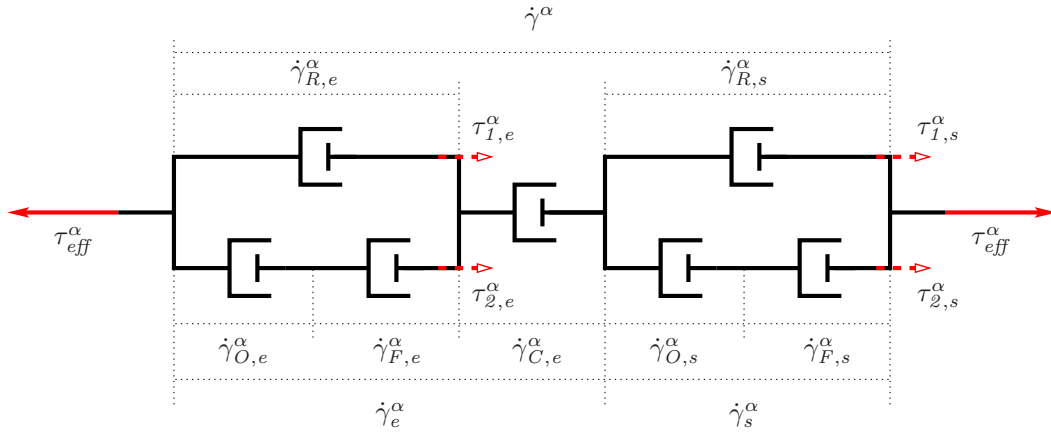


Figure 5.1: Mechanical analogue of the new constitutive law for a slip system in a particle strengthened alloy. In the figure, α denotes the slip plane and runs over 1..12 for fcc metals, τ^α is the effective resolved shear stress, $\dot{\gamma}^\alpha$ is the total slip rate corresponding to τ_{eff}^α , $\tau_{1,e}^\alpha$ and $\tau_{2,e}^\alpha$ are the stresses in the first and second branches. $\dot{\gamma}_R^\alpha$, $\dot{\gamma}_O^\alpha$, $\dot{\gamma}_F^\alpha$ and $\dot{\gamma}_C^\alpha$ are the slip rates of the dashpot representing the dislocation-dislocation interactions, the Orowan, the Friedel and the climb dashpots, respectively. Subscripts $(\cdot)_e$ and $(\cdot)_s$ represent the quantities for edge and screw dislocations.

by

$$\dot{\gamma}_e^\alpha = \dot{\gamma}_{R,e}^\alpha + \dot{\gamma}_{C,e}^\alpha = \dot{\gamma}_{O,e}^\alpha + \dot{\gamma}_{F,e}^\alpha + \dot{\gamma}_{C,e}^\alpha, \quad (5.7)$$

$$\dot{\gamma}_s^\alpha = \dot{\gamma}_{R,s}^\alpha = \dot{\gamma}_{O,s}^\alpha + \dot{\gamma}_{F,s}^\alpha, \quad (5.8)$$

where subscripts $(\cdot)_R$, $(\cdot)_O$, $(\cdot)_F$ and $(\cdot)_C$ stand for the slip resistance arising from the dislocation-dislocation interactions, the Orowan process, the Friedel process and dislocation climb. Furthermore, the effective stress is given by

$$\tau_{eff}^\alpha = \tau_{1,e}^\alpha + \tau_{2,e}^\alpha = \tau_{1,s}^\alpha + \tau_{2,s}^\alpha. \quad (5.9)$$

In this equation, τ_{eff}^α , $\tau_{1,j}^\alpha$ and $\tau_{2,j}^\alpha$ with $j^1 = \{e, s\}$ are the effective resolved shear stresses in the main branch, the first branch (for dislocation-dislocation interactions) and the second branch (for dislocation-particle interactions), respectively, see figure 5.1.

The effective resolved shear stress is given by the difference between the applied resolved shear stress τ^α and the resolved back stress τ_b^α :

$$\tau_{eff}^\alpha = \tau^\alpha - \tau_b^\alpha \quad \text{with} \quad \tau^\alpha = \mathbf{S} : \mathbf{P}_0^\alpha. \quad (5.10)$$

The incorporation of the back stress within the extended SGCP framework enables the prediction of a size dependent material behavior arising from the strain gradients. The back stress is calculated via the integration of the stress fields of a distribution of geometrically necessary dislocations (GNDs) in a cylindrical volume, where the radius of the volume is a length scale. The internal

¹From here onwards, subscript j is used as an index for dislocation type and reads e and s for edge and screw dislocations, respectively.

stress field due to edge dislocations is given by [15, 16] as:

$$\boldsymbol{\sigma}_e^{int} = \frac{G_m b R^2}{8(1 - \nu_m)} \sum_{\xi=1}^{12} \nabla_0 \rho_{GND,e}^{\xi} \cdot \left(3\mathbf{n}_0^{\xi} \mathbf{s}_0^{\xi} \mathbf{s}_0^{\xi} + \mathbf{n}_0^{\xi} \mathbf{n}_0^{\xi} \mathbf{n}_0^{\xi} + 4\nu \mathbf{n}_0^{\xi} \mathbf{p}_0^{\xi} \mathbf{p}_0^{\xi} - \mathbf{s}_0^{\xi} \mathbf{s}_0^{\xi} \mathbf{n}_0^{\xi} - \mathbf{s}_0^{\xi} \mathbf{n}_0^{\xi} \mathbf{s}_0^{\xi} \right), \quad (5.11)$$

and for the screw GNDs, it is defined as:

$$\boldsymbol{\sigma}_s^{int} = \frac{G_m b R^2}{4} \sum_{\xi=13}^{18} \nabla_0 \rho_{GND,s}^{\xi} \cdot \left(-\mathbf{n}_0^{\xi} \mathbf{s}_0^{\xi} \mathbf{p}_0^{\xi} - \mathbf{n}_0^{\xi} \mathbf{p}_0^{\xi} \mathbf{s}_0^{\xi} + \mathbf{p}_0^{\xi} \mathbf{s}_0^{\xi} \mathbf{n}_0^{\xi} + \mathbf{p}_0^{\xi} \mathbf{n}_0^{\xi} \mathbf{s}_0^{\xi} \right), \quad (5.12)$$

with $\mathbf{p}_0^{\xi} = \mathbf{s}_0^{\xi} \times \mathbf{n}_0^{\xi}$ associated with slip system ξ and R the radius of the cylindrical integration volume. G_m and ν_m are the shear modulus and Poisson's ratio of the matrix, respectively. Following [13–16], two of the screw dislocations with the same Burgers vector are coupled into one set, leading to 6 screw dislocations whereas the number of slip systems for edge dislocations is 12. The back stress on a slip system α is then calculated by:

$$\tau_b^{\alpha} = -(\boldsymbol{\sigma}_e^{int} + \boldsymbol{\sigma}_s^{int}) : \mathbf{P}_0^{\alpha} \quad \text{for } \alpha = 1, 2, \dots, 12. \quad (5.13)$$

The SGCP model involves also statistically stored dislocations (SSD), the unsigned fraction of dislocations. The evolution of SSD densities on each slip system ξ is described by the generalized form of the relation originally proposed by [56]:

$$\dot{\rho}_{SSD}^{\xi} = \frac{1}{b} \left(\frac{1}{L^{\xi}} - 2 y_c \rho_{SSD}^{\xi} \right) |\dot{\gamma}^{\xi}| \quad \text{with } \rho_{SSD}^{\xi}(t=0) = \rho_{SSD_0}^{\xi} \quad \text{for } \xi = 1, 2, \dots, 12. \quad (5.14)$$

The first term within the parentheses in equation (5.14) is the accumulation rate, whereby L^{ξ} equals the average dislocation segment length given by:

$$L^{\xi} = \frac{K}{\sqrt{\sum_{\alpha=1}^{12} H^{\xi\alpha} |\rho_{SSD}^{\alpha}| + \sum_{\alpha=1}^{18} H^{\xi\alpha} |\rho_{GND}^{\alpha}|}}. \quad (5.15)$$

Here, $H^{\xi\alpha}$ are the components of a matrix that represents the mutual interactions anticipated between dislocations [13]. The second term in the parentheses is the annihilation rate in terms of the critical annihilation length y_c , the average distance between two oppositely signed dislocations, below which they annihilate. $\rho_{SSD_0}^{\xi}$ is the density of SSDs that are initially present in the material.

The non-uniform distribution of densities of GNDs leads to long range back stresses (equal and opposite to the internal interaction stress) which are given via equations (5.11)-(5.13). The GNDs also contribute to isotropic hardening processes. The densities of GNDs are calculated via the gradients of the crystallographic slips. The slip gradients in the direction of slip \mathbf{s}_0^{α} give the densities of edge GNDs, while the gradients in the direction of \mathbf{p}_0^{α} give screw GND densities. A gradient of slip in the direction of the slip plane normal \mathbf{n}_0^{α} does not introduce any GNDs [26]. Hence, a

balance equation for the densities of the GNDs can be written as

$$\rho_{GND,e}^{\xi} = \rho_{GND,e_0}^{\xi} - \frac{1}{b} \mathbf{s}_0^{\xi} \cdot \nabla_0 \gamma^{\xi}, \quad (5.16)$$

$$\rho_{GND,s}^{\xi} = \rho_{GND,s_0}^{\xi} + \frac{1}{b} \left(\mathbf{p}_0^{\alpha_1(\xi)} \cdot \nabla_0 \gamma^{\alpha_1(\xi)} + \mathbf{p}_0^{\alpha_2(\xi)} \cdot \nabla_0 \gamma^{\alpha_2(\xi)} \right). \quad (5.17)$$

Here, ξ runs over 1, 2, ..., 12 for edge GNDs and over 13, 14, ..., 18 for screw GNDs. ρ_{GND,e_0}^{ξ} and ρ_{GND,s_0}^{ξ} denote the initial densities of edge and screw GNDs, if any present in the material, $\alpha_1(\xi)$ and $\alpha_2(\xi)$ represent two slip systems with the same slip direction but different plane normals for each screw GND.

The rate equations for the crystallographic slip are formulated based on the Orowan type flow rule:

$$\dot{\gamma}_{i,j}^{\alpha} = \rho_{m,j}^{\alpha} b \bar{v}_{i,j}^{\alpha}, \quad (5.18)$$

where $\rho_{m,j}^{\alpha}$ is the density of mobile dislocations, b is the magnitude of the Burgers vector and $\bar{v}_{i,j}^{\alpha}$ is the average velocity of mobile dislocations in slip system α . Here, i indicates the type of the interaction between dislocations and particles: for edge dislocations $i = \{R, O, F, C\}$, whereas for screw dislocations $i = \{R, O, F\}$.

The densities of mobile edge and screw dislocations in equation (5.18) are calculated via

$$\rho_{m,j}^{\alpha} = \Phi \left(|\rho_{GND,j}^{\alpha}| + |\rho_{SSD,j}^{\alpha}| \right), \quad (5.19)$$

with Φ a constant determining the mobile fraction of total dislocations on a slip system. It should be noticed that equation (5.19) involves 12 screw GNDs whereas equation (5.17), following [13–16], contains 6 screw GNDs. In this work, 12 screw GNDs are obtained by distributing 6 screw GNDs equally between the associated slip systems with the same plane normals. Note also that equation (5.19) has 12 edge and 12 screw SSDs. Equation (5.14) was proposed by [13–16] assuming that all SSDs were of edge type. In this work, SSD densities calculated via equation (5.14) are equally divided into edge and screw types.

In the following subsections, the average velocity of mobile edge and screw dislocations are derived based on the type of their interactions with the obstructions for their glide.

5.2.2 Dislocation-dislocation interactions

The resistance in slip system α , s^{α} , originating from the short-range interactions between dislocations, is given by [13–16]

$$s^{\alpha} = c \frac{G_m b}{L_d^{\alpha}}, \quad (5.20)$$

where c is a material constant [52] and L_d^{α} is the effective mean planar distance between the dislocations, which is given by:

$$L_d^{\alpha} = \left[\sum_{\xi=1}^{12} A^{\alpha\xi} \left(|\rho_{SSD,e}^{\xi}| + |\rho_{SSD,s}^{\xi}| \right) + \sum_{\xi=1}^{18} A^{\alpha\xi} |\rho_{GND}^{\xi}| \right]^{-1/2}. \quad (5.21)$$

Here, $A^{\alpha\xi}$ are the components of the interaction matrix which represents the strength of the interactions between slip systems as determined by [53]. It is composed of the six interaction coefficients corresponding to self hardening, coplanar hardening, Hirth lock, Glissile junction, Lomer-Cottrell lock and cross slip, cf. [70]. L_d^α is taken identical for edge and screw dislocations. Note that the slip resistance in equation (5.20) contains screw SSDs via L_d^α in contrast to [13, 14].

In the current formulation, s^α acts as a stress barrier around which a transition occurs between two different regimes of dislocation motion [159]. Dislocations driven by the effective resolved shear stresses lower than s^α move in a jerky manner: the time between two sequential hits of an obstruction is mainly spent in front of obstacles, from which dislocations escape by the help of thermal fluctuations, referred to as thermally activated release. Here, the average velocity of dislocations during thermally activated motion is obtained by the generalization of the rate equation given by [159] for the rate of thermal activated release of dislocations from obstructions and reads:

$$\bar{v}_{th,j}^\alpha = \frac{1}{2} L_d^\alpha \left(\frac{\hat{F}_{R,j}}{2\Gamma_{c,j}} \right)^{1/2} v_G \exp \left(-\frac{\Delta G_{R,j}^\alpha}{kT} \right) \left[1 - \exp \left(-\frac{|\tau_{1,j}^\alpha| b (L_d^\alpha)^2}{kT} \right) \right] \text{sign}(\tau_{1,j}^\alpha) \quad (5.22)$$

with v_G the Granato frequency, $\hat{F}_{R,j}$ the maximum force that can be sustained by dislocation-dislocation interactions and $\Gamma_{c,j}$ the line tension of a dislocation experiencing $\hat{F}_{R,j}$. The fraction $\hat{F}_{R,j}/2\Gamma_{c,j}$ is a measure for the magnitude of the slip resistance offered by dislocation-dislocation interactions and is approximated here by $\hat{F}_{R,j}/2\Gamma_{c,j} = c^{2/3}$. The pre-exponential term excluding v_G determines an effective jumping distance that a dislocation spans between two successive encounters with obstructions. $\Delta G_{R,j}^\alpha$ is the activation energy for the thermally activated overcoming of the resistance provided by the dislocation-dislocation interactions and is defined as

$$\Delta G_{R,j}^\alpha = \Delta F_0 \left(1 - \frac{|\tau_{1,j}^\alpha|}{s^\alpha} \right), \quad (5.23)$$

in which ΔF_0 represents the energy required at zero stress [13–16]. When the effective resolved shear stress is larger than s^α , the applied stress is sustained by viscous drag forces originating from the interaction of mobile dislocations with phonons and electrons in case of metals with low lattice resistance [159], such as fcc metals. In this case, dislocation motion is rather continuous in comparison with thermally activated dislocation glide and the velocity of gliding dislocations is proportional to the effective resolved shear stress [159].

In this work, the average velocity of mobile dislocations within the viscous drag regime is calculated by:

$$\bar{v}_{dr,j}^\alpha = \frac{b}{B} \tau_{1,j}^\alpha, \quad (5.24)$$

which is obtained by the simplification of the average dislocation velocity defined by [159] for the viscous drag regime by assuming a relatively large separation distance between the obstructions in comparison with the dislocation-dislocation interaction regime [159, 160]. B is the drag coefficient and approximated by [159]

$$B \simeq \frac{kT}{\Omega \omega_A}, \quad (5.25)$$

with Ω the atomic volume and ω_A the atomic frequency. B is taken as the same for edge and screw dislocations.

Finally, an expression for the average velocity of mobile edge and screw dislocations $\bar{v}_{R,j}^\alpha$ is obtained by the combination of these two different regimes of dislocation motion by considering the times to cover the same distance in case of thermally activated glide only and viscous glide only [159, 160], which leads to

$$\bar{v}_{R,j}^\alpha = \frac{L^\alpha}{t_{tot}^\alpha} = \left(\frac{1}{\bar{v}_{dr,j}^\alpha} + \frac{1}{\bar{v}_{th,j}^\alpha} \right)^{-1}. \quad (5.26)$$

Equation (5.26) implies that the average velocity of mobile dislocations will be governed by the slowest of $\bar{v}_{dr,j}^\alpha$ and $\bar{v}_{th,j}^\alpha$.

5.2.3 Dislocation-particle interactions

In the extension of the SGCP framework, it is assumed that the material involves one type of second phase particles which are treatable by Friedel-Fleischer (FF) statistics [96, 120]. The particles are considered to have a spherical shape with an average planar radius r_s [111, 112]

$$r_s = \frac{\pi r}{4} \quad (5.27)$$

and a mean planar spacing in a regular square lattice arrangement L_{cc} [111, 113, 114]

$$L_{cc} = \left(\frac{2\pi}{3f} \right)^{1/2} r, \quad (5.28)$$

on a glide plane intersecting the particles randomly, where r is the average particle size and f is the particle volume fraction.

Particles contribute to the strength by hindering the dislocation motion on the slip planes passing through them. In this work, three different interaction processes are assumed to occur, outlined below.

Friedel process

When particles that obstruct gliding dislocations have a finite strength, the dislocations can overcome them by shearing if the driving stress is sufficiently large. An expression for the critical resolved shear stress required for the shearing of particles by mobile edge and mobile dislocations based on FF statistics [111–115, 117] reads:

$$\tau_{c,j} = \frac{2\Gamma_{c,j}}{bL_{cc}} \left(\frac{\hat{F}_{F,j}}{2\Gamma_{c,j}} \right)^{\frac{3}{2}}. \quad (5.29)$$

In the current framework, the Friedel stress is calculated by using

$$\tau_{FR,j} = C_1(1 + C_2\eta_{0,j})^{C_3}\tau_{c,j} \quad (5.30)$$

as proposed by [123] for the incorporation of the effect of finite particle size and the randomness of their distribution on the Friedel stress. In this equation, C_1 , C_2 and C_3 are constants given by [112, 119] as $C_1 = 0.94$, $C_2 = 2.5$, $C_3 = 0.33$ and $C_1 = 0.94$, $C_2 = 0.82$, $C_3 = 1$ for elastically interacting particles and energy storing particles [111, 117, 118], respectively. $\eta_{0,j}$ is a measure

for the applicability of FF statistics and is defined as [123]

$$\eta_{0,j} = \frac{y_0}{L_{cc}} \frac{1}{(\hat{F}_{F,j}/2\Gamma_{c,j})^{1/2}}. \quad (5.31)$$

with y_0 being the range of the interaction force. It is proposed that for $\eta_{0,j} \ll 1$, FF statistics can still be used to predict the critical shear stress [123]. When $\eta_{0,j} \gg 1$, the dislocation-particle interaction becomes similar to that in solid-solution alloys, which are well treated by Mott-Labusch (ML) statistics [124–126].

The line tension of edge and screw dislocations is calculated by using an improved version [111] of de Wit-Koehler model [154]:

$$\Gamma_{c,e} = \frac{G_m b^2}{4\pi} \left[1 + \nu_m - 3\nu_m \left(1 - \frac{\cos^2 \phi_{c,e}}{3} \right) \right] \ln \frac{R_o}{R_i}, \quad (5.32)$$

$$\Gamma_{c,s} = \frac{G_m b^2}{4\pi} [1 + \nu_m - \nu_m \cos^2 \phi_{c,s}] \ln \frac{R_o}{R_i}, \quad (5.33)$$

which is derived by the calculation of the average line tension along the length of a circular arc [111, 155]. Here, $\cos \phi_{c,j} = \hat{F}_{R,j}/2\Gamma_{c,j}$, $R_i \approx b$ is the inner cut-off radius and R_o is the outer cut-off radius which is approximated by the mean planar spacing L_{cc} .

The Friedel stress of a particle, $\tau_{FR,j}$, and the activation energy $\Delta G_{F,j}$ are assumed to be determined by the source of strengthening that offers the largest shear resistance among the four different types below:

- a) Chemical strengthening denotes the additional energy required to generate new interfaces during the shearing of energy storing particles. The maximum force that a screw dislocation feels during this process reads [111, 112, 114, 115, 119, 129]

$$\hat{F}_{CHE,s} = 2\chi_s b, \quad (5.34)$$

with χ_s the specific energy of the particle-matrix interface. The resistance force for an edge dislocation is approximated to be equal for a screw dislocation [114, 115, 119, 129]. The energy barrier corresponding to chemical strengthening is described by [112]

$$\Delta G_{CHE,j}^\alpha = 2\hat{F}_{CHE,j} r \left[1 - \left(\frac{|\tau_{2,j}^\alpha|}{\tau_{FR,j CHE}} \right)^{2/3} \right]. \quad (5.35)$$

- b) Stacking fault (SF) strengthening is an elastic type of dislocations-particle interaction [119] that results from the difference in the SF energies of the matrix and particles ($\Delta\chi$). The SF strengthening model of [131] is adopted here due to its simplicity. In this model, the maximum resistance force experienced by a straight dislocation due to the mismatch of SF energies is given by

$$\hat{F}_{SFS,j} = 2(2\hat{d}_j r_s - \hat{d}_j^2)^{1/2} |\Delta\chi|, \quad (5.36)$$

with $\hat{d}_j = \min(w_{m,j}, r_s)$. $w_{m,j}$ is the equilibrium distance between Shockley partial disloca-

tions in the material matrix and calculated by [132]

$$w_{m,j} = \frac{G_m b^2}{24\pi\chi} \frac{2 - 3\nu_m}{1 - \nu_m} \left[1 + \frac{4\nu_m}{2 - 3\nu_m} \sin^2 \beta_j \right], \quad (5.37)$$

where β_j is the angle between the total Burgers vector and the dislocation line. An equation for the activation energy of SF strengthening is suggested by [112]:

$$\Delta G_{SFS,j}^\alpha = r \hat{F}_{SFS,j} \left[1 - \frac{3}{2} \left(\frac{|\tau_{2,j}^\alpha|}{\tau_{FR,j,SFS}} \right)^{4/9} + \frac{1}{2} \left(\frac{|\tau_{2,j}^\alpha|}{\tau_{FR,j,SFS}} \right)^{4/3} \right]. \quad (5.38)$$

- c) Coherency hardening originates from the interaction of dislocations with the stress fields due to the lattice misfit (ε) between the coherent particles and the matrix, which is of an elastic and diffuse type [131]. The maximum resistance force that an edge dislocation may experience reads [111, 129, 135–138]

$$\hat{F}_{COH,e} = 4G_m |\varepsilon| br, \quad (5.39)$$

and occurs when its slip plane intersects the particle at a distance of $r/\sqrt{2}$ from the center of the particle. Strain fields due to a lattice misfit do not pose any resistance against the motion of a long straight screw dislocation. The critical resolved shear stress necessary to overcome coherent spherical particles is given by [111, 114, 129, 135–138]

$$\tau_{FR,eCOH} = C_4 (G_m \varepsilon)^{\frac{3}{2}} \left[\frac{f r b}{2\Gamma_{c,e}} \right]^{\frac{1}{2}} \quad \text{and} \quad \varepsilon = \frac{a_p - a_m}{a_m} \left[1 + \frac{2G_m(1 - 2\nu_p)}{G_p(1 + \nu_p)} \right], \quad (5.40)$$

where a is the lattice dimension of the matrix and C_4 is a constant to take into account the diffuse nature of the interaction [111, 119]. Equation (5.40) is used to estimate the additional strength provided by the lattice mismatch between the particles and the matrix by setting $C_4 \approx 3.9$, which results from the substitution of equation (5.39) into equation (5.29). The associated activation energy is described by

$$\Delta G_{COH,e}^\alpha = r \hat{F}_{COH,j} \left[1 - \frac{3}{2} \left(\frac{|\tau_{2,e}^\alpha|}{\tau_{FR,eCOH}} \right)^{4/9} + \frac{1}{2} \left(\frac{|\tau_{2,e}^\alpha|}{\tau_{FR,eCOH}} \right)^{4/3} \right], \quad (5.41)$$

as proposed by [112].

- d) Modulus hardening occurs due to the difference in elastic moduli of the matrix and particles (ΔG). In this type of hardening, the matrix dislocations interact elastically with the particles [131]. Here, an empirical equation which is derived by [139] is used for the calculation of the maximum force that is experienced by an edge dislocation due to the modulus misfit:

$$\hat{F}_{MOD,e} = C_5 \Delta G b^2 \left(\frac{r}{b} \right)^{C_6}, \quad (5.42)$$

where $C_5 \approx 0.05$ and $C_6 \approx 0.85$ are constants [111]. This equation is also used for screw dislocations with a reduction by 25%, which is qualitatively in line with the numerical results in [139] for screw type dislocations. Following [112], an expression for the energy barrier to

overcome the additional resistance offered by the modulus misfit can be written as

$$\Delta G_{MOD,j}^{\alpha} = r \hat{F}_{MOD,j} \left[1 - \frac{3}{2} \left(\frac{|\tau_{2,j}^{\alpha}|}{\tau_{FR,j_{MOD}}} \right)^{4/9} + \frac{1}{2} \left(\frac{|\tau_{2,j}^{\alpha}|}{\tau_{FR,j_{MOD}}} \right)^{4/3} \right]. \quad (5.43)$$

The Friedel stress is then given by

$$\tau_{FR,j} = \max\{\tau_{FR,j_{CHE}}, \tau_{FR,j_{SFS}}, \tau_{FR,j_{MOD}}, \tau_{FR,j_{COH}}\}. \quad (5.44)$$

In the present work, mobile dislocations overcome particles by means of thermal activation, and hence the average velocity of dislocations is formulated in a way similar to equation (5.26) such that

$$\bar{v}_{F,j}^{\alpha} = \frac{1}{2} L_{cc} v_G \left(\frac{\hat{F}_{F,j}}{2\Gamma_{c,j}} \right)^{1/2} \exp\left(-\frac{\Delta G_{F,j}^{\alpha}}{kT}\right) \left[1 - \exp\left(-\frac{|\tau_{2,j}^{\alpha}| b L_{cc}^2}{kT}\right) \right] \text{sign}(\tau_{2,j}^{\alpha}). \quad (5.45)$$

In this equation, the fraction $\hat{F}_{F,j}/2\Gamma_{c,j}$ and the activation energy $\Delta G_{F,j}^{\alpha}$ come from the same strengthening source that determines $\tau_{FR,j}$.

Orowan process

If the particles are strong because of, for instance, being incoherent or large, gliding dislocations cannot shear them. However, the particles can still be passed by bowing around them, which is referred to as the Orowan process. The stress required to complete this process is called the Orowan stress.

The Orowan stress, $\tau_{OR,j}$, is calculated here by using the expression derived by [119]

$$\tau_{OR,j} = 0.93 \frac{G_m b}{2\pi\sqrt{1-\nu_m} w_l r} \ln\left(\frac{2w_d r}{b}\right) \left[\frac{\ln(2w_d r/b)}{\ln(w_l r/b)} \right]^{1/2} \quad (5.46)$$

where w_r , w_q , w_l and w_d are statistical parameters given by

$$w_r = \frac{\pi}{4}, \quad w_q = \frac{2}{3}, \quad w_l = \sqrt{\frac{\pi w_q}{f}} - 2w_r \quad \text{and} \quad w_d = (w_l^{-1} + (2w_r)^{-1})^{-1}. \quad (5.47)$$

Note that, the Orowan stresses for edge and screw dislocations are assumed to be the same in this work.

The Orowan mechanism is almost temperature independent. Such a property can be described using a relatively large activation energy such as $\Delta G_O > 2G_m b^3$ following [106]. Hence, a stress dependent energy barrier for the Orowan process is used here as

$$\Delta G_{O,j}^{\alpha} = 3G_m b^3 \left(1 - \frac{|\tau_{2,j}^{\alpha}|}{\tau_{OR,j}} \right), \quad (5.48)$$

which is then used in the formulation of the average velocity of dislocations to circumvent the

particles via the Orowan process:

$$\bar{v}_{O,j}^{\alpha} = L_{cc} v_G \exp\left(-\frac{\Delta G_{O,j}^{\alpha}}{kT}\right) \left[1 - \exp\left(-\frac{|\tau_{2,j}^{\alpha}| b L_{cc}^2}{kT}\right)\right] \text{sign}(\tau_{2,j}^{\alpha}). \quad (5.49)$$

Dislocation climb

Within the extended SGCP framework, when applied stress levels are low for overcoming the obstacles via the Orowan or Friedel processes, a diffusional process, dislocation climb, may assist mobile edge dislocations to continue their glide.

The climb of edge dislocations is described here by the thermally activated detachment model of [152] by assuming that there is a sufficiently strong attractive interaction between the particle and a dislocation climbing over it. In this model, the line tension of the dislocation during its climb is relaxed due to the attractive interaction. Hence, for its detachment from the particle, an additional energy must be supplied for the compensation of the energy loss. This detachment energy E_d is formulated by [152]

$$E_{d,e} = 2\Gamma_e r \left[(1 - k_r) \left(1 - \frac{|\tau_{eff}|}{\tau_{d,e}} \right) \right]^{\frac{3}{2}} \quad (5.50)$$

for spherical particles of average radius r , where

$$\tau_{d,e} = \sqrt{1 - k_r^2} \tau_{OR,e} \quad (5.51)$$

is the detachment threshold stress [146]. k_r is a relaxation constant that represents the strength of the interaction between climbing dislocations and particles. A lower k_r means a stronger interaction, leading to a larger relaxation of line energy during climb. In reality, $k_r > 0.7$ and it attains its lowest values for incoherent particles [151]. Another expression for the detachment threshold stress was suggested by [153]

$$\tau_{d,e} \approx \left(1 + \frac{1}{\sqrt{1 - k_r^2}} \right)^{3/2} \tau_{OR,e}, \quad (5.52)$$

by considering a rather weak behavior of dispersions during the thermal detachment in contrary to the strong obstacle approximation of [146]. Equation (5.52) yields lower threshold stresses for the detachment than the original formulation [146]. It also leads to a shift of the critical relaxation parameter, which marks the transition between detachment controlled slip and climb controlled slip, from 0.94 to 0.96. In the current work, equation (5.52) is used for the calculation of the detachment threshold stress. The line tension Γ_e is calculated by using equation (5.32) with $R_o = 2r_s$ which is a suitable approximation for the outer cut-off radius since the dislocation configuration in the thermal detachment model is similar to that in the Orowan process. An attempt frequency of dislocations, v , in the thermally activated detachment model of climb is defined in [152] by

$$v = v_v \exp\left(-\frac{E_d}{kT}\right) \quad \text{with} \quad v_v = \frac{n}{2} \nu_D \exp\left(-\frac{Q_f + Q_m}{kT}\right) = \frac{3D_l}{b^2}, \quad (5.53)$$

where v_v is frequency of vacancy absorption, $D_l = \frac{1}{6} n b^2 \nu_D \exp\left(-\frac{Q_l}{kT}\right)$ is the lattice diffusivity, ν_D is the Debye frequency, Q_f and Q_m are the activation energies for vacancy nucleation and

migration that together define Q_l , the activation energy for self diffusion. In line with equation (5.53), an expression is used here for the average velocity of the mobile edge dislocations which is limited by dislocation climb in a way similar to equations (5.26), (5.45) and (5.49):

$$\bar{v}_{C,e}^\alpha = L_J \frac{3D_{eff}}{b^2} \exp\left(-\frac{E_{d,e}^\alpha}{kT}\right) \left[1 - \exp\left(-\frac{|\tau_{eff,e}^\alpha| b(L_{cc})^2}{kT}\right)\right] \text{sign}(\tau_{eff,e}^\alpha). \quad (5.54)$$

L_J in this equation can be interpreted as the average distance to be traveled after the detachment from a particle until the next contact with another particle. Here, L_J is approximated by an effective travel distance $L_{cc}^2/\lambda_{c,e}$ if $\tau_{FR} < \tau_{OR}$ where $\lambda_{c,e}$ is the Friedel sampling length for edge dislocations and given by $\lambda_{c,e} = L_{cc}/\sqrt{\cos\phi_{c,e}}$. Otherwise, it is taken as equal to L_{cc} . Note that the self diffusion constant D_l in equation (5.53) is replaced by an effective diffusion constant D_{eff} in equation (5.54).

5.3 Multiphysical simulations with the extended SGCP model

The extended SGCP framework [179] is next used in multiphysical simulations in order to study the influence of service conditions and material properties on the performance of a capacitive RF-MEMS switch shown in figure 5.2a. The studied factors are:

- i. particle size at constant volume fraction,
- ii. volume fraction at constant particle size,
- iii. surface constraints,
- iv. film thickness,
- v. cyclic loading.

By assuming that the grain texture of the device is symmetric about the x and y axes, only one-fourth of the switch is numerically modeled [75]. The grains are generated by voronoi tessellations and have their [111] axes parallel to the z axis and in-plane random orientations. The switch is made of a Al-Cu [1 wt%] alloy with incoherent particles. The upper electrode has a thickness of $4.75 \mu\text{m}$ and is suspended via the springs by $3.2 \mu\text{m}$ over the bottom electrode. To save computation time, the SGCP model is employed only in the parts of the switch where relatively large stress levels are anticipated, i.e. only for the free-standing spring and the region where it is connected to the electrode. An inhomogeneous diffusion constant is used with $D_{eff,gb} = 1 \cdot 10^{-9} \mu\text{m}^2/\text{s}$ for the regions near grain boundaries and $D_{eff} = 8.9 \cdot 10^{-18} \mu\text{m}^2/\text{s}$ for grain interiors. The rest of the electrode plate is modeled as a transversely isotropic medium, see figure 5.2b. Some of the material parameters in the simulations are given in table 5.1. The parameters that are varied in the simulations here are listed in table 5.2. The remaining parameters can be found in literature [13–16]. The electric domain is idealized by using the electromechanical transducer elements with a parallel plate approximation and involving fringe field effects, see section 3.3 of chapter 3. The contact between the thin film and the dielectric layer on the bottom electrode is modeled via non-linear spring elements with the contact curve given in the appendix of chapter 3. The transducer elements and contact elements are located in the gap between the electrodes as depicted in figure 3.4 in chapter 3. Simulations are performed in two sets. In the first set, the effect of the factors i-iv are investigated for a loading-unloading cycle within the period of $[0, t_3]$. The second set involves

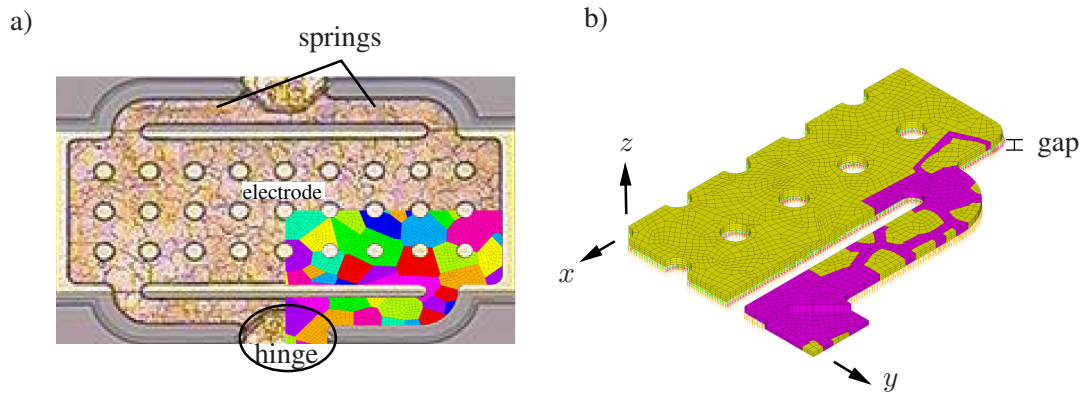


Figure 5.2: a) Top view of a capacitive RF-MEMS switch (Courtesy of EPCOS). Only one-fourth of the switch is considered in the numerical model. Each color highlights a grain with different orientation. b) The extended SGCP model is used only in the regions with magenta color. The yellow parts are modeled as a transversely isotropic elastic medium.

two simulations with multiple loading-unloading cycles with the material parameters belonging to the reference set in table 5.2. The simulations in this set have the same loading and unloading times. However, for the time spend during the anelastic strain recovery, which occurs during the unloaded stage between the completion of a loading-unloading cycle and the start of the next cycle, different values of 10000 s and 100 s are used. The loading scheme is illustrated in figure 5.3. The results of the first set of simulations are presented in figure 5.4 and table 5.3.

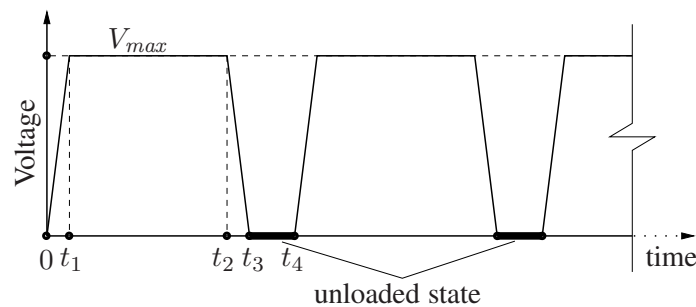


Figure 5.3: Loading scheme used in the simulations. Only one loading-unloading cycle is considered in the first set of simulations with $t_1 = 180$ ms, $t_2 - t_1 \approx 10000$ s, and $t_3 - t_2 \approx t_1$ and the unloaded stage $t_4 - t_3 \approx 10000$ s. $V_{max} = 60$ V. The second set is composed of two simulations involving 4 loading-unloading cycles with the same loading and unloading times as defined via $t_1 - t_3$ but different durations of the unloaded state, 10000 s and 100 s.

Figure 5.4a shows the maximum change in the gap between the plates. Note that the data plotted here does not necessarily belong to a single node. It is seen in comparison with the reference curve that the residual displacement at $t = t_3$ decreases with decreasing particle size since the detachment threshold stress grows proportionally with the Orowan stress which increases with decreasing particle size at constant volume fraction. The opposite effect is created by reducing the volume fraction of particles at constant size, which results in a smaller Orowan stress. The factors that lead to an increase in the detachment threshold stress also reduce the amount and rate of deformation recovery. Similarly, those resulting in smaller detachment threshold stresses yield

Table 5.1: Material parameters used in the simulations.

Parameter	Meaning	Value	Unit	Reference
C_{11}	Elastic constant	108000	MPa	[70, 76, 77]
C_{12}	Elastic constant	61300	MPa	[70, 76, 77]
C_{44}	Elastic constant	28500	MPa	[70, 76, 77]
ν_m	Poisson's ratio	0.347	-	[78]
k	Boltzmann constant	$1.38054 \cdot 10^{-11}$	pJ/K	-
T	Temperature	293	K	-
b	Burgers vector length	$2.86 \cdot 10^{-4}$	μm	[70]
K	Material constant	10	-	[13–16]
y_c	Critical annihilation length	$1.6 \cdot 10^{-3}$	μm	[13–16]
c	Material constant	0.3	-	[52]
ρ_{SSD_0}	Initial SSD density	5	μm^{-2}	-
R	Length scale	2	μm	-
v_G	Granato frequency	$1 \cdot 10^{11}$	s^{-1}	-
ω_A	Atomic frequency	$1.07 \cdot 10^{-13}$	1/s	-
Ω	Atomic volume of Al	16.50	\AA^3	-
G_m	Shear modulus	26000	MPa	[70, 76]
ΔF_0	Activation energy	$64 \cdot 10^{-8}$	pJ	[12]
k_r	Relaxation coefficient	0.94	-	-
D_{eff}	Eff. latt. diff. for grain interiors	$8.9 \cdot 10^{-18}$	$\mu\text{m}^2/\text{s}$	-
$D_{eff,gb}$	Eff. latt. diff. for grain boundary regions	$1 \cdot 10^{-9}$	$\mu\text{m}^2/\text{s}$	-
ϕ	Mobile fraction of dislocations	$5 \cdot 10^{-3}$	-	-

Table 5.2: Material parameters used in the simulations. Unspecified values are the same as those in the first row.

Sim.	Particle size [nm]	Volume fraction [%]	Surface condition	Thickness [μm]
Ref.	4	0.4	Passivated	5
i	8	-	-	-
ii	-	1.2	-	-
iii	-	-	Free	-
iv	-	-	-	3.17
v	2	2	-	3.17

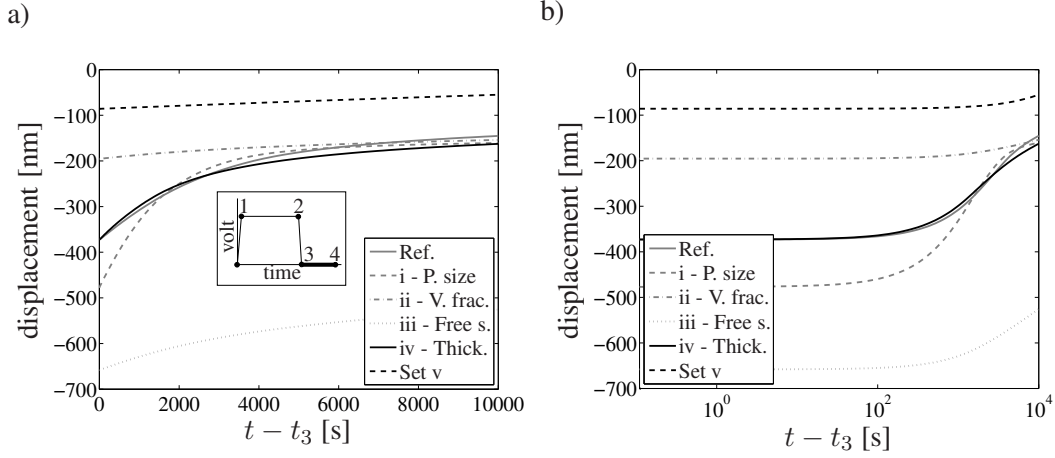


Figure 5.4: Gap displacement during the unloaded stage over time with: a) linear scale, b) logarithmic scale. The curve belonging to the case with a free surface condition almost coincides with the curve of the reference parameter set.

Table 5.3: Residual gap displacement $u_{z,r}$ at $t = t_3$, displacement recovery δu_z during the unloaded stage and the percentage of the recovered deformation.

Sim.	$u_{z,r}$ [nm]	δu_z [nm]	$\delta u_z / u_{z,r}$ [%]
Ref.	-373.1	-145.3	61.1
i	-477	-160.6	66.6
ii	-195.4	-154	21.2
iii	-658.1	-525.8	20.1
iv	-372.9	-162.7	56.4
v	-85.8	-55.0	35.9

larger amounts and rates of deformation recovery, see figure 5.4a and b and table 5.3. Figure 5.4a shows that the maximum residual deformation is significantly affected by changing the surface condition: the free surface condition leads to a substantial decrease in the gap at both $t = t_3$ and $t = t_4$. Furthermore, the smallest percentage of the deformation recovery is recorded in this simulation. The figure also demonstrates that for the same set of material parameters, reducing the thickness of the free-standing beam to two-third of the original thickness has no significant influence on the maximum residual change of the gap at $t = t_3$ and at $t = t_4$ deformation at $t = t_4$ (which is here explicitly referred to as permanent deformation).

The effect of a smaller thickness on the mechanical behavior is illustrated further in contour plots of the gap change and norm of the GND densities² at $t = t_3$ and $t = t_4$ in figures 5.5 and 5.6. Figure 5.5 reveals that the beam thickness has an important effect on the amount of the residual displacement at $t = t_3$ and the permanent deformation remaining at $t = t_4$. In the case with the smaller thickness, the major portion of the beam deforms much less than for the case with the reference parameter set. However, there is a large gradient in the vertical displacement field of the plate and the maximum residual displacements at $t = t_3$ and $t = t_4$ are comparable to those

²Given by $\sqrt{\sum_{i=1}^{12} \left({}^n \rho_{GND,e}^i \right)^2 + 0.5 \sum_{i=13}^{18} \left({}^n \rho_{GND,s}^i \right)^2}$, where ${}^n(\cdot)$ denotes that the term is a nodal quantity.

from the simulations with the reference parameter set. This explains why figure 5.4a misleadingly suggests that thickness has a negligible influence on the residual and permanent deformations. It can be seen in figure 5.6 that less GNDs are generated in case of the thinner beam. The pull-in and release voltages, at which the upper electrode snaps on the bottom electrode during loading and springs back during unloading, respectively, are compared in figure 5.7. It is found for the simulations with the reference parameter set and the parameter sets (i)-(iii), in which the beam thickness is the same, that the influence of the deformations accumulated during creep loading on the release voltage is limited; they vary between 9 – 10 V. Although the residual and permanent deformations from the simulation with the parameter set (iii) is about three times as large as those with the parameter set (ii) (see table 5.3), the difference between the release voltages of two simulations is only about 1 V. As expected, there is no difference in pull-in voltages (41 V) in these four simulations as it is determined by the elastic properties of the beams, which are the same. For the switch with the smaller thickness corresponding to parameter set (iv), the pull-in voltage reads about 14 V. The release voltage is around 9 V and close to the values from the simulations with the other parameter sets.

The results presented in figures 5.4, 5.5 and 5.6 suggest that a switch with an upper electrode that is made of a thinner film with large number of small incoherent particles would display a better mechanical performance. A surface passivation is expected to make a significant contribution to the prevention of plastic strains, though this contribution may be very limited. In this respect, a simulation is performed with the parameter set (v) given in table 5.2. The residual displacement and permanent deformation are greatly reduced in this case, see table 5.3 and figures 5.4 and 5.8a, and the GND densities are much lower, cf. figure 5.8b. The pull-in voltage and the release voltage are close to those from the simulation with parameter set (iv) and read 14 V and 7 V, respectively.

The results of the second set of simulations that involve four successive loading-unloading cycles are presented in figures 5.9 and 5.10. Figure 5.9a shows the maximum gap displacement over time that is obtained from the first simulation of this set (i.e. with equal duration of creep loading and unloaded state). The direct comparison of the change of the maximum gap displacement over time after each loading-unloading cycle in figure 5.9c demonstrates that the residual displacements just at the end of the unloading stage (which is the beginning of the unloaded state) of a cycle and at the end of the following unloaded state (which is the beginning of the next loading-unloading cycle) increase with the number of applied loading-unloading cycles, however at a decreasing rate. The noticeable drop in the magnitude of the change of the gap displacement with the third and especially the fourth loading-unloading cycle suggests that the magnitude of the residual displacements at the start and at the end of unloaded state will be saturated after a number of cycles. Figure 5.9b, which contains the results of the second simulation (i.e. with a duration of unloaded state that is equal to 1% of the duration of creep loading), shows that although the magnitude of the residual displacement will still saturate with further cycling, the saturation will require a larger number of cycles and the magnitude of the residual deformations at saturation will be larger provided that no sufficiently long time for anelastic strain recovery is given. Such prediction of the material behavior by the extended SGCP model is due to the larger amount of dislocation accumulation in the material in case of shorter durations of unloaded states between loading cycles, which acts as a reservoir of mobile dislocations for the next subsequent loading cycle. The pull-in and release voltages within each loading cycle are plotted in figure 5.10. The figure indicates that in the simulation with an unloaded state of 10000 s between sequential loading-unloading cycles, the pull-in voltage for the second loading cycle decreases. This is due to the residual deformation at the beginning of the second loading-unloading cycle. Since the change in the residual deformation is small after the second cycle, the pull-in voltage remains almost the same for the subsequent cycles. For the simulation with a shorter duration of the unloaded state (100 s), the pull-in voltage for the

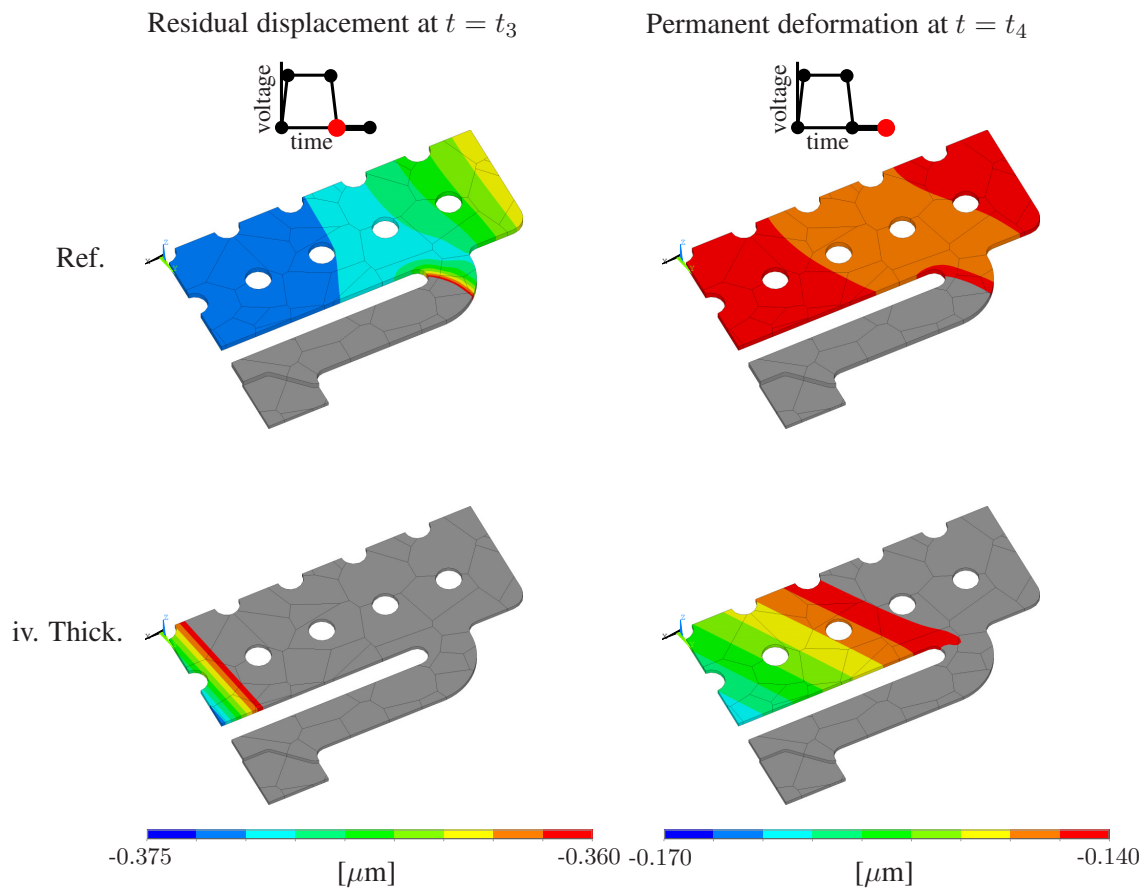


Figure 5.5: Contour plots of residual displacement at $t = t_3$ and permanent deformation at $t = t_4$ obtained from the simulations with the reference parameter set (Ref.) and with a thinner beam (Thick.), see table 5.2. Gray color shows displacements that are larger than the upper bound of the contour bars.

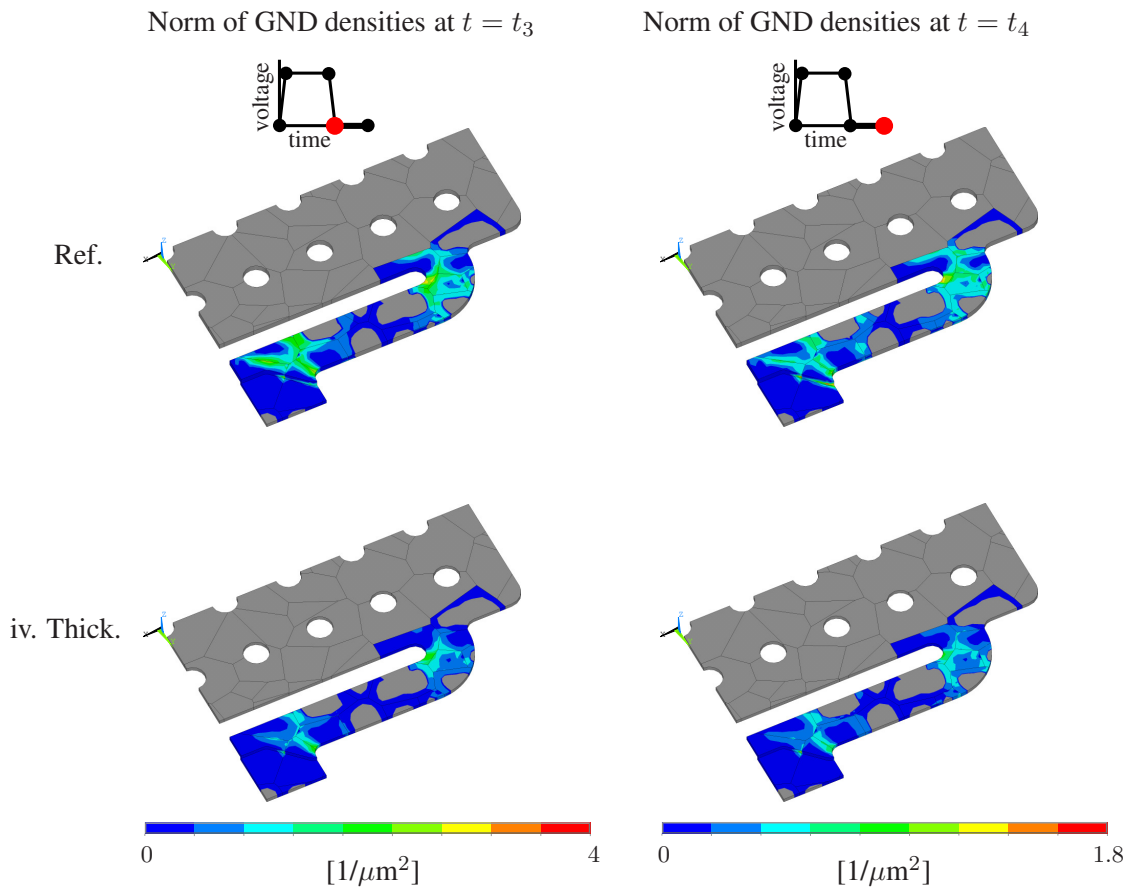


Figure 5.6: Contour plots of norm of GND densities at $t = t_3$ and permanent deformation at $t = t_4$ obtained from the simulations with the reference parameter set (Ref.) and with a thinner beam (Thick.), see table 5.2. Gray color shows the elastic elements.

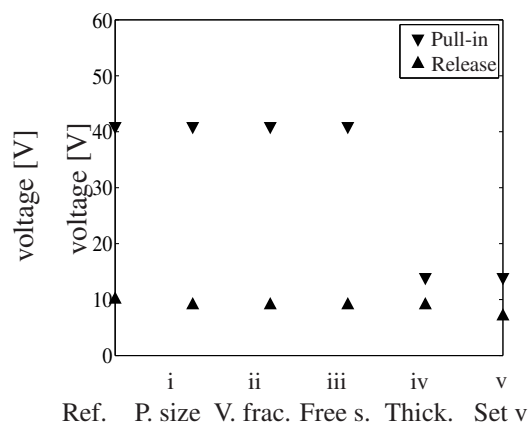


Figure 5.7: Pull-in and release voltages obtained from the first set of simulations.

second loading cycle is smaller due to the larger residual deformation at the start of the second loading cycle. The pull-in voltage for the third loading cycle is even smaller than for the second loading cycle due to the large contribution of the second loading cycle to the residual deformation that remains at the start of the third cycle. The figure suggests that pull-in voltages will saturate

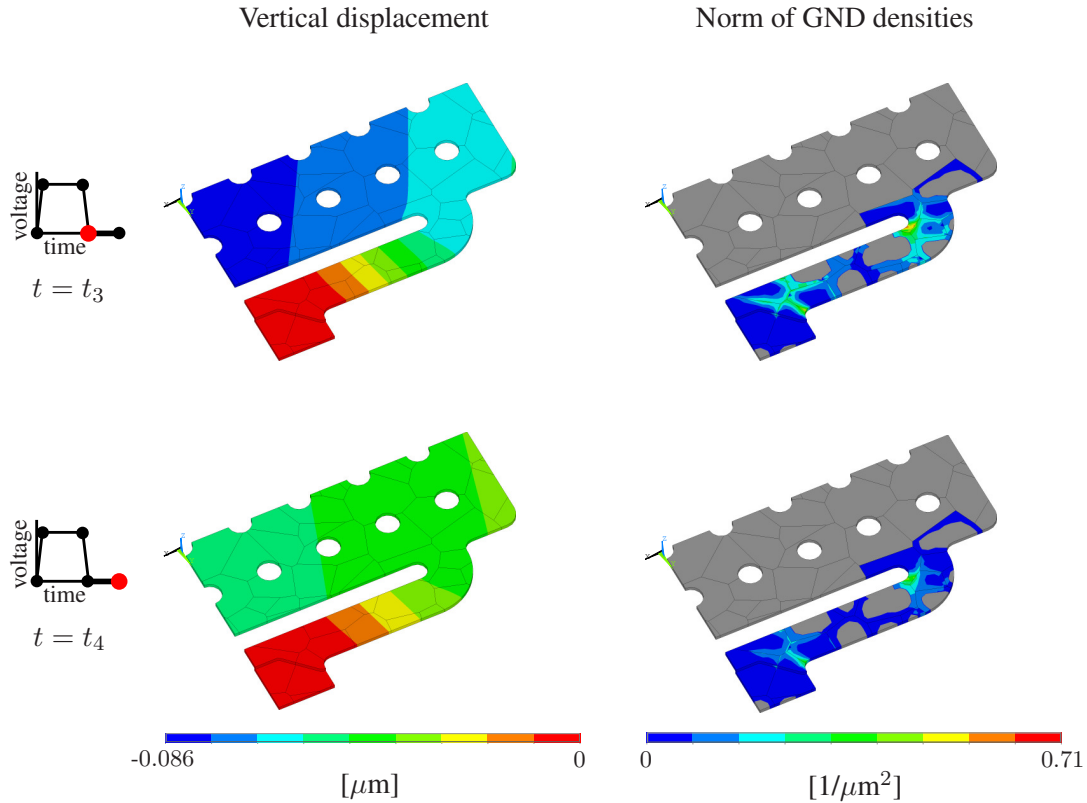


Figure 5.8: Results of the simulation with parameter set (v). a) The residual deformation (at $t = t_3$) and permanent deformation (at $t = t_4$). b) The GND density norms taken at $t = t_3$ and $t = t_4$. Gray color shows the elastic elements.

and will not decrease further after a number of additional loading-unloading cycles as the residual deformation will saturate. In contrast to the pull-in voltage, the release voltage does not change between loading cycles and also between two simulations.

5.4 Discussion and concluding remarks

This work presents multiphysical finite element simulations of an RF-MEMS switch by using an extended SGCP model for the description of the mechanical behavior of its thin film components. The influence of particle size and volume fraction, surface condition, film thickness and the cyclic loading on the mechanical performance of the switch is investigated.

In all of these simulations, the extended SGCP model results in residual changes in the gap after the switches are completely unloaded. It is also found that the gap increases over time due to anelastic strain recovery during the unloaded state. The magnitude of the residual deformation and the amount and the rate of the deformation recovery are highly sensitive to the properties of the free-floating thin film. The simulation results show that the residual deformations can be significantly reduced by incorporating small incoherent particles with a large volume fraction because of relatively large Orowan stresses required for passing by the particles. The extended SGCP framework employs the thermally activated detachment model of [152] for modeling dislocation glide, the rate of which is limited by the climb of edge dislocations over particles at low stress (and high temperature) levels. The detachment model [152] contains a threshold stress which is proportional

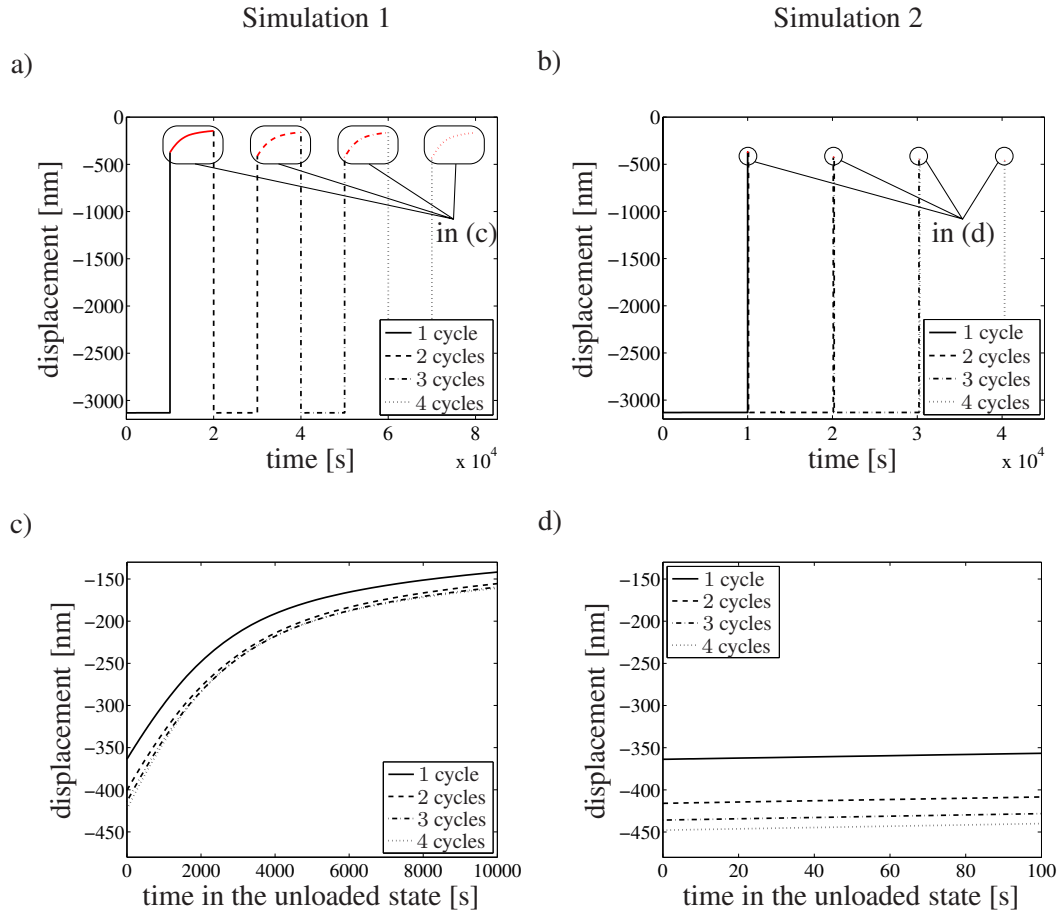


Figure 5.9: Change of the maximum gap displacement over time obtained from two simulations which involve four loading-unloading cycles with the same loading-unloading times but different durations of the unloaded state (red curves) between sequential loading-unloading cycles, which are 10000 s, in (a) and (c), and 100 s, in (b) and (d).

to the Orowan stress. In the present case, the increase in the threshold stress with decreasing particle size is important for lowering the residual deformations. A larger particle volume fraction results in lower residual deformations also due to the reduced separation distance between the particles, which increases the number of times mobile dislocations hit particles within a unit distance. The simulations demonstrate that surface passivation makes the upper plate of the switch more resistant against plastic deformations.

The anelastic deformation recovery captured by the extended SGCP model is due to the reverse glide of mobile dislocations upon the reduction or the removal of applied loads, which is driven by the back stresses (internal stresses) that arise from the inhomogeneous distribution of GND densities. Within this context, two quantities are important, the resistance against reverse glide and the magnitude of the back stress available for reverse glide. As simulation results indicate, any modification that leads to a larger resistance against crystallographic slip will also increase the resistance against the reverse slip of dislocations. Therefore, a large number of small particles also effectively limits time dependent changes in the clearance between the plates, i.e. by reducing the amount and the rate of anelastic deformation recovery. The anelastic recovery will continue as long as the magnitude of the back stress is sufficiently large in comparison with the slip resistance that is determined by the combined effect of the resistance due the dislocation-dislocation interactions s^α , the Orowan stress $\tau_{OR,j}$ (in case of (semi)coherent particles also the Friedel stress $\tau_{FR,j}$) and

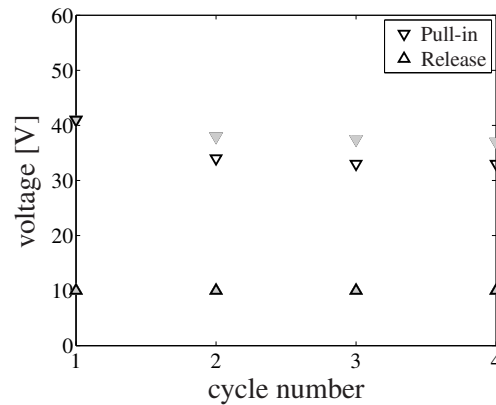


Figure 5.10: Pull-in and release voltages obtained from the two simulations which involve four loading-unloading cycles with the same loading-unloading times but different durations of the unloaded state between sequential loading-unloading cycles, which are 10000 s (closed triangles) and 100 s (open triangles).

the detachment stress $\tau_{d,e}$. The observation of the anelastic strain recovery in all simulations and the relatively stronger (i.e. more elastic) behavior of the switch with a thinner plate suggest that the mechanical performance of capacitive RF-MEMS switches is intrinsically exposed to size effects arising from strain gradients.

This study also reveals that under cyclic loading conditions, the residual and permanent changes in the gap increase at a decreasing rate. The saturation magnitude of the residual and permanent deformations and the number of loading cycles required for the saturation tend to be larger with decreasing duration of the unloaded state between sequential loading-unloading cycles. The pull-in voltage decreases together with the reduction of the gap with each loading cycle. Although the drop in the pull-in voltage is large after the first loading-unloading cycle, the pull-in voltage levels off as residual deformation saturates within a few cycles. The simulation results show that the release voltage is less sensitive to the plastic strains than the pull-in voltage. It can be stated that measures for reducing the residual deformations will also reduce the degradation of the pull-in voltage (and the release voltage).

Conclusion and recommendations

This thesis mainly focuses on the development of a strain gradient crystal plasticity formulation for modeling of creep and anelasticity in fcc thin film alloys as an extension of a previously developed SGCP framework [13–16]. The SGCP framework [13–16] was developed for the description of size effects on the behavior of fcc pure metals, arising from strain gradients. For this purpose, a physically based back stress was formulated, incorporating the gradients of crystallographic slip and the energetic dislocation-dislocation interactions. The framework involved a phenomenological power-law type relation as the constitutive equation for the rate of crystallographic slip, governed by a short range slip resistance originating from dislocation-dislocation interactions. In the second chapter of this thesis, the thermodynamical consistency of this framework was demonstrated by a direct comparison with a thermodynamically consistent strain gradient theory of crystal plasticity by Gurtin et al. [37, 43–45]. This study also showed that:

- The energetic micro-stresses for the Gurtin type formulation derived based on the physical description of the back stresses of the Evers-Bayley type models provide a physical interpretation for the micro stress terms in the Gurtin type formulation.
- The micro-stress based on the definition of the full-internal back stress formulation of Bayley et al. [15, 16] involves the energetic interactions between different slip systems. It no longer resides in the plane of its slip system, which is believed to be a result of the defect forces exerted by the other slip systems with non-parallel slip planes. This micro-stress vector differs from those of Evers et al. [13, 14], Gurtin [44, 45] and Kuroda and Tvergaard [38], which were derived from a quadratic defect energy omitting the interactions between different slip systems. It is also different from the micro-stress of Gurtin [37] derived from a constitutive equation that couples different glide systems in a phenomenological way and is incapable of handling a micro-stress vector of a slip system with out of plane components. The defect energy function associated to the micro stress resulting from Bayley et al. takes a form that is more complex than a simple quadratic function and is expected to be non-convex.
- Despite the different additional field equations (GND density balance equations vs. the micro-force balance law) used for each model within the finite element context, similar boundary conditions can be defined for the Evers-Bayley type and Gurtin type models.

Next, in chapter 3, the capabilities of the SGCP model to describe the time dependent mechanical behavior of thin metal films are investigated via multiphysical finite element simulations. It is found that:

- The SGCP model is able to predict anelastic deformation recovery after load removals, resulting from the reverse glide of dislocations under the effect of residual internal stresses. However, the observed time dependent deformation recovery is a result of the phenomenological rate dependent modeling of crystal plasticity since the amounts of the recovery and the associated relaxation times rely strongly on the parameters of the flow rule for crystallographic slip, such as initial dislocation density or activation energy, that serve for the definition of slip resistance and are not directly relevant for the time scales of the dislocation motion.
- The results of the simulations of electrostatic thin beam bending experiments on an Al-Cu alloy suffer from a significant inaccuracy in predicting the experimentally observed permanent deformations. This is believed to originate from the fact that the SGCP framework was developed for modeling the behavior of pure fcc materials whereas the thin film sample used in the experiments was made of an alloy containing solute atoms and small precipitates.

Hence, it is concluded that together with the dislocation-dislocation interactions, the incorporation of the interaction mechanisms between gliding dislocations and particles/solute atoms into the physically motivated constitutive rules, including terms for the characteristic time scales of the relevant mechanisms, is indispensable for an accurate modeling of the (time dependent) mechanical behavior of thin films made of alloys.

In chapter 4, a new constitutive law for crystallographic slip is developed in order to describe creep and anelasticity in fcc thin film materials with small second phase particles. This constitutive law is obtained by combining separate Orowan type slip rate equations for dislocation-dislocation interactions, the Orowan process, the Friedel process and the climb of edge dislocations over particles. The analysis of the new crystallographic slip law at a material point level reveals that:

- The crystallographic slip rate is highly sensitive to particle type, size and volume fraction as well as the strength of dislocation-dislocation interactions.
- For coherent particles, the new model predicts that mobile edge dislocations experience a larger resistance than mobile screw dislocations. For edge dislocations, the particle overcoming mechanism (the Orowan or Friedel process) is determined by the particle properties (e.g. size) whereas screw dislocations always pass the particles through shearing them.
- When dislocation climb is omitted, the total slip rate is mainly determined by mobile screw dislocations at all stress levels for fully coherent particles. If climb is considered, in the existence of an attractive interaction between climbing dislocations and particles, the total slip rate is determined by the climb of edge dislocations and mobile screw dislocations at low stress levels and mainly by screw dislocations at larger stress levels. In case of incoherent particles, dislocation climb governs the total slip rate at low stresses.

The SGCP framework is extended by the integration of the new constitutive law. The extended SGCP model is used in the finite element simulations of bending of a single crystalline thin beam (at low stress levels) and the micro-clamp bending experiment on a polycrystalline thin beam [7]. The conclusions obtained from these simulations are summarized as follows:

- The extended SGCP model is capable of describing the plastic deformations emerging during the load application via the process for dislocation-dislocation interactions and the Orowan and Friedel processes. The strain accumulation during creep loading is also well captured by the extended model by the glide of edge dislocations governed by climb over particles. Moreover, the model is able to produce a time dependent deformation recovery following the load removal via the reverse glide of dislocations driven by the residual internal stresses, the rate of which is governed by dislocation climb. The amount of the residual deformation, the recovery percentage and the associated relaxation times are determined by the parameters of the climb model such as diffusion constant, detachment threshold stress (determined by the particle size and volume fraction) and the relaxation constant.
- Although the single crystalline beam bending simulations suggest that values of the homogeneous diffusion constant comparable to the grain boundary diffusion constant are necessary for traceable anelastic deformation recovery, the simulations of the micro clamp bending experiment on a polycrystalline thin beam reveals that the use of an inhomogeneous diffusion constant, with the values of the lattice diffusion constant within grain interiors and values close to the grain boundary diffusion constant in the vicinity of the grain boundaries, yields more accurate results. Such an inhomogeneous diffusion constant results in strong grain interiors and weak grain boundary regions during the creep phase, leading to the accumulation of plastic strains within the grain boundary regions. Hence, larger internal stresses are achieved for smaller plastic deformations due to larger gradients of GND densities, which ensure the recovery of a larger percentage of the residual deformations after the load removal.

Furthermore, multiphysical simulations are performed with the extended SGCP model to analyze the time dependent behavior of a capacitive RF-MEMS switch with a free-standing thin film (under cyclic loading conditions). The simulations demonstrate that:

- The gap between the electrodes of the switch, an important parameter for the functionality of the device, is reduced after a loading-unloading cycle in a way highly sensitive to the microstructural properties of the thin film electrode. The amount of the residual changes can be controlled by small incoherent particles with a relatively large volume fraction, providing a more effective obstruction for dislocation motion. It is also observed that surface passivation limits the plastic slip activity.
- After the unloading, the clearance between the electrodes increases over time (as the internal stresses arising from the gradients of GND densities are relaxed via the reverse glide of dislocations governed by climb). The measures for the restriction of forward dislocation motion will also inhibit the time dependent variations of the gap since firstly the internal levels will be reduced and, secondly, the resistance against the reverse glide of dislocations will increase.
- The mechanical behavior of the thin film electrode of the switch may be prone to size effects, since, on average, the amount of the residual change in the gap and its variation over time in the unloaded state are decreased for a smaller film thickness.
- Under cyclic loading conditions, the gap is reduced at a decreasing rate after each loading-unloading cycle towards a saturation value. The saturation value of the change of the gap and the number of cycles required for saturation increase with shorter durations of the unloaded state between successive loading-unloading cycles.

- In relation to the gap reduction, the pull-in voltage decrease after the first loading-unloading cycle, with a larger drop for the shorter duration of the unloaded state before the second cycle. The change in the pull-in voltage after the subsequent loading-unloading cycles is small and tends to zero within a few cycles. The release voltage is almost not affected by the residual deformations of the free-standing thin film.

A proper assessment of the capabilities of the extended SGCP formulation may require dedicated experiments on single crystalline materials. Such experiments will allow to characterize the abilities to model creep and, if existing, anelastic behavior of thin films (and the effect of surface diffusion) without any interference arising from grain boundaries. The simulation results show that the thin film behavior predicted by the extended SGCP model is highly sensitive to the material's unique (micro)structure, e.g. grain orientations, type, size and volume fraction of particles. Moreover, the possibilities of the validation of the model are also limited by the accuracy of the experiments. Therefore, a healthier evaluation of the performance of the model is possible only in the presence of sufficiently accurate experimental data for samples with a sufficiently well characterized microstructure.

The simulations of the micro-clamp bending experiment on an Al-Cu thin film showed a permanent deformation at the end of the time allocated for the anelastic strain recovery whereas in the experiment, the residual deformation was fully recovered over time. Disregarding the experimental inaccuracies, the enhancement of the internal stress formulation in the extended SGCP model by considering additional sources of residual stresses may be necessary to improve the accuracy of the model to reproduce the experimental result.

The elimination of the assumptions made in the development of the new constitutive law for crystallographic slip will provide a more complete framework for modeling the material behavior. For instance, the dislocation loops left around the particles as a result of the Orowan process can lead to local stress fields and add to the overall slip resistance against dislocation glide. Similarly, solute atoms in the matrix phase may diffuse to dislocations and, hence, restrict their motion. Also, in its current form, the new slip law can handle only one particle type, either coherent or incoherent. However, it can be extended straightforwardly for the treatment of multiple types of particles. Furthermore, the effect of semi-coherent particles on the material response can be taken into account in a way similar to the incoherent particles (or coherent particles) with a correction factor.

Finally, the application of the extended SGCP model to different types of fcc metals with spherical precipitates and dispersions may provide valuable insights into the description of the mechanical behavior of thin films.

Bibliography

- [1] V. Kaajakari. *Practical MEMS*. Small Gear Publishing, 2009.
- [2] M. van Gils, J. Bielen, and G. McDonald. Evaluation of creep in RF-MEMS devices. *EuroSime 2007: 8th International Conference on Thermal, Mechanical and Multi-Physics Simulation Experiments in Micro-electronics and Micro-Systems*, pages 1–6, 2007.
- [3] N. A. Fleck, G. M. Muller, M. F. Ashby, and J. W. Hutchinson. Strain gradient plasticity: theory and experiment. *Acta Metallurgica*, 42:475–487, 1994.
- [4] J. S. Stölken and A. G. Evans. A microbend test for measuring the plastic length scale. *Acta Metallurgica*, 46:5109–5115, 1998.
- [5] W. D. Nix and H. Gao. Indentation size effects in crystalline materials: a law for strain gradient plasticity. *Journal of the Mechanics and Physics of Solids*, 46:411–425, 1998.
- [6] A. J. Kalkman, A. H. Verbruggen, G. C. A. M. Janssen, and S. Radelaar. Transient creep in free-standing thin polycrystalline aluminum films. *Applied Physics Letters*, 92(9):4968–4975, 2002.
- [7] L. I. J. C. Bergers, J. P. M. Hoefnagels, N. K. R. Delhey, and M. G. D. Geers. Measuring time-dependent deformations in metallic mems. *Microelectronics Reliability*, 51:1054–1059, 2011.
- [8] H. Lee, P. Zhang, and J. C. Bravman. Stress relaxation in free-standing aluminum beams. *Thin Solid Beams*, 476:118–124, 2005.
- [9] J. M. J. den Toonder and A. R. van Dijken. Optimization of mechanical properties of thin free-standing metal films for RF-MEMS. *Materials Research Society Symposium Proceedings*, 820:O8.3.1–6, 2004.
- [10] R. Modlinski, P. Ratchev, A. Witvrouw, R. Puers, and I. De Wolf. Creep characterization of Al alloy thin films for use in MEMS applications. *Microelectronics Reliability*, 76:272–278, 2004.
- [11] R. Modlinski, A. Witvrouw, P. Ratchev, A. Jourdain, V. Simons, H. A. C. Tilmans, J. M. J. den Toonder, R. Puers, and I. De Wolf. Creep as a reliability problem in MEMS. *Microelectronics Reliability*, 44:1133–1738, 2004.
- [12] R. Modlinski, P. Ratchev, A. Witvrouw, R. Puers, and I. De Wolf. Creep-resistant aluminum alloys for use in MEMS. *Journal of Micromechanics and Microengineering*, 15:S165–S170, 2005.

- [13] L. P. Evers, W. A. M. Brekelmans, and M. G. D. Geers. Non-local crystal plasticity model with intrinsic SSD and GND effects. *Journal of the Mechanics and Physics of Solids*, 52:2379–2401, 2004.
- [14] L. P. Evers, W. A. M. Brekelmans, and M. G. D. Geers. Scale dependent crystal plasticity framework with dislocation density and grain boundary effects. *International Journal of Solids and Structures*, 41:5209–5230, 2004.
- [15] C. J. Bayley, W. A. M. Brekelmans, and M. G. D. Geers. A comparison of dislocation induced back stress formulations in strain gradient crystal plasticity. *International Journal of Solids and Structures*, 43:7268–7286, 2006.
- [16] C. J. Bayley, W. A. M. Brekelmans, and M. G. D. Geers. A three dimensional dislocation field crystal plasticity approach applied to miniaturized structures. *Philosophical Magazine*, 87:1361–1378, 2007.
- [17] M. G. D. Geers, W. A. M. Brekelmans, and P. J. M. Janssen. Size effects in miniaturized polycrystalline FCC samples: strengthening versus weakening. *International Journal of Solids and Structures*, 43:7304–7321, 2006.
- [18] H. D. Espinosa, B. C. Prorok, and B. Peng. Plasticity size effects in free-standing submicron polycrystalline FCC films subjected to pure tension. *Journal of the Mechanics and Physics of Solids*, 52:667–689, 2004.
- [19] W. D. Nix, J. R. Greer, G. Feng, and E. T. Lilleodden. Deformation at the nanometer and micrometer length scales: Effects of strain gradients and dislocation starvation. *Thin Solid Films*, 515:3152–3157, 2007.
- [20] Y. Xiang and J. J. Vlassak. Bauschinger and size effects in thin-film plasticity. *Acta Materialia*, 54:5449–5460, 2006.
- [21] L. Nicola, Y. Xiang, J. J. Vlassak, E. van der Giessen, and A. Needleman. Plastic deformation of freestanding thin films: Experiments and modeling. *Journal of the Mechanics and Physics of Solids*, 54:2089–2110, 2006.
- [22] K. J. Hemker and W. N. Sharpe. Microscale characterization of mechanical properties. *Annual Review of Materials Research*, 37:93–126, 2007.
- [23] D. M. Dimiduk, M. D. Uchic, S. I. Rao, C. Woodward, and T. A. Parthasarathy. Overview of experiments on microcrystal plasticity in FCC-derivative materials: selected challenges for modelling and simulation of plasticity. *Modelling and Simulations in Materials Science and Engineering*, 15:135–146, 2007.
- [24] R. K. Abu Al-Rub. Prediction of micro and nano-indentation size effect from conical or pyramidal indentation. *Mechanics of Materials*, 39:787–802, 2007.
- [25] P. A. Gruber, J. Beohma, F. Onuseit, A. Wanner, R. Spolenak, and E. Arzt. Size effects on yield strength and strain hardening for ultra-thin Cu films with and without passivation: A study by synchrotron and bulge test techniques. *Acta Materialia*, 56:2318–2335, 2008.
- [26] M. F. Ashby. The deformation of plastically non-homogeneous alloys. *Philosophical Magazine*, 21:399–424, 1970.

- [27] J. F. Nye. Some geometrical relations on in dislocated solids. *Acta Metallurgica*, 1:153–162, 1953.
- [28] E. C. Aifantis. On the microstructural origin of certain inelastic models. *Journal of Engineering Materials and Technology*, 106:326–330, 1984.
- [29] A. Needleman and J. Gil Sevillano. Preface to the viewpoint set on: geometrically necessary dislocations and size dependent plasticity. *Scripta Materialia*, 48:109–111, 2003.
- [30] A. Acharya and J. L. Bassani. Lattice incompatibility and a gradient theory of crystal plasticity. *Journal of the Mechanics and Physics of Solids*, 48:1565–1595, 2000.
- [31] E. P. Busso, F. T. Meissonnier, and N. P. O’Dowd. Gradient-dependent deformation of two-phase single crystals. *Journal of the Mechanics and Physics of Solids*, 48:2333–2361, 2000.
- [32] J. L. Bassani. Incompatibility and a simple gradient theory of plasticity. *Journal of the Mechanics and Physics of Solids*, 49:1983–1996, 2001.
- [33] L. P. Evers, D. M. Parks, W. A. M. Brekelmans, and M. G. D. Geers. Crystal plasticity model with enhanced hardening by geometrically necessary dislocation accumulation. *Journal of the Mechanics and Physics of Solids*, 50:2403–2424, 2002.
- [34] G. Yun, J. Qina, Y. Huangb, and K. C. Hwanga. A study of lower-order strain gradient plasticity theories by the method of characteristics. *European Journal of Mechanics A/Solids*, 23:387–394, 2004.
- [35] C. Han, H. Gao, Y. Huang, and W. D. Nix. Mechanism based strain gradient crystal plasticity–I. theory. *Journal of the Mechanics and Physics of Solids*, 53:1188–1203, 2005.
- [36] S. Brinckmann, T. Siegmund, and Y. Huang. A dislocation density based strain gradient model. *International Journal of Plasticity*, 22:1784–1797, 2006.
- [37] M. E. Gurtin. A finite-deformation, gradient theory of single-crystal plasticity with free energy dependent on densities of geometrically necessary dislocations. *International Journal of Plasticity*, 52:702–725, 2008.
- [38] M. Kuroda and V. Tvergaard. A finite deformation theory of higher-order gradient plasticity. *Journal of the Mechanics and Physics of Solids*, 56:2573–2584, 2008.
- [39] N. A. Fleck and J. W. Hutchinson. Lattice incompatibility and a gradient theory of crystal plasticity. *Advanced Applied Mechanics*, 33:295–361, 1997.
- [40] H. Gao, Y. Huang, W. D. Nix, and J. W. Hutchinson. Mechanism-based strain gradient plasticity–I. theory. *Journal of the Mechanics and Physics of Solids*, 47:1239–1263, 1999.
- [41] V. Levkovitch and B. Svendsen. On the large-deformation- and continuum-based formulation of models for extended crystal plasticity. *International Journal of Solids and Structures*, 43:7246–7267, 2006.
- [42] N. Ohno and D. Okumura. Higher-order stress and grain size effects due to self-energy of geometrically necessary dislocations. *Journal of the Mechanics and Physics of Solids*, 55:1879–1898, 2007.

- [43] M. E. Gurtin. A gradient theory of single-crystal viscoplasticity that accounts for geometrically necessary dislocations. *Journal of the Mechanics and Physics of Solids*, 50:5–32, 2002.
- [44] M. E. Gurtin. The burgers vector and the flow of screw and edge dislocations in finite-deformation single-crystal plasticity. *Journal of the Mechanics and Physics of Solids*, 54:1882–1898, 2006.
- [45] M. E. Gurtin, L. Anand, and S. P. Lele. Gradient single-crystal plasticity with free energy dependent on dislocation densities. *Journal of the Mechanics and Physics of Solids*, 55:1853–1878, 2007.
- [46] M. Kuroda and V. Tvergaard. Studies of scale dependent crystal viscoplasticity models. *Journal of the Mechanics and Physics of Solids*, 54:1789–1810, 2006.
- [47] M. Kuroda and V. Tvergaard. On the formulations of higher-order strain gradient crystal plasticity model. *Journal of the Mechanics and Physics of Solids*, 56:1591–1608, 2008.
- [48] A. Roy, R. H. J. Peerlings, M. G. D. Geers, and Y. Kasyanyuk. Continuum modeling of dislocation interactions: Why discreteness matters? *Material Science and Engineering A*, 486:653–661, 2008.
- [49] I. Groma, F. F. Csikor, and M. Zaiser. Spatial correlations and higher-order gradient terms in a continuum description of dislocation dynamics. *Acta Materialia*, 51:1271–1281, 2003.
- [50] E. Kröner. Allgemeine kontinuumstheorie der versetzungen und eigenspannungen. *Archieve for Rational Mechanics and Analysis*, 4:273–334, 1960.
- [51] E. H. Lee. Elastic-plastic deformation at finite strains. *Journal of Applied Mechanics*, 36:1–6, 1969.
- [52] F. F. Lavrentev. The type of dislocation interaction as the factor determining work hardening. *Material Science and Engineering*, 46:191–208, 1980.
- [53] P. Franciosi and A. Zaoui. Multislip in F.C.C. crystals: a theoretical approach compared with experimental data. *Acta Metallurgica*, 30:1627–1637, 1982.
- [54] A. Arsenlis and D. M. Parks. Modeling the evolution of crystallographic dislocation density in crystal plasticity. *Journal of the Mechanics and Physics of Solids*, 50:1979–2009, 2002.
- [55] M. G. D. Geers, W. A. M. Brekelmans, and C. J. Bayley. Second-order crystal plasticity: internal stress effects and cyclic loading. *Modelling and Simulation in Materials Science and Engineering*, 15:S133–S145, 2007.
- [56] U. Essmann and H. Mughrabi. Annihilation of dislocations during tensile and cyclic deformation and limits of dislocation densities. *Philosophical Magazine*, 40:731–756, 1979.
- [57] S. Sun, B. L. Adams, C. Shet, S. Saigal, and W. King. Mesoscale investigation of the deformation field of an aluminum bicrystal. *Scripta Materialia*, 39:501–508, 1998.
- [58] A. Arsenlis and D. M. Parks. Crystallographic aspects of geometrically-necessary and statistically-stored dislocation density. *Acta Materialia*, 47:1597–1611, 1999.

- [59] M. E. Gurtin and A. Needleman. Boundary conditions in small-deformation, single-crystal plasticity that account for the burgers vector. *Journal of Mechanics and Physics of Solids*, 53:1–31, 2005.
- [60] G. M. Rebeiz. *RF MEMS Theory, Design, and Technology*. Wiley-Interscience, 2003.
- [61] A. L. Hartzell, M. G. da Silva, and H. R. Shea. *Failure Modes and Mechanisms: Failure Modes and Mechanisms in MEMS*. Springer US, 2011.
- [62] H. J. Lee, G. Cornella, and J. C. Bravman. Stress relaxation in free-standing aluminum beams for microelectromechanical systems applications. *Applied Physics Letters*, 76(23):3415–3417, 2000.
- [63] X. Yan, W. L. Brown, Y. Li, J. Papapolymerou, C. Palego, J. C. M. Hwang, and R. P. Vinci. Anelastic stress relaxation in gold films and its impact on restoring forces in MEMS devices. *Journal of Microelectromechanical Systems*, 18(3):570–575, 2005.
- [64] X. Li, Y. Wei, and H. Gao. Competing grain boundary and dislocation mediated mechanisms in plastic strain recovery in nanoscale aluminum. *Proceedings of the National Academy of Sciences*, 106(38):16108–16113, 2009.
- [65] M. McLean, W. L. Brown, and R. P. Vinci. Temperature dependent viscoelasticity in thin Au films and consequences for MEMS devices. *Journal of Microelectromechanical Systems*, 19(6):1299–1308, 2010.
- [66] F. R. N. Nabarro. Creep in commercially pure metals. *Acta Materialia*, 54:263–295, 2006.
- [67] E. Arzt. Creep of dispersion strengthened materials: a critical assesment. *Res mechanica*, 31:399–453, 1991.
- [68] V. Burg, J. M. J. den Toonder, A. R. van Dijken, J. P. M. Hoefnagels, and M. G. D. Geers. Characterization method for mechanical properties of thin freestanding metal films for rf-mems. *EuroSime 2006: 7th International Conference on Thermal, Mechanical and Multi-physics Simulation and Experiments in Micro-Electronics and Micro-Systems*, pages 1 –7, 2006.
- [69] M. Gyimesi and D. Ostergaard. Electro-mechanical capacitor element for MEMS analysis in ANSYS. *Proceedings of Modelling and Simulation of Microsystems Conference*, page 270, 1999.
- [70] A. Arsenlis and D. M. Parks. Modeling the evolution of crystallographic dislocation density in crystal plasticity. *Journal of the Mechanics and Physics of Solids*, 50:1979–2009, 2002.
- [71] ANSYS Release 11. Element reference. ANSYS©, 2007.
- [72] ANSYS Release 11. Theory reference. ANSYS©, 2007.
- [73] İ. Ertürk, J. A. W. van Dommelen, and M. G. D. Geers. Energetic dislocation interactions and thermodynamical aspects of strain gradient crystal plasticity theories. *Journal of the Mechanics and Physics of Solids*, 57:1801–1814, 2009.
- [74] J. Bielen. Personal communication. *EPCOS, The Netherlands*.

- [75] J. Bielen and J. Stulemeijer. Efficient electrostatic-mechanical modeling of C-V curves of RF-MEMS switches. In *Thermal, Mechanical and Multi-Physics Simulation Experiments in Microelectronics and Micro-Systems, 2007. EuroSime 2007. International Conference on*, pages 1–6, 2007.
- [76] B. Clausen, T. Lorentzen, and T. Leffers. Self-consistent modelling of the plastic deformation of f.c.c. polycrystals and its implications for diffraction measurements of internal stresses. *Acta Materialia*, 46(9):3087–3098, 1998.
- [77] Z. Zhao, M. Ramesh, D. Raabe, A. Cuitino, and R. Radovitzky. Investigation of three-dimensional aspects of grain-scale plastic surface deformation of an aluminum oligocrystal. *International Journal of Plasticity*, 54(4):545, 2008. in press.
- [78] J. P. Hirth and J. Lothe. *Theory of dislocations*. Krieger, 1982.
- [79] F. Stellari and A.L. Lacaita. New formulas of interconnect capacitances based on results of conformal mapping method. *Electron Devices, IEEE Transactions on*, 47(1):222–231, 2000.
- [80] R. Modlinski, A. Witvrouw, P. Ratchev, A. Jourdain, V. Simons, H. A. C. Tilmans, J. M. J. den Toonder, R. Puers, and I. De Wolf. Creep as a reliability problem in MEMS. *Microelectronics Reliability*, 44:1133–1738, 2004.
- [81] D. Choi, H. Kim, and W. D. Nix. Anelasticity and damping of thin aluminum films on silicon substrates. *Journal of Microelectromechanical Systems*, 13(2):230–237, 2004.
- [82] J. Proost, A. Witvrouw, P. Cosemans, Ph. Roussel, and K. Maex. Stress relaxation in al(Cu) thin films. *Microelectronic Engineering*, 33:137–147, 1997.
- [83] A. Witvrouw, J. Proost, and Ph. Roussel. Stress relaxation in Al-Cu and Al-Si-Cu thin films. *Journal of Materials Research*, 14(4):1246–1254, 1999.
- [84] S. Hyun, T.K. Hooghan, W. L. Brown, and R. P. Vinci. Linear viscosity in aluminum thin films. *Applied Physics Letters*, 87:061902–1–3, 2005.
- [85] B.S. Berry and W.C. Pritchett. Defect studies of thin layers by the vibrating-reed technique. *Journal de Physique*, 42(10):C5–1111–1122, 1981.
- [86] M. Prieler, H.G. Bohn, W. Schilling, and H. Trinkaus. Grain boundary sliding in thin substrate-bonded Al films. *Journal of Alloys and Compounds*, 211–212:424–427, 1994.
- [87] H.G. Bohn, M. Prieler, C.M. Su, H. Trinkaus, and W. Schilling. Internal friction effects due to grain boundary sliding in large- and small-grained aluminium. *Journal of Physics and Chemistry of Solids*, 55(10):1157–1164, 1994.
- [88] Y. Wei, A. F. Bower, and H. Gao. Recoverable creep deformation due to heterogeneous grain boundary diffusion and sliding. *Scripta Materialia*, 57:933–936, 2007.
- [89] Y. Wei, A. F. Bower, and H. Gao. Recoverable creep deformation and transient local stress concentration due to heterogeneous grain boundary diffusion and sliding in polycrystalline solids. *Journal of the Mechanics and Physics of Solids*, 56:1460–1483, 2008.
- [90] W. G. Ferguson, A. Kumar, and J. E. Dorn. Dislocation damping in aluminum at high strain rate. *Journal of Applied Physics*, 38(4):1863–1869, 1967.

- [91] W. P. Mason. Mechanism for electron damping of dislocations in Pb. *Applied Physics Letters*, 6:111–112, 1965.
- [92] W. P. Mason. Effect of electron-damped dislocations on the determination of the superconducting energy gaps of metals. *Physical Review*, 143(1):229–235, 1966.
- [93] A. Kumar, F. E. Hauser, and J. E. Dorn. Viscous drag on dislocations in aluminum at high strain rates. *Acta Metallurgica*, 16:1189–1197, 1968.
- [94] M. P. Victoria, C. K. H. Drahan, F. E. Hauser, and J. E. Dorn. Dislocation damping at high strain rates in aluminum and aluminum-copper alloy. *Journal of Applied Physics*, 41(2):674–677, 1970.
- [95] L. F. Mondolfo. *Aluminum alloys: structure and properties*. Butterworth, London, 1976.
- [96] J. Friedel. *Dislocations*. Pergamon Press, 1964.
- [97] H. Sehitoglu, T. Foglesong, and H. J. Maier. Precipitate effects on the mechanical behavior of Aluminum Copper alloys: Part I. experiments. *Metallurgical and Materials Transactions A*, 36A:749–761, 2005.
- [98] S. C. Wang and M. J. Starink. Precipitates and intermetallic phases in precipitation hardening Al-Cu-Mg-(Li) based alloys. *International Materials Reviews*, 50:193–215.
- [99] R. Bonnet and M. Loubradou. Crystalline defects in a B.C.T. Al₂Cu single crystal obtained by unidirectional solidification along [001]. *Physica Status Solidi A*, 194(1):173–191, 2002.
- [100] T. Bončina, Miha Čekada, B. Markoli, and Frank Zupanič. Microindentation of dispersed phases in an Al₉₄Mn₂Be₂Cu₂ alloy. *Journal of Alloys and Compound*, 505:486–491, 2010.
- [101] M. A. Marcus and J. E. bower. Precipitation of Al₂Cu in blanket Al-Cu films. *Journal of Applied Physics*, 82(8):3821–3827, 1997.
- [102] Y. Gao, Q. Mo, Z. Luo, L. Zhang, and C. Huang. Atomic bonding and properties of Al-Cu alloy with θ (Al₂Cu). *Journal of Electronic Materials*, 35(10):1801–1805, 2006.
- [103] N. Boukhris, S. Lallouche, M. Y. Debili, and M. Draissia. Microhardness variation and related microstructure in Al-Cu alloys prepared by HF induction melting and RF sputtering. *The European Physical Journal Applied Physics*, 45:30501–1–8, 2009.
- [104] S. Mader and S. Herd. Formation of second phase particles in Al-Cu alloy films. *Thin Solid Films*, 10:377–378, 1972.
- [105] J. P. Looker, A. J. Botker, W. G. Sloof, F. D. Tichelaar, G. C. A. M. Janssen, and S. Radelaar. Phase transformations in Al-Cu thin films: precipitation and vopper redistribution. *Acta Materialia*, 49:1339–1349, 2001.
- [106] H. J. Frost and M. F. Ashby. *Deformation-Mechanism Maps: The Plasticity and Creep of Metals and Ceramics*. Pergamon, 1982.
- [107] R. W. Evans and B. Wilshire. *Creep of metals and alloys*. The Institute of Metals, 1985.
- [108] T. G. Langdon. Identifying creep mechanisms at low stresses. *Materials Science and Engineering A*, 283(1–2):266–273, 2000.

- [109] B. Wilshire, H. Burt, and A.J. Battenbough. Grain and grain boundary zone contributions to strain accumulation during creep of polycrystalline copper. *Material Science and Engineering A*, 410–411:16–19, 2005.
- [110] B. Wilshire and A.J. Battenbough. Creep and creep fracture of polycrystalline copper. *Material Science and Engineering A*, 443:156–166, 2007.
- [111] A. J. Ardell. Precipitation hardening. *Metallurgical Transactions*, 16A:2131–2165, 1985.
- [112] A. S. Argon. *Strengthening mechanisms in crystal plasticity*. Oxford University Press, New York, 2008.
- [113] J. W. Martin, editor. *Precipitation hardening*. Pergamon Press, Oxford, 1968.
- [114] L. M. Brown and R. K. Ham. *Strengthening methods in crystals*. Elsevier, 1971.
- [115] J. W. Martin. *Micromechanisms in particle-hardened alloys*. Cambridge university Press, Cambridge, 1980.
- [116] J. E. Foreman and M. J. Makin. Dislocation movement through random arrays of obstacles. *Philosophical Magazine*, 14(131):911–924, 1966.
- [117] D. Hull and D. J. Bacon. *Introduction to dislocations*. Butterworth–Heinemann, 2001.
- [118] F. R. N. Nabarro. *The Physics of Metals: Defects*, volume 2. Cambridge University Press, 1975.
- [119] E. Nembach. *Particle Strengthening of Metals and Alloys*. John wiley & Sons, Inc., New York, 1996.
- [120] R. L. Fleischer and W. R. Hibbard Jr. *The relation between the structure and mechanical properties of metals*. Her Majesty’s Stationery Office, London, 1963.
- [121] K. Hanson and J. W. Morris. Limiting configuration in dislocation glide through a random array of point obstacles. *Journal of Applied Physics*, 46:983–990, 1975.
- [122] U. F. Kocks. A statistical theory of flow stress and work-hardening. *Philosophical Magazine*, 123(13):541 – 566, 1966.
- [123] R. B. Schwarz and R. Labusch. Dynamic simulation of solution hardening. *Journal of Applied Physics*, 49:5174–5187, 1978.
- [124] N. F. Mott and F. R. N. Nabarro. *Report on Strength of Solids*. Physical Society, London, 1948.
- [125] N. F. Mott. *Imperfections in Nearly Perfect Crystals*. Wiley, New York, 1950.
- [126] R. Labusch. Statistische theorien der mischkristallhärtung. *Acta Metallurgica*, 20(7):917–927, 1972.
- [127] H. Gleiter and E. Hornbogen. Precipitation hardening by coherent particles. *Materials Science and Engineering*, 2:285–302, 1967.
- [128] G. E. Dieter. *Mechanical metallurgy*. McGraw–Hill, 1981.

- [129] E. Nembach and G. Neite. Precipitation hardening of superalloys by ordered γ' - particles. *Progress in Materials Science*, 29:177–319, 1985.
- [130] J. M. Howe. *Interfaces in materials*. John Wiley & Sons, 1997.
- [131] E. Nembach. Stacking fault strengthening in F.C.C. alloys. *Scripta Metallurgica*, 20:763–768, 1986.
- [132] V. Gerold and K. Hartmann. Theoretical and experimental investigations on stacking-fault strengthening. In *Proceedings of International Conference on the Strength of Metals and Alloys*, volume 9. Japan Institute of Metals, 1968.
- [133] P. B. Hirsch and A. Kelly. Stacking-fault strengthening. *Philosophical Magazine*, 12(119):881–900, 1965.
- [134] E. Nembach, T. Pretorius, and D. Rönnpagel. Stacking fault energy mismatch strengthening revisited. *Philosophical Magazine*, 78(4):949–963, 1991.
- [135] V. Gerold and H. Haberkorn. On the critical resolved shear stress of solid solutions containing coherent precipitates. *Physica Status Solidi*, 16:675–684, 1966.
- [136] V. Gerold. On the calculations of the CRSS of alloys containing coherent precipitates. *Acta Metallurgica*, 16:823–827, 1968.
- [137] V. Gerold and H. M. Pham. Precipitation hardening by misfitting particles and its comparison with experiments. *Scripta Metallurgica*, 13:895–898, 1979.
- [138] E. Nembach. Hardening by coherent precipitates having a lattice mismatch: the effect of dislocation splitting. *Scripta Metallurgica*, 18:105–110, 1984.
- [139] E. Nembach. Precipitation hardening caused by a difference in shear modulus between particle and matrix. *Physica Status Solidi A*, 78(2):571–581, 1983.
- [140] R. E. Peierls. The size of a dislocation. *Proceedings of the Physical Society*, 52(1):34–37, 1940.
- [141] F. R. N. Nabarro. Dislocations in a simple cubic lattice. *Proceedings of the Physical Society*, 59(2):256–272, 1947.
- [142] J. N. Wang. Prediction of Peierls stresses for different crystals. *Materials Science and Engineering*, A206:259–269, 1996.
- [143] J. N. Wang. A new modification of the formulation of Peierls stresses. *Acta Materialia*, 44(4):1541–1546, 1996.
- [144] R. S. W. Shewfelt and L. M. Brown. High-temperature strength of dispersion-hardened single crystals II: Theory. *Philosophical Magazine*, 35(4):945–962, 1977.
- [145] E. Arzt and D. S. Wilkinson. Threshold stresses for dislocation climb over hard particles: the effect of an attractive interaction. *Acta Metallurgica*, 34(10):1893–1898, 1986.
- [146] E. Arzt and J. Rösler. The kinetics of dislocation climb over hard particles–II: Effects of an attractive particle-dislocation interaction. *Acta Metallurgica*, 36(4):1053–1060, 1988.
- [147] J. Rösler and E. Arzt. The kinetics of dislocation climb over hard particles–I: Climb without attractive particle-dislocation interaction. *Acta Metallurgica*, 36(4):1043–1051, 1988.

- [148] J. Rösler. Back-stress calculation for dislocation climb past non-interacting particles. *Materials Science and Engineering A*, 339:334–339, 2003.
- [149] R. S. Mishra. Dislocation-particle interaction at elevated temperatures. *Journal of the Minerals, Metals and Materials Society*, 61(2):52–55, 2009.
- [150] D. J. Srolovitz, M. J. Luton, R. Petkovic-Luton, D. M. Barnett, and W. D. Nix. Diffusionally modified dislocation-particle elastic interactions. *Acta Metallurgica*, 32(7):1079–1088, 1984.
- [151] E. Arzt, G. Dhem, P. Gumbsch, O. Kraft, and D. Weiss. Interface controlled plasticity in metals: dispersion hardening and thin film deformation. *Progress in Materials Science*, 46:283–307, 2001.
- [152] J. Rösler and E. Arzt. A new model-based creep equation for dispersion strengthened materials. *Acta Metallurgica et Materialia*, 38(4):671–681, 1990.
- [153] B. Reppich. On the attractive particle-dislocation interaction in dispersion-strengthened material. *Acta Materialia*, 46(1):61–67, 1998.
- [154] G. de Wit and J. S. Koehler. Interaction of dislocations with an applied stress in anisotropic crystals. *Physical Review*, 116:1113–1120, 1959.
- [155] A. Melander and P. Persson. Strength and structure of an AlZnMg alloy after double ageing treatments. *Scandinavian Journal of Metallurgy*, 7(4):181–186, 1978.
- [156] J. P. Hirth, T. Jossang, and J. Lothe. Dislocation energies and concept of line tension. *Journal of Applied Physics*, 37(1):110–116, 1966.
- [157] U. F. Kocks. The theory of an obstacles-controlled yield strength— report after an international workshop. *Materials Science and Engineering*, 27:291–298, 1977.
- [158] E. Nembach. How the choice of the dislocations’ outer cut-off radius affects the evaluation of precipitation hardening data. *Scripta Metallurgica*, 16(11):1261 – 1265, 1982.
- [159] U. F. Kocks, A. S. Argon, and M. F. Ashby. Thermodynamics and kinetics of slip. *Progress in Materials Science*, 19:1–281, 1975.
- [160] G. Regazzoni, U. F. Kocks, and P. S. Follansbee. Dislocation kinetics at high strain rates. *Acta Metallurgica*, 35(12):2865–285, 1987.
- [161] F. R. Eshelman and J. F. Smith. Single-crystal elastic constants of Al₂Cu. *Journal of Applied Physics*, 49(6):3284–3288, 1978.
- [162] W. Zhou, L. Liu, B. Li, Q. Song, and P. Wu. Structural, elastic and electronic properties of Al-Cu intermetallics from first-principles calculations. *Journal of Electronic Materials*, 38(2):356–364, 2009.
- [163] F. Apostol and Y. Mishin. Interatomic potential for the Al-Cu system. *Physical Review B*, 83:054116–1–8, 2011.
- [164] P. C. J. Gallagher. Influence of alloying, temperature, and related effects on the stacking fault energy. *Metallurgical Transactions*, 1:2429–61, 1970.
- [165] L. E. Murr. *Interfacial Phenomena in Metals and Alloys*. Addison-Wesley, 1975.

- [166] G. C. Weatherly and R. B. Nicholson. An electron microscope investigation of the interfacial structure of semi-coherent precipitates. *Philosophical Magazine*, 17(148):801–831, 1968.
- [167] V. Vaithyanathan, C. Wolverton, and L. Q. Chen. Multiscale modeling of precipitate microstructure evolution. *Acta Materialia*, 52(10):2973 – 2987, 2004.
- [168] A. Ma, F. Roters, and D. Raabe. A dislocation density based constitutive model for crystal plasticity fem including geometrically necessary dislocations. *Acta Materialia*, 54:2169–2179, 2006.
- [169] A. S. Oates. Electromigration transport mechanisms in Al thin-film conductors. *Journal of Applied Physics*, 79(1):163–169, 1996.
- [170] N. A. Gjostein. *Diffusion*. American Society for Metals Proceedings, 1973.
- [171] R. W. Balluffi and J. M. Blakely. Special aspects of diffusion in thin films. *Thin Solid Films*, 25:363–392, 1975.
- [172] T. O. Ogurtani T. G. Stoebe, R. D. Gulliver II and R. A. Huggins. Nuclear magnetic resonance studies of diffusion of Al²⁷ in aluminum and aluminum alloys. *Acta Metallurgica*, 13(7):701–708, 1965.
- [173] T. D. Sullivan K. Y. Lee C. K. Hu, K. P. Rodbell and D. P. Bouldin. Electromigration and stress-induced voiding in fine Al and Al-alloy thin-film lines. *IBM Journal of Research and Development*, 39(4):465–497, 1995.
- [174] A. Gangulee and F. M. D’Heurle. Anomalous large grains in alloyed aluminum thin films II. electromigration and diffusion in thin films with very large grains. *Thin Solid Films*, 16(2):227–236, 1973.
- [175] H.-U. Schreiber. Activation energies for the different electromigration mechanisms in aluminum. *Solid-State Electronics*, 24(6):583 – 589, 1981.
- [176] F. Fantini A. Scorzoni, B. Neri C. Caprile. Electromigration in thin-film interconnection lines: models, methods and results. *Materials Science Reports*, 7:143–220, 1991.
- [177] C. Witt, C. A. Volkert, and E. Arzt. Electromigration-induced Cu motion and precipitation in bamboo Al-Cu interconnects. *Acta Materialia*, 51(1):49–60, 2003.
- [178] J. C. Gibeling and W. D. Nix. Observations of anelastic backflow following stress reductions during creep of pure metals. *Acta Metallurgica*, 29:1769–1784, 1981.
- [179] İ. Ertürk, J. A. W. van Dommelen, and M. G. D. Geers. Modeling time and scale dependent behavior of particle hardened alloys by a strain gradient crystal plasticity theory. *In preparation*.

Samenvatting

Samenvatting Voor kleine volumes materiaal kunnen lengteschaaleffecten, zoals door de aanwezigheid van interfaces of heterogene rekvelden, significant bijdragen aan het mechanische gedrag van metalen. Hierdoor kan een deformatie mechanisme dat minder belangrijk is voor het gedrag van het materiaal in bulk vorm bepalend worden voor de prestaties van het materiaal. Zulke tweede orde effecten zijn experimenteel vastgesteld en vormen belangrijke uitdagingen voor de ontwikkeling en productie van geavanceerde moderne technologie. Zo kunnen bijvoorbeeld kruip en anelasticiteit, zoals waargenomen in dunne metallische componenten van capacitieve RF-MEMS schakelaars, leiden tot tijdsafhankelijke afwijkingen van ontwerpspecificaties van een product. Karakterisatie en begrip van het mechanische gedrag van het materiaal zijn cruciaal voor het oplossen van betrouwbaarheidsvraagstukken voor deze schakelaars, die commercialisering van deze producten in de weg staan. In dit proefschrift wordt een numeriek model gepresenteerd voor het beschrijven van het tijdsafhankelijke mechanische gedrag van dunne films van deeltjesversterkte fcc legeringen als een uitbreiding van een eerder ontwikkeld rekgradiënten kristalplasticiteitsmodel (SGCP) voor pure fcc metalen, waarnaar verwezen wordt als het Evers-Bayley type model. Een vloeiwet met een fysische achtergrond voor kristallografische slip is ontwikkeld gebaseerd op mechanismen voor dislocatie-dislocatie en dislocatie-deeltje interacties. Het uitgebreide SGCP model is in staat om de effecten van een inhomogene verdeling van geometrisch noodzakelijke dislocatiedichtheden op het materiaalgedrag te beschrijven via de formulering van een back stress met daarin een lengteschaal.

In hoofdstuk 2 zijn het fysisch gebaseerde Evers-Bayley type model en een thermodynamisch consistente rekgradiënttheorie voor kristalplasticiteit van Gurtin vergeleken door middel van het afleiden van de microspanningen voor het Gurtin type model gebaseerd op de energetische back stresses van het Evers-Bayley type model waarin dislocatie-dislocatie interacties zijn opgenomen. Aangevoerd is dat de energiefunctie voor een microspanning die gebaseerd is op de fysische beschrijving van de interactie tussen dislocaties in verschillende slip systemen een meer gecompliceerde vorm heeft dan gesuggereerd wordt in de literatuur en mogelijk niet convex is. Het is ook aangetoond dat vergelijkbare randvoorwaarden gedefinieerd kunnen worden voor het Evers-Bayley type model en het Gurtin type model ondanks de verschillende toegevoegde vergelijkingen in de eindige elementenformulering. Vervolgens is in hoofdstuk 3 het SGCP model toegepast in elektromechanische eindige elementensimulaties van buiging van polykristallijne dunne balken van een zuiver metaal en een tweefasen legering met daarbij een nadruk op anelastisch materiaalgedrag. Numerieke resultaten verkregen met het SGCP model laten een macroscopisch rekherstel in de tijd volgend op het verwijderen van de belasting zien. Een gedetailleerde analyse laat echter zien dat de anelastische relaxatietijd en sterkte geen goede fysische basis hebben. Een vergelijking van de resultaten met experimentele data laat zien dat een enkel deformatiemechanisme mogelijk

niet voldoende is voor het beschrijven van het materiaalgedrag. Verder is de slipwet niet in staat om het gedrag van een deeltjesversterkt materiaal te beschrijven. Een uitbreiding van het SGCP model voor een meer realistische beschrijving van het tijdsafhankelijke mechanische gedrag van tweefasen legeringen, te weten kruip en anelasticiteit, is gegeven in hoofdstuk 4 en de toepassing ervan in multifysische simulaties van een capacitieve RF-MEMS schakelaar is gepresenteerd in hoofdstuk 5. Een nieuwe constitutieve wet voor kristallografische slip is ontwikkeld waarbij dislocatie-dislocatie interacties en drie verschillende interacties tussen dislocaties en deeltjes zijn beschouwd: i) het Orowan proces, ii) het Friedel proces en iii) het klimmen van dislocaties over deeltjes. De nieuwe constitutieve wet is verkregen door het combineren van de afzonderlijke slipwetten voor ieder type interactie en is opgesteld gebaseerd op de fysisch onderbouwde Orowan type snelheidsafhankelijke formulering. Een vloeiwet voor de slipsnelheid door mobiele dislocaties en gebaseerd op dislocatie-dislocatie interacties is opgesteld waarbij onregelmatige en continue regimes van dislocatiebeweging zijn opgenomen. Slip wetten overeenkomstig met de Orowan en Friedel processen zijn opgesteld gebaseerd op thermisch geactiveerde dislocatiebeweging. Het klimmen van randdislocaties is beschreven via een thermisch scheidingsmodel. Resultaten van eindige elementensimulaties van buiging van een dunne balk van een éénkristal en een microklem experiment met het uitgebreide SGCP model laten zien dat kruip en anelastisch gedrag van een metallische dunne film beschreven kunnen worden. De hoeveelheden van de plastische deformatie, anelastisch herstel en de bijbehorende relaxatietijden hangen sterk af van de eigenschappen van de deeltjes, de diffusiesnelheid en de grootte van de interne spanningen. De resultaten van de simulaties van het microklem experiment laten zien dat inhomogene diffusie mogelijk een grote rol speelt in het anelastische gedrag van polykristallijne dunne films. De resultaten laten ook zien dat de interne spanningsformulering van het uitgebreide SGCP model mogelijk uitgebreid dient te worden met extra bronnen voor interne spanningen. Het uitgebreide SGCP model is toegepast voor de analyse van het gedrag van een capacitieve RF-MEMS schakelaar in multifysische simulaties. De elektrodes van de schakelaar zijn verondersteld te bestaan uit een metalen dunne film met incoherente tweede fase deeltjes en een polykristalijne structuur met kolomvormige korrels door de dikte met gepassiveerde oppervlakten. De variatie van de spleet tussen de elektrodes in de tijd is geanalyseerd. De invloed van de deeltjesgrootte, volume fractie, oppervlaktecondities en filmdikte op het gedrag van de schakelaar na een cyclus van belasting en ontlasting zijn bestudeerd. Vervolgens zijn de effecten van een cyclische belasting en de duur van de onbelaste toestand tussen twee opeenvolgende cycli bestudeerd. De resultaten laten zien dat de residuele veranderingen in de spleetgrootte en de hoeveelheid en snelheid van tijdsafhankelijk herstel na verwijdering van de belasting zeer gevoelig zijn voor de microstructuur en de filmdikte. De kleinste hoeveelheid permanente deformatie en anelastisch herstel zijn verkregen met een bovenste elektrode gemaakt van een relatief dunne film met een gepassiveerd oppervlakte en kleine incoherente deeltjes met een relatieve grote volumefractie. Verder blijkt uit de simulaties dat de maximale residuele verandering van de spleetgrootte gemeten na voltooiing van het onbelaste stadium van iedere cyclus verzadigt binnen enkele cycli. Een kortere duur van de onbelaste toestand tussen opeenvolgende cycli van belasting en ontlasting leidt tot een grotere maximale verandering van de residuele spleetgrootte. Door de afnemende spleetgrootte neemt het pull-in voltage tevens af binnen enkele cycli en vlakkt deze verandering af naar een bepaald niveau. Echter, het release voltage blijkt niet zo gevoelig te zijn voor residuele deformaties als het pull-in voltage.

Tenslotte worden in hoofdstuk 6 de conclusies en aanbevelingen voor toekomstig onderzoek gegeven.

Acknowledgements

I would like to express my deepest gratitude to Marc Geers not only for giving me the opportunity to become a member of his research group, but also for his continuous encouragement, which was indeed not limited to scientific matters. I would like to acknowledge my advisor, Hans van Domelen, for his willingness to provide all kinds of support. I should emphasize that I particularly enjoyed working with him during the last months of my work despite a range of extra difficulties involved. I also would like to thank Ron Peerlings, who always gave of his time when I knocked on his door several times for a discussion.

I sincerely thank the committee members, prof.dr. Esteban Busso, prof.dr.ir. Fred van Keulen, prof.dr.ir. J.M.J. den Toonder, prof.dr.ir. Laurent Delannay and dr. Marcel van Gils for their interest and constructive comments on this thesis.

I like to thank Jeroen Bielen for sharing his time for fruitful discussions, his support in numerical modeling and providing experimental data. In addition, I thank my student Kun Gao, who is involved in this research during his master thesis studies, the results of which contributed to this dissertation.

My special thanks go to Leo Wouters for his assistance and patience regarding the hardware and software problems that I had and that I led to. I also thank Alexei for diverting me to Ubuntu. I am very grateful to Alice, who generously offered her help anytime needed. I thank Marleen and Yvon for their kindness.

I would like to acknowledge my former and current colleagues, with whom I enjoyed chatting on different topics during coffee breaks, symposia and conferences. My (ex-)officemates Lambert, Michiel, Müge, Sam, Sebastiaan and Zhe, thank you all for the peaceful working environment and for the joyful conversations. Thank you Selim, for everything!

I would love to thank gratefully Kurtuluş, Atike & Koray, Barış, İlhan and Uğur, who were always available not only at the good moments, but also through my hard times, making the life in Eindhoven meaningful. I sincerely thank to Saliha & Ferhat for our long-lasting friendship and for pleasing me now with their presence! I gladly acknowledge the current line-up of The Endings, Ela, İlhan, Koray, Uğur, and our former crew Berkan, Gözde, Hilal, Marco and Pelin, with whom I have been having the best Fridays and the best memories of my life in Eindhoven.

Last but not least, I would like to take the opportunity to thank my parents Ayşe and Rafet, to whom I am deeply indebted for their endless love and support. My brother Hüseyin and my sister Nigar, thanks a million my best friends.

Eindhoven, April 2012

İsa Ertürk

Curriculum Vitae

İsa Ertürk was born on November 9, 1983 in Samsun, Türkiye. After finishing his high school education at Samsun Namık Kemal Lisesi in 2000, he studied Civil Engineering at Middle East Technical University in Ankara and received his B.Sc. degree in 2005. Afterwards, he continued his master studies with a full scholarship from German Academic Exchange Service (DAAD)-Turkish Education Foundation (TEV) at the University of Stuttgart and got his M.Sc. degree on computational mechanics of materials and structures (COMMAS) in 2007. He has been working in the MicroNed project on the mechanics of dynamically loaded free-standing thin films, at the Mechanical Engineering Department of the Eindhoven University of Technology, under the supervision of Prof.Dr.Ir. M.G.D. Geers and Dr.Ir. J.A.W. van Dommelen since 2007.

